

KWAME NKRUMAH UNIVERSITY OF SCIENCE AND TECHNOLOGY, KUMASI

COLLEGE OF SCIENCE

DEPARTMENT OF CHEMISTRY

SYNTHESIS OF LEAD CHALCOGENIDE NANOPARTICLES AND THIN FILMS
FROM SINGLE-SOURCE PRECURSORS.

A THESIS SUBMITTED TO THE DEPARTMENT OF CHEMISTRY,
KWAME NKRUMAH UNIVERSITY OF SCIENCE AND TECHNOLOGY, KUMASI
IN PARTIAL FULFILMENT OF THE REQUIREMENTS FOR THE AWARD OF PHD
INORGANIC CHEMISTRY DEGREE.

BY

NATHANIEL OWUSU BOADI

MSc. ENVIRONMENTAL CHEMISTRY

DECEMBER, 2014

Declaration

I hereby declare that no part of this thesis has been submitted in support of an application for any degree or qualification of the Kwame Nkrumah University of Science and Technology or any other university or institution of learning except where due acknowledgement has been made in the text.

.....

Nathaniel Owusu Boadi (PG6148511)

.....

date

Student Name and ID

Certified by:

.....

Dr. J.A.M. Awudza

.....

date

(Supervisor)



4/5/15

.....

Prof. P. O'Brien

.....

date

(Supervisor)

.....

Dr. G. Darko

.....

date

(Head of Department)

Dedication

To my wife Mercy and our children, Amoanimaa, Kwame and Kobby.

Table of Contents

Declaration.....	II
Dedication.....	III
Table of Contents.....	IV
Table of Figures.....	XIII
List of Tables.....	XIX
List of Abbreviations.....	XX
Acknowledgement.....	XXII
Abstract.....	XXIII
Chapter 1.....	1
Introduction.....	1
1.1 Relevance of work.....	3
1.2 Statement of problem.....	3
1.3 Scope of work.....	4
1.4 Objectives.....	5
1.5 Thesis layout.....	5
Chapter 2.....	7
Literature review.....	7
2.2 General introduction.....	7
2.3 Structure of Pb(II) complexes.....	12
2.4 Single-source precursors.....	13
2.4.1 Lead dichalcogenocarbamato complexes.....	14

2.4.2	Lead dichalcogenophosphinato complexes.....	15
2.4.3	Lead dichalcogenophosphato complexes.....	19
2.4.4	Lead imidodichalcogenodiphosphinato complexes	20
2.4.5	Lead selenoureato complexes	22
2.4.6	Lead xanthato complexes.....	25
2.4.7	Other Single-source precursors.....	27
2.5	Electronic structure of semiconductors	29
2.6	Extrinsic and intrinsic semiconductors	31
2.7	Direct and indirect band gap semiconductors	32
2.8	Deposition of thin films.....	35
2.9	Types of chemical vapour deposition.....	36
2.10	Nanocrystals of semiconductors.....	38
2.11	Synthesis of nanocrystals (NCs)	39
2.12	Growth process of nanocrystals	40
2.13	Applications of semiconductor nanocrystals.....	41
2.13.1	Photovoltaics	41
2.13.2	Thermoelectrics	42
2.13.3	Light emitting diodes.....	42
2.13.4	Counterfeiting applications.....	43
2.13.5	Biological applications	44
2.14	Lead sulphide (PbS) nanocrystals	45

2.15	Lead selenide (PbSe) nanocrystals	47
2.16	Lead telluride (PbTe) nanocrystals	48
2.17	Applications of lead chalcogenide nanocrystals (NCs).....	50
2.17.1	Photovoltaic devices	50
2.17.2	Photonic devices	53
2.17.3	Quantum dot-polymer light emitters	55
2.17.4	Biological applications	56
Chapter 3	58
General Experimental Procedures	58
3.1	Summary	58
3.2	Synthesis and characterisation of ligands and complexes.....	59
3.2.1	Synthesis of ${}^i\text{Pr}_2\text{P}(\text{Se})\text{NHP}(\text{Se}){}^i\text{Pr}_2$ ligand (1)	59
3.2.2	Synthesis of ${}^i\text{Pr}_2\text{P}(\text{S})\text{NHP}(\text{S}){}^i\text{Pr}_2$ ligand (2).....	60
3.2.3	Synthesis of ${}^i\text{Pr}_2\text{P}(\text{Se})\text{NHP}(\text{S}){}^i\text{Pr}_2$ ligand (3).....	60
3.2.4	Synthesis of $[\text{Pb}((\text{SeP}{}^i\text{Pr}_2)_2\text{N})_2]$ complex (4)	61
3.2.5	Synthesis of $[\text{Pb}((\text{SP}{}^i\text{Pr}_2)_2\text{N})_2]$ complex (5)	62
3.2.6	Synthesis of $[\text{Pb}(\text{SeS}(\text{P}{}^i\text{Pr}_2)_2\text{N})_2]$ complex (6).	62
3.2.7	Synthesis of $[\text{Ph}_2\text{P}(\text{Se})\text{NHP}(\text{Se})\text{Ph}_2]$ ligand (7).....	62
3.2.8	Synthesis of $[\text{Ph}_2\text{P}(\text{S})\text{NHP}(\text{S})\text{Ph}_2]$ ligand (8)	63
3.2.9	Synthesis of $[\text{Pb}((\text{SePPh}_2)_2\text{N})_2]$ complex (9).....	64
3.2.10	Synthesis of $[\text{Pb}((\text{SPPh}_2)_2\text{N})_2]$ complex (10).....	64

3.2.11	Synthesis of <i>Bis</i> (thiourea) lead (II) complex (11).....	65
3.2.12	Synthesis of diphenylselenophosphinate $[\text{HNEt}_3]^+[\text{Ph}_2\text{PSe}_2]^-$ ligand (12)	65
3.2.13	Synthesis of $\text{Pb}(\text{S}_2\text{CNET}_2)_2$ complex (13).....	66
3.2.14	Synthesis of $\text{Pb}(\text{S}_2\text{CNMe}_2)_2$ complex (14).....	66
3.2.15	Synthesis of $[\text{Pb}(\text{S}_2\text{COEt})_2]$ complex (15).....	67
3.2.16	Synthesis of <i>N</i> -methyl- <i>N</i> -hexyldithiocarbamatolead(II) (16).....	67
3.3	Thermogravimetric analysis (TGA).....	68
3.4	Single crystal X-ray crystallography and powder X-ray diffraction.....	68
3.5	Aerosol assisted chemical vapour deposition (AACVD) apparatus	68
3.6	Deposition procedure of lead chalcogenide thin films of by AACVD	69
3.7	Characterisation techniques.....	70
3.7.1	Transmission electron microscopy (TEM)	70
3.7.2	Powder X-ray diffraction	71
3.7.3	Scanning electron microscopy (SEM)	73
3.7.4	Energy dispersive X-ray analysis (EDAX)	74
Chapter 4	75
Synthesis and characterisation of binary lead chalcogenide nanocrystals and thin films.....		75
4.1	Summary	75
4.2	Introduction	75
4.3	Materials and methods	77
4.3.1	Synthesis of lead chalcogenide nanoparticles.....	77

4.3.2	Spectroscopic and analytical measurements	78
4.3.3	Single-crystal X-ray diffraction studies	78
4.4	Results	80
4.4.1	X-ray single crystal structures of [Pb((SP ⁱ Pr ₂) ₂ N) ₂] (5) and [Pb(SeS(P ⁱ Pr ₂) ₂ N) ₂] (6).	80
4.4.2	Thermogravimetric analysis.....	82
4.4.3	Lead chalcogenide nanoparticles	83
4.4.3.1	p-XRD of PbSe nanoparticles	83
4.4.3.1.1	High Resolution Transmission Electron Microscope (HRTEM) and TEM images of nanoparticles obtained from complex 4.....	84
4.4.3.2	p-XRD of PbS nanoparticles	84
4.4.3.2.1	HRTEM and TEM images of nanoparticles obtained from complex 5	85
4.4.3.3	p-XRD of nanoparticles from mixed ligand complex 6.....	86
4.4.3.3.1	HRTEM and TEM images of nanoparticles obtained from complex 6	87
4.4.4	Optical properties of lead chalcogenides	87
4.4.4.1	Band gap of PbSe nanoparticles from bis(imidodiisopropyldiselenophosphinato) lead (II).....	88
4.4.4.2	Band gap of PbS nanoparticles from bis(imidodiisopropyldithiophosphinato) lead (II).	89
4.4.4.3	Band gap of nanoparticles from bis(imidodiisopropylthioselenophosphinato) lead (II).	90

4.4.5	Deposition of lead chalcogenide thin films by Aerosol Assisted Chemical Vapour Deposition (AACVD).....	91
4.4.5.1	p-XRD of Lead selenide thin films	92
4.4.5.1.1	SEM images of lead selenide thin films.....	92
4.4.5.2	p-XRD of lead sulphide thin films	93
4.4.5.2.1	SEM images of lead sulphide thin films	94
4.4.5.3	p-XRD of lead selenide thin films.....	94
4.4.5.3.1	SEM images of thin films from complex 6.....	95
4.5	Conclusion.....	96
Chapter 5.....		97
Synthesis of novel Single-source precursors for the production of ternary lead chalcogenides		97
5.1	Summary	97
5.2	Introduction	97
5.3	Experimental	98
5.3.1	Synthesis of $[\text{Pb}((\text{SeP}^i\text{Pr}_2)(\text{SP}^i\text{Pr}_2)\text{N})_2]$, $[\text{Pb}((\text{SeP}^i\text{Pr}_2)_2\text{N}(\text{S}_2\text{CNEt}_2))]$ and $[\text{Pb}((\text{SeP}^i\text{Pr}_2)_2\text{N}(\text{S}_2\text{CNHexMe}))]$ complexes	98
5.4	Results.....	98
5.4.1	Spectroscopic studies of $[\text{Pb}((\text{SeP}^i\text{Pr}_2)(\text{SP}^i\text{Pr}_2)\text{N})_2]$ complex.....	98
5.4.1.1	^1H NMR.....	98
5.4.1.2	^{31}P NMR.....	99
5.4.1.3	^{77}Se NMR	101

5.4.1.4	Melting point	101
5.4.1.5	FT-IR Analysis of $[\text{Pb}((\text{SeP}^i\text{Pr}_2)(\text{SP}^i\text{Pr}_2)\text{N})_2]$	102
5.4.1.6	p-XRD Analysis of $[\text{Pb}((\text{SeP}^i\text{Pr}_2)(\text{SP}^i\text{Pr}_2)\text{N})_2]$	102
5.4.1.7	X-ray single crystal structures of $[\text{Pb}((\text{SeP}^i\text{Pr}_2)(\text{SP}^i\text{Pr}_2)\text{N})_2]$ (6).	103
5.4.2	Spectroscopic studies of $[\text{Pb}((\text{SeP}^i\text{Pr}_2)_2\text{N}(\text{S}_2\text{CNEt}_2))]$	105
5.4.2.1	^1H NMR.....	105
5.4.2.2	^{31}P NMR.....	106
5.4.2.3	^{13}C NMR	107
5.4.2.4	^{77}Se NMR	108
5.4.2.5	Melting point for $[\text{Pb}((\text{SeP}^i\text{Pr}_2)_2\text{N}(\text{S}_2\text{CNEt}_2))]$	109
5.4.2.6	J-resolved NMR for $[\text{Pb}((\text{SeP}^i\text{Pr}_2)_2\text{N}(\text{S}_2\text{CNEt}_2))]$	109
5.4.2.7	Diffusion ordered spectroscopy (DOSY).....	113
5.4.2.8	FT-IR analysis for $[\text{Pb}((\text{SeP}^i\text{Pr}_2)_2\text{N}(\text{S}_2\text{CNEt}_2))]$	114
5.4.2.9	Melting point and micro elemental analysis	114
5.4.2.10	p-XRD analysis of $[\text{Pb}((\text{SeP}^i\text{Pr}_2)_2\text{N}(\text{S}_2\text{CNEt}_2))]$ product (18).....	115
5.4.2.11	Single-crystal X-ray diffraction studies	116
5.4.3	Spectroscopic studies of $\text{Pb}(((\text{SeP}^i\text{Pr}_2)_2\text{N})(\text{S}_2\text{CNHexMe}))]$	118
5.4.3.1	^1H NMR	118
5.4.3.2	^{31}P NMR.....	119
5.4.3.3	^{13}C NMR	120
5.4.3.4	^{77}Se NMR.....	121

5.4.3.5 FT-IR for Pb[(SeP ⁱ Pr ₂) ₂ N(S ₂ CNHexMe)]	122
5.4.3.6 Melting point and micro elemental analysis	123
5.4.3.7 p-XRD for Pb[(SeP ⁱ Pr ₂) ₂ N(S ₂ CNHexMe)].....	124
5.4.3.8 Single-crystal X-ray diffraction studies of Pb[((SeP ⁱ Pr ₂) ₂ N)(S ₂ CNHexMe)].	125
Chapter 6.....	128
Synthesis of PbS _x Se _{1-x} Thin Films by Pyrolysis and Aerosol Assisted Chemical Vapour Deposition.....	128
6.1 Summary	128
6.2 Introduction	128
6.3 Result.....	129
6.3.1 Thermogravimetric analysis	129
6.3.2 Synthesis of PbS _x Se _{1-x} thin films by aerosol assisted chemical vapour deposition (AACVD)	130
6.3.2.1 p-XRD of thin films	131
6.3.2.2 SEM images of thin films	133
6.3.2.2.1 SEM images of thin films deposited from [Pb((SeP ⁱ Pr ₂)(SP ⁱ Pr ₂)N) ₂] by AACVD.....	133
6.3.2.2.2 SEM images of thin films deposited from [Pb((SeP ⁱ Pr ₂) ₂ N(S ₂ CNEt ₂) ₂)] by AACVD.....	135
6.3.2.2.3 SEM images of thin films deposited from [Pb((SeP ⁱ Pr ₂) ₂ N(S ₂ CNHexMe))] by AACVD.....	137

6.3.2.3 Effect of temperature on particle size distribution for $\text{PbS}_x\text{Se}_{1-x}$ thin films from $[\text{Pb}((\text{SeP}^i\text{Pr}_2)(\text{SP}^i\text{Pr}_2)\text{N})_2]$, $[\text{Pb}((\text{SeP}^i\text{Pr}_2)\text{N}(\text{S}_2\text{CNEt}_2))]$, $[\text{Pb}((\text{SeP}^i\text{Pr}_2)\text{N}(\text{S}_2\text{CNHexMe}))]$..	138
6.3.3 Comparison of PbSe thin films obtained from Single-source precursors suitable....	141
for depositing binary and ternary lead chalcogenides.....	141
6.3.4 Pyrolysis of $[\text{Pb}((\text{SeP}^i\text{Pr}_2)_2\text{N}(\text{S}_2\text{CNEt}_2))]$	143
6.3.4.1 Powder XRD of pyrolysed mixed $[\text{Pb}((\text{SeP}^i\text{Pr}_2)_2\text{N}(\text{S}_2\text{CNEt}_2))]$	143
6.3.4.1.1 SEM analysis of pyrolysed $[\text{Pb}((\text{SeP}^i\text{Pr}_2)_2\text{N}(\text{S}_2\text{CNEt}_2))]$	144
6.4 Conclusion.....	145
Chapter 7.....	147
Summary and conclusions	147
7.1 Summary	147
7.2 Conclusion.....	148
7.3 Future work	149
References.....	150
APPENDICES	182
List of Publications.....	183

Table of Figures

Figure 2.1 Some common ligands used to prepare lead complexes. (a) dichalcogenocarbamate, (b) dichalcogenophosphinate, (c) dichalcogenophosphate, (d) dichalcogenoimidodiphosphinate, (d) selenourea, (e) xanthate.....	13
Figure 2.2 Crystal structure of $\text{Pb}(\text{Se}_2\text{CNEt}_2)_2$	15
Figure 2.3 Crystal structure of $[\text{Pb}\{(\text{C}_6\text{H}_5)_2\text{PSSe}\}_2]$	16
Figure 2.4 Possible decomposition routes of $[\text{Pb}\{(\text{C}_6\text{H}_5)_2\text{PSSe}\}_2]$ by Chemical Vapour Deposition	18
Figure 2.5 Crystal structure of $\text{Pb}_2(\text{Se}_2\text{P}(\text{OMe})\text{Ph})_4$	19
Figure 2.6. Crystal structure of $\text{Pb}[\text{S}_2\text{P}(\text{O}i\text{Bu})_2]_2\cdot\text{phen}$	20
Figure 2.7. Crystal structure of imidodiselenophosphinatolead(II)	22
Figure 2.8. Synthetic scheme for <i>bis</i> (<i>N,N</i> -diisobutyl- <i>N'</i> -4-nitrobenzoylselenoureato) lead(II)	23
Figure 2.9. TEM images of PbSe nanoparticles prepared from <i>Bis</i> [<i>N,N</i> -diisobutyl- <i>N'</i> -4-nitrobenzoylselenoureato]lead(II) complex. (a) and (b) are TEM and HRTEM images respectively of spherical shaped PbSe nanoparticles at 200 °C, (c) and (d) are TEM and HRTEM images respectively of cubic shaped PbSe nanoparticles cubic shape PbSe nanoparticles prepared at 250 °C (all in TOP/Oleic acid/Octadecene).....	24
Figure 2.10. Crystal structure of <i>bis</i> [<i>N,N</i> -diisobutyl- <i>N'</i> -4-nitrobenzoylselenoureato]lead(II)	24
Figure 2.11. Crystal Structure of $\text{Pb}(\text{S}_2\text{COEt})_2\cdot\text{bipy}$	25
Figure 2.12. Reaction mechanism for the preparation of O-alkylxanthato complexes	26
Figure 2.13. Chugaev elimination reaction.....	26
Figure 2.14. SEM images of PbS nanoparticles synthesised from $[\text{Pb}(\text{pic})_2(\text{ths})_2]_2$ by using aqueous CTAB: (A) 2, (B, C) 5, and (D) 16 h. All scale bars = 1 μm	28

Figure 2.15. A diagram showing direct and indirect band gaps.	33
Figure 2.16. A direct transition from the valence band (VB) to the conduction band (CB)....	33
Figure 2.17 Money printed with anti-erasing ink	43
Figure 2.18 Nanoparticles used as drug delivery vehicles	44
Figure 2.19 Structure of photovoltaic devices with A. having a PbS layer and B. having a PbSe layer	51
Figure 2.20 Diagram depicting silicon photonic crystal nano-cavity light emitting diode	54
Figure 3.1 AACVD setup	69
Figure 3.2 An illustration of Tecnai f30 Transition Electron Microscope	71
Figure 3.3. A photograph of Bruker AXE D8 Discover X-ray Diffractometer.....	73
Figure 3.4. A photograph of Scanning Electron Microscope	74
Figure 4.1 X-ray crystal structure of $C_{24}H_{56}N_2P_4PbS_4$	81
Figure 4.2 X-ray crystal structure of $C_{24}H_{56}N_2P_4PbS_2Se_2$	81
Figure 4.3 Thermogravimetric analysis of (a) complex 4, (b) complex 5 and (c) complex 6	82
Figure 4.4 p-XRD plot for PbSe nanoparticles.....	83
Figure 4.5 HRTEM (a) and TEM (b) images of PbSe nanoparticles.....	84
Figure 4.6 p-XRD for PbS nanoparticles.....	85
Figure 4.7. HRTEM (a) and TEM (b) images of PbS nanoparticles	86
Figure 4.8 p-XRD for nanoparticles synthesised from complex 6. Major peaks match with PbSe nanoparticles.....	86
Figure 4.9 HRTEM (a) and TEM (b) images obtained from decomposition of complex 6. ...	87
Figure 4.10. Band gap determination using the absorption spectrum fitting procedure for the synthesised lead selenide nanoparticles.....	88
Figure 4.11 Band gap determination using the absorption spectrum fitting procedure for the synthesised lead sulphide nanoparticles	89

Figure 4.12. Band gap determination using the absorption spectrum fitting procedure for the synthesised nanoparticles from <i>bis</i> (imidodiisopropylthioselenophosphinato)lead (II) complex.	90
Figure 4.13 p-XRD of PbSe thin films	92
Figure 4.14 SEM images of PbSe thin films at (a) 10000x and (b) 5000x magnification.....	93
Figure 4.15 p-XRD of PbS thin films	93
Figure 4.16 SEM images of PbS thin films at (a) 10000x and (b) 5000x magnification	94
Figure 4.17 p-XRD of PbSe thin films from complex 6.....	95
Figure 4.18 SEM images of PbSe thin films deposited from complex 6 at (a) 10000x and (b) 5000x magnification.....	96
Figure 5.1 A stacked set of three ¹ H NMR spectra; the two starting materials, A, <i>bis</i> (imidodiisopropylselenophosphinato) lead(II) B, the product and C, <i>bis</i> (imidodiisopropylthiophosphinato) lead(II).	99
Figure 5.2: A stacked set of three ³¹ P NMR spectra; the two starting materials, A, <i>bis</i> (imidodiisopropylselenophosphinato) lead(II) B, the product and C, <i>bis</i> (imidodiisopropylthiophosphinato) lead(II).	100
Figure 5.3: A stacked set of two ⁷⁷ Se NMR spectra; the starting material, A, <i>bis</i> (imidodiisopropylselenophosphinato) lead(II) and B, the product.	101
Figure 5.4: A stacked set of three FT-IR spectra; the two starting materials, A, <i>bis</i> (imidodiisopropylselenophosphinato)lead(II) and C, <i>bis</i> (imidodiisopropylthiophosphinato) lead(II). B is the spectrum of the product.	102
Figure 5.5: A stacked set of three p-XRD spectra showing peaks corresponding to A, [Pb((SP ⁱ Pr ₂) ₂ N) ₂]; B, [Pb((SeP ⁱ Pr ₂)(SP ⁱ Pr ₂)N) ₂] and C, [Pb((SeP ⁱ Pr ₂) ₂ N) ₂].	103
Figure 5.6. Crystal structure for [Pb((SeP ⁱ Pr ₂)(SP ⁱ Pr ₂)N) ₂] product.....	105

Figure 5.7. A stacked set of three ^1H NMR spectra; the two starting materials, A, <i>bis</i> (diethyldithiocarbamato) lead (II) and C, <i>bis</i> (imidodiisopropylselenophosphinato) lead(II), and B, the product.....	106
Figure 5.8. ^{13}C NMR spectrum of $[\text{Pb}((\text{SeP}^i\text{Pr}_2)_2\text{N}(\text{S}_2\text{CNEt}_2))]$ showing peaks corresponding to $[\text{Pb}((\text{SeP}^i\text{Pr}_2)_2\text{N})_2]$ in oval and that corresponding to $[\text{Pb}(\text{S}_2\text{CNEt}_2)]$ in rectangles. The other peaks suggest the formation of a new product.	107
Figure 5.9 ^{77}Se NMR for $[\text{Pb}((\text{SeP}^i\text{Pr}_2)_2\text{N}(\text{S}_2\text{CNEt}_2))]$	108
Figure 5.10. A J-resolved spectrum of <i>bis</i> (diethyldithiocarbamato) lead II (13) showing scalar couplings of the triplet and quartet from the ethyl groups.	110
Figure 5.11. A J-resolved spectrum of <i>bis</i> (imidodiisopropylselenophosphinato) lead(II) (4), showing scalar couplings of overlapping septets with the two outer components too weak to be seen and four doublets in the overlap region 1.1 -1.4 ppm.....	111
Figure 5.12. A J-resolved spectrum of the product (18) showing a quartet superimposed onto a singlet (the latter an impurity), overlapping septets with the two outer components too weak to be seen, and in the region of overlap a triplet, four doublets and two sets of four impurity doublets.....	112
Figure 5.13. A DOSY ^1H NMR spectrum of the synthesised product in the overlap region 1.20 ppm to 1.35 ppm. Good separation is achieved indicating two species of diffusion coefficients approx. $8 \times 10^{-10} \text{ m}^2 \text{ s}^{-1}$ and $7.2 \times 10^{-10} \text{ m}^2 \text{ s}^{-1}$	113
Figure 5.14 FT-IR Spectra for A. $[\text{Pb}((\text{SeP}^i\text{Pr}_2)_2\text{N})_2]$ B. $[\text{Pb}((\text{SeP}^i\text{Pr}_2)_2\text{N})(\text{S}_2\text{CNEt}_2)]$ and C. $[\text{Pb}(\text{S}_2\text{CNEt}_2)_2]$	114
Figure 5.15. A stacked p-XRD spectra showing peaks corresponding to A, $[\text{Pb}((\text{SeP}^i\text{Pr}_2)_2\text{N})_2]$, B, $[\text{Pb}((\text{SeP}^i\text{Pr}_2)_2\text{N})(\text{S}_2\text{CNEt}_2)]$ and C, $[\text{Pb}(\text{S}_2\text{CNEt}_2)_2]$	116
Figure 5.16 Crystal structure of $[\text{Pb}((\text{SeP}^i\text{Pr}_2)_2\text{N})(\text{S}_2\text{CNEt}_2)]$	118

Figure 5.17. Stacked ^1H NMR for A, hexylmethyl dithiocarbamate, B, product and C, imidodiselenophosphinate lead(II) complex	119
Figure 5.18. Stacked ^{31}P NMR for A, imidodiselenophosphinato lead (II) complex and B, product.....	120
Figure 5.19. Stacked ^{13}C NMR for A, hexylmethyl dithiocarbamate, B mixed hexylmethyl dithiocarbamate and imidodiselenophosphinato lead(II) complex and C, imidodiselenophosphinate lead(II) complex.	121
Figure 5.20. Stacked ^{77}Se NMR for A, imidodiselenophosphinato lead (II) complex and B, product.....	122
Figure 5.21. Stacked FT-IR spectra of A, hexylmethyl dithiocarbamate, B, product and C, <i>bis</i> (imidodiisopropyldiselenophosphinato lead (II)).....	123
Figure 5.22. A stacked plot of p-XRD for A, hexylmethyldithiocarbamate, B, $\text{Pb}[(\text{SeP}^i\text{Pr}_2)_2\text{N}(\text{S}_2\text{CNHexMe})]$ and C, imidodiselenophosphinato lead (II)	125
Figure 5.23 Crystal structure of $[\text{Pb}((\text{SeP}^i\text{Pr}_2)_2\text{N})(\text{S}_2\text{CNHexMe})]$	127
Figure 6.1 TGA Plot for Single-source precursors $[\text{Pb}((\text{SeP}^i\text{Pr}_2)(\text{SP}^i\text{Pr}_2)\text{N})_2]$ (A), $[\text{Pb}((\text{SeP}^i\text{Pr}_2)_2\text{N})(\text{S}_2\text{CNET}_2)]$ (B) and $[\text{Pb}((\text{SeP}^i\text{Pr}_2)_2\text{N})(\text{S}_2\text{CNHexMe})]$ (C).....	130
Figure 6.2. A stacked set of four p-XRD spectra showing the diffracting pattern of thin films deposited from $[\text{Pb}((\text{SeP}^i\text{Pr}_2)(\text{SP}^i\text{Pr}_2)\text{N})_2]$ complex at 300, 350, 400 and 450 °C.	131
Figure 6.3. A stacked set of four p-XRD spectra showing the diffracting pattern of thin films deposited from $[\text{Pb}((\text{SeP}^i\text{Pr}_2)_2\text{N})(\text{S}_2\text{CNET}_2)]$ complex at 300, 350, 400 and 450 °C.....	132
Figure 6.4. A stacked set of four p-XRD spectra showing the diffracting pattern of thin films deposited from $[\text{Pb}((\text{SeP}^i\text{Pr}_2)_2\text{N})(\text{S}_2\text{CNHexMe})]$ complex at 300, 350, 400 and 450 °C.	133
Figure 6.5 SEM images 5000x magnification of thin films deposited from $[\text{Pb}((\text{SeP}^i\text{Pr}_2)(\text{SP}^i\text{Pr}_2)\text{N})_2]$ at A. 300 °C, B. 350 °C, C. 400 °C and D. 450 °C	134

Figure 6.6 EDAX spectrum of thin films deposited from $[\text{Pb}((\text{SeP}^{\text{i}}\text{Pr}_2)(\text{SP}^{\text{i}}\text{Pr}_2)\text{N})_2]$	135
Figure 6.7 SEM images 5000x magnification of thin films deposited from $[\text{Pb}((\text{SeP}^{\text{i}}\text{Pr}_2)_2\text{N}(\text{S}_2\text{CNEt}_2))]$ at A. 300 °C, B. 350 °C, C. 400 °C and D. 450 °C.	136
Figure 6.8 EDAX spectrum of thin films deposited from $[\text{Pb}((\text{SeP}^{\text{i}}\text{Pr}_2)_2\text{N}(\text{S}_2\text{CNEt}_2))]$	136
Figure 6.9 SEM images 5000x magnification of thin films deposited from $[\text{Pb}((\text{SeP}^{\text{i}}\text{Pr}_2)_2\text{N}(\text{S}_2\text{CNHexMe}))]$ at A. 300 °C, B. 350 °C, C. 400 °C and D. 450 °C. .	137
Figure 6.10 EDAX spectrum of thin films deposited from $[\text{Pb}((\text{SeP}^{\text{i}}\text{Pr}_2)_2\text{N}(\text{S}_2\text{CNHexMe}))]$	138
Figure 6.11 A graph of particle size against temperature for $\text{PbS}_x\text{Se}_{1-x}$ thin films deposited from $[\text{Pb}((\text{SeP}^{\text{i}}\text{Pr}_2)(\text{SP}^{\text{i}}\text{Pr}_2)\text{N})_2]$	139
Figure 6.12 A graph of particle size against temperature for $\text{PbS}_x\text{Se}_{1-x}$ thin films deposited from $[\text{Pb}((\text{SeP}^{\text{i}}\text{Pr}_2)\text{N}(\text{S}_2\text{CNEt}_2))]$	140
Figure 6.13 A graph of particle size against temperature for $\text{PbS}_x\text{Se}_{1-x}$ thin films deposited	141
Figure 6.14 p-XRD of thin films synthesised from $[\text{Pb}((\text{SeP}^{\text{i}}\text{Pr}_2)_2\text{N}(\text{S}_2\text{CNEt}_2))]$ indicating a PbSe phase.....	144
Figure 6.15 SEM images of mixed $[\text{Pb}((\text{SeP}^{\text{i}}\text{Pr}_2)_2\text{N}(\text{S}_2\text{CNEt}_2))]$ at (a) 10000x and (b) 5000x magnification	145
Figure 6.16 EDAX spectrum of mixed $[\text{Pb}((\text{SeP}^{\text{i}}\text{Pr}_2)_2\text{N}(\text{S}_2\text{CNEt}_2)_2)]$	145

List of Tables

Table 2.1 Properties of PbS, PbSe and PbTe	9
Table 3.1 List of chemicals and reagents	58
Table 4.1 Crystal structure data for, $[\text{Pb}((\text{SP}^{\text{i}}\text{Pr}_2)_2\text{N})_2]$ and $[\text{Pb}(\text{SeS}(\text{P}^{\text{i}}\text{Pr}_2)_2\text{N})_2]$	79
Table 4.2 Comparison of band gaps obtained for the synthesised nanoparticles with the band gaps of their corresponding bulk material	91
Table 5.1 Crystal structure refinement data for $[\text{Pb}((\text{SeP}^{\text{i}}\text{Pr}_2)(\text{SP}^{\text{i}}\text{Pr}_2)\text{N})_2]$	104
Table 5.2. Melting point of $[\text{Pb}((\text{SeP}^{\text{i}}\text{Pr}_2)_2\text{N})_2]$, $[\text{Pb}(\text{S}_2\text{CNEt}_2)_2]$ and product $[\text{Pb}((\text{SeP}^{\text{i}}\text{Pr}_2)_2\text{N}(\text{S}_2\text{CNEt}_2))]$ complexes	115
Table 5.3 Crystal structure data for mixed $[\text{Pb}((\text{SeP}^{\text{i}}\text{Pr}_2)_2\text{N})(\text{S}_2\text{CNEt}_2)]$	117
Table 5.4. Melting point determination for $[\text{Pb}((\text{SeP}^{\text{i}}\text{Pr}_2)_2\text{N})_2]$, $[\text{Pb}((\text{SP}^{\text{i}}\text{Pr}_2)_2\text{N})_2]$ and product $\text{Pb}[(\text{SeP}^{\text{i}}\text{Pr}_2)_2\text{N}(\text{S}_2\text{CNHexMe})]$ complexes.....	124
Table 5.5 Crystal structure data for mixed $\text{Pb}[(\text{SeP}^{\text{i}}\text{Pr}_2)_2\text{N}(\text{S}_2\text{CNHexMe})]$	126
Table 6.1 Comparison of PbSe thin films obtained at 450 °C from Single-source precursors suitable for depositing binary and ternary lead chalcogenides.....	142

List of Abbreviations

AACVD	aerosol assisted chemical vapour deposition
AFM	atomic force microscopy
AM	air mass coefficient
Bu	Butyl
CVD	Chemical Vapour Deposition
EDAX	energy dispersive X-ray analysis
E _g	band gap energy
E _g	example
Eq	equation
Et	ethyl
eV	electron volts
FWHM	full width at half maximum
HRTEM	high resolution transmission electron microscope
Hex	hexyl group
ⁱ Bu	isobutyl
CB	conduction band
CTAB	cetyl trimethylammonium bromide
ICDD	International Centre for Diffraction Data
ⁱ Pr	iso-propyl group
ITO	indium tin oxide
LED	light emitting diode
LP-MOCVD	low pressure metal organic chemical vapour deposition
Me	methyl group
MEG	multiple exciton generation

MOCVD	metal organic chemical vapour deposition
MS	mass spectrometry
NC	nanocrystal
NMR	nuclear magnetic resonance spectroscopy
Ph	phenyl group
PL	photoluminescence
ppm	part per million
PV	photovoltaic
p-XRD	powder X-ray diffraction
^s Bu	secondary butyl
SEM	scanning electron microscopy
SSP	Single-source precursor
^t Bu	tertiary butyl
TEM	transmission electron microscopy
TGA	thermogravimetric analysis
UV/Vis	ultra-violet/visible
VB	valence band
Voc	open circuit voltage
XRD	X-ray diffraction

Acknowledgement

I wish to express my profound gratitude to the Leverhulme Trust-Royal Society Africa Award Scheme for providing funds for my research work.

My sincere thanks go to my supervisors, Prof. Paul O'Brien and Dr. Johannes A.M. Awudza, for their excellent supervision and support during the course of this study.

I also thank Dr. Mohammad Azad Malik and Dr. Paul McNaughter, for their timely assistance and advice.

My Special thanks to Dr. James Raftery, Dr. Christopher Wilkins, Dr. Alan Harvey, Gary Harrison, Dr. Nicky Savjani, Dr. David Lewis, Dr. Claire Lydon and Christine Taylor for their help and support.

To my Mum, Dad, siblings, wife and children, I say a big thank you.

For the love and affection you have shown me, for the life and strength you have given me and for always being there for me, I sincerely thank you Almighty God.

Abstract

The work described herein deals with the synthesis and characterisation of lead chalcogenide thin films and nanocrystals from Single-source precursors. Single-source precursors of type imidodiisopropyl –dithio, -diseleno and -thioselenophosphinato complexes of lead have been synthesised and characterised. The as-synthesised compounds have been used for the fabrication of lead sulphide and lead selenide thin films by aerosol-assisted chemical vapour deposition and for the synthesis of nanocrystals by colloidal hot injection method. The as-grown thin films and nanoparticles of lead sulphide and lead selenide have been characterised by X-ray diffraction, scanning electron microscopy, transmission electron microscopy and energy dispersive X-ray (EDAX) analyses. Optical band gaps of the nanoparticles produced have been evaluated using the absorption spectrum fitting procedure. The band gaps of the nanoparticles were wider than those of their respective bulk particles, indicating a significant tuning. $\text{PbS}_x\text{Se}_{1-x}$ thin films have also been prepared by aerosol assisted chemical vapour deposition (AACVD) using novel Single-source precursors synthesised, characterised and their structures elucidated in this project. The complexes are $[\text{Pb}((\text{SeP}^i\text{Pr}_2)(\text{SP}^i\text{Pr}_2)\text{N})_2]$, $[\text{Pb}((\text{SeP}^i\text{Pr}_2)_2\text{N})(\text{S}_2\text{CNET}_2)]$ and $[\text{Pb}((\text{SeP}^i\text{Pr}_2)_2\text{N})(\text{S}_2\text{CNHexMe})]$. The thin films deposited from all three complexes showed the formation of $\text{PbS}_x\text{Se}_{1-x}$ at temperatures ranging from 300 °C to 400 °C and PbSe at 450 °C. Distribution of sulphur and selenium within alloyed thin films is confirmed by scanning electron microscope studies and EDAX analysis.

Chapter 1

Introduction

Until now, photovoltaics have been dominated by solid state junction devices, often made of silicon. This dominance is presently being contested by the development of another era of photovoltaic cells, based, for instance, on nanocrystalline materials. These materials can be manufactured at low cost together with other desirable features, for example, flexibility. The progress in creating and characterising nanocrystalline materials has opened up new vistas of opportunity. A portion of these new devices have proved to have significantly high conversion efficiencies, which is a good alternative to those of conventional devices. (Grätzel, 2001).

The inquiry to produce large-area cheap solar cells in recent times has prompted research on photovoltaic (PV) frameworks considering nanocomposites containing conjugated polymers. These composite materials can be produced at lower cost and with better flexibility than the solid state inorganic semiconductors that make up today's sunlight based cells. However, good quality nanocomposite solar cells are based on complex structural framework, containing a fine blend of interpenetrating and pervading donor and acceptor materials (Gur *et al.*, 2007). Cell performance is subject to blend structure, and solution-based fabrication methods regularly bring about uncontrolled and irreproducible blends, with composite morphologies are hard to accurately characterise (Gur *et al.*, 2007).

Inorganic thin film solar cells are being pursued with much anticipation as viable alternatives to silicon solar cells, which dominate today's market. A critical aspect of these solar cells is

the current conduction across the illuminated side of the device in the transparent conductor. The conventional anode of choice for inorganic solar cells has been indium tin oxide (ITO) (Rowell *et al.*, 2006). However, ITO is costly, contains indium that may be excessively constrained in supply for widespread use in solar cell applications, cannot be solution processed, and may not have the necessary flexibility for certain applications. These are major set-backs, as making commercial quantities will probably require the use of key qualities, for example, non-vacuum roll-to-roll type fabrication and opportunities in flexible applications. One of the extensively studied types of thin-film devices is the polycrystalline cell based on CdS/CdTe heterojunction, with a record efficiency of 16.5 % (Chopra *et al.*, 2004). Such devices are among the best candidates for terrestrial applications because of the relatively high efficiency, long-term stability in performance, and potential for low-cost production (Saga, 2010). Due to the high absorption coefficient of CdTe ($>10^4 \text{ cm}^{-1}$), a film of this material with a thickness of only about 2 μm is sufficient to absorb most of the visible, near infra-red and near ultraviolet parts of the solar spectrum.

Solar cells made of PbS and PbSe nanocrystals have also been reported (Choi *et al.*, 2009; Jiang *et al.*, 2007). The lead chalcogenide family of nanocrystals is being actively investigated for nanocrystal solar cell applications because they have such large exciton Bohr radii (PbS 18 nm, PbSe 46 nm, and PbTe 46 nm). In the limit where the nanocrystals are about a tenth of the bulk exciton diameter, electrons and holes can move through a thin organic surface coating and hence, strong electronic coupling between particles speed up transport of charges between nanocrystals. Schottky solar cells of binary compositions of PbSe and PbS nanocrystals have been reported (Ma *et al.*, 2009). PbSe nanocrystal solar cells generate larger short circuit photocurrents while PbS nanocrystal devices with similar band gap have shown a larger open circuit voltage (V_{OC}) (Luther *et al.*, 2008). This makes it

possible to tune the nanoparticles, by developing ternary $\text{PbS}_x\text{Se}_{1-x}$ to maximise both carrier transport and voltage at the same time. The properties of PbS and PbSe also lead to an ideal substitutional alloy; the atomic anion radii are within 15 % of each other, lattice mismatch factor is 2 % between PbS and PbSe (Alivisatos *et al.*, 2009) and the anions, are of equal valency. The synthesis of ternary $\text{PbS}_x\text{Se}_{1-x}$ nanocrystals remains underdeveloped (Akhtar *et al.*, 2011a; Brumer *et al.*, 2005; Kigel *et al.*, 2005; Onicha *et al.*, 2012).

1.1 Relevance of work

High efficiencies above 20 % have been achieved by monocrystalline silicon solar cells (Schultz *et al.*, 2004), their manufacturing cost and energy utilization, however, during production are high. Consequently, the interest of producing low cost solar cells has grown in recent times. Lead chalcogenide nanoparticles have several advantages, for example, size tunability and high absorption coefficients.

1.2 Statement of problem

The energy sector in most developing countries and the world at large has suffered greatly due to the expensive nature of producing energy and also depletion of some natural resources. It has, therefore, become very important to make optimum use of the scanty resources available and develop mechanisms to produce energy that is cost effective, environmentally friendly, and accessible to a larger group of people. Photovoltaic cells have been used extensively to produce electrical energy despite the high cost, due to the abundance of solar energy. There is therefore a great need for inexpensive routes to prepare advanced photovoltaics. Colloidal nanocrystals may be a building block for such materials, since they afford the possibility of inexpensively preparing samples that display quantum size effects.

By tuning the size of the nanocrystals, it is possible to adjust the band gap and oscillator strength of the absorbing medium. Lead chalcogenides, PbE (E = S, Se, Te), as nanocrystals (NCs) have been found to possess multiple exciton generation (MEG) (Ellingson *et al.*, 2005), which could ultimately lead to more efficient solar energy conversion (Luther *et al.*, 2008). Due to the toxicity of lead, it is expedient to develop less toxic methods for the synthesis of lead chalcogenide nanoparticles. The use of Single-source precursors for the synthesis of lead chalcogenide nanoparticles solves this problem.

Several Single-source precursors suitable for the synthesis of binary lead chalcogenide nanoparticles and thin films have been synthesised. They include dichalcogenocarbamates (Lee *et al.*, 2002; Trindade *et al.*, 1997, 1999), dichalcogenophosphinates (Akhtar *et al.*, 2011b; Hagihara *et al.*, 1968; Zhu *et al.*, 2002), dichalcogenophosphates (Bolundut *et al.*, 2010; Krishnan and Zingaro, 1969) and xanthates of lead (Akhtar *et al.*, 2011d; Clark *et al.*, 2011). These Single-source precursors have been successfully used to produce binary lead chalcogenides, however, their use for the synthesis of ternary lead chalcogenides are at the developmental stages.

This work seeks to explore the use of imidodichalcogenophosphinato lead complexes as suitable Single-source precursors for the synthesis of binary and ternary lead chalcogenides.

1.3 Scope of work

This work is focussed on synthesising lead imidodichalcogenophosphinate complexes that are suitable as Single-source precursors for the synthesis of lead chalcogenide nanoparticles and thin films. The work also includes the production of binary and ternary lead chalcogenide thin films using aerosol assisted chemical vapour deposition method and the synthesis of colloidal binary lead chalcogenide nanoparticles using hot injection method.

1.4 Objectives

The main objective is to synthesise lead chalcogenide nanoparticles and prepare thin films from lead imidodichalcogenophosphate Single-source precursors.

The specific objectives of this project are:

1. To synthesise and characterise lead chalcogenide Single-source precursors
2. To synthesise and characterise lead chalcogenide nanoparticles from Single-source precursors.
3. To produce and characterise lead chalcogenide thin films from Single-source precursors.

1.5 Thesis layout

This thesis is composed of seven chapters:

- Chapter 1 is an introduction underlining the interest and the aims of this work
- Chapter 2 is a literature review that defines the main notions used throughout this study and summarises the scientific knowledge related to the subjects mentioned in this thesis;
- Chapter 3 gives all the details necessary to understand the experiments performed in this work, and eventually to reproduce them if need be.
- Chapter 4 is the first result chapter. It is based on the synthesis of binary lead chalcogenide nanoparticles and thin films.
- Chapter 5 is the second result chapter in which the synthesis of Single-source precursors suitable for making ternary lead chalcogenide nanoparticles and thin films are presented.

- Chapter 6 discusses the synthesis of $\text{PbS}_x\text{Se}_{1-x}$ thin films by pyrolysis and aerosol assisted chemical vapour deposition
- Chapter 7 summarises the conclusions from this study and suggests some outlooks for the future and possible future studies.

Some papers produced from this research are presented in the appendix.

Chapter 2

Literature review

2.1 Summary

In this chapter, the use of single-source molecular complexes for lead chalcogenide thin films by chemical vapour deposition (CVD) or as nanoparticles by solution methods is reviewed. The potential applications of these materials in solar energy are discussed along with the relative advantages of the various methods.

2.2 General introduction

There is considerable current interest in metal chalcogenides (sulphides, selenides or tellurides) stemming from their useful properties as thin films or in highly dispersed form (Afzaal and O'Brien, 2006). Potential applications of these materials are in devices such as solar cells (II–VI and III–VI), infrared detectors (IV–VI) and in room-temperature thermoelectric generators (V–VI). Inexpensive and environmentally benign protocols are needed that also provide control over issues such as composition, size and morphology; facilitating the use of these materials in light emitting diodes, non-linear optics, lasers or solar cells (Rao *et al.*, 2006).

Lead is classified as a borderline soft metal in the hard/soft acid–base concept of Pearson, (Pearson, 1963) and shows a wide variety of coordination numbers. Lead (IV) compounds are known to have coordination numbers between 4 and 8, but the majority of them have the coordination number of four. Lead (II) can bind as few as two and as many as 10 ligands, with preferred coordination numbers of 4 or 6 (Shimoni-Livny *et al.*, 1998). Lead (II) forms

stable complexes with both soft and hard donor atom ligands. In similar coordination environments, the affinity of lead (II) towards sulphur-based ligands tends to be higher than for harder oxygen- or nitrogen-donor groups. Despite considerable study of the coordination chemistry of lead (II) with S- or Se-donor atom ligands, (Davidovich *et al.*, 2010) the rational design of complexes remains a challenge. Tuning of the structure of the ligands to satisfy the coordination preferences and requirements of the lead(II) atom is still not that well understood (Claudio *et al.*, 2003); the same is true in design of complexes for chalcogenides. Lead (II) complexes with sulphur, selenium or tellurium donor atom ligands have been studied widely during the last few decades (Davidovich *et al.*, 2010). The reason for the sustained interest in these compounds lies in their significant structural diversity and potential for applications (Claudio *et al.*, 2003).

Lead chalcogenides in various forms with critical dimensions on the order of nanometers have attracted considerable interest because of their unique physical and chemical properties and potential in many applications (Calvert, 1999). The sulphides, selenides and tellurides are narrow band gap semiconductors. Their crystal structures are face-centered cubic, with coordination number six, and the rock-salt (halite) structure. The bonding between Pb and S, Se or Te is considered to be mostly ionic with the ionic property increasing down the group (Kothiyal and Ghosh, 1990). The minimum energy gap, E_g , between the conduction band and the valence band is direct and its values are listed in Table 2.1. The band gaps can be tailored by making solid solutions, such as $\text{PbSe}_{1-x}\text{Te}_x$ or $\text{PbS}_x\text{Se}_{1-x}$ (Kothiyal and Ghosh, 1990). This has recently been achieved for materials in nano dispersed form for a wide range of compositions in the $\text{PbS}_x\text{Se}_{1-x}$ system (Akhtar *et al.*, 2011a; Ma *et al.*, 2009).

Table 2.1 Properties of PbS, PbSe and PbTe

	PbS	PbSe	PbTe	Ref
E_g at 77K(ev)	0.307	0.176	0.217	(Kothiyal and Ghosh, 1990)
E_g at 300K(ev)	0.410	0.270	0.310	(Kothiyal and Ghosh, 1990)
E_g at 373K(ev)	0.440	0.310	0.340	(Kothiyal and Ghosh, 1990)
$P(\text{gcm}^{-1})$	7.610	8.150	8.160	(Kothiyal and Ghosh, 1990)
Static dielectric constant	161	280	360	(Kothiyal and Ghosh, 1990)
Bohr Radius (nm)	18	46	46	(Li <i>et al.</i> , 2003; Tai <i>et al.</i> , 2008)
Lattice Constant (Å)	6.007	6.212	6.562	(Bencherif <i>et al.</i> , 2011)

Lead sulphide nanoparticles may be useful in electroluminescent devices such as light-emitting diodes. In addition, the exceptional third-order non-linear optical properties of PbS nanoparticles lead to the potential for application in high-speed switching (Colvin *et al.*, 1994). This material is also potentially useful for making devices that require small band-gap semiconductors with optical absorption and emission in the red and near-infrared region of the spectrum. Lead selenide is a promising material in many other applications including lasers (Cui *et al.*, 2006), thermoelectric devices (Harman *et al.*, 2002; Murray *et al.*, 2001), near-infrared (near-IR) luminescence emitters (Schaller *et al.*, 2003) and IR detectors (Qi *et al.*, 2005). The selenide and telluride of lead are potentially superior to other materials such as bismuth telluride for thermoelectric cooling and electric power generation (Bode *et al.*, 1965; Harman *et al.*, 2002; Shchennikov and Ovsyannikov, 2003). Stable solution-processed photovoltaic devices from colloidal lead selenide quantum dots having 3.6% power

conversion efficiency in the infrared region have been reported (Barkhouse *et al.*, 2008; Klem *et al.*, 2007). The devices reach external quantum efficiencies of 46% in the infrared and 70% across the visible region. Ultra efficient multiple exciton generation (MEG) for single photon absorption in colloidal lead selenide and lead sulphide quantum dots have been reported (Ellingson, *et al.*, 2005). Studies indicate that the threshold photon energy for MEG in quantum dots is twice the lowest exciton absorption energy. The biexciton effect which shifts the transition energy for absorption of a second photon also influences the early time transient absorption data and may contribute to a modulation observed when probing near the lowest inter-band transition (Ellingson, *et al.*, 2005).

The pursuit of synthetic routes to lead chalcogenide quantum dots is not a recent endeavour. Bulk PbE (E = S, Se, or Te) have been prepared through the solid-state reaction of elements at elevated temperatures (950-1150 °C) (Tamari and Shtrikman, 1979; Yellin and Ben-Dor, 1983). Metal organic complexes (eg. carbamates and xanthates) have also been used to obtain bulk powders and thin films of PbE and ZnS at significantly lower temperatures (200–300 °C) (Seligson and Arnold, 1993; Wilhelmy and Matijević, 1984). Rees and Kräuter (1993, 1994a, 1994b) have synthesised the lead thiolates $\text{Pb}(\text{SR})_2$ (R= ^tBu, ⁱBu and ^sBu), which were converted into lead sulphide by thermolysis (Chen *et al.*, 2007; Cheng *et al.*, 1996; Kraeuter *et al.*, 1994; Rees and Kräuter, 1996; Zhang *et al.*, 2000). Low-temperature approaches include the precipitation of metal chalcogenides from aqueous solutions of the metal cation (Lu *et al.*, 2002), the arrested precipitation from micelles (Schneider *et al.*, 1997), and the trapping of metal chalcogenides within a polymer matrix (Sankaran *et al.*, 1990). Gases of the form H₂E (E = S, Se, or Te) are often used as the chalcogen source and these are notably noxious. Non aqueous solvents with elemental S, Se, or Te as the chalcogen source were used to synthesize metal chalcogenides (Dusastre *et al.*, 1997). It has been reported that the

reaction of sulphur, selenium, or tellurium with elemental lead in n-butylamine at room temperature produces crystalline PbE (E = S, Se, or Te) (Dusastre *et al.*, 1997).

Single-source approaches involve the use of an organometallic or metal-organic molecule as a source for the elements required in the growth of the target compound at the desired stoichiometry (O'Brien and Nomura, 1995). Single-molecule complex approach provides several key advantages over other routes (Arif *et al.*, 1986; Cowley and Jones, 1989). For example, the existence of preformed bonds may lead to material with lower defect concentrations. In the case of thin film deposition by chemical vapour deposition, conditions of flow and temperature become simpler. It is also possible to carry out deposition with relatively simple installations (Fan *et al.*, 2007). Most of Single-source precursors are air-stable, non-toxic and easy to handle, often employ clean, low-temperature decomposition routes and yield crystalline nanomaterials with minimal impurity incorporation (Pickett and O'Brien, 2001). In CVD, the presence of only one complex molecule in the supply stream reduces the likelihood of pre-reaction and the associated contamination of the deposited film and permits intrinsic control of film stoichiometry. Ligand design allows a degree of control over both the type and the level of impurities incorporated into the films such as carbon from an alkyl group.

A number of lead complexes with S- and Se-donor atoms have been proposed as Single-source precursors for bulk or nanostructured PbS or PbSe (Afzaal *et al.*, 2004; Boudjouk *et al.*, 1998; Zhang *et al.*, 2005). The complexes for these materials are designed to contain the required elements in a correct ratio. Under favourable conditions, the use of a molecular complex also allows nanocrystal growth under mild conditions with good control over size-dispersity and crystallinity.

Some relevant examples of the use of lead chalcogenide Single-source precursors from different classes of S- Se- and Te- containing compounds including metal carbamates (Heard, 2005), xanthates (Tiekink and Haiduc, 2005), phosphates, phosphinates (Haiduc and Sowerby, 1996; Haiduc *et al.*, 1995; Lobana *et al.*, 2007), and ureates (Douglass, 1937) have been highlighted in this review.

2.3 Structure of Pb(II) complexes

Divalent lead, with its electronic configuration $[\text{Xe}]4f^{14}5d^{10}6s^2$, is one of the post-transition metal elements held to exhibit the ‘inert-pair effect’ (Pyykko and Desclaux, 1979; Sidgwick and Powell, 1940). This term refers to the resistance of the pair of outer electrons on Pb(II) to removal or to participation in covalent bond formation or hydrogen bonding (Shimoni-Livny *et al.*, 1998). The structures of Pb(II) complexes with S- and Se- containing ligands have been explained using this idea as the basis of a valence shell electron pair repulsion (VSEPR) model with the lone pair as a component- ‘the stereochemically active inert lone pair effect’ (Sidgwick and Powell, 1940). The lone pair of electrons can be held to cause a non-spherical charge distribution around the Pb(II) cation, that is, the disposition of ligands around the cation results in an identifiable void (Sidgwick and Powell, 1940). This gap in the coordination sphere has been considered evidence of a stereochemically active lone pair of electrons (Gillespie and Nyholm, 1957). The 6s electrons have larger binding energies than the corresponding 5s ones and 6s-6p hybridization is energetically less favourable causing the formation of a $6s^2$ inert pair (Chen *et al.*, 2004; Holloway and Melnik, 1997; Orgel, 1959; Parr, 1997, 2004; Walsh and Watson, 2005). This chemically inert pair of electrons has been considered to be sterically active, resulting in distorted crystal structures (Trindade *et al.*, 1997).

However, it has been demonstrated using partial electron densities of states (PEDOS) that the asymmetric electron density formed by Pb(II) is as a result of the interaction of the antibonding combination of Pb 6s and anion p states with unfilled Pb 6p (Chen *et al.*, 2004). This analysis shows that coupling of Pb 6p with the antibonding Pb 6s–anion p states gives rise to the net asymmetry in the electron density on Pb. As the Pb 6s and 6p states are too distant in energy to couple directly, this coupling can only take place when there is an appropriate anion that can interact with Pb 6s generating Pb 6s states close to the Fermi level. The sulphur anion does not have the required energy to achieve this and, therefore, the directed asymmetric density produced by PbS is weak and cannot stabilize the distorted structure relative to a symmetric structure of higher coordination. This explains why the rocksalt structure is the thermodynamically stable phase of PbS (Chen *et al.*, 2004).

2.4 Single-source precursors

Several classes of Single-source precursors have been used for the preparation or deposition of lead chalcogenides. The structures of some more commonly used ligands for the preparation of such lead complexes are shown in Figure 2.1.

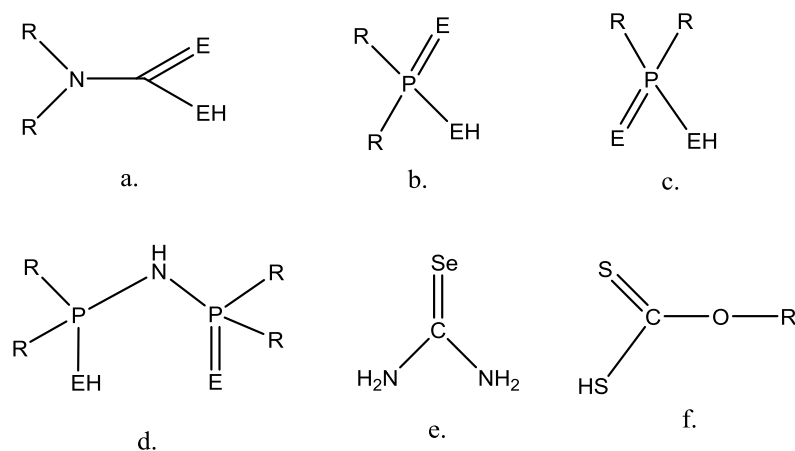


Figure 2.1 Some common ligands used to prepare lead complexes. (a) dichalcogenocarbamate, (b) dichalcogenophosphinate, (c) dichalcogenophosphate, (d) dichalcogenoimidodiphosphinate, (d) selenourea, (e) xanthate

2.4.1 Lead dichalcogenocarbamate complexes

The first report of the use of lead(II) dithiocarbamate complexes $\text{Pb}(\text{S}_2\text{CNRR}')_2$ ($\text{R}, \text{R}' = \text{Et}, \text{Bu}, \text{}^i\text{Bu}$) as single-source complexes was by Trindade *et al.*, in 1997 (Trindade *et al.*, 1997). These compounds were used as single molecule complexes to produce nanocrystalline PbS by their thermolysis in trioctylphosphine oxide. It was found that the optical and morphological properties of the PbS nanocrystallites were strongly dependent on the temperature of synthesis and less so on the chemical nature of the complex (Trindade *et al.*, 1997). PbS nanocrystals prepared by decomposition of $\text{Pb}(\text{S}_2\text{CN}^i\text{Bu}_2)_2$ exhibited different morphologies depending on the temperature used for the preparation (Trindade *et al.*, 1997). The nanocrystals synthesised at 100 °C were spherical with average diameters of 6.3 nm. At 150 °C, a mixture consisting of a large fraction of cubic crystallites with average size of about 60 nm and a small fraction of spherical nanocrystals was obtained. In a related work by Lee and co-workers (Lee *et al.*, 2002), large cubes were obtained by the decomposition of $\text{Pb}(\text{S}_2\text{CNEt}_2)_2$ at 230 °C in hot phenyl ether and dodecylamine. In the work developing this theme, an interesting observation was made and well defined, but structurally unprecedented, star-shaped PbS nanocrystals were synthesised when the complex $\text{Pb}(\text{S}_2\text{CNEt}_2)_2$, was injected into a hot phenyl ether solvent at 230 °C containing the capping molecule, dodecanethiol (Lee *et al.*, 2002).

The preparation of PbSe nanocrystals using diethyldiselenocarbamatolead(II) complex as a molecular complex has been reported (Trindade *et al.*, 1999). The crystal structure is shown in Figure 2.2. Similarly, using $\text{Pb}(\text{Se}_2\text{CNMe}^n\text{Hex})_2$, PbSe nanocrystals with cubic shape have been obtained (Trindade *et al.*, 1999).

Subsequently, several lead dithiocarbamate $\text{Pb}(\text{S}_2\text{CNRR}')_2$ ($\text{R}, \text{R}' = \text{Et}, \text{Bu}, \text{}^i\text{Bu}$) were tested by sublimation experiments to check their suitability for low pressure metal organic chemical vapour deposition (LP-MOCVD) growth. On this basis, $\text{Pb}(\text{S}_2\text{CN}^n\text{Bu}_2)_2$ was selected as the most promising complex for the deposition of PbS (Trindade *et al.*, 1997).

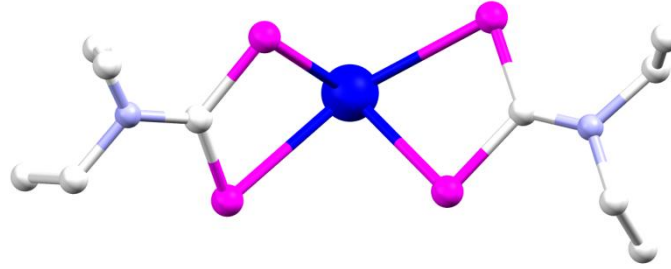
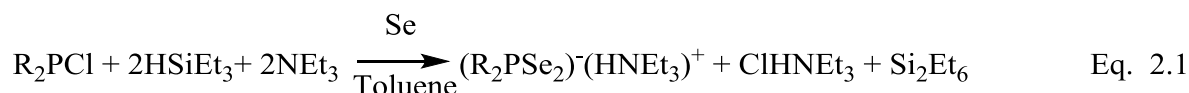


Figure 2.2 Crystal structure of $\text{Pb}(\text{Se}_2\text{CNET}_2)_2$ (Trindade *et al.*, 1999).

2.4.2 Lead dichalcogenophosphinato complexes

The coordination chemistry of dithiophosphinato compounds has been well described and reviewed by others (Haiduc and Sowerby, 1996; Haiduc, 2001). Until recently the examples of fully characterised selenophosphinates were rare. The reported synthetic methods for the preparation of selenophosphinato ligands gave unstable and relatively air sensitive products and their preparations involved difficult reaction conditions (Pilkington *et al.*, 1991). However, the X-ray single crystal structure of $[\text{Na}_2(\text{Se}_2\text{PPh}_2) \cdot 2\text{THF} \cdot 5\text{H}_2\text{O}]$ had been reported (Nguyen *et al.*, 2006). Other notable examples of metal selenophosphinates include $[\text{Ph}_2\text{PSe}_2\text{Li} \cdot \text{THF} \cdot \text{TMEDA}]$ and $[\text{K}(\text{Se}_2\text{PPh}_2)(\text{THF})_2]_2$ (Davies *et al.*, 2004). A series of metal complexes of *bis*-(di-alkylselenophosphinyl)selenide $[(\text{R}_2\text{PSe}_2)\text{Se}]$ with the general formula $[\text{M}(\text{R}_2\text{PSe}_2)_n]$ ($\text{M} = \text{Zn}, \text{Cd}, \text{Pb}, \text{In}, \text{Ga}, \text{Cu}, \text{Bi}, \text{Ni}$; $\text{R} = \text{}^i\text{Pr}, \text{Ph}$) and $[\text{MoV}_2\text{O}_2\text{Se}_2(\text{Se}_2\text{P}^i\text{Pr}_2)_2]$ have subsequently been synthesised and used for the deposition of metal selenide thin films by the CVD method (Hagihara *et al.*, 1968; Zhu *et al.*, 2002). Further investigations on diselenophosphinate ligands have led to new synthetic procedures. The method develops the idea that the $(\text{R}_2\text{PSe}_2)^-$ anion may be stabilized, and crystallized as an ionic compound if there

is enough counter ion in reaction solution, an excess amount of $\text{HSiCl}_3/\text{NEt}_3$ was used. However, HSiCl_3 reacts readily with NEt_3 to form $(\text{HNEt}_3)(\text{SiCl}_3)$ as a precipitate, making Se insertion difficult. The use of HSiEt_3 instead of HSiCl_3 overcame this problem and produced the ionic compound $(\text{HNEt}_3^+)(\text{R}_2\text{PSe}_2^-)$. The synthesis is presented in Eq. 2.1.



Bis(di-phenylthioselenophosphinato)lead(II) $[\text{Pb}\{(\text{C}_6\text{H}_5)_2\text{PSSe}\}_2]$ has been synthesised at room temperature. This complex has been used to make nanoparticles and to deposit PbSe thin films (Akhtar *et al.*, 2011b). The compound is perfectly air stable and can be stored for long periods of time. Suitable crystals for single crystal X-ray analysis were obtained from a concentrated tetrahydrofuran (THF) solution at room temperature. The crystal structure is shown in Figure 2.3 below (Akhtar *et al.*, 2011b; Nguyen *et al.*, 2006).

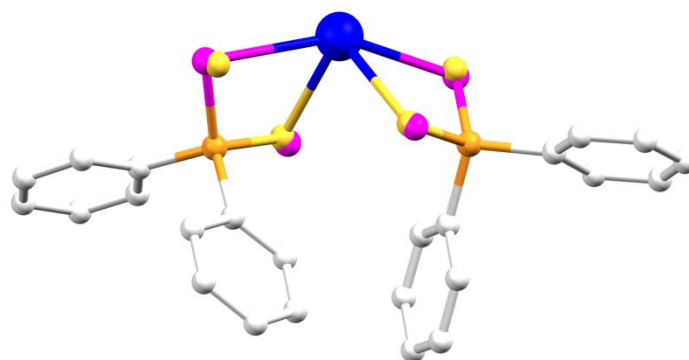
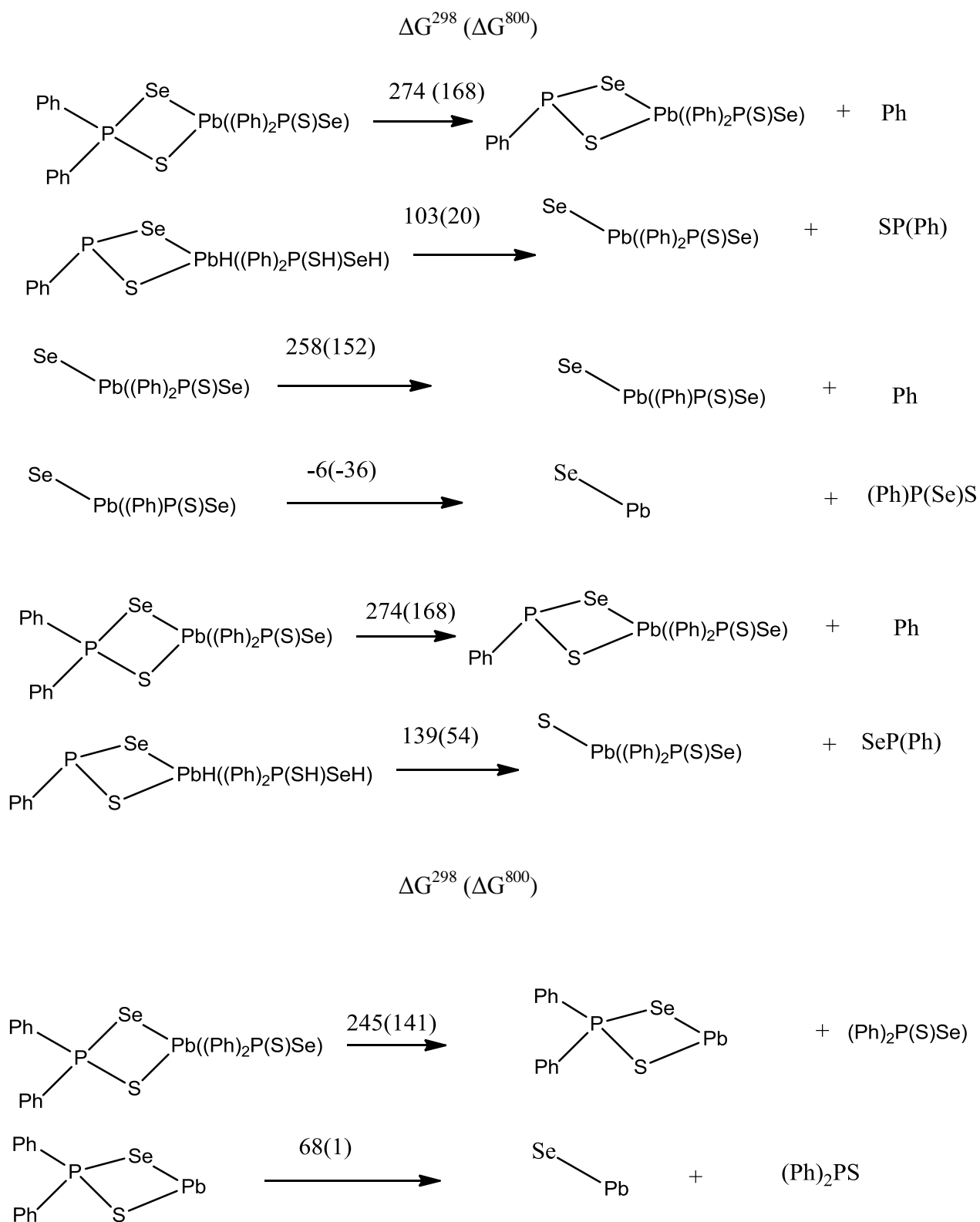


Figure 2.3 Crystal structure of $[\text{Pb}\{(\text{C}_6\text{H}_5)_2\text{PSSe}\}_2]$ (Akhtar *et al.*, 2011b).

The geometry at the lead atom is a distorted square pyramidal with two sulphur and two selenium atoms, forming the base of the pyramid and the lone pair occupying the axial position (Krishnan and Zingaro, 1969). The decomposition behaviour of the compound was studied by thermographic analysis which indicated a single-step weight loss between 287-385 °C. The remaining residue was in slight excess of the theoretical value for bulk PbSe. Energy dispersive X-ray spectroscopic (EDAX) analysis on the thin films produced did not detect any sulphur peaks however, phosphorus accumulated during the decomposition of the complex. The complex was also used to synthesize nanoparticles which resulted in a black precipitate and was confirmed by p-XRD analysis as cubic PbSe without any impurities (Akhtar *et al.*, 2011b).

Density functional calculations of the formation of PbSe from $[\text{Pb}\{(\text{C}_6\text{H}_5)_2\text{PSSe}\}_2]$ concluded that the formation of PbSe in CVD may involve more than one mechanism but the steps that lead to the formation of PbSe are somewhat more favourable on thermodynamic grounds than those that lead to the formation of PbS (Akhtar *et al.*, 2011b). The scheme below (Figure 2.4) shows the decomposition pathway of $[\text{Pb}\{(\text{C}_6\text{H}_5)_2\text{PSSe}\}_2]$.

Figure 2.4 Possible decomposition routes of $[\text{Pb}\{(\text{C}_6\text{H}_5)_2\text{PSSe}\}_2]$ by Chemical VapourDeposition (Akhtar *et al.*, 2011b).

2.4.3 Lead dichalcogenophosphato complexes

Diselenophosphates have been shown to form monomeric, cluster, and polymeric complexes with a wide variety of metal ions due to their capability of adopting several binding modes through the two selenium atoms (Sidgwick and Powell, 1940). The coordination chemistry of the ligands was investigated with the synthesis and study of the spectral properties of several (O,O'-diethyldiselenophosphato) (Bolundut *et al.*, 2010; Haiduc and Sowerby, 1996; Krishnan and Zingaro, 1969). $\text{Pb}_2(\text{Se}_2\text{P}(\text{OMe})\text{Ph})_4$ exists as a dimer and it has a central Pb_2Se_2 ring and each Pb has a distorted trigonal bipyramid geometry formed by chelating and bridging dsepo ligands. Each Pb atom is chelated by two dsepo ligands to presumably form a monomeric unit $\text{Pb}(\text{Se}_2\text{P}(\text{OMe})\text{Ph})_2$, and two units of this monomer dimerize via two Pb-Se bonds. The dimeric units are weakly held together in a network of $\text{Pb} \cdots \text{Se}$ and $\text{Se} \cdots \text{Se}$ interactions in the solid state. Its structure is shown in Figure 2.5 below.

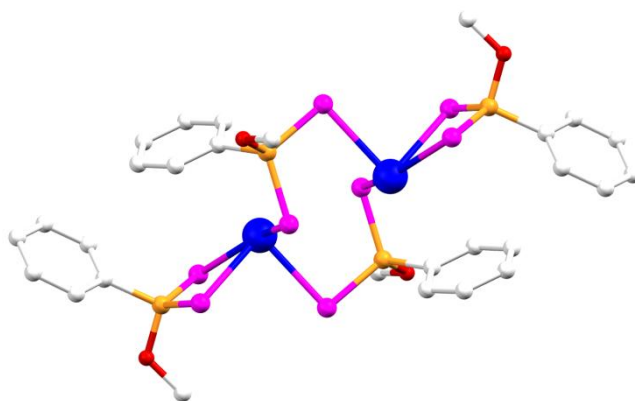


Figure 2.5 Crystal structure of $\text{Pb}_2(\text{Se}_2\text{P}(\text{OMe})\text{Ph})_4$ (Haiduc and Sowerby, 1996).

The polymeric complex, $[\text{Pb}\{\text{Se}_2\text{P}(\text{O}^i\text{Pr})_2\}_2]_n$, has been successfully used to prepare PbSe materials as cubes and eight-armed rod dendrites, via a solvothermal process with the inclusion of the capping agents, polyvinylpyrrolidone (PVP) and ethylenediamine. A few polymeric complexes involving its lighter congener, dithiophosphates, are known (Bolundut

et al., 2010). The molecular structure of the 1, 10- phenanthroline adduct of $\text{Pb}[\text{S}_2\text{P}(\text{O}^i\text{Bu})_2]_2$ is shown in Figure 2.6.

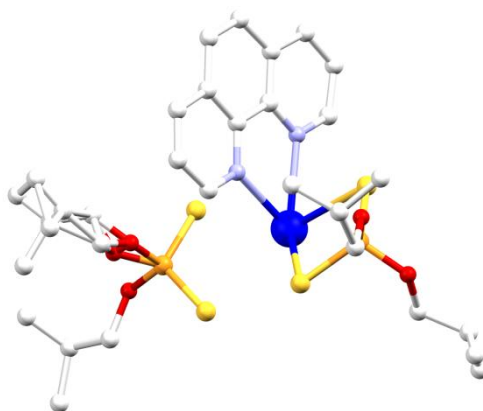
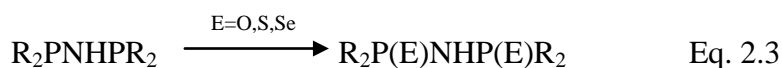
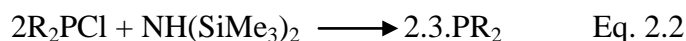


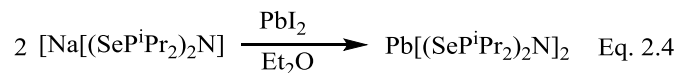
Figure 2.6. Crystal structure of $\text{Pb}[\text{S}_2\text{P}(\text{O}^i\text{Bu})_2]_2$.phen (Bolundut *et al.*, 2010)

2.4.4 Lead imidodichalcogenodiphosphinato complexes

Imidodiphosphinic acid derivatives $\text{R}_2\text{P}(\text{E})\text{NH}(\text{E})\text{PR}_2'$ ($\text{R}, \text{R}' = \text{CH}_3, \text{C}_6\text{H}_5$; $\text{E} = \text{O}, \text{S}, \text{NH}$) were first prepared by Schmidpeter and colleagues (Schmidpeter *et al.*, 1964). The synthetic process has since been adapted and improved by others to make a wide range of derivatives with $\text{R}, \text{R}' = ^i\text{Pr}, ^t\text{Bu}, \text{Et}, \text{OEt}, \text{OPh}$ and $\text{E} = \text{S}, \text{Se}$ (Cupertino *et al.*, 1996, 1999; Wang *et al.*, 1978). A typical synthesis involves two steps: a simple condensation reaction of R_2PCl with $\text{NH}(\text{SiMe}_3)_2$ to give phosphorus(III) compound, followed by oxidation with O, S or Se to give the desired product. The equations are shown in Eq. 2.2 and 2.3.



The deprotonation of the amine H-N bond in $R_2P(E)NH(E)PR_2$ derivative leads to a bidentate chelating ligand that can form neutral complexes of the type $M(N(R_2PE)_2)_n$ with transition or main group metals. An alternative route using (TMEDA) $[Na[(SeP^iPr_2)_2N]]$ has been used to prepare $Pb[(SeP^iPr_2)_2N]_2$. The synthetic process is shown in Eq. 2.4 below. The product was yellow with 53% yield and the crystal structure was determined and is as shown in Figure 2.7 (Ritch *et al.*, 2010).



The tellurium analogue of $R_2P(E)NH(E)PR_2$ cannot be prepared by oxidizing R_2PNHPR_2 with tellurium, following the scheme outlined in Eq. 2.2 - Eq. 2.4 because of the unstable nature of the ligand. Chivers and co-workers have developed a new scheme, in which R_2PNHPR_2 is first metalated by NaH to form $Na[R_2PNPR_2]$ followed by a reaction with tellurium powder in hot toluene in the presence of N,N,N',N'- tetramethylethylenediamine (Briand *et al.*, 2002; Chivers *et al.*, 2005a; 2005b). The as-produced ligand, $Na[N(TePPr^i)_2]$, when reacting with appropriate metal halide produce complexes $M[N(TeP^iPr_2)]_n$ with a range of metals .

Dichalcogenoimidodiphosphinato complexes of lead $[Pb[(EP^iPr_2)_2N]_2]$ (E= S, Se, Te) have proved to be useful Single-source precursors for lead chalcogenide thin films (Afzaal *et al.*, 2004; Ritch *et al.*, 2010). All the complexes are air-stable except $[Pb[(TeP^iPr_2)_2N]_2]$ which is prone to oxidation by air. These complexes have been used to deposit PbS or PbSe thin films by LPMOCVD (Afzaal *et al.*, 2004) and PbTe thin films by aerosol assisted chemical vapour deposition (AACVD) (Ritch *et al.*, 2010).

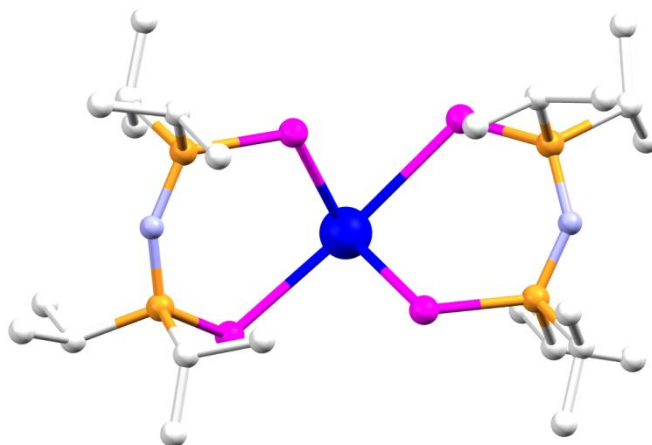


Figure 2.7. Crystal structure of imidodiselenophosphinatolead(II) (Ritch *et al.*, 2010)

2.4.5 Lead selenoureato complexes

N,N-dialkyl-*N'*-arylselenoureas are another class of compound potentially useful as chalcogenide complexes. They were first prepared and reported by Douglass in 1937 (Douglass, 1937). *N,N*-dialkyl-*N'*-arylselenourea acts as a bidentate ligand and during complexation the loss of selenoamidic proton promotes the co-ordination of O and Se donor atoms with metal ions. The (4-nitro-*N,N*-di-iso-butyl-*N*-benzoylselenoureato)Pb(II) and *N,N*-diethyl-*N*-benzoylselenoureato) Pb(II) complexes have been used as SSP for the deposition of PbSe thin films (Akhtar *et al.*, 2011c). *Bis*(*N,N*-di-iso-butyl-*N'*-4-nitrobenzoylselenoureato)lead(II) was prepared according to the scheme in Figure 2.8 by modifying the method previously reported in literature (Douglass, 1937). The crystal structure is shown in Figure 2.10.

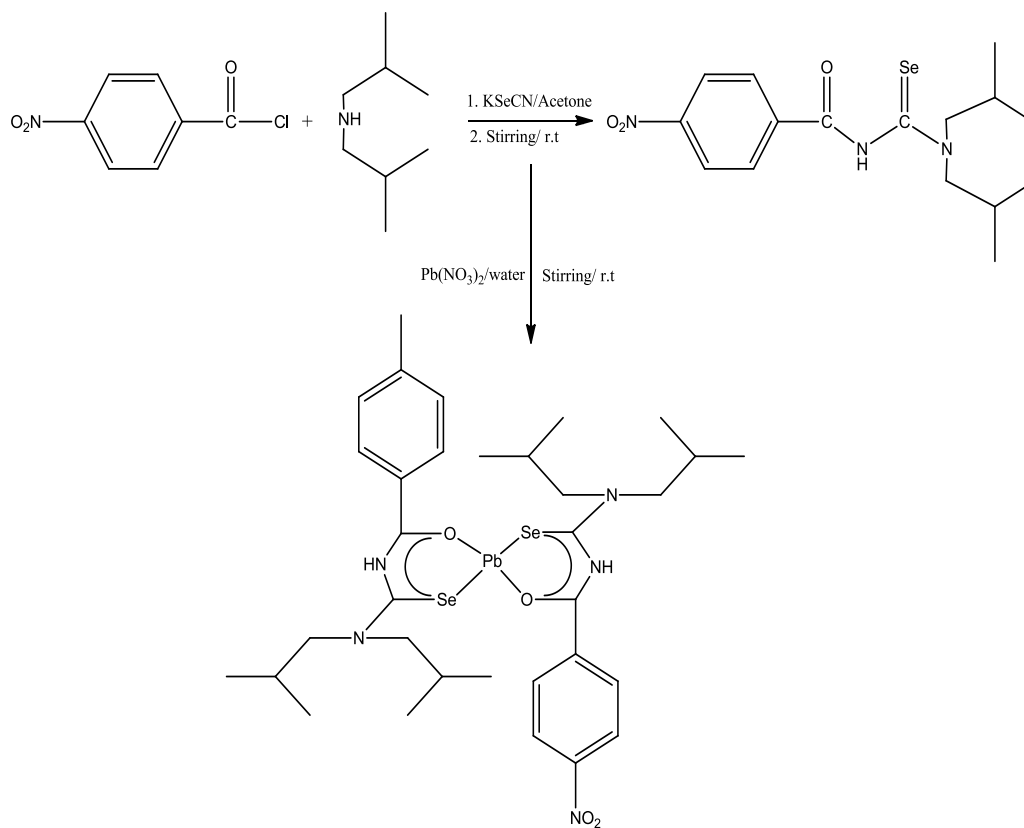


Figure 2.8. Synthetic scheme for *bis(N,N-diisobutyl-N'-4-nitrobenzoylselenoureato) lead(II)* (Akhtar *et al.*, 2011c).

The complex was used for the deposition of phosphorus free PbSe thin films by AACVD and nanoparticles by solution thermolysis. The TEM images are shown in Figure 2.9.

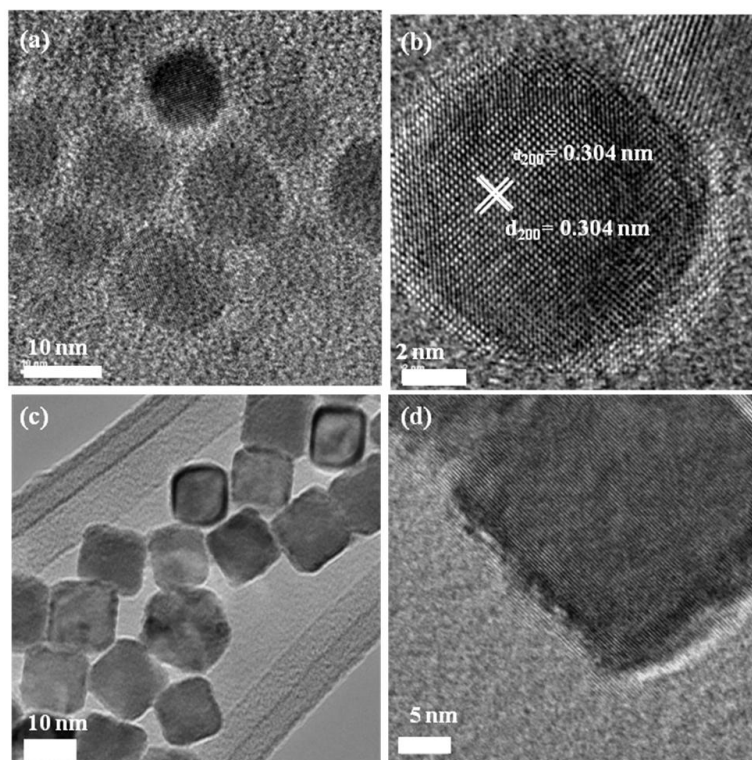


Figure 2.9. TEM images of PbSe nanoparticles prepared from *Bis*[*N,N*-diisobutyl-*N'*-4-nitrobenzoylselenoureato]lead(II) complex. (a) and (b) are TEM and HRTEM images respectively of spherical shaped PbSe nanoparticles at 200 °C, (c) and (d) are TEM and HRTEM images respectively of cubic shaped PbSe nanoparticles cubic shape PbSe nanoparticles prepared at 250 °C (all in TOP/Oleic acid/Octadecene) (Akhtar *et al.*, 2011c).

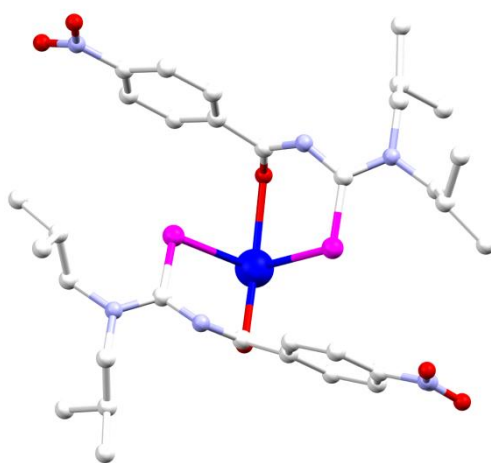


Figure 2.10. Crystal structure of *bis*[*N,N*-diisobutyl-*N'*-4-nitrobenzoylselenoureato]lead(II)

(Akhtar, *et al.*, 2011c)

2.4.6 Lead xanthato complexes

Xanthates ($-S_2COR$) are a class of inorganic compounds which have been successfully used for the synthesis of metal sulphides (Alam *et al.*, 2008; Castro *et al.*, 2008) with deposition temperatures for thin films as low as $250\text{ }^\circ\text{C}$. The successful growth of PbS thin films on polyimide (Kapton) substrates by AACVD from $[Pb(S_2COBu)_2]$ at temperatures as low as $150\text{ }^\circ\text{C}$ has been reported (Akhtar *et al.*, 2011d). Clark *et al.*, (2011) have also synthesised lead xanthates including the $Pb(S_2COEt)_2$ bipyridal adduct (Figure 2.11) and have deposited PbS from these complexes on pyrex glass, molybdenum-coated glass and silicon wafer by AACVD at $200\text{ }^\circ\text{C}$. The X-ray structure of the bipyridal adduct of $Pb(S_2COEt)_2$ is shown in Figure 2.11. The pyridine adducts of nickel xanthates have been used to deposit nickel sulphide films at $300\text{ }^\circ\text{C}$ and above (Alam *et al.*, 2008).

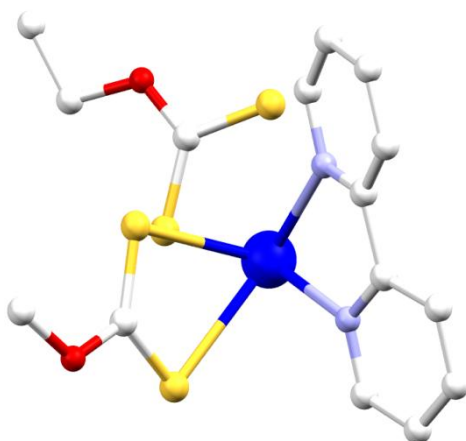


Figure 2.11. Crystal Structure of $Pb(S_2COEt)_2.bipy$ (Clark *et al.*, 2011)

The decomposition of xanthates is suggested to take place via the Chugaev elimination reaction in which alkene (R-H), OCS and MSH fragment are formed (Pradhan *et al.*, 2003).

In the first step, of the classically written organic formation, a potassium xanthate is produced when the alkoxide reacts with carbon disulphide in the presence of methyl iodide (Figure 2.12)

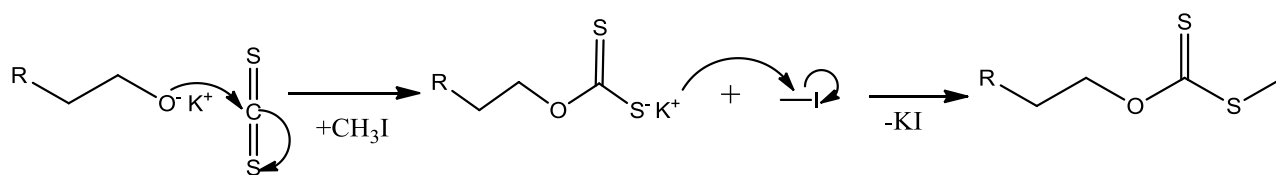


Figure 2.12. Reaction mechanism for the preparation of O-alkylxanthato complexes

The Chugaev elimination typically can occur at 200 °C, an alkene is formed by a syn-elimination, via a 6-membered cyclic transition state and the hydrogen atom is moved from the β -C-atom to the sulphur. The side product decomposes to carbonyl sulphide (OCS) and methanethiol (Figure 2.13).

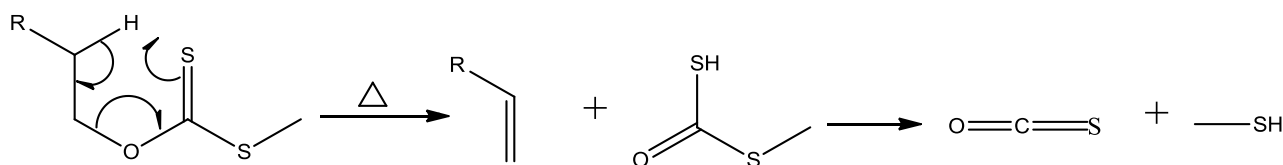


Figure 2.13. Chugaev elimination reaction

This clean elimination which also happens in metal xanthato complexes (Akhtar *et al.*, 2011d; Clark *et al.*, 2011) may be important in CVD and other materials processing environments by leading to low temperature decomposition.

In solution based preparation of nanoparticles, amines are reported to substantially lower the decomposition temperatures of both xanthate and thiocarbamate complexes (Pradhan *et al.*,

2003). Sun *et al.*, (2011) exhibited this when they successfully synthesised PbS cubes by adding lead xanthate into ethylene diamine solution at room temperature. It has also been found that complexation of the metal xanthate with various donor ligands can mitigate both the decomposition profile and solubility of the species and hence offer additional control over the conditions for metal sulphide formation (Jung *et al.*, 2010) .

There is no report on the synthesis of lead selenoxanthate complexes. However, selenoxanthate complexes of Ni (II), Pd(II), Cd(II), Cr(II) and Co(III) have been synthesised using the diselenoxanthogente ($C_2H_5OCSe_2^-$) ligand (Cauletti and Cervone, 1973). All these compounds are crystalline, monomeric in solution and non-electrolytes. These complexes are potentially interesting as Single-source precursors for the synthesis of nanoparticles or the deposition of thin films.

2.4.7 Other Single-source precursors

The monomeric homoleptic chalcogenolates lead(II) *bis*(2,4,6-trifluoromethylphenyl-selenolate) $Pb[SeC_6H_2(CF_3)_3]_2$ and lead(II) *bis*[*tris*(trimethylsilyl)silyltellurolate] $Pb[TeSi(SiMe_3)_3]_2$ were used as Single-source precursors for the thermolytic formation of the lead chalcogenides (PbTe and PbSe) by a spin coating procedure using a polymer/complex mixture (Erk *et al.*, 2010). As the decomposition temperature of the lead chalcogenide complex is below the degradation temperature of the polymer, nanoparticles of the semiconductor with diameter of 30–50 nm are formed in the polymer layer.

Lead thiobenzoate was used as Single-source precursor for the preparation of PbS nanoparticles by thermolysis in oleylamine/dioctyleamine/or trioctylamine as well as in ethylene diamine and dodecanthiol. The shape and size of the nanoparticles were strongly influenced by the type of amine or thiol used as capping agent and/or solvent (Zhang *et al.*, 2006).

A series of complexes were synthesised by Mandal *et al.* (2011) by the reaction of lead acetate, with picolinic (Hpic), 2,6-dipicolinic (H₂dipic) or salicylic (H₂sal) acid followed by the addition of thiourea (tu) or thiosemicarbazide (ths). The compounds [Pb(Hsal)₂(tu)₂], [Pb(Hsal)₂(ths)₃·2H₂O], [Pb(pic)₂(tu)], [Pb(pic)₂(ths)₂]₂, [Pb(dipic)(tu)(H₂O)]₂·2H₂O, and [Pb(dipic)(ths)₂]₃·2H₂O were used as Single-source precursors by thermolysing in both aqueous and nonaqueous media leading to pure crystalline galena in all cases. Depending upon conditions such as temperature, time, concentration and type of surfactants, truncated octahedra, dendrites, nanocubes, interlinked nanocubes, nanohexapods and cubes were obtained. The growth of particles (faceting/dissolution) in aqueous media was monitored with time. The reaction was quenched at intervals of 1, 2, 5, 8, and 16 h. The reactions were carried out in stainless-steel lined teflon vessel maintained at 170 °C in the hydrothermal oven. Figure 2.14 shows the SEM images of galena synthesised from [Pb(pic)₂(ths)₂]₂ for (A) 2 h, (B, C) 5 h and (D) 16 h (Mandal *et al.*, 2011).

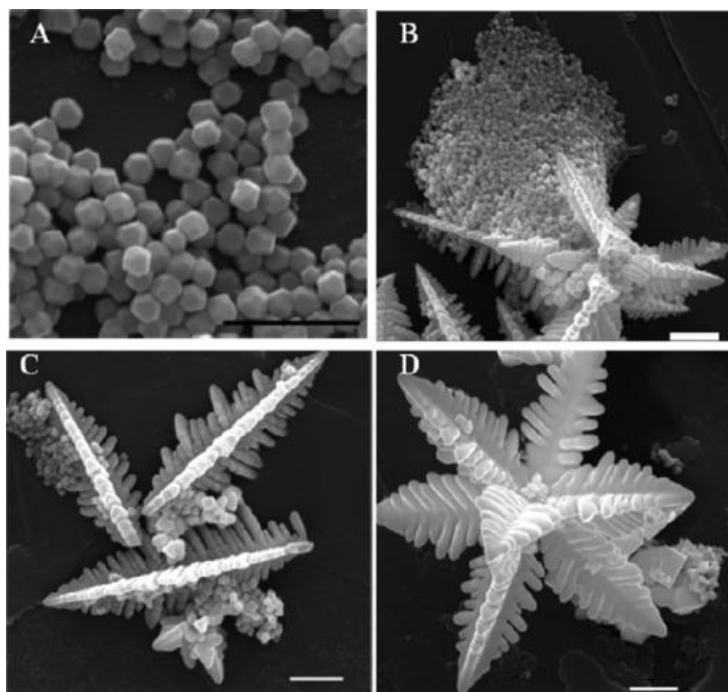


Figure 2.14. SEM images of PbS nanoparticles synthesised from [Pb(pic)₂(ths)₂]₂ by using aqueous CTAB: (A) 2, (B, C) 5, and (D) 16 h. All scale bars = 1 μm (Mandal *et al.*, 2011).

Salavati-Niasari *et al.* (2010) used [*bis*(thiosemicarbazide)lead(II)], [Pb(TSC)₂]Cl₂ (TSC = H₂NNHCSNH₂ (thiosemicarbazide)) as Single-source precursor by solvothermal method to grow PbS with different shapes and morphology. The complex was synthesised by the simple reaction of a solution of lead (II) chloride in water with thiosemicarbazide in water in 1:2 molar ratios and dropwise addition of 37 % hydrochloric acid while stirring at room temperature. The mixture was then refluxed for about 6 h to give a white crystalline solid as product. Different shapes of PbS nanostructures were prepared by hydrothermal process at 150 °C, using oleylamine or triphenylphosphine acting both as medium and the stabilizing reagents. Also the complex was pyrolysed in the solid state at 400 and 500 °C for 5 h. The effects of reaction time on hydrothermal method on the morphology and shape of PbS powders are similar to those described by Mandal *et al.*, (2011).

2.5 Electronic structure of semiconductors

In order to understand the physics and the applications of semiconductors, it is necessary to study band theory. Band theory is derived from molecular orbital theory (MOT) (House, 2008). According to MOT the linear combination of atomic orbitals approximation (LCAO) results in the formation of molecular orbitals on the basis of interaction of wave functions. Hydrogen molecule (H₂) is a typical example in which the single s electron wave functions of two hydrogen atoms (commonly represented as χ_A and χ_B) interact with all possible linear combinations to generate a bonding and antibonding orbital (ψ_1 and ψ_2) respectively.

$$\psi_1 = \chi_A + \chi_B \text{ and } \psi_2 = \chi_A - \chi_B \quad \text{Eq. 2.5}$$

The molecular orbitals formed thus have different energy levels than the corresponding overlapping atomic s orbitals. The bonding orbitals have lower energy while the antibonding

orbitals are higher in energy than the original atomic orbitals. The two s electrons from hydrogen atoms in this case occupy the lowest possible energy configuration therefore populating the bonding orbitals whereas the antibonding orbitals remain unoccupied (Albright *et al.*, 2013). In a similar way, due to large number of combining atomic orbitals in materials (conductors, insulators and semiconductors), these energy levels merge together to form energy bands (Jungwirth *et al.*, 2006; Qi and Zhang, 2011). Each band has a different energy and the electrons fill these bands from the lowest energy to the highest, similar to the way electrons occupy the orbitals in a single atom. The band that contains electrons and has lower energy is called the valence band, whereas the band which is empty and has highest energy is known as the conduction band. The band gap is the difference in energy between the valence and conduction bands. The laws of quantum mechanics forbid electrons from being in the band gap (E_g); thus, an electron must always be in one of the bands (Singh, 2006).

Absorption of energy results in transition of an electron from the valence band that crosses the band gap and shifts to the conduction band. The energy required for this transition is characteristic of the particular material in question. These unique band gaps are usually measured in electron-volts (eV).

In a metal, the valence band is only partially filled with electrons. This means that the electrons can access empty areas within the valence band, and move freely across all atoms that make up the solid. A semiconductor is a special case in which the band gap is small enough that electrons in the valence band can jump into the conduction band using thermal energy. Thus, an important property of semiconductors is that their conductivity increases as they heat up and more electrons fill the conduction band. In an electrical insulator, there is no possibility for electron transition because the valence band is completely filled with electrons, and the conduction band is too far away in terms of energy to be accessed by these electrons.

2.6 Extrinsic and intrinsic semiconductors

For every electron excited into the conduction band, a vacant site, known as a hole, is created in the valence band. This hole behaves like a positive charge carrier with the same magnitude of charge as the electron, but with opposite sign. In a pure semiconductor, the number of electrons in the conduction band must be equal to the number of holes in the valence band because each electron gives rise to one hole. In the presence of an electric field, the position of the hole within the crystalline lattice can be thought of as moving as other valence electrons repeatedly fill the vacant site. Under such conditions, electrons and holes move in opposite directions. The electrical conductivity of semiconductors is therefore a direct function of the number of free electrons and holes. Beside the temperature, the presence of impurities in the crystal lattice also affects the conductivity. Intrinsic semiconductors display electrical properties based on the inherent electronic structure such as silicon (Si), gallium (Ga). On excitation, each electron is promoted into the conduction band creating a hole (vacant site) in the valence band (West, 1999).

Extrinsic semiconductors have their electrical properties based on impurities, also known as dopants. They have considerably higher conductivity compared to intrinsic semiconductors. The commercially available semiconductors belong to this type. The process of addition of controlled impurities is known as doping which can tailor the electronic and conductivity properties. The addition of impurity atoms into a semiconductor material produces new energy levels within the band gap. When a semiconductor is doped with atoms having more valence electrons, for example, doping of silicon with phosphorus, the materials obtained are termed as n-type (West, 1999). The extra non-bonded electron remains bonded to phosphorus atom. When this electron is promoted to the conduction band by utilizing thermal energy at room temperature, a positive charge on each phosphorus atom is created. This positive charge

remains attached to the phosphorus nuclei and does not act as mobile hole. Under the charge imbalance, fermi level (the term used to describe the top of the collection of electron energy levels at absolute zero temperature) shifts towards the conduction band and a new energy level is thus formed. However, when doping is created with such atoms which have one less valence electron than host, impurity atoms act as electron acceptor and create holes (positive charge) in host materials. They are known as p-type and fermi level shifts close to valence band (West, 1999).

Besides, a number of compound semiconductors can act as n-type or p-type materials based on defects within the crystal lattice. These defects arise due to vacant sites in the lattice corresponding from stoichiometry. For example, in PbS, due to excess of Sulphur vacancies it acts as n-type or p-type due to excess of Pb sites.

2.7 Direct and indirect band gap semiconductors

Band-to-band absorption occurs due to the photoexcitation of an electron from the valence band to the conduction band. In crystalline solids, the band structures depend on the electron wave vector K . On the basis of transition between band to band, semiconductors can be grouped as direct and indirect band gap semiconductors (Kudman and Seidel, 1962; Rakhshani, 1997).

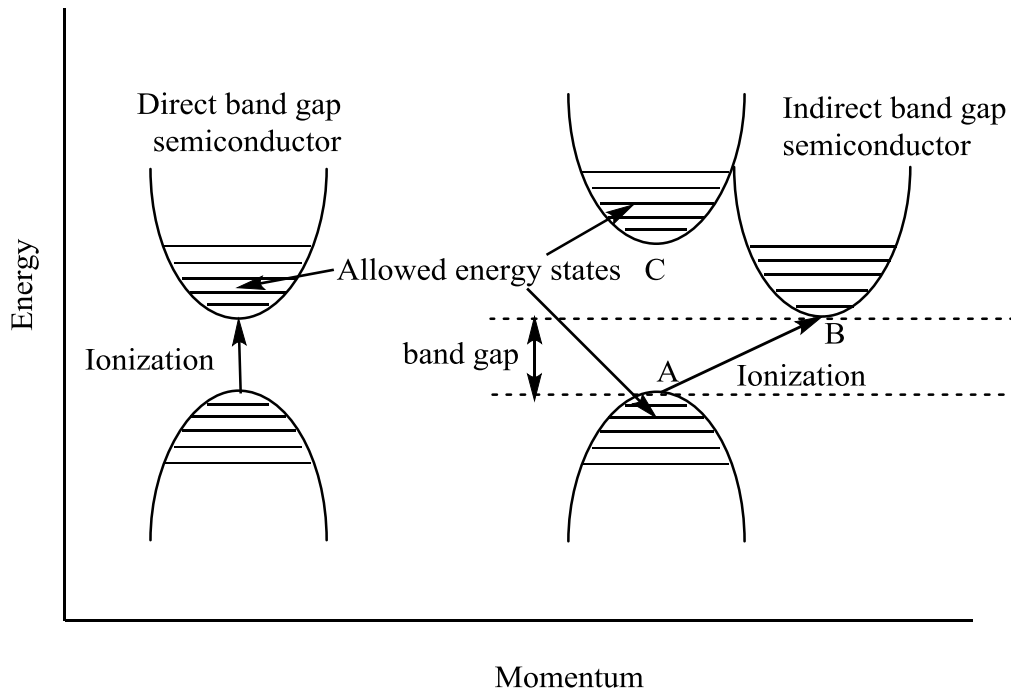


Figure 2.15. A diagram showing direct and indirect band gaps.

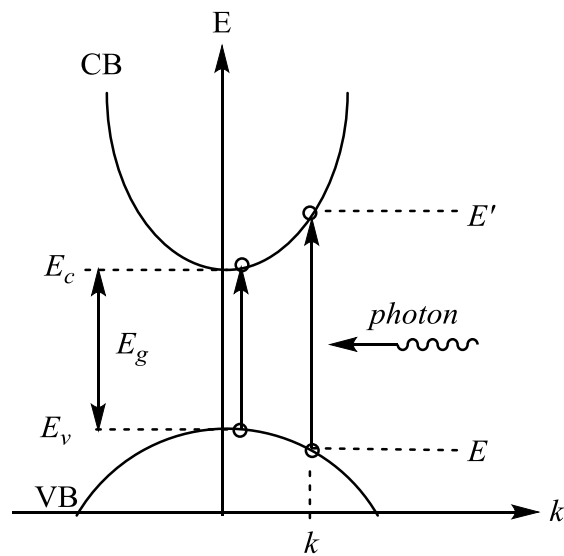


Figure 2.16. A direct transition from the valence band (VB) to the conduction band (CB)

In direct band gap semiconductors (GaAs, PbS or ZnO), the excitation does not involve phonons. Since photon momentum is negligible compared with electron momentum, the K-vector does not change. A direct transition on the E-K diagram is a vertical transition from an initial energy E and wave vector K in the valence band (VB) to the final energy E' and wave vector K' in the conduction band (CB) where $K'=K$ as shown in Figure 2.16 (Singh, 2006). The energy $(E'-E_c)$ is the kinetic energy of the electron with an effective mass Q , and E_v-E is the kinetic energy of the hole left behind in VB. The E_g is band gap energy (E_c-E_v) (Singh, 2006).

In indirect band gap semiconductors, absorption of photons requires the absorption or emission of phonons as illustrated in Figure 2.15. For indirect band gap semiconductor like silicon, an electron cannot be directly excited to the conduction band with energy E_g . Additional energy is required as a phonon, the electron undergoes a change in momentum and an indirect transition with energy $h\nu = E_g + E_{\text{phonon}}$ is obtained. The phonon energy, E_{ph} , is very small compared to E_g . Since indirect transitions require the participation of phonons (lattice vibrational energy) and hence are unambiguously dependent on temperature, the absorption coefficient for indirect semiconductors is smaller than that for direct semiconductors; in essence light absorption is a less efficient process for indirect semiconductors. Indirect band gap semiconductors have lower absorption coefficient for example, 99 % of light photons with energy equal to the band gap of CdTe (~1.45 eV) are absorbed by a 1 μm thick layer. By comparison, crystalline silicon (indirect band gap material) requires 20 μm thickness layers.

Similarly, in the case of light emission, a direct band gap material is also more likely to emit a photon than an indirect band gap material. Indirect band gap materials are occasionally used for some LEDs; they result in low conversion efficiency. Direct band gap materials are used exclusively for semiconductor laser diodes.

2.8 Deposition of thin films

Thin film of semiconductor materials can be grown by a number of techniques: physical vapour deposition (PVD), chemical bath deposition (CBD), liquid phase epitaxy (LPE) and chemical vapour deposition (CVD). CVD technique has many advantages over physical processes, such as a good conformal coverage, the possibility of epitaxial growth and selective deposition, the capability of large-scale production, and the ability to produce metastable materials. The deposition of thin films by CVD process involves the thermally induced reaction of the complexes on a heated surface. The process can be divided into several steps:

- (1) Mass transport of reagents to the deposition zone;
- (2) Gas phase reactions in the boundary layer to produce film complexes and by-products;
- (3) Mass transport of film complex to surface;
- (4) Adsorption of film complex on surface;
- (5) Surface diffusion of complex to growth site;
- (6) Surface chemical reactions lead to film deposition and by-product de-sorption,
- (7) Mass transport of by-product out of reaction zone (Jones and O'Brien, 1997)

2.9 Types of chemical vapour deposition

Traditionally, thermal energy is used to activate the chemical reactions in CVD. However, the CVD reactions can also be initiated using different energy sources. This has led to the development of many different kinds of CVD methods such as plasma enhanced CVD (PECVD) and photo-assisted CVD (PACVD). In these methods, plasma and light are respectively used to activate the complex and to activate the chemical reactions. Another variant of CVD include metal-organic CVD (MOCVD), which uses metal-organic as the complex rather than the inorganic complex used in the conventional CVD methods.

The metal-organic chemical vapour deposition (MOCVD) process for the growth of compound semiconductor materials originated from the pioneering work of Manasevit (Manasevit, 1968; Manasevit *et al.*, 1971). Since then, it has been developed especially for the growth of III–V (Chatterjee *et al.*, 1982; Duchemin, 1981; Duchemin *et al.*, 1985), II–VI (Chen *et al.*, 1994; Cockayne and Wright, 1984; Kamata and Yoshida, 1996; Yoshikawa *et al.*, 1986) and IV–VI semi-conducting material (Afzaal *et al.*, 2004; Schneider *et al.*, 1997) for opto-electronic applications (e.g. light-emitting diode, hetero-junction bipolar transistors, solar cells, photo-cathodes, advanced laser designs such as quantum well and double hetero-structures, etc.). Variation in complex transportation mode has also led to different CVD techniques. Aerosol assisted CVD (AACVD) can be used for complexes that are less volatile but can be dissolved in organic solvents. In AACVD, a solution of complex in high boiling organic solvent, or mixture of solvents is transformed into finely divided sub-micrometer liquid droplets, i.e. aerosol. The droplets are generated using the ultrasonic aerosol generator, electrostatic aerosol generator or electro-spraying method. The generated aerosol is delivered into a heated zone, where the solvent is rapidly evaporated or combusted, and the intimately mixed chemical complexes undergo subsequent decomposition and/or chemical reaction near or on a heated substrate to deposit the desired film.

The main advantages of AACVD are: (a) it simplifies the generation of vapours and delivery method as compared to the conventional CVD method which uses a bubbler/vaporizer method (b) AACVD uses Single-source precursors which enable the synthesis of multi-component materials with well controlled stoichiometry (c) it allows rapid formation of the deposited phases at relatively low temperatures due to the small diffusion distances between reactant and intermediates and (d) it is a relatively low cost process as compared to conventional MOCVD because, the AACVD process can be performed in an open atmosphere for the deposition of oxide and some less oxygen sensitive non-oxide materials without the need of any sophisticated reactor and/or vacuum system.

In spite of these promising advantages, industrial applications of the AACVD process are still limited, probably because the commercial availability of starting molecular compounds is limited. Thus, much effort has been aimed at the synthesis of new complexes.

An ideal complex should (a) have good volatility, (b) have good thermal stability during its evaporation and transport in the gas phase, (c) decompose cleanly on pyrolysis, (d) have a high purity (e) be non-toxic and non-pyrophoric, (f) be stable when stored over a long period and (g) be readily available in consistent quality and quantity at low cost.

The conventional complexes for AACVD are usually highly volatile and toxic compounds such as metal alkyls, phosphines, and hydrogen selenide. The conventional multiple source AACVD processes have many disadvantages such as (a) difficulty to control stoichiometry (b) impurity incorporation, (c) unwanted side reactions (d) high processing temperature which may cause inter-diffusion of layers. In order to overcome these disadvantages, during the past few decades, much attention has been paid on the development of the alternative Single-source precursors. A Single-source precursor is a metal-organic molecule which contains all the desired elements for the growth of a compound material. The use of such molecular complex reagents may provide significantly improved processes for the fabrication

of films due to the inherent control of the stoichiometry, fewer toxic complexes, and simplified fabrication compared to multiple-source processes. In addition, such complexes usually allow deposition of the desired phase at temperatures lower than those of the conventional multiple source processes.

2.10 Nanocrystals of semiconductors

The term 'nanocrystal' is used to describe a particle having size in the range of 1 to 100 nm, at least in one of the three possible dimensions (Roduner, 2006). Semiconducting nanocrystals (NCs) have been an area of immense research interest in the last two decades. The driving factor behind such interest in NCs is their shape and size-dependent unique electronic, optical, catalytical and chemical properties compared to their bulk counterparts (Heath and Shiang, 1998; Ramesh, 2009; Takagahara, 1993). They are considered as artificial atoms and occupy a unique position as a bridge between atoms and bulk solids.

The properties of bulk materials are determined by intramolecular bonding forces as their strength is much stronger than intermolecular binding forces, therefore, electronic, optical properties of such materials are independent of the size of crystal (Brus, 1984).

On the other hand, inorganic semiconductors and metals consist of a network of ordered atoms, where electronic excitation from valence band to conduction band results in the formation of a loosely bound electron-hole pair usually delocalized over a length longer than the lattice constant of the material. As the size of semiconductor crystallite approaches this excitonic Bohr diameter, electronic properties start to change. This effect is known as quantum size effect (QSE). Nanocrystals can be made of materials of diverse chemical nature, the most common being metals, metal oxides, silicates, nonoxide ceramics, polymers, organics, carbon and biomolecules. Nanocrystals exist in several different morphologies such as spheres, cylinders, platelets, tubes, etc.

Generally, they are designed with surface modifications tailored to meet the needs of specific applications. Nanostructures have a large fraction of surface atoms per unit volume. The ratio of surface atoms to interior atoms changes dramatically if one successively divides a macroscopic object into smaller parts. Such a dramatic increase in the ratio of surface atoms to the interior atoms in nanostructures and nanomaterials might illustrate why changes in the size range of nanometers are expected to lead to great changes in the physical and chemical properties of the materials. The total surface energy increases with the overall surface area, which is in turn strongly dependent on the dimension of material (Shih and Jona, 1976).

2.11 Synthesis of nanocrystals (NCs)

A number of synthetic strategies are used for nanocrystals including gas phase synthesis, colloidal thermolysis, solvothermal synthesis, synthesis in confined matrices and interface (Heath and Shiang, 1998; Ramesh, 2009; Takagahara, 1993). The desired characteristics of the synthesised nanocrystals (NCs) include a narrower size and shape distribution, high degree of crystallinity, appropriate surface layer composition and higher luminescence quantum yield. Moreover, synthetic methods should be readily available, reproducible and those involving reagents with low toxicity.

In comparison to above described methods, colloidal thermolysis is regarded as the most successful and reproducible method of synthesis of desired size and shape of NCs. Colloidal thermolysis involves the injection of complexes (single or dual source) in hot solvent in the presence of surfactants. This method was first introduced in 1993 by Bawendi and co-workers (Murray *et al.*, 1993). They employed dimethyl cadmium or dimethyl zinc compounds to prepare CdSe or ZnS in the presence of trioctylphosphine oxide (TOPO). However, the use of pyrophoric and air sensitive starting materials limits this technique to be

employed on industrial scale. Single-source metal-organic route was then developed to lower the risk associated with colloidal thermolysis. To date, a large number of Single-source precursors have been synthesised and used to deposit metal sulphide, selenide and telluride nanomaterials. The driving factor behind such an interest is not only to avoid using pyrophoric and toxic materials but also carefully design metal-complexes, provide the relevant elements entities and suppress the impurities associated with multiple source materials. The presence of only one complex molecule in the supply stream reduces the likelihood and extent of pre-reaction and controls intrinsic stoichiometry.

2.12 Growth process of nanocrystals

According to classical model of crystallization, a crystal is formed via addition of atom by atom or monomer by monomer to an inorganic or organic template or alternatively by dissolution of unstable phases and precipitation of the more thermodynamically stable phase (Kim and Kim, 2003; LaMer and Dinegar, 1950). Extensive research has been carried out to understand these processes and factors affecting them aiming to get insight to prepare nanocrystals in desired shape and size. Interestingly, for a specific solute there is certain limit of solubility in a particular solvent and addition of excess solute will result in precipitation and formation of nanocrystals. Broadly, two stages can be identified during the growth of nanocrystals, namely, nucleation and growth (LaMer and Dinegar, 1950). For the nucleation stage, the solution should be supersaturated either by directly dissolving the solute at higher temperature and subsequently cooling to room temperature or by introduction of reactants to yield supersaturating solution during the reaction. Nucleation stage is followed by particle growth stage. Growth occurs either by diffusion or coalescence. In diffusion growth, monomers in solution interact with the solid seeds to form a bigger particle, whereas in

coalescence nuclei merge into a bigger particle. The coalescence mechanism creates defects and grain boundaries in resulting nanocrystals due to utilization of energy process.

With the passage of time when the reactants are depleted due to particle growth, size defocusing or ostwald ripening will take place, where larger nuclei continue to grow and smaller ones get smaller and finally dissolve. Stopping the reaction at this stage will result in the particles having broad size distribution. Thus, it is difficult to get monodisperse particles unless the reaction time is extended to deplete the super saturation and the smaller nuclei. Thus, by rapid injection of complexes in solvent which generates sudden burst of nuclei simultaneously followed by self-sharpening growth process nearly monodisperse sized particles can be obtained by stopping the reaction.

2.13 Applications of semiconductor nanocrystals

Nanocrystals of metals and semiconductors have potential applications in a number of fields including, in energy and power, biomedicine, electronics, environmental applications, new engineering materials, consumer goods, personal care products, food and transportation. To perform these functions nanocrystals have to be synthesised, passivated to control their chemical reactivity, stabilized against particle aggregation, and functionalized to achieve specific performance (Bruchez Jr. *et al.*, 1998; Heath and Shiang, 1998; Ma *et al.*, 2003; Pantarotto *et al.*, 2003; Ramesh, 2009; Takagahara, 1993).

2.13.1 Photovoltaics

Semiconductor nanocrystals have the potential to enable new advances in the solar cell industry. Since the world's oil and other fuel resources are finite and depleting, efforts have been dedicated towards finding energy alternatives (Dresselhaus and Thomas, 2001). The

main disadvantage of photovoltaic (PV) solar cells is manufacturing cost. The advantage of using NCs in solar cell is ability to tune band gap, which allows control of the wavelength at which they will absorb or emit radiation (Kamat, 2008; Mora-Seró and Bisquert, 2010). It is known that the greater the band gap of a solar cell semiconductor, the greater the output voltage provided towards electricity generation. On the other hand, a lower band gap results in a higher current output but lower voltage. Both high currents and voltages are desired for efficient solar-electric conversion. Thus, there exists an optimum band gap that corresponds to the highest possible solar-electric energy conversion. Nanocrystals (NCs) offer more cost effective and cheap PV materials. They employ relatively inexpensive materials.

2.13.2 Thermoelectrics

Thermoelectric is a device which converts heat into electrical current and vice versa. Thermoelectric devices made up of nanocrystals (PbTe) would be of particular use to the silicon chip industry. Due to small size, loss of electrical current as heat often occurs which affect other components of devices. Nanocrystals thermoelectric devices are ideal to electrically cool silicon chips, ensuring that heat damage does not occur.

2.13.3 Light emitting diodes

Nanocrystals of semiconductors are useful materials to be used in Light emitting diodes (LED). Nanocrystals (LEDs) offer substantial advantages over organic LEDs (OLEDs) which make use of organic fluorophores to emit radiation. This is because OLEDs have poor photostability and short lifetimes relative to nanocrystals LEDs. Significant cost savings can be realized in the production of high quality white light from nanocrystals LEDs over OLEDs.

2.13.4 Counterfeiting applications

Counterfeiting is one of major problem around the world. Efforts are being focused to develop and improve to combat counterfeiting (Varadarajan *et al.*, 2010). The anti-counterfeiting technology involves tagging the products with codes, dye, ink or placing specific trademarks which distinguish from imitation items (Kaish *et al.*, 1999; Kirkman, 2002; Labgold and Kolo, 2006). Nanocrystals tagged products would represent an exceptionally difficult to duplicate system (Varadarajan *et al.*, 2010). This is due to their narrow and specifiable emission peaks, and their excitation wavelength dependent emission intensity. Thus, based on these properties, nanocrystals of different sizes can be combined to produce unique and nearly unlimited variety of different spectral 'barcode'. The micro-resonant structure allows a band of specific colours to transmit. When both the quantum dots and spectral structure are used together, the bar codes become almost impossible to reproduce. Figure 2.17 Shows an image of money printed with an anti-erasing ink as a measure to prevent counterfeiting.



Figure 2.17 Money printed with anti-erasing ink (Walker, 2013)

2.13.5 Biological applications

Nanocrystals of metals and semiconductors have received considerable interest due to their applications in biological world (Bruchez Jr. *et al.*, 1998; Ma *et al.*, 2003; Pantarotto *et al.*, 2003). Important applications include: fluorescent biological labels, drug and gene delivery, detection of pathogens, probing of DNA structure, tissue engineering and cancer detection. The use of nanocrystals as fluorescent biological labels is one of major application. Traditionally, organic dyes have been preferred materials for such type of applications. However, organic dyes have limited absorption and emission range. Peak emission of organic dyes cannot be changed and often it lies outside the spectral range. Organic dyes produce 'shoulders' in their emission and absorption peaks, which is a major disadvantage if the applications requires Gaussian type emission patterns in order to work correctly. Moreover, organic dyes are less stable and have low lifetimes. Infrared emitting nanocrystals (lead chalcogenide) are suitable materials for such applications. Figure 2.18 shows the potential use of nanoparticles as drug delivery vehicles.

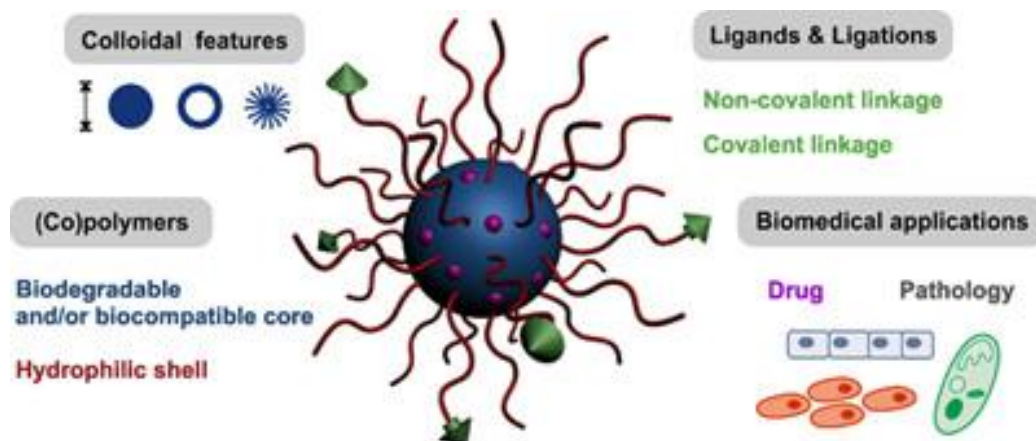


Figure 2.18 Nanoparticles used as drug delivery vehicles (Beck-Broichsitter *et al.*, 2015)

2.14 Lead sulphide (PbS) nanocrystals

Lead sulphide (galena) has been known as a distinct entity since antiquity and valued as a source of the important metal. PbS is often readily recognized in nature for its distinctive crystal habit as small cubes. Amongst the lead chalcogenides PbS is the most widely studied material and many synthetic routes to NCs of different shapes have been devised enabling the study of shape-specific optical and electronic properties (Jung *et al.*, 2010; Liu *et al.*, 2008; Pradhan *et al.*, 2003; Trindade *et al.*, 1997). The preparation of NCs which are uniform in size, shape, composition and surface chemistry is crucial for successfully mapping their properties. The synthetic schemes have typically ranged from using mild aqueous conditions to high temperature routes. Many different combinations of reagents and / or surfactants have been used, and synthesis often requires anaerobic conditions. Joo and co-workers (Joo *et al.*, 2003) synthesised PbS NCs using lead-oleylamine complex, prepared by the reaction of PbCl_2 with oleyamine (OLA) at 90 °C. Elemental Sulphur dissolved in OLA was injected at 90 °C and resulting mixture was heated to 220 °C for 1 hour to produce PbS quantum dots. The size of nanoparticles can be adjusted by simply varying the amount of starting materials. The resulting PbS NCs have been used for the fabrication of functional flexible films of densely packed NCs exhibiting Near-Infrared photoluminescence. Anisotropic growth of PbS via hot colloidal synthesis in the presence of Au nanoparticles has been reported (Yong and Sahoo, 2006). The authors have shown that the use of Au nanoparticles produces more uniform diameter nanowires and by altering the molar ratios of the complexes, various morphologies like nanorods, nanotubes, nano cauliflowers and core shell particles can be produced. They concluded that the Au particles provide nucleation sites to seed anisotropic growth of NCs. Highly luminescent (quantum yield ~ 20 %) PbS NCs that have band gaps tuneable throughout the NIR region are also reported from a reaction between lead oleate and *bis*(trimethylsilyl)sulphide (TMS) (Hines and Scholes, 2003). The spectra of PbS NCs with a

1s transition spanning the range of 800–1800 nm are presented as well as narrow emissions with small Stoke shifts.

A modification in the preparation of narrow size monodisperse particles of metal-chalcogenide by thermolysis is to employ Single-source precursors in a suitable co-ordinating solvent. This approach provides both elements within a single molecule which allow the preparation of semiconductor nanoparticles in one step. Various complexes such as dithiocarbamates, dithiophosphinates and thiobenzoates have been used to prepare PbS nanoparticles (Zhang *et al.*, 2006). Zhang *et al.*, have synthesised PbS particles by employing Lewis-base catalyzed approach to decompose metal alkyl xanthates by using alkyl amines as a solvent to promote decomposition as well as capping ligand for the particles formed (Zhang *et al.*, 2006). Spherical PbS NCs of diameters 5-10 nm were obtained when long chain alkylamines were used.

When bi-functional ethylenediamine was used instead, PbS dendrites were isolated from the same complex at room temperature. Uniform six- and four-armed dendrites were observed, with regular branches of ~20 nm in diameter growing in a parallel order (Zhang *et al.*, 2006). Lee and co-workers have provided some insight into factors underlying the ripening observed with the PbS NCs from a Single-source precursor (Lee *et al.*, 2003). By varying the injection temperature, the shape of the resulting particles evolved from rods to multi-pods to cubes. By varying the ratio of dodecanethiol ligand to the Single-source precursor, the shape can be tuned from nearly spherical to tetra decahedrons to almost cubic. It has been suggested that the dodecanethiol ligand blocks growth of the (111) faces and enhances growth on the (001) faces. On the other hand, dodecylamine, a weakly bonded ligand for Pb metal atoms, promotes growth on the (111) faces and the resulting particles are cubes.

Decomposition of lead hexadecylxanthate on trioctylamine (TOA) has been reported to yield ultra-narrow rods with diameter of ~ 1.7 nm and length of 12-15 nm (Acharya *et al.*, 2008).

A strong quantum confinement is observed in the absorption and photoluminescence spectra. The absorption spectra is strongly blue shifted and indicates sharp excitonic band at 278 nm and a shoulder at 365 nm. These bands are of excitonic origin corresponding to 1Pc to 1Ph, 1Sc to 1Ph, and 1Sc to Sh transitions. The photoluminescence (PL) spectrum shows strong and sharp band edge emission at 410 and 434 nm along with a shoulder at 465 nm, and a weak band at 500 nm.

2.15 Lead selenide (PbSe) nanocrystals

Lead selenide (PbSe) has potential applications in thermal imaging and infrared detectors, operating at wavelengths between 1.5-5.2 μm . It does not require cooling, but performs better at lower temperatures. The peak sensitivity depends on temperature and varies between 4.0-4.7 μm . PbSe nanocrystals have been prepared by a number of methods (Klokkenburg *et al.*, 2007; Lifshitz *et al.*, 2003, 2006; Xu *et al.*, 2006; Zhu *et al.*, 2006). Free-standing PbSe nanocrystals, including quantum wires, multipods, quantum rods, quantum dots, and cubes, were produced in a colloidal solution in the presence of alkyl-diamine solvent at 10–117 $^{\circ}\text{C}$. The morphology of the nanocrystals was governed by a solvent coordinating molecular template mechanism, which was further adjusted by the temperature and duration of the reaction (Lifshitz *et al.*, 2006). PbS and PbSe have a simple cubic crystal structure with nearly identical lattice constants (5.93 \AA and 6.12 \AA at 300 K, respectively), which facilitates the formation of heterostructures. Nanocrystal heterostructures represent unique systems in which the optical and electronic properties can be tuned by varying the chemical composition of their components and their mutual distance. In one study, formation of PbSe/PbS and PbSe/PbSe_xS_{1-x} core/shell NCs with luminescence quantum efficiencies of 65 % is reported (Ma *et al.*, 2009). These structures showed chemical robustness over months and years and band-gap tunability in the near infrared spectral regime, with a reliance on the NCs size and

composition. The fluorescence line-narrowing (FLN) spectra of these NCs indicate a negligible reduction of the full width at half-maximum (FWHM) of the resonance photoluminescence (PL) band with respect to the FWHM of the non-resonance PL band, suggesting the minor contribution of an inhomogeneous broadening due to a size distribution. The facets of wurtzite rods provide a substrate with various degrees of reactivity for the growth of PbSe nanosphere. Such remarkable differences in reactivity among the various facets are demonstrated in the CdS rods as PbSe NCs can be selectively grown either on both tips of a rod or just on one tip, by carefully adjusting the reaction conditions (Kudera *et al.*, 2005).

2.16 Lead telluride (PbTe) nanocrystals

Despite the immense interest in PbTe and PbTe-based materials for use in solid-state thermoelectric cooling or electrical power generation devices (Harman *et al.*, 2002), only a few reports exist for the preparation of PbTe NCs. Like other lead chalcogenides, initial reports about electronic structures, photoluminous properties and quantum confinement in PbTe nanocrystals obtained by preparing in a glass matrix showed that by controlling the heat treatment temperatures and times, quantum confined energy gaps of the PbTe quantum dots can be changed in the wavelength range from 1.1 to 2.0 μm (Hsu *et al.*, 2004). Other methods reported in literature for the preparation of PbTe crystals include:

- One-dimensional, single-crystalline PbTe NCs have also been grown on lead foils by a hydrothermal reaction between lead foil and tellurium powder. It has been predicted that 1D NCs are assembled by a hydrothermally driven rolling-up of thin PbTe layers formed in situ (Zhang *et al.*, 2005).
- Another method for controlling the shape of PbTe NCs reported (cubes, cuboctahedra, and octahedral) is by manipulating the reaction kinetics, using surfactant, high

temperature, and changing the concentration between lead oleate and TOP-Te. The reaction was carried out using trioctyl phosphine (TOP) or diphenyl ether as the growth solvent and phosphonic acid or long chain amines as stabilizer surfactant (Mokari *et al.*, 2007).

Monodisperse and defect-free PbTe NCs ranging from 4-10 nm have also been synthesised by Urban *et al.* (2006). The results showed that decreasing the concentration of oleic acid led to the formation of smaller number of nuclei. They hypothesized that this is probably due to the formation of lead oleate- which is more stable and reacts slowly and produced smaller nuclei-therefore more concentration of lead oleate produces larger size of particles and lower concentration of lead oleate yield smaller number of PbTe NCs because there exists less Pb and Te feedstock per nuclei formed. Similarly, the longer time growth duration and higher temperature results in polydispersity of NCs and average size increases up to 200-500 nm. Urban *et al.*, (2006) subsequently prepared nanocrystal superlattices or glassy films by manipulating deposition conditions by using these PbTe NCs. The electrical conductivity of films prepared from these PbTe NCs showed insulating behaviour due to difficulty in transporting the charge across the large interparticle spaces (1.8 nm as determined from grazing-incidence small-angle X-ray scattering, GISAXS) due to presence of organic ligand on the surface of NCs. Upon treatment with hydrazine solution of acetonitrile showed a remarkable 9-12 order of magnitude increased in electronic conductivity. The hydrazine activates the films by removing oleic acid from NCs. A novel bimolecular-assisted route for PbTe nanotubes by the self-assembly of NCs is reported (Tong *et al.*, 2006). Polycrystalline complex nanowires self-assembled from NCs synthesised using cysteine play crucial roles as both the lead source and the template in the formation of PbTe nanotubes. These polycrystalline nanotubes also display a quantum confinement effect.

2.17 Applications of lead chalcogenide nanocrystals (NCs)

2.17.1 Photovoltaic devices

An increased attention is being directed towards the manufacture of efficient, low cost, large-area coverage and flexible photovoltaic modules. Since the first report of a NCs PV device attention has been focused on absorber optimization using quantum sized rods or tetrapods (Huynh *et al.*, 2002; Wijayantha *et al.*, 2004). However, less attention has been paid towards the infrared photovoltaic considering half of the sun's power reaching the surface lies in the infrared region (McDonald *et al.*, 2004). Solar cells based on conjugated polymers with infrared emitting NCs provide a great opportunity for accessing infrared region. One strategy for hybrid solar cells is to use blends of inorganic nanocrystals with semiconductive polymers as a photovoltaic layer. In 2004, Sargent and co-workers reported the photoconductivity in a nanocomposite containing a sensitized polymer poly[2-methoxy-5-(2'-ethylhexyloxy-phenylenevinylene)] (MEH-PPV) with PbS NCs (Zhang *et al.*, 2005). However, the system had a low internal quantum efficiency of 10^{-5} . Later, the same group reported a three-order-of-magnitude improvement in infrared photoconductive internal quantum efficiency of a solution-processed device (Maria *et al.*, 2005). This was also the first time that an infrared photovoltaic effect is observed in such devices. Figure 2.19 shows the structure of photovoltaic devices.

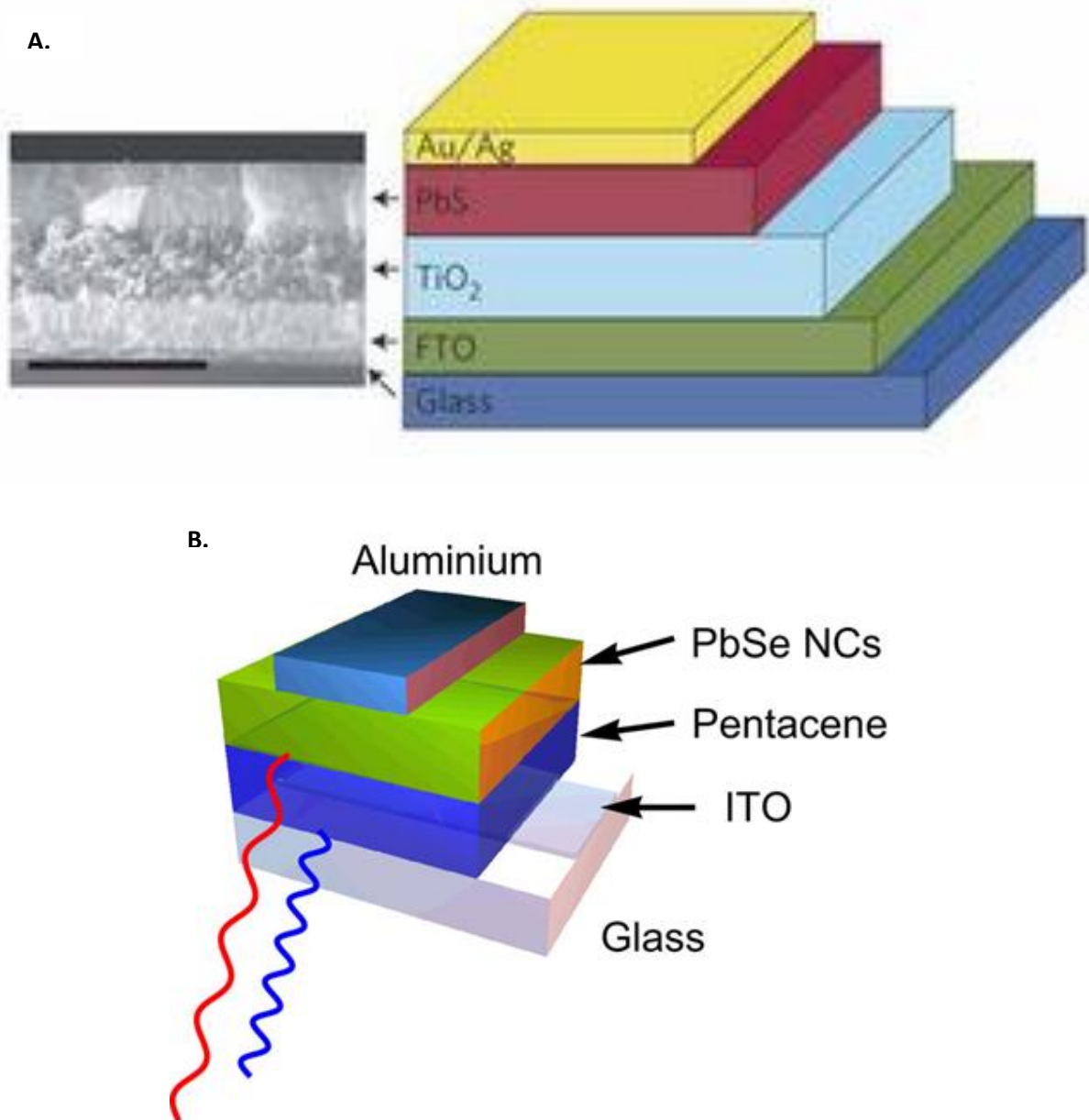


Figure 2.19 Structure of photovoltaic devices with **A.** having a PbS layer and **B.** having a PbSe layer (Ehrler *et al.*, 2012; Tang *et al.*, 2011)

In another study, Zhang *et al.*, (2005) demonstrated a bulk heterojunction hybrid solar cell containing MEH-PPV blend and octylamine capped PbS NCs (abs = 935 and 1300 nm). Herein, the devices constructed using octylamine capped PbS NCs allowed over two orders of magnitude more photocurrent as well as showed infrared photovoltaic response whereas,

oleic acid NCs did not. This is a possible result of charge carriers being able to tunnel through the ligand barrier or to transfer directly from the polymer to NC structure sites left free by incomplete ligand exchange process. The device exhibited short-circuit current (250 nA) and an open circuit voltage (0.47 eV). A bilayer photovoltaic device containing butylamine capped PbS NCs (abs = 1260 nm) and poly-3(octylthiophene) (P3OT) showed an internal quantum efficiency of 11.3 % and an external quantum efficiency exceeding 1 % for an infrared photovoltaic response at $\lambda=720$ nm (Maria *et al.*, 2005). The overall power conversion efficiency of the device was however, not reported. Klem *et al.* (2007) reported hybrid photovoltaic devices infrared power conversion efficiencies of 1.3 %. The authors used ethanedithiol as a multiple cross-linker and high-temperature sintering processes to achieve smooth films on rough ITO surfaces. Planar Schottky photovoltaic devices have been prepared from solution processed PbS NCs films with aluminum and indium tin oxide contacts (Johnston *et al.*, 2008). These devices exhibited up to 4.2 % infrared power conversion efficiency. More recently, hybrid bilayer photovoltaic devices based on PbS NCs on ITO substrates covered with a poly (3-hexyothiophene-2,5-dilyl) (P3HT) layer has shown to enhance the interfacial layer and improve charge carrier separation and mobility, yielding better performing solar cells (Fritz *et al.*, 2008).

Cui and co-workers (2006) reported a bulk heterojunction solar cell containing oleic acid capped PbSe NCs in a P3HT matrix. The device exhibited an incident monochromatic photon to current conversion efficiency of 1.3 % at $\lambda= 805$ nm. Under AM (air mass coefficient) 1.5 illumination, overall power conversion efficiency of 0.14 % was achieved from the device. A more stable solution-processed photovoltaic devices having 3.6 % power conversion efficiency have been reported by Jiang *et al.*, (2007). The device exhibited photovoltaic response only after being subjected to the strongly bound bidentate linker, benzenedithiol as it offers passivation of dangling bonds. Polymer-free photovoltaic devices

have recently been fabricated via a solution process using PbSe NCs and an organic semiconductor, tetrabenzoporphyrin (Koleilat *et al.*, 2008). Flat heterojunction and bulk heterojunction devices were fabricated and in both cases, photovoltaic conversion was observed. However, the energy conversion efficiency of the bulk heterojunction device was $1.8 \times 10^{-3} \%$ which was 40 times that of the flat heterojunction junction under 100 mW cm^{-2} illumination at 800 nm.

2.17.2 Photonic devices

Cademartiri *et al.*, (2006) have demonstrated the formation of NC solid arrays derived from the ordered packing of the mono disperse PbS NCs whose emission could be tuned from 1245 to 1625 nm with a FWHM of 65 meV with no trace of trap emission up to 2100 nm. The photoluminescence life time of NCs under excitation of 1.064 μm was found to be mono exponential and longer (1.828 μs) than previously reported (1 μm) (Warner *et al.*, 2005). The lifetimes in the layered structures were found to be shorter and non-exponential due to Förster energy transfer between neighbouring NCs. It is also possible to couple PbS NCs dissolved in poly(methyl methacrylate) (PMMA) to photonic crystal cavities at room temperature (Fushman *et al.*, 2005). Subsequently, NCs emission is shown to map out the structure resonance. It could enable isolation of a single emitter inside a cavity which would be beneficial for the construction of single photon sources which are cheap and reusable as opposed to the self-assembled NCs embedded in a photo crystal cavity (Englund *et al.*, 2005). In another study, silicon on insulator photonic crystal nanostructures have been fabricated and characterised by photoluminescence spectroscopy by doping the photonic crystals with PbS NCs embedded in a PMMA matrix (Dorfner *et al.*, 2007). The cavity modes quality factors of $Q = 88$ were observed as prominent peaks in the emission were recorded from the cavity locations. It is also possible to infiltrate PbS NCs into the photonic colloidal crystals

(Paquet *et al.*, 2006). The technique is based on capillary forces to load PbS NCs in the interstitial voids of the colloid crystals. The shifts in the stop band from resulting infiltration of the colloidal crystal show that PbS NCs occupy nearly 100 % of the volume of the interstitial space. PbSe NC/sol-gel composites have been used to develop a new optically detected band with a well-defined threshold of 0.2 mW and a clear super linear growth, which are signatures of amplified spontaneous emission (Schaller *et al.*, 2003). The optical band of composite containing 4.8 PbSe NCs was observed to be tuneable from 1450-1550 nm which is the important “telecommunication window”. At the same time, it has been demonstrated that free standing silicon photonic crystal membrane micro-cavities can exhibit Q factors (quality factor) as large as 10⁶ (Asano *et al.*, 2006). Fabrication and characterisation of 1.55 μm Si-based photonic crystal micro-cavity light emitters utilizing PbSe NCs has been reported (Wu *et al.*, 2007). Enhancement of spontaneous emission is observed at 1550 nm at room temperature. Figure 2.20 depicts a silicon photonic crystal nano-cavity light emitting diode, which operates in 1300-1600nm wavelength range.

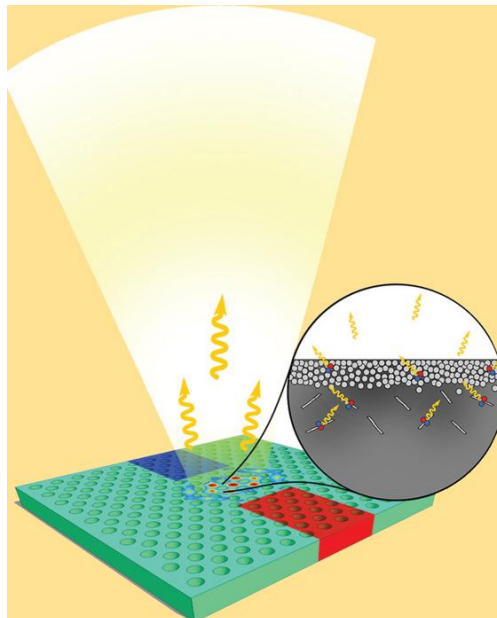


Figure 2.20 Diagram depicting silicon photonic crystal nano-cavity light emitting diode (“Front Cover Picture: Laser & Photon. Rev. 7(1)/2013”, 2013)

2.17.3 Quantum dot-polymer light emitters

The properties of organic light emitting diodes can be made attractive by combining with the attractive properties of NCs. Due to limited choice of polymers and organic dyes emitting in the range of the telecommunications windows (1.3 and 1.55 μm), IR emitting NCs in hybrid organic-inorganic LEDs provide an attractive option. Nano composites consisting of PbS NCs in conducting conjugated polymers have been fabricated and their resulting electroluminescence (EL) spectra across the range of 1000-1600 nm has been reported (Bourdakos *et al.*, 2008). The EL intensity of the octylamine capped PbS NCs was found to be much higher than oleic acid capped PbS NCs which is possible due to either suppression of Förster energy transfer or direct carrier transfer from the polymer to the NCs in the case of the longer ligands. Internal quantum efficiency up to 1.2 % was reported (Bourdakos *et al.*, 2008). In another study, the same group has reported the internal efficiency of electroluminescence to 3.1 % by replacing oleate with longer octadecylamine ligands. The surface exchange of capping ligands on PbS NCs in favor of short insulating ligands appears to have an important role in achieving high EL quantum efficiency devices. Recently, fabrication of NIR EL devices emitting at 1.2 μm has been reported in which excitons are directly created on the NCs therefore, removing the need for exciton generation on organic molecules (Bourdakos *et al.*, 2008). These devices have quantum efficiency of \sim 5-12 %. These devices also represent a significant improvement in the development of low cost NIR devices. NIR electroluminescence using PbSe NCs in organic host materials has been demonstrated. By changing the size of NCs, the EL can be tuned from 1.33 to 1.56 μm with peak external quantum efficiencies of 0.001% which was limited by the reduced PL quantum efficiency of closely packed PbSe NCs in the solid state. Similar to the previous observation, NIR emission of the PbSe NC polyphenylvinylene blend also rarely goes above the noise

level of the system and the efficiency at NIR is negligibly small (Solomeshch *et al.*, 2005). It could be a result of polymer HOMO and LUMO levels not being wrapped around the levels of the embedded PbSe NCs.

2.17.4 Biological applications

Fluorescent NCs provide a powerful tool for studying molecular and cellular biology along with imaging and medical diagnostics (He and Wang, 2004). Most of the fluorescence imaging has been performed in the visible region, especially non-invasive *in vivo* imaging requires deep penetration of light into and out of tissue. The best penetration by the light is achieved with an NIR wavelength (He and Wang, 2004). The penetration depth of light depends on the absorption and scattering properties of the tissue and the absorbance of the water. The studies indicated that the wavelength over 1000 nm gives better contrast due to decrease in scattering (Lim *et al.*, 2003). Therefore, water soluble NCs over 1000 nm are crucial for NIR fluorescence imaging. A simple and rapid protocol for transferring PbS and PbSe NCs into water has been demonstrated (Hyun *et al.*, 2007). Chemical modification via a carboxylic group on the NCs has been used for target-specific labeling of cells. Moreover, NIR fluorescence imaging of human colon cells is also demonstrated as an example. The potential uses of NIR NCs as fluorescent contrast agents for biomedical imaging in living tissue are exceptionally high, given the limited choice of suitable organic dyes (Cy7, IRDye78, indocyanine green) that can be utilized within the biological window (Rogach *et al.*, 2007).

NIR emitting NCs used as contrast agents in both cells and tissue also offer additional benefits in terms of significantly reduced auto fluorescence background signal. The NCs surface also serves the additional purpose of providing selective binding to a target such as a protein. PbS bioconjugates have been used as NIR contrast agents for targeting molecular

imaging with expanded emission wavelength beyond 1000 nm (Sun *et al.*, 2007). In their work, Sun and co-workers performed imaging experiments at the molecular level using surface modified PbS dots and indicated that PbS NCs /antibody bioconjugates are promising candidates for targeted molecular imaging.

Considerable interest has been generated for opto-biological detection using NCs (Liu and Lin, 2007). The electrochemical stripping of the metal component of the NCs (CdS, PbS, ZnS) have intrinsic redox properties which causes the labels in the electrochemical biosensors to be very sensitive (Wang, 2005, 2007). Wang *et al.*, (2003) demonstrated the use of different NCs (CdS, ZnS, PbS) tags for multi-target electrochemical detection of DNA. Introduction of an effective and inexpensive multi target electrochemical immunoassay based on the use of different NCs tags has also been reported (Liu *et al.*, 2004). Carbamate linkages were used for conjugating the hydroxyl-terminated NCs with the secondary antibodies. The concept was demonstrated for a simultaneous immunoassay of a 2-microglobulin, bovine serum, albumin, and C-reactive protein in connections with NCs. Hansen *et al.* (2006) have reported a NCs /aptamer-based ultrasensitive electrochemical biosensor to detect multiple protein targets. The technique is based on a single-step displacement assay involving the co-immobilization of several thiolated polymers on a gold surface, adding the protein sample, and monitoring the displacement through electrochemical detection of the remaining NCs. Such electronic transduction of aptamer-protein interactions is extremely attractive for meeting the low power, size, and cost requirements of decentralized diagnostic systems.

Chapter 3

General Experimental Procedures

3.1 Summary

This chapter presents the general experimental procedures used in this research. Single crystal structure of newly synthesised compounds was determined by Dr. Madeleine Helliwell and Dr. James Raftery of the School of Chemistry, The University of Manchester, United Kingdom.

All chemicals and reagents were purchased from Sigma-Aldrich, United Kingdom and were used as received. The list of chemicals and reagents are shown in table 3.1.

Table 3.1 List of chemicals and reagents

Item	Chemical	Grade	Assay
1	Chlorodiisopropylphosphine	-	96 %
2	Toluene	ACS reagent	99.5 %
3	Methanol	ACS reagent	≥99.8 %
4	Dichloromethane	ACS reagent	99.5 %
5	Chloroform	ACS reagent	≥99.8 %
6	Hexane	Laboratory reagent	≥95 %
7	Acetone	ACS reagent	≥99.5 %
8	Tetrahydrofuran	ACS reagent	≥99.0 %
9	Oleylamine	Technical grade	70 %
10	Trioctylphosphine	Technical grade	90 %

11	Lead(II)acetate trihydrate	ACS Reagent	≥99 %
12	Lead(II) chloride	-	98 %
13	Sodium methoxide	Laboratory Reagent	95 %
14	1,1,1,3,3,3-Hexamethyl disilazane	ACS Reagent	99.9 %
15	Sulphur powder	-	99.98 % trace metals basis
16	Selenium powder	-	99.99 % trace metals basis

3.2 Synthesis and characterisation of ligands and complexes

All synthetic reactions were performed under an inert atmosphere of dry nitrogen using standard Schlenk line techniques. All reagents were purchased from Sigma-Aldrich and used as received. ^1H NMR spectra were obtained using a Bruker AC400 FT-NMR spectrometer. Mass spectra were recorded on a Kratos concept 1S instrument. Infrared spectra were obtained on a Bruker Alpha single reflectance ATR instrument ($4000\text{--}400\text{ cm}^{-1}$). Elemental analysis was performed by the University of Manchester Micro-analytical facility.

3.2.1 Synthesis of $^i\text{Pr}_2\text{P}(\text{Se})\text{NHP}(\text{Se})^i\text{Pr}_2$ ligand (1)

The reaction was performed under nitrogen. A solution of $^i\text{Pr}_2\text{PCl}$ (12.5 g, 13.0 ml, 82 mmol) in toluene (25 ml) was added dropwise to a solution of $\text{HN}(\text{SiMe}_3)_2$ (6.61 g, 8.54 ml, 41.0 mmol) in hot ($50\text{ }^\circ\text{C}$) toluene (25 ml) over 30 min. Heating and stirring was continued for 3 hours after which time the reaction was cooled to room temperature and selenium powder (6.47 g, 82 mmol) was added. The resulting mixture was then refluxed for a further 6 hours and cooled to $0\text{ }^\circ\text{C}$. The resulting white precipitate was filtered off and washed with diethyl ether and cold toluene. Excess selenium was removed by dissolving the product in CH_2Cl_2

and filtering through celite, followed by removal of solvent in vacuo. The crude product was recrystallised from CH₂Cl₂/ hexane at 1:3 ratio.

Elemental analysis: C₁₂H₂₉NP₂Se₂: Found: C, 37.14, H, 7.56, N, 3.48, P, 14.93 %. Calculated: C, 35.37, H, 7.18, N, 3.44, P, 15.22 %. ³¹P {1H} NMR (CDCl₃): 89.5 ppm. FT-IR: n(N–H) 3203(s); d(N–H) 1384(m); n(PNP) 900(s), 875(s) cm⁻¹; MS: m/z 407 corresponds to HN(ⁱPr₂PSe)₂. Mpt.: 178-180 °C, yield, 22.74 %

3.2.2 Synthesis of ⁱPr₂P(S)NHP(S)ⁱPr₂ ligand (2)

A solution of ⁱPr₂PNHPⁱPr₂ was prepared as for ligand (1). Sulphur (2.63 g, 82 mmol) was added and the reaction was then refluxed for a further 6 hours and cooled to room temperature. The resulting white precipitate was filtered off and washed with carbon disulphide CS₂ (2 x 10 mL) and light petroleum ether (2 x 10 mL). The crude product was recrystallized from CH₂Cl₂/hexane at 1:3 ratio.

Elemental analysis: C₁₂H₂₉NP₂S₂: Found: C, 45.34; H, 9.36; N, 4.61; P, 18.79. Calculated: C, 45.99; H, 9.33; N, 4.47; P, 19.78.; ³¹P {1H} NMR (CDCl₃): 91.2 ppm; FT-IR: n(N–H) 3241(s); d(N–H) 1385(s); n(PNP) 901(s), 877(s) cm⁻¹ MS: m/z =314 corresponding to [M + H]⁺ was observed with the expected isotopic distribution patterns. Mpt.: 179-181 °C, yield, 35.08 %

3.2.3 Synthesis of ⁱPr₂P(Se)NHP(S)ⁱPr₂ ligand (3)

A solution of ⁱPr₂PNHPⁱPr₂ was prepared as for ligand (1). Selenium (3.24 g, 41 mmol) was added and the solution stirred overnight. Sulphur (1.32 g, 41 mmol) was then added and

stirring continued for 6 hours. The solvent was removed in vacuo and the off-white product recrystallised from CH_2Cl_2 and hexane at 1:3 ratio.

Elemental analysis: $\text{C}_{12}\text{H}_{29}\text{NP}_2\text{SeS}$: Found: C, 39.52; H, 8.34; N, 3.94; P, 16.49 %. Calculated: C, 39.99; H, 8.12; N, 3.89; P, 17.20%. ^{31}P {1H} NMR (CDCl_3): 92.1, 89.2 ppm. FT-IR: $\nu(\text{N-H})$ 3204(s); $\delta(\text{N-H})$ 1385(s); $\nu(\text{PNP})$ 901(s), 876(s) cm^{-1} . MS: m/z 360 corresponds to $^i\text{Pr}_2\text{P}(\text{Se})\text{NHP}(\text{S})^i\text{Pr}_2$. Mpt.: 177-179 °C, yield, 30.94 %

3.2.4 Synthesis of $[\text{Pb}((\text{Se}^i\text{Pr}_2)_2\text{N})_2]$ complex (4)

Sodium methoxide (0.27 g, 4.9 mmol) was added to a stirred solution of $^i\text{Pr}_2\text{P}(\text{Se})\text{NHP}(\text{Se})^i\text{Pr}_2$ (**1**) (2 g, 4.9 mmol) in anhydrous (dried on molecular sieves) methanol (100 ml). The resulting pink solution was stirred at room temperature for 10 minutes. PbCl_2 (0.68 g, 2.45 mmol) was added and the reaction mixture stirred at room temperature for 3 hours. The resulting suspension was filtered and the recovered solid washed with methanol (100 ml) before drying under vacuum. Recrystallisation from chloroform/methanol (1:3) yielded a yellow powder.

Elemental Analysis: $\text{C}_{24}\text{H}_{56}\text{N}_2\text{P}_4\text{Se}_4\text{Pb}$. Calculated: C= 28.25, H= 5.54, N= 2.75, P= 12.15 %. Observed: C= 29.37, H= 5.60, N= 2.79, P: 12.46 %. ^1H NMR (d, CdCl_2 , 400 MHz): 1.15 (m, 48H, 16 CH_3 -R), 2.13 (m, 8H, 8R-CH); FT-IR ; 2961 $\nu(\text{C-H})$, 1453 $\nu(\text{C-N})$, 880 $\nu(\text{C-S})$ cm^{-1} ; MS (ESI), m/z ~ [M1] 1019, $[(\text{Se}^i\text{Pr}_2)_2\text{N}]$ 408; Mpt. 131-133 °C, yield, 39.79 %

3.2.5 Synthesis of [Pb((SPⁱPr₂)₂N)₂] complex (5)

This preparation is as for complex **4**, except that the reaction involved the following quantities of materials. NH(SPⁱPr₂)₂ (**2**) (3 g, 9.7 mmol), NaOMe (0.52 g, 9.7 mmol), PbCl₂ (1.33 g, 4.85 mmol). Recrystallisation was carried out from dichloromethane.

Elemental analysis: C₂₄H₅₆N₂P₄S₄Pb. Calculated: C= 34.64, H= 6.79, N: 3.37, P: 14.90 %.

Observed: C= 36.87, H=7.45, N=3.58, P= 15.41 %. ¹H NMR (d, CdCl₃, 400 MHz): 1.15 (m, 48H, 16CH₃-R), 2.08 (m, 8H, 8R-CH); FT-IR , 2961 ν(C-H), 1450 ν(C-N), 880 ν(C-S) cm⁻¹; MS (ESI), m/z~[M+H] 833, [(SPⁱPr₂)₂N] 314; Mpt. 98-100 °C, yield, 41.43 %

3.2.6 Synthesis of [Pb(SeS(PⁱPr₂)₂N)₂] complex (6).

This preparation is as for complex **4**, except that the reaction involved the following quantities of materials. NHSSe(PⁱPr₂)₂ (**3**) (3 g, 8.33 mmol), NaOMe (0.52 g, 8.33 mmol), PbCl₂ (1.16 g, 4.17 mmol). Recrystallisation was carried out from dichloromethane.

Elemental analysis: C₂₄H₅₆N₂P₄S₂Se₂Pb. Calculated: C=31.13, H=6.10, N=3.03, P=13.38 %

Observed: C=31.15, H=6.10, N=2.92, P=12.40 %; ¹H NMR (d, CdCl₃, 400 MHz): 1.16 (m, 48H, 16CH₃-R), 2.10 (m, 8H, 8R-CH); FT-IR , 2955 ν(C-H), 1455 ν(C-N), 880 ν(C-S) cm⁻¹; m/z= 927 (M+1), [(SeSPⁱPr₂)₂N] =360; Mpt. 115-117 °C, yield, 30.30 %

3.2.7 Synthesis of [Ph₂P(Se)NHP(Se)Ph₂] ligand (7)

The reaction was performed under nitrogen. A solution of Ph₂PCl (6.142g, 5.0 ml, 27.85 mmol) in toluene (25 ml) was added dropwise to a solution of HN(SiMe₃)₂ (6.61 g, 8.54 ml, 41.0 mmol) in hot (50 °C) toluene (25 ml) over 30 min. Heating and stirring was continued for 3 hours after which time the reaction mixture was cooled to room temperature and

selenium powder was added (6.47 g, 82 mmol). The reaction mixture was then refluxed for a further 6 hours and cooled to room temperature. The resulting white precipitate was filtered off and washed with diethyl ether and cold toluene. Excess selenium was removed by dissolving the product in CH_2Cl_2 and filtering through celite, followed by removal of solvent in vacuo. The crude product was recrystallised from CH_2Cl_2 and hexane.

Elemental analysis calculated for $\text{C}_{24}\text{H}_{21}\text{NP}_2\text{Se}_2$: Calculated: C=53.06, H=3.90, N=2.58, P=11.40. Observed: C= 53.00, H=3.74, N=2.57, P= 11.10. FT-IR: $\nu(\text{N-H})$ 279(s); $\delta(\text{N-H})$ 1434(m); $\nu(\text{PNP})$ 913(s) cm^{-1} ; MS [ES⁻]: $m/z = 544$ corresponds to $\text{HN}(\text{Ph}_2\text{PSe})_2$. Mpt: 217-220 °C, yield, 68.87 %

3.2.8 Synthesis of $[\text{Ph}_2\text{P}(\text{S})\text{NHP}(\text{S})\text{Ph}_2]$ ligand (8)

A solution of $\text{Ph}_2\text{PNHPPH}_2$ was prepared as for $(\text{Ph}_2\text{P}(\text{Se})\text{NHP}(\text{Se})\text{Ph}_2)$. Sulphur (2.63g, 82 mmol) was added and the reaction mixture was then refluxed for a further 6 hours and cooled to room temperature. The resulting white precipitate was filtered off and washed with carbon disulphide CS_2 (2 x 10 mL) and light petroleum ether (2 x 10 mL). The crude product was recrystallized from CH_2Cl_2 /hexane at 1:3 ratio.

Elemental analysis calculated for $\text{C}_{12}\text{H}_{29}\text{NP}_2\text{S}_2$: C=64.13; H=4.71; N=3.12; S=14.27; P=13.78. Observed: C=64.74; H=4.75; N=3.20; S=13.92; P= 13.38; FT-IR: $\nu(\text{N-H})$ 3018(s); $\delta(\text{N-H})$ 1435(s); $\nu(\text{PNP})$ 918(s) cm^{-1} MS [ES⁻]: $m/z = 448$ corresponding to $[\text{M} - \text{H}]^+$ was observed with the expected isotopic distribution patterns. Mpt.: 216-218 °C, yield, 58.72 %.

3.2.9 Synthesis of [Pb((SePPh₂)₂N)₂] complex (9)

Sodium methoxide (0.27 g, 4.9 mmol) was added to a stirred solution of PhP(Se)NHP(Se)Ph₂ (2 g, 4.9 mmol) in anhydrous methanol (100 ml). The resulting pink solution was stirred at room temperature for 10 minutes. PbCl₂ (0.68 g, 2.45 mmol) was added and the resulting mixture stirred at room temperature for 3 hours. The resulting suspension was filtered and the recovered solid washed with methanol (100 ml) before drying under vacuum. Recrystallization from chloroform/methanol yielded a yellow powder.

Elemental Analysis: C₂₄H₂₁N₂P₄Se₄Pb. Calculated: C= 44.63, H= 3.12, N= 2.15, P= 9.59 %.

Observed: C= 42.90, H= 2.97, N= 2.13, P: 9.39 %. ¹H NMR (d,CdCl₃, 400 MHz): 7.3, 7.9 (m, 40H, 8C₆H₅-R) ; FT-IR ; 3008 v(C-H), 1434 v(C-N), 917 v(C-S) cm⁻¹; Mpt. 201-203 °C, yield, 75.03 %

3.2.10 Synthesis of [Pb((SPPH₂)₂N)₂] complex (10).

This preparation is as for [Pb((SePPh₂)₂N)₂] complex , except that the reaction involved the following quantities of materials. NH(SPⁱPr₂)₂ (3 g, 9.7 mmol), NaOMe (0.52 g, 9.7 mmol), PbCl₂ (1.33 g, 4.85 mmol). Recrystallisation was carried out from dichloromethane.

Elemental Analysis: C₂₄H₂₁N₂P₄S₄Pb. Calculated: C= 52.21, H= 3.65, N= 2.54, S= 11.62 P= 11.22 %. Observed: C= 50.76, H= 3.47, N= 2.52, S= 11.32 P: 11.05 %. ¹H NMR (d,CdCl₃, 400 MHz): 7.3, 7.9 (m, 40H, 8C₆H₅-R) ; FT-IR ; 3008 v(C-H), 1434 v(C-N), 917 v(C-S) cm⁻¹; Mpt. 218-221 °C, yield, 69.31 %

3.2.11 Synthesis of Bis (thiourea) lead (II) complex (11)

First, thiourea (2.28 g, 30 mmol) was added to 80 mL of methanol. Lead nitrate (4.97 g, 15 mmol) was added to that solution, after thiourea had been completely dissolved in methanol. The solution was stirred for approximately 30 min and then centrifuged to remove a small amount of undissolved material. The obtained clear solution was condensed to 20 mL under reduced pressure and allowed to stand overnight at room temperature. White crystalline precipitate was obtained in solution and filtered. The filtrate was washed with ethanol, and dried under vacuum. It was recrystallized in hot toluene.

Elemental Analysis: $C_2H_8N_4S_2Pb$. Calculated: C=6.68, H=2.24, N=15.59, S=17.84 %. Observed: C=6.15, H=2.63, N=19.59, S=16.42. MS [ES+] m/z 283= $[PbSCN_2H_4]^+$, MS [ES-] m/z 250= PbSC. Yield, 84.95 %.

3.2.12 Synthesis of diphenylselenophosphinate $[HNEt_3]^+[Ph_2PSe_2]^-$ ligand (12)

Chlorodiphenylphosphine, Ph_2PCl (5.00 mL, 6.145 g, 27.85 mmol) and triethylsilane, $HSiEt_3$ (8.90 mL, 6.477 g, 55.70 mmol) were dissolved in 60 mL cold dry toluene under nitrogen, followed by triethylamine, NEt_3 (10.35 mL, 7.52 g, 74.27 mmol). The mixture was stirred for 8 hours at room temperature forming a white cloudy solution. Selenium powder (4.398 g, 55.70 mmol) was added to the solution which was further refluxed for 24 hours leading to the formation of yellow precipitate. The precipitate was filtered from solution and washed with cold hexane. It was recrystallized in hot toluene forming yellow crystals.

Elemental Analysis: $C_{18}H_{26}NPSe_2$. Calculated: C=48.53, H=5.89, N=3.15, P=6.96 %. Observed: C=49.41, H=6.88, N=4.04, P=5.63 %.

ESI-MS: $m/z = 446 [M^+]$; $m/z = 102 [HNEt_3]^+$; $m/z = 343 [Ph_2PSe_2]^-$. 1H NMR (400 MHz, $CDCl_3$): δ ppm 1.29 (t, 6 H), 3.10 (q, 4 H), (m, 7.22, q, 8.06). ^{13}C NMR (400 MHz, $CDCl_3$): δ ppm 46.17, 8.71. ^{31}P NMR (400 MHz, $CDCl_3$): δ ppm 22.20. Mpt.: 119-121 °C

3.2.13 Synthesis of $Pb(S_2CNEt_2)_2$ complex (13)

Lead nitrate (3.975 g, 11.09 mmol) was mixed with sodium diethyldithiocarbamate (5.000 g, 22.19 mmol) in methanol at room temperature and stirred for one hour. The precipitate obtained was filtered and recrystallized from boiling toluene to give white crystals.

ESI-MS: $m/z = 504 (M^+)$; $m/z = 356 (PbCS_2NEt_2)$. 1H NMR (400 MHz, $CDCl_3$): δ ppm 3.72 (q, 8 H), 1.26 (t, 12 H). ^{13}C NMR (400 MHz, $CDCl_3$): δ ppm 47.31, 12.29. Anal. Calcd. for $PbC_{10}H_{20}N_2S_4$: C=23.84, H=4.01, N=5.56, S=25.41 Found: C=23.88, H=4.24, N=5.49, S=25.36 FT-IR ; 2963 $\nu(C-H)$, 1479 $\nu(C-N)cm^{-1}$, 838 $\nu(C-S)$. Mpt.: 211-213 °C, yield 80.43 %

3.2.14 Synthesis of $Pb(S_2CNMe_2)_2$ complex (14)

Lead acetate (3.79 g, 10.00 mmol) was mixed with sodium dimethyldithiocarbamate (3.00 g, 20.90 mmol) in methanol at room temperature and the mixture stirred for one hour. The precipitate obtained was filtered and recrystallized from boiling toluene to give white crystals.

Anal. Calcd. for $PbC_6H_{12}N_2S_4$: C=16.10, H=2.70, N=6.26, S=28.60 Found: C=16.55, H=2.45, N=5.89, S=27.52. Mpt.: >300°C. Yield: 76.89 %

3.2.15 Synthesis of [Pb(S₂COEt)₂] complex (15)

Lead acetate (3.55 g, 9.36 mmol) was mixed with sodium diethylxanthate (3.00 g, 18.71 mmol) in methanol at room temperature and the mixture stirred for one hour. The precipitate obtained was filtered and recrystallized from boiling toluene to give white crystals.

ESI-MS: $m/z = 450 [M^+]$; $m/z = 121 [S_2COC_2H_5]$. ¹H NMR (400 MHz, CDCl₃): δ ppm 1.55 (t, 6 H), 4.72 (q, 4 H). ¹³C NMR (400 MHz, CDCl₃): δ ppm 50.17, 15.71.

Elemental analysis Calcd. for PbC₆H₁₀O₂S₄: C=16.03, H=2.24, S=28.47 Found: C=15.93, H=2.06, S=28.00 Mpt.: 132-134 °C. Yield: 93.74 %

3.2.16 Synthesis of *N*-methyl-*N*-hexyldithiocarbamatolead(II) (16)

Typical procedure of synthesis of *N*-methyl-*N*-hexyldithiocarbamatolead(II) involved the stirring of 6.64 mL (44 mmol) of *N*-methyl-*N*-hexylamine dissolved in 50 mL of methanol with 1.32 mL (22 mmol) of CS₂ at 0 °C for 30 minutes. The solution gradually turned yellow in colour. Finally, (2.09 g, 5.5 mmol) of Pb(CH₃COO⁻)₂ dissolved in 10 mL of methanol was added dropwise and the whole mixture was stirred for 30 minutes. The obtained white precipitate was recrystallized in toluene and methanol.

ESI-MS: $m/z = 589 [M^+ + 1]$; $m/z = 190 [S_2NC_8H_{16}]$. ¹H NMR (400 MHz, CDCl₃): δ ppm 0.91(m, 3H), 1.33 (m, 16 H), 1.59 (s, 5H), 2.18 (s, 1H), 3.32 (s, 7H), 3.75 (m, 5H).

Elemental analysis % Calc. for C₁₆H₃₂N₂S₄Pb: C=32.69, H=5.49, N=4.77, S=21.77 Found: C= 31.96, H=6.27, N=4.64, S=21.54. Melting point: 88-90 °C. Yield: 94.00 %

3.3 Thermogravimetric analysis (TGA)

TGA measurements were carried out using a Seiko SSC/S200 thermal analyzer under a heating rate of $10\text{ }^{\circ}\text{C min}^{-1}$ and nitrogen flow rate 10 mL/min .

3.4 Single crystal X-ray crystallography and powder X-ray diffraction

Single crystal X-ray crystallography measurements were made using graphite monochromated Mo $K\alpha$ radiation on a Bruker APEX diffractometer. The structures were solved by direct methods and refined by full-matrix least-squares on F2 (Sheldrick, 1997, 2008). All calculations were carried out using the SHELXTL package (Lee *et al.*, 2004; Sheldrick, 2008). All non-hydrogen atoms were refined with anisotropic atomic displacement parameters. Hydrogen atoms were placed in calculated positions and were assigned isotropic atoms.

X-ray powder diffraction patterns were obtained using a Bruker D8 AXE diffractometer (Cu- $K\alpha$). The samples were scanned between 20 to 80 degrees in a step size of 0.05 with a count rate of 10 sec.

3.5 Aerosol assisted chemical vapour deposition (AACVD) apparatus

Deposition of PbS and PbSe thin films was carried out in an improvised aerosol assisted chemical vapour deposition (AACVD) apparatus (Figure 3.1).

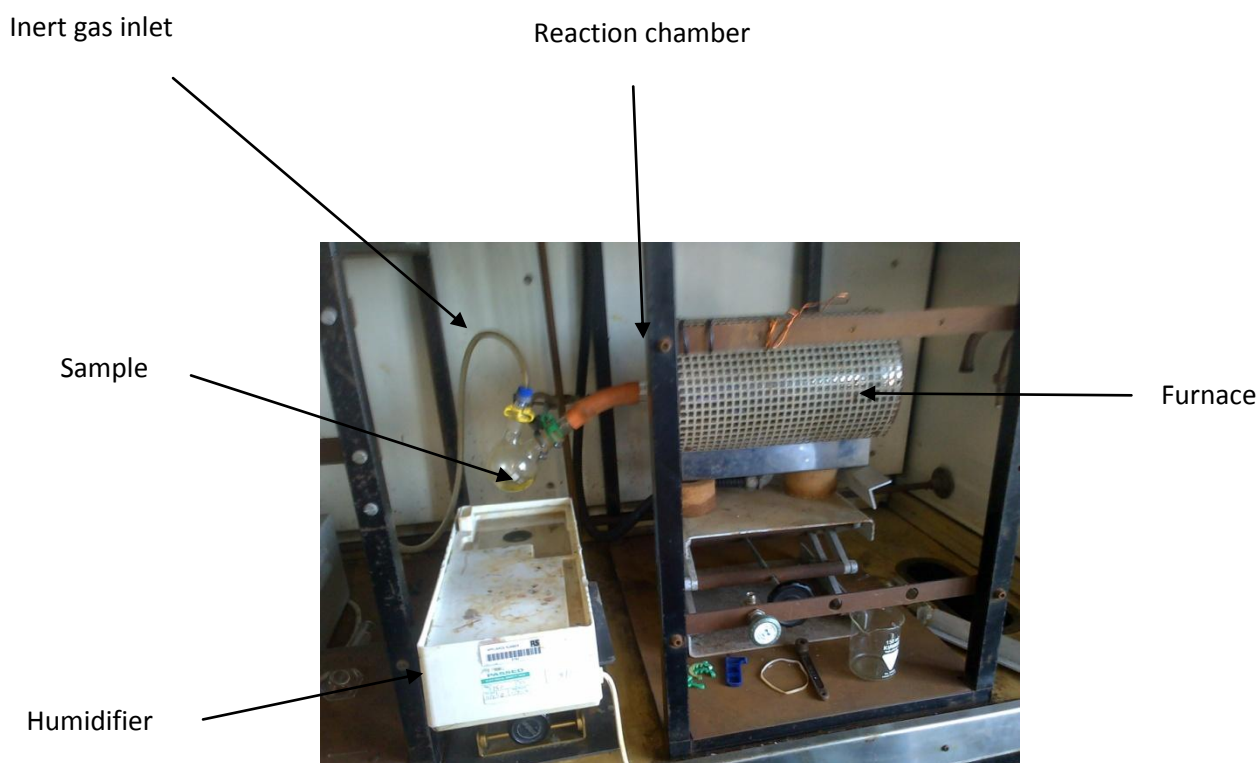


Figure 3.1 AACVD setup

The glass substrates were cleaned by rinsing them in acetone and then placed in an ultrasonic washer (in distilled water) for 10 minutes and dried in an oven. The substrates were placed in a quartz reaction chamber and inserted into a furnace. A solution of complex in tetrahydrofuran was put in a round-bottomed flask. The aerosol droplets were generated from the complex solution by Pifco ultrasonic humidifier. Flow of carrier gas (Ar) transferred the aerosol droplets to the deposition chamber where the film deposition took place. The complex vapours settled on heated substrate surface where decomposition occurred.

3.6 Deposition procedure of lead chalcogenide thin films of by AACVD

In a typical deposition experiment, 0.2 g of complex was dissolved in 10 ml tetrahydrofuran in a two-necked 100 ml round-bottom flask with a gas inlet that allowed the carrier gas

(argon) to pass into the solution to aid transport of the aerosol. This flask was connected to the reactor tube by a piece of reinforced tubing (Ramasamy *et al.*, 2011; Saeed *et al.*, 2013). The argon flow rate was controlled by a Platon flow gauge. Eight glass substrates (approx. 1 x 3 cm) were placed inside the reactor tube and put in a Carbolite furnace. Complex solution in a round-bottom flask was kept in a water bath above the piezoelectric modulator of a PIFCO ultrasonic humidifier (Model No. 1077). The aerosol droplets of the complex thus generated were transferred into the hot-wall zone of the reactor by carrier gas where the complex decomposes to deposit a thin film of the required material.

3.7 Characterisation techniques

3.7.1 Transmission electron microscopy (TEM)

The transmission electron microscope (TEM) is an essential tool for the structural imaging of nanometer-sized features. As its name implies, the TEM is used to obtain structural information from specimens thin enough to transmit electrons. In the TEM, electrons are transmitted through a thinly sliced specimen and form an image on a fluorescent screen or photographic plate.

Those areas of the sample that are more dense will transmit fewer electrons (i.e. will scatter more electrons) and will therefore appear darker in the image. When TEM is compared to a slide projector, the slide is (specimen) illuminated by light (electron beam) that first passes through the condenser lens (electromagnetic condenser lens). In operation, electrons are thermo ionically emitted from the gun and typically accelerated to anywhere from 125 to 300 keV or higher (e.g., 1 MeV) in some image diffraction pattern. In addition, TEM also provides the means to obtain a diffraction pattern from a small specimen area, selected area electron diffraction (SAED). This diffraction pattern is obtained in diffraction mode, where the post-specimen lenses are set to examine the information in the transmitted signal at the

back focal plane of the objective lens. In SAED, the condenser lens is defocused to produce parallel illumination at the specimen and a selected-area aperture is used to limit the diffracting volume. Many spots, or reflections, are evident in this pattern, due in part to the special orientation of the sample. SAED patterns often are used to determine the Bravais lattice and lattice parameters of crystalline materials. An image of Tecnai f30 TEM is shown in Figure 3.2.



Figure 3.2 An illustration of Tecnai f30 Transition Electron Microscope

3.7.2 Powder X-ray diffraction

X-ray diffraction (XRD) is a powerful technique used to identify the crystalline phases present in materials and to measure the structural properties (strain state, grain size, epitaxy, phase composition, preferred orientation, and defect structure) of these phases (Suresh *et al.*, 2013). X-ray diffraction is a non-contact and non-destructive technique, which makes it ideal for structural studies. A simple basic principle of X-ray diffraction can be understood from the Bragg equation (Eq. 3.1).

$$n\lambda = 2d \sin \theta \quad (\text{Eq. 3.1})$$

(where n is an integer, λ is the wavelength of a beam of rays incident on a crystal with lattice planes by distance d , and θ is the Bragg's angle.)

It shows that the angle of incidence could be calculated very easily in terms of the path difference between a ray reflected by one plane and that reflected by the next plane after it in the lattice. By comparing the positions and intensities of the diffraction peaks against a library of known crystalline materials, the target material can be identified. In addition to this, multiple phases in a sample can be identified and quantified. If one of the phases is amorphous, XRD can still determine the relative amount of each phase. When crystallites are less than approximately 100 nm in size, appreciable broadening in the X-ray diffraction lines will occur. Peak broadening corresponds to the actual size of the crystallites. The observed line broadening can be used to estimate the average particle size using the Scherrer equation

$$D = \frac{K\lambda}{\beta \cos\theta} \quad (\text{Eq. 3.2})$$

where:

- D is the mean size of the ordered (crystalline) domains, which may be smaller or equal to the grain size;
- K is a dimensionless shape factor, with a value close to unity. The shape factor has a typical value of about 0.9, but varies with the actual shape of the crystallite;
- λ is the X-ray wavelength
- β is the line broadening at half the maximum intensity (FWHM), after subtracting the instrumental line broadening, in radians. This quantity is also sometimes denoted as $\Delta(2\theta)$;
- θ is the Bragg angle.

The extent of broadening is described by the full width at half maximum intensity of the peak. A photograph of Bruker AXE D8 Discover X-ray diffractometer is shown in Figure 3.3.



Figure 3.3. A photograph of Bruker AXE D8 Discover X-ray Diffractometer

3.7.3 Scanning electron microscopy (SEM)

Scanning electron microscope (SEM) (Figure 3.4) is used to observe the surface morphology of the sample. It uses high energy beams of electrons which interact with atoms present on the surface and produce the image. Different types of signals are produced in SEM, including X-rays, back scattered electrons (BSE) and secondary electrons. Secondary electrons are important to study the surface morphology of samples. BSE and X-rays emitted from sample are used for analytical study of sample.



Figure 3.4. A photograph of Scanning Electron Microscope

3.7.4 Energy dispersive X-ray analysis (EDAX)

Energy dispersive X-ray analysis (EDAX) is another useful analytical technique to determine the composition of a sample. In this case, incident beam of electrons ejects an electron from inner shell (K, L). This process creates a hole in the inner shell, this hole is filled by an outer electron. The difference in energy between the higher-energy shell and the lower energy shell is released in the form of an X-ray. The number and the energy of the X-rays emitted from a specimen can be measured by an energy-dispersive spectrometer. The energy of the X-rays is characteristic of the difference in energy between the two shells. It is also characteristic of the atomic structure of the element and this technique can be used to determine the chemical composition of sample.

Chapter 4

Synthesis and characterisation of binary lead chalcogenide nanocrystals and thin films

4.1 Summary

A series of lead dichalcogenoimidodiphosphinato complexes, $[\text{Pb}((\text{EP}^i\text{Pr}_2)_2\text{N})_2]$ ($\text{E} = \text{S}, \text{Se}$) have been synthesised and characterised. These compounds have been employed as Single-source precursors for the synthesis of lead chalcogenide nanoparticles by thermal decomposition in trioctylphosphine/oleylamine. They have also been used to produce thin films by Aerosol Assisted Chemical Vapour Deposition (AACVD). X-ray powder diffraction (p-XRD) studies show cubic PbS/Se for both the nanoparticles and thin films. The crystal structures of these complexes have been determined by single-crystal X-ray crystallography.

4.2 Introduction

Imidodichalcogenphosphinates $[\text{N}(\text{Pr}_2\text{E}_2)]^-$ ($\text{R}=\text{alkyl}, \text{aryl}$) have been studied by researchers since its discovery in the early 1960s (Schmidpeter *et al.*, 1964). They are chelating ligands that readily form cyclic complexes with s-, p-, d-, and f- block metals (Chivers *et al.*, 2010). The structural chemistry of the resulting metal complexes ($\text{E} = \text{O}, \text{S}, \text{Se}$ and Te) have been studied extensively (Afzaal *et al.*, 2004; Chivers *et al.*, 2010; Chivers, *et al.*, 2005; Ritch *et al.*, 2007, 2010; Robertson and Chivers, 2008) and a variety of potential applications have been identified such as NMR shift reagents, luminescent complexes in photonic devices, or Single-source precursors for metal sulphides and selenides (Chivers *et al.*, 2010).

There has been a renewed interest in the use of imidodichalcogenophosphinate complexes of both the isopropyl and phenyl derivatives as Single-source precursors for the synthesis of colloidal nanocrystals and the production of thin semiconducting films of binary metal chalcogenides (ME) where M= Zn, Cd, Hg, Pb and E= S, Se, Te. The deposition methods used include Low Pressure Metal Organic Chemical Vapour Deposition (LP-MOCVD) (Afzaal *et al.*, 2004) and Aerosol Assisted Chemical Vapour Deposition (Afzaal *et al.*, 2003, 2004; Crouch *et al.*, 2003; Waters *et al.*, 2004). Solvothermal system of colloidal CdSe quantum dots has been reported (Crouch *et al.*, 2003).

Lead chalcogenides are narrow band gap semiconductor materials with band gaps of ca. 0.41 (PbS) and 0.27 eV (PbSe) (Afzaal *et al.*, 2004). Both PbS and PbSe have cubic (rock salt) structures and exist as either p- or n-type semiconductors. They mainly absorb in the infra-red region and can be used in very high performance photoconductive infrared detectors (Afzaal *et al.*, 2004; Boadi *et al.*, 2012). The electronic band structures of both PbS and PbSe have been reported (Kohn *et al.*, 1973) and show minimum direct band gaps at the L point (a central point of a hexagonal face of a face centered cubic lattice with symmetry points $\frac{1}{2}, \frac{1}{2}, \frac{1}{2}$ and point group 3m) in the first Brillouin zone (Afzaal *et al.*, 2004). The intrinsic band gaps of PbS and PbSe decrease significantly with reduction in temperature. This is an unusual property in semiconductors (Afzaal *et al.*, 2004; Ellingson *et al.*, 2005).

Several different approaches are known for the preparation of PbE (E=S, Se) nanoparticles (Fu and Tsang, 2012). These include thermal decomposition of single or dual source complexes in alkyl amines (Jung *et al.*, 2010; Liu *et al.*, 2008; Pradhan *et al.*, 2003), in TOPO/TOP (Trindade *et al.*, 1999), solvothermal single-source method (Haiduc, 2001), hydrothermal method (Ding *et al.*, 2009) and other colloidal methods (Clark *et al.*, 2011; Zhou *et al.*, 2006).

In this work, lead chalcogenide nanoparticles were synthesised by thermal decomposition using Single-source precursors of type $\text{Pb} [{}^i\text{Pr}_2(\text{E})\text{NHP}(\text{E}){}^i\text{Pr}_2]$ ($\text{E}=\text{S}, \text{Se}$) in trioctylphosphine (TOP)/Oleylamine. Lead chalcogenide thin films were also deposited on glass substrates by Aerosol Assisted Chemical Vapour Deposition (AACVD) using tetrahydrofuran as the solvent.

4.3 Materials and methods

All solvents and reagents were purchased from Sigma-Aldrich chemical company and used as received. ${}^i\text{Pr}_2\text{P}(\text{Se})\text{NHP}(\text{Se}){}^i\text{Pr}_2$ (**1**), ${}^i\text{Pr}_2\text{P}(\text{S})\text{NHP}(\text{S}){}^i\text{Pr}_2$ (**2**) and ${}^i\text{Pr}_2\text{P}(\text{Se})\text{NHP}(\text{S}){}^i\text{Pr}_2$ (**3**) ligands were synthesised from 1,1,1,3,3,3-hexamethyldisilazane according to literature methods (Cupertino *et al.*, 1996, 1999). $[\text{Pb}((\text{SeP}{}^i\text{Pr}_2)_2\text{N})_2]$ (**4**), $[\text{Pb}((\text{SP}{}^i\text{Pr}_2)_2\text{N})_2]$ (**5**) and $[\text{Pb}(\text{SeS}(\text{P}{}^i\text{Pr}_2)_2\text{N})_2]$ (**6**), were also synthesised according to literature methods (Afzaal *et al.*, 2004) with some modifications.

4.3.1 Synthesis of lead chalcogenide nanoparticles

In a typical experiment 5 ml (31.0 mmol) of oleylamine was heated in a three neck flask under nitrogen until the temperature reached 200 °C. In a separate flask, 0.1 mmol of complex was dissolved in 1 ml (4.4 mmol) of trioctylphosphine (TOP) under nitrogen gas. The dissolved complex was then injected into hot oleylamine (OA) at 200 °C while stirring. The temperature was maintained at 200 °C for 30 minutes at which time a brown-black precipitate was formed. The heating was stopped and the flask was then allowed to cool to room temperature. An excess of acetone was added to precipitate the nanoparticles. The precipitate was separated by centrifuging at 4000 rpm for 10 minutes. The obtained solid nanoparticles were then washed with acetone twice by centrifugation and re-dispersed in toluene for further characterisation.

4.3.2 Spectroscopic and analytical measurements

NMR spectra were carried out using a Bruker AC400 FT NMR spectrometer. Mass spectra were recorded on a Kratos concept 1S instrument. Infrared spectra were recorded on a Bruker Alpha FTIR instrument. X-ray powder diffraction studies were conducted on a Bruker AXS D8 Advance diffractometer using monochromated Cu-K α radiation. The samples were mounted flat and scanned from 5 to 85 degrees in a step size of 0.07 with a count rate of 10 s/step. Nanoparticles dispersed in toluene were spotted on lacy carbon grids before TEM analyses. TEM was carried out using Philips CM 30 transmission electron microscope.

4.3.3 Single-crystal X-ray diffraction studies

Measurements were made using graphite monochromated Mo-K α radiation (~ 0.71073 Å) on a Bruker APEX diffractometer. The structures were solved by direct methods and refined by full-matrix least squares on F2 (Sheldrick, 2008). All calculations were carried out using the SHELXTL package Version 6.10. Non-hydrogen atoms were refined with anisotropic atomic displacement parameters. Hydrogen atoms were placed in calculated positions, assigned isotropic thermal parameters and allowed to ride on their parent carbon atoms. Crystallographic details and selected bond lengths and bond angles are summarized in Tables 1 and 2.

Table 4.1 Crystal structure data for, [Pb((SPⁱPr₂)₂N)₂] and [Pb(SeS(PⁱPr₂)₂N)₂]

	5	6
Chem formula	C ₂₄ H ₅₆ N ₂ P ₄ PbS ₄	C ₂₄ H ₅₆ N ₂ P ₄ PbS ₂ Se ₂
Formula wt	832.02	925.82
Cryst syst	Monoclinic	Monoclinic
Space group	C2/c	P2(1)/c
a(Å)	61.018(8)	23.402(4)
b(Å)	15.831(2)	9.7890(16)
c(Å)	27.338(4)	15.571(3)
α(deg)	90	90
β(deg)	107.496(2)	90.063(3)
γ(deg)	90	90
V(Å ³)	25186(6)	3567.1(10)
Z	28	4
D _{calcd} (g cm ⁻³)	1.536	1.724
μ(Mo Kα) (mm ⁻¹)	8.750	7.084
R1 (I>2σ(I)) ^b	0.0268	0.0323
wR2 (all data)	0.0584	0.0734
GOF on F ²	0.983	1.041

4.4 Results

4.4.1 X-ray single crystal structures of $[\text{Pb}((\text{SP}^{\text{i}}\text{Pr}_2)_2\text{N})_2]$ (5) and $[\text{Pb}(\text{SeS}(\text{P}^{\text{i}}\text{Pr}_2)_2\text{N})_2]$ (6).

Crystals of $[\text{Pb}((\text{SP}^{\text{i}}\text{Pr}_2)_2\text{N})_2]$ and $[\text{Pb}(\text{SeS}(\text{P}^{\text{i}}\text{Pr}_2)_2\text{N})_2]$ suitable for X-ray diffraction studies were obtained by slow evaporation of chloroform/methanol 1:2 mixture containing dissolved complex. The crystal structures of the compounds are shown in Figures 4.1 and 4.2 respectively. The geometry at the lead atom in both complexes is a distorted square pyramidal with four chalcogenide (S or Se) atoms, forming the base of the pyramid and the lone pair occupying the axial position.

In complex (5), the lead atom is coordinated to four sulphur atoms, two from each imidodithiophosphate chelating ligand. The crystalline phase of the compounds belongs to the monoclinic space group with $C2/c$. Apart from the differing chalcogenide constituents of the molecules, the crystal structure cores are similar to those reported in the literature for $[\text{Pb}((\text{SeP}^{\text{i}}\text{Pr}_2)_2\text{N})_2]$ (4) (Ritch *et al.*, 2010).

In complex (6), lead atom is coordinated to two sulphur and two selenium atoms, two of each atom from each imidodithioselenophosphate chelating ligand. The structure is disordered with 50 % occupancy of sulphur and selenium at each of the four chalcogen sites. The crystalline phase of the compound belongs to the monoclinic space group with $P21/c$. Although a different chelating ligand, this structural arrangement is similar to that reported for *bis*(diphenylthioselenophosphinato)lead(II) by Akhtar *et al.*, (2011b).

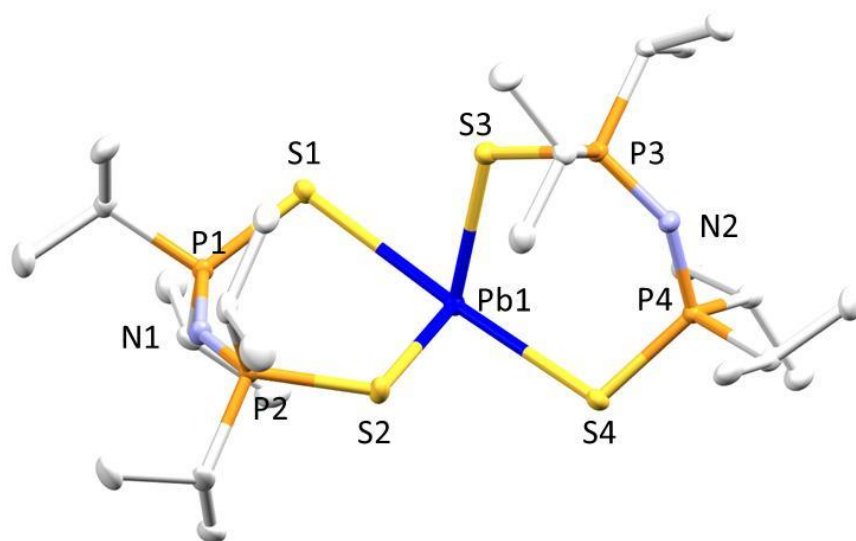


Figure 4.1 X-ray crystal structure of $C_{24}H_{56}N_2P_4PbS_4$

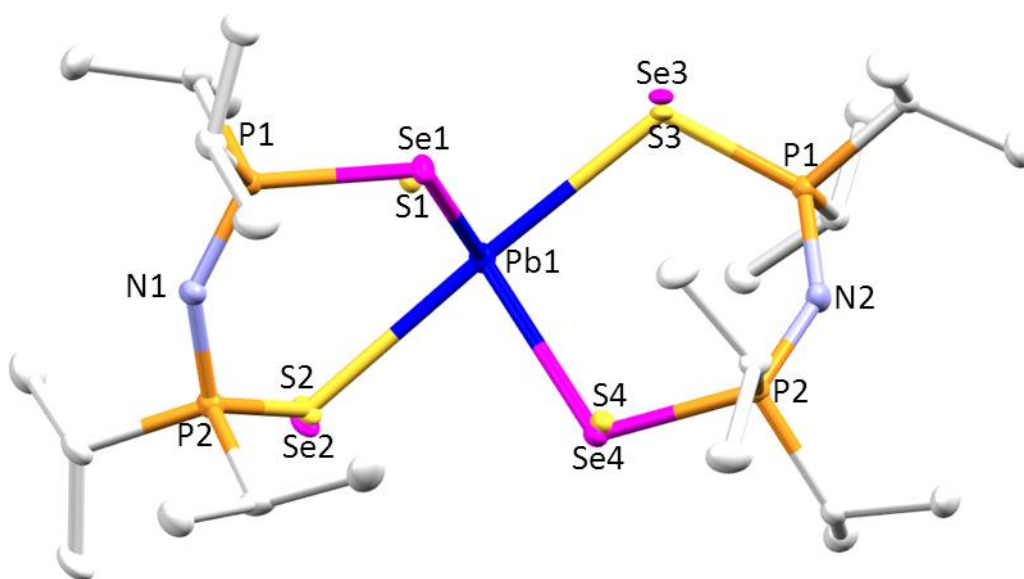


Figure 4.2 X-ray crystal structure of $C_{24}H_{56}N_2P_4PbS_2Se_2$

4.4.2 Thermogravimetric analysis

Thermogravimetric analysis (TGA) was conducted on complexes **4**, **5** and **6** and the result shown in Figure 4.3 below and labelled a, b and c respectively. Complex **4** (a.) showed single step decomposition. The remaining residue (20.7 %) was lower than the theoretical value (28.07 %) for bulk PbSe. This may be due to the volatility of PbSe at elevated temperatures (600 °C) thereby leading to a further weight loss. A similar trend was observed in the TGA for complexes **5** (b) and **6** (c). The residue remaining for complex **5** had weight corresponding to 8.35 % of the complex which is lower than the theoretical value (28.8 %) for bulk PbS. In the case of complex **6**, the same trend was observed with the theoretical value being 28.38 % and the observed, 21.47 %.

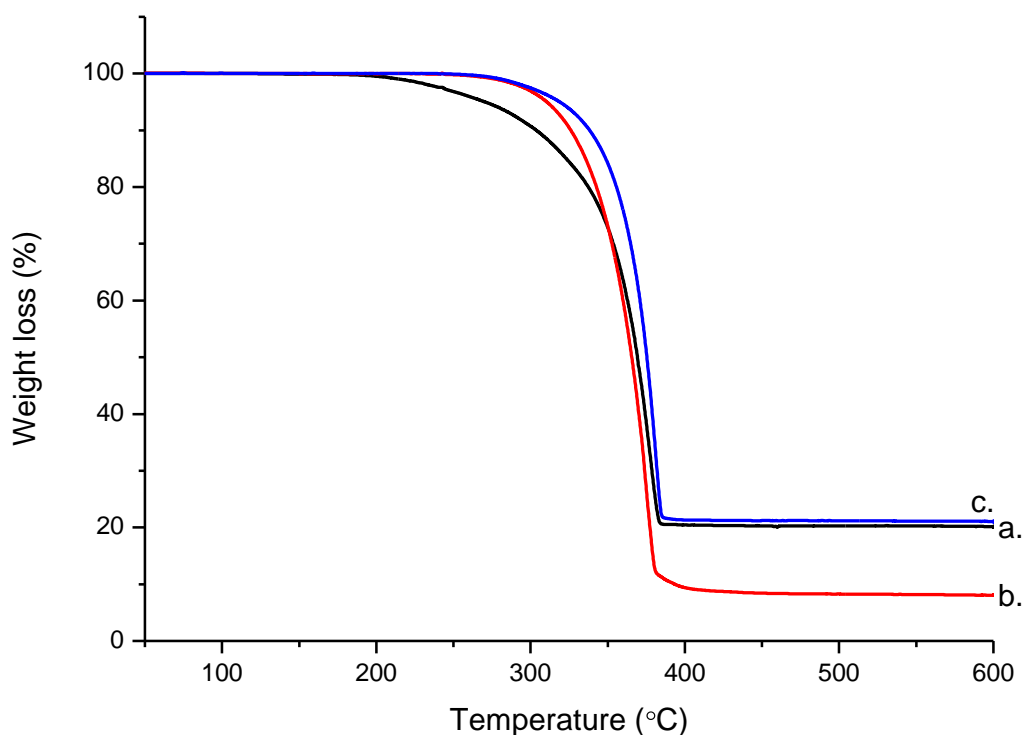


Figure 4.3 Thermogravimetric analysis of (a) complex **4**, (b) complex **5** and (c) complex **6**

4.4.3 Lead chalcogenide nanoparticles

Lead chalcogenide nanoparticles have been synthesised from three different Single-source precursors of dichalcogenoimidodiphosphinato complexes. The compounds used in these experiments were all air-stable. The nanoparticles synthesised from all three complexes (**4**, **5** and **6**) were brown-black in colour.

4.4.3.1 p-XRD of PbSe nanoparticles

Powder X-ray diffraction analysis carried out on the nanoparticles synthesised from complex (**4**) (Figure 4.4) showed a pure cubic PbSe (ICDD 04-004-4328).

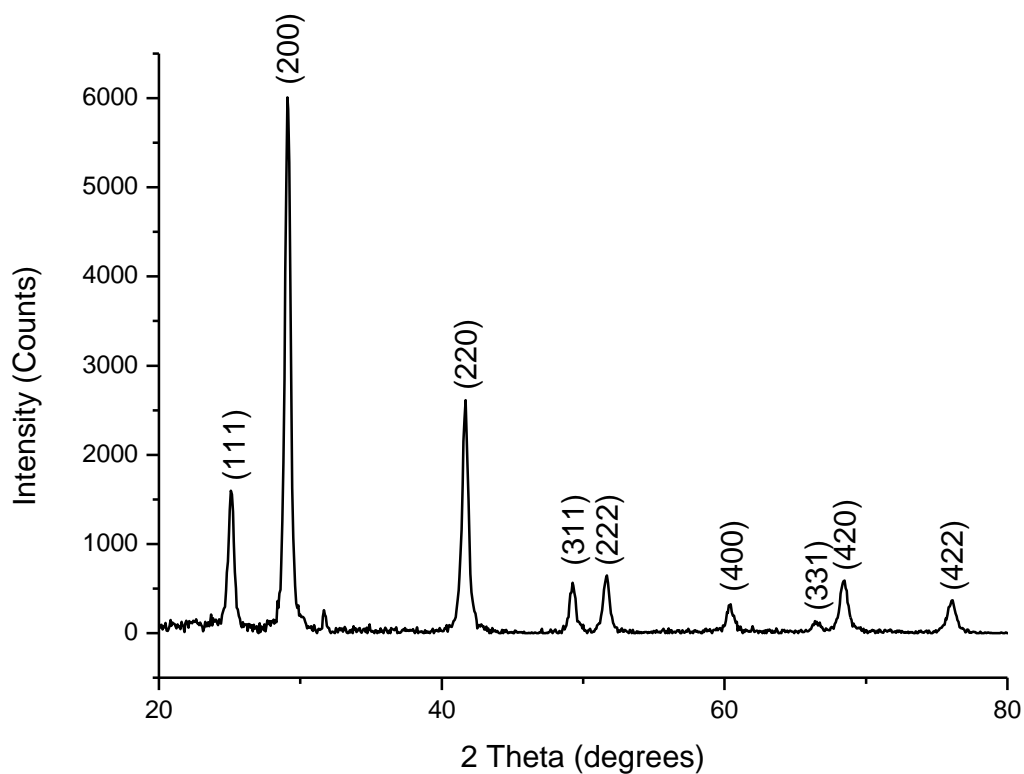


Figure 4.4 p-XRD plot for PbSe nanoparticles

4.4.3.1.1 High Resolution Transmission Electron Microscope (HRTEM) and TEM images of nanoparticles obtained from complex 4.

The images obtained from High Resolution Transmission Electron Microscope (HRTEM) and Transmission Electron Microscope (TEM) analysis of the produced nanoparticles from complex 4 in oleylamine/TOP are shown in Figure 4.5 (a) and (b) respectively. The HRTEM image showed crystalline lattice fringes with a d spacing of 3.0 Å, indicating an orientation of the particles along the (200) plane. The TEM image showed a mixture of rods and spheres. The average size of the crystallites was calculated to be 16.81 nm using Scherrer equation. This was close to the particle size of 16.52 nm obtained from the TEM image.

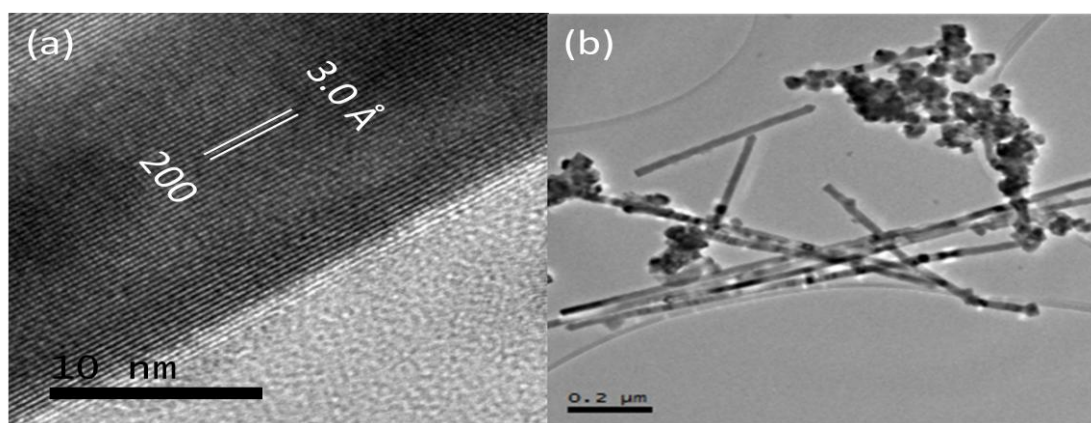


Figure 4.5 HRTEM (a) and TEM (b) images of PbSe nanoparticles

4.4.3.2 p-XRD of PbS nanoparticles

The powder XRD pattern for the nanoparticles produced from complex 5 corresponded to cubic PbS with the face centred cubic (FCC) rock-salt structure (ICDD 04-004-4329) (Figure 4.6). The sharpness of the peaks indicates the highly crystalline nature of the particles. The preferred orientation plane from the p-XRD was (200).

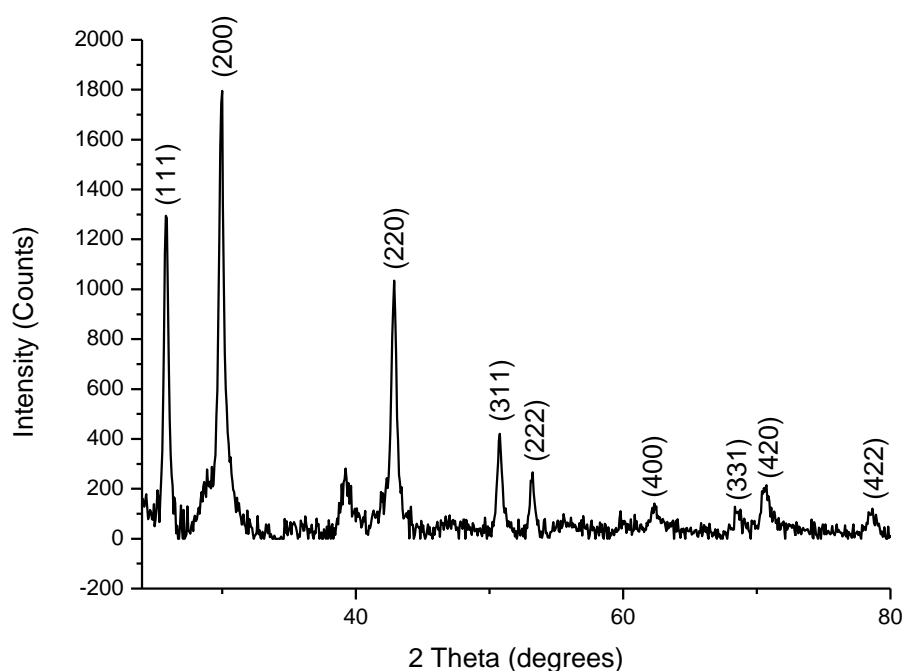


Figure 4.6 p-XRD for PbS nanoparticles

4.4.3.2.1 HRTEM and TEM images of nanoparticles obtained from complex 5

The HRTEM and TEM images of nanoparticles obtained from complex **5** are shown in Figures 4.7a and 4.7b respectively. The HRTEM image showed highly crystalline lattice fringes along the 220 orientation with a d-spacing of 2.0 Å. The TEM image showed a cluster of non-uniform sized cubic nanoparticles. The average size of the crystallites was calculated to be 17.63 nm using Scherrer equation. The average particle size obtained from TEM was 16.55 nm. Cubic shaped PbS nanoparticles obtained from various Single-source precursors have been reported in literature (Akhtar *et al.*, 2011d; Sun *et al.*, 2011). However, there has been no report on the synthesis of PbS nanoparticles from complex **5**.

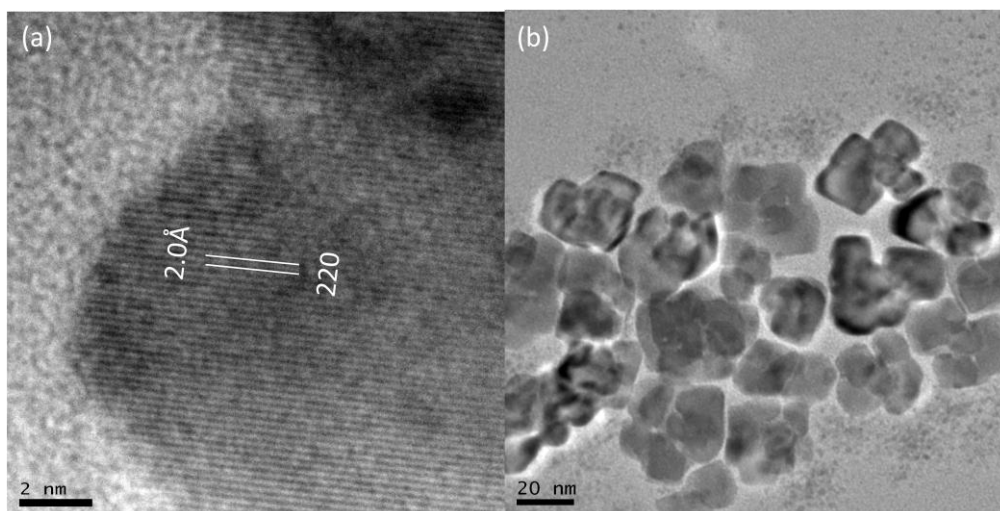


Figure 4.7. HRTEM (a) and TEM (b) images of PbS nanoparticles

4.4.3.3 p-XRD of nanoparticles from mixed ligand complex 6

The powder XRD pattern for nanoparticles synthesised from complex **6** showed peaks that matched mainly with cubic PbSe (ICDD 04-004-4328) (Figure 4.8). However, there were some peaks that were identified as PbSeS (ICDD 00-020-0597). The decomposition agrees with DFT calculations reported in literature (Akhtar *et al.*, 2011b).

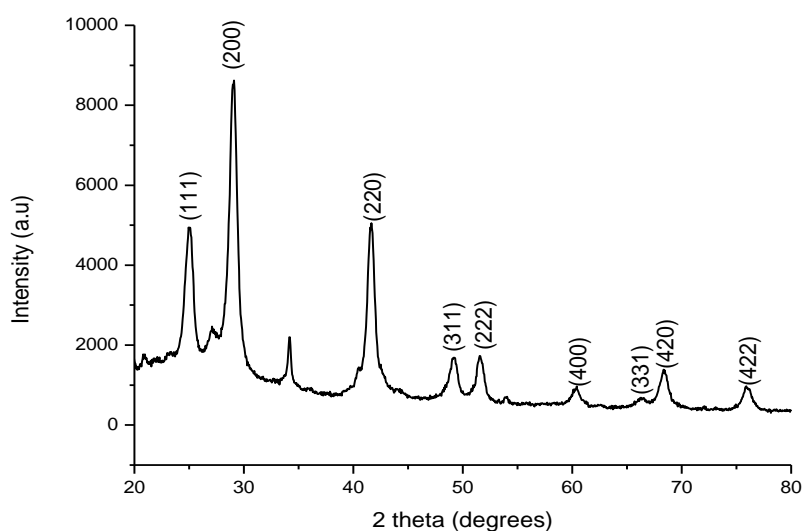


Figure 4.8 p-XRD for nanoparticles synthesised from complex 6. Major peaks match with PbSe nanoparticles.

4.4.3.3.1 HRTEM and TEM images of nanoparticles obtained from complex 6

The HRTEM image of nanoparticles synthesised from complex 6 is shown in Figure 4.9a. The image shows lattice fringes which indicate the crystalline nature of the nanoparticles with a d-spacing of 2.0 Å along a (220) plane orientation. The TEM image of nanoparticles obtained from complex 6 indicate that the material consists of a mixture of randomly orientated cubes and truncated cubes as shown in Figure 4.9b. Though they are uniform in shape, they vary in size. The average particle size obtained from the TEM image was 11.71 nm.

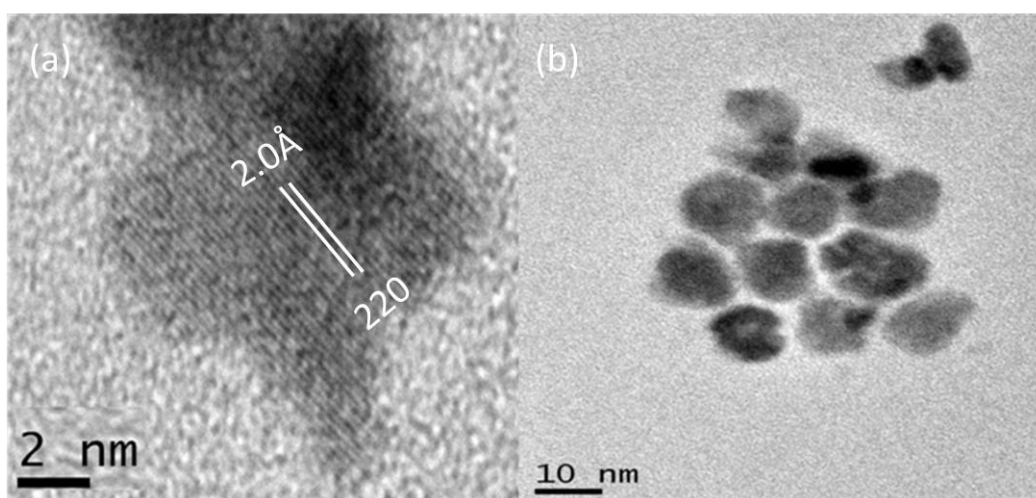


Figure 4.9 HRTEM (a) and TEM (b) images obtained from decomposition of complex 6.

4.4.4 Optical properties of lead chalcogenides

The optical band gap of the lead chalcogenides were determined using the absorption spectrum fitting procedure (Ghobadi, 2013). A Varian UV-VIS-NIR spectrophotometer that scans up to a wavelength of 1500 nm was used to measure the absorbance of the nanoparticles. The square of the absorption coefficient was plotted against energy (eV). A tangent to the straight line part of the curve was extrapolated to cut the x axis and the intercept was read as the band gap. The plots for the various nanoparticles are shown in Figures 4.10 to 4.12.

4.4.4.1 Band gap of PbSe nanoparticles from bis(imidodiisopropylselenophosphinato)

lead (II).

The band gap for bulk lead selenide is 0.27 eV (Kothiyal and Ghosh, 1990) however, the band gap obtained for the lead selenide nanoparticles synthesised was 1.17 eV (Figure 4.10). This indicates a significant tuning of the band gap. Lead selenide is known to have wider tunable band gap than lead sulphide and can be tuned over a wide range from the infra-red region to the visible region (Pietryga *et al.*, 2004) and therefore has a wide range of applications. The band gap obtained compares with that obtained from other works reported in literature (Cho and Talapin, 2005; Ma *et al.*, 2011; Zhu *et al.*, 2000).

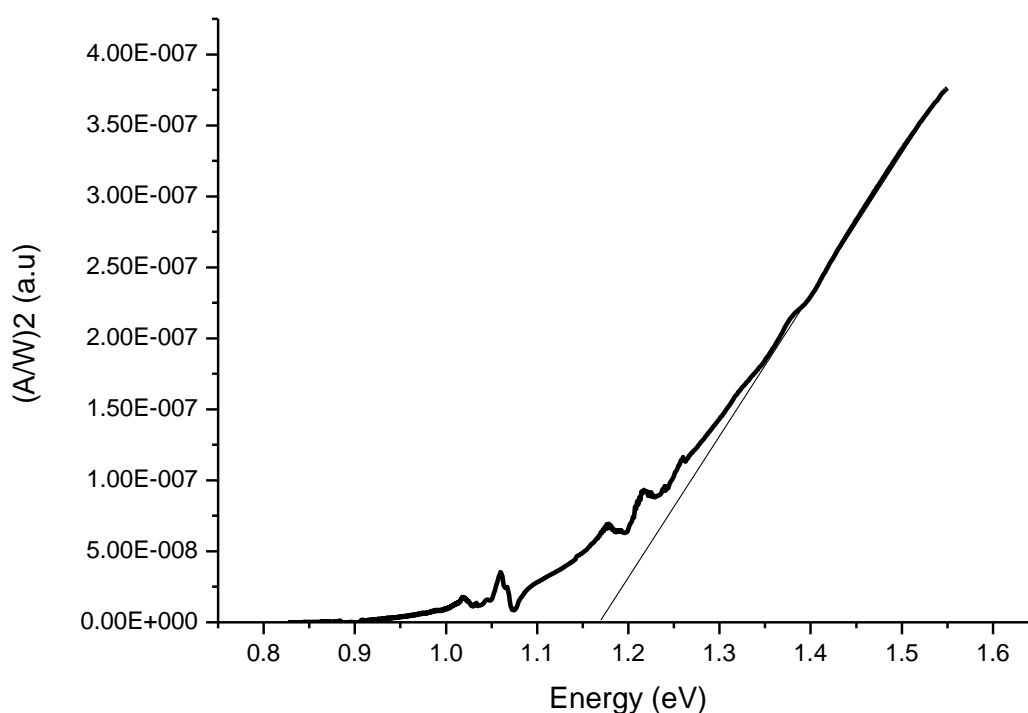


Figure 4.10. Band gap determination using the absorption spectrum fitting procedure for the synthesised lead selenide nanoparticles.

4.4.4.2 Band gap of PbS nanoparticles from bis(imidodiisopropyldithiophosphinato) lead**(II).**

The band gap for bulk lead sulphide is 0.41 eV (Kothiyal and Ghosh, 1990) however, the band gap obtained for the lead sulphide nanoparticles synthesised was 1.03 eV (Figure 4.11). This indicates a significant tuning of the band gap. Lead sulphide is known to have size tunable band gap and can be tuned over a wide range from the infra-red region to the near visible region (Bakueva *et al.*, 2003) and, therefore, has a wide range of applications. Tuned band gaps of PbS nanoparticles ranging from 0.5 to 2.0 eV have been reported (Nanda *et al.*, 2002).

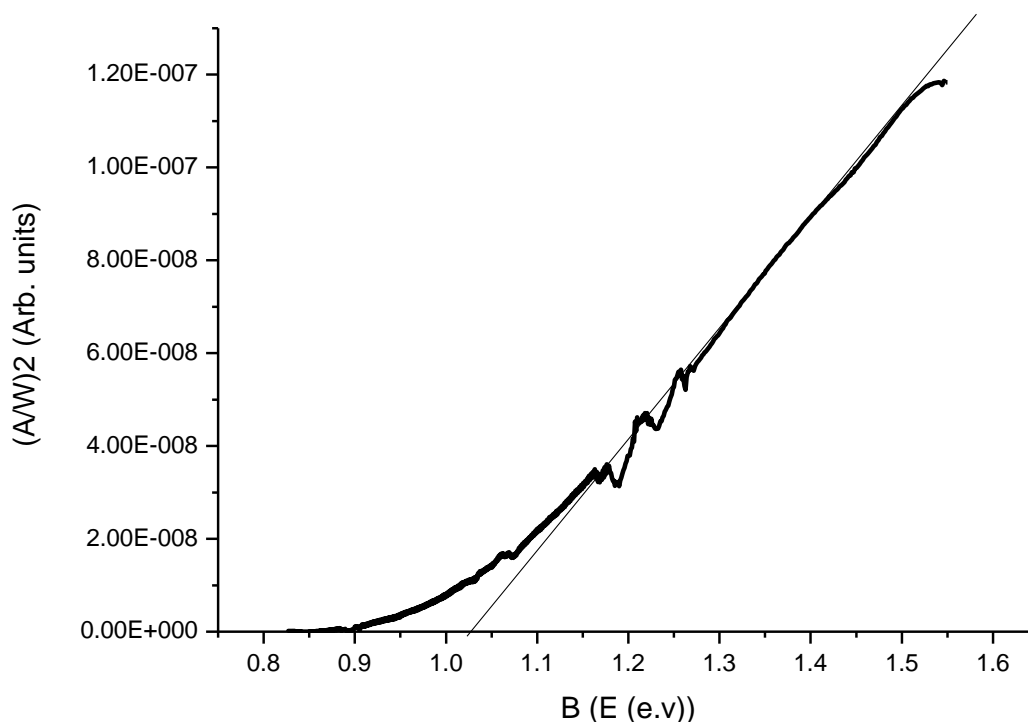


Figure 4.11 Band gap determination using the absorption spectrum fitting procedure for the synthesised lead sulphide nanoparticles

4.4.4.3 Band gap of nanoparticles from *bis*(imidodiisopropylthioselenophosphinato) lead (II).

The band gap for bulk lead selenide is 0.27 eV and that for bulk PbS is 0.41 eV (Kothiyal and Ghosh, 1990) however, the band gap obtained for the nanoparticles synthesised from the mixed ligand complex was 1.38 eV (Figure 4.12). There is, therefore, a tremendous change between the bulk band gap and that obtained, indicating significant tuning. Alloyed semiconductor nanomaterials provide an alternative approach for band gap control in addition to the size-dependent quantum confinement effects and they give access to families of materials with distinct properties (Akhtar *et al.*, 2011d). The properties of alloys vary with composition making it possible to tune the band gap while maintaining a similar small size.

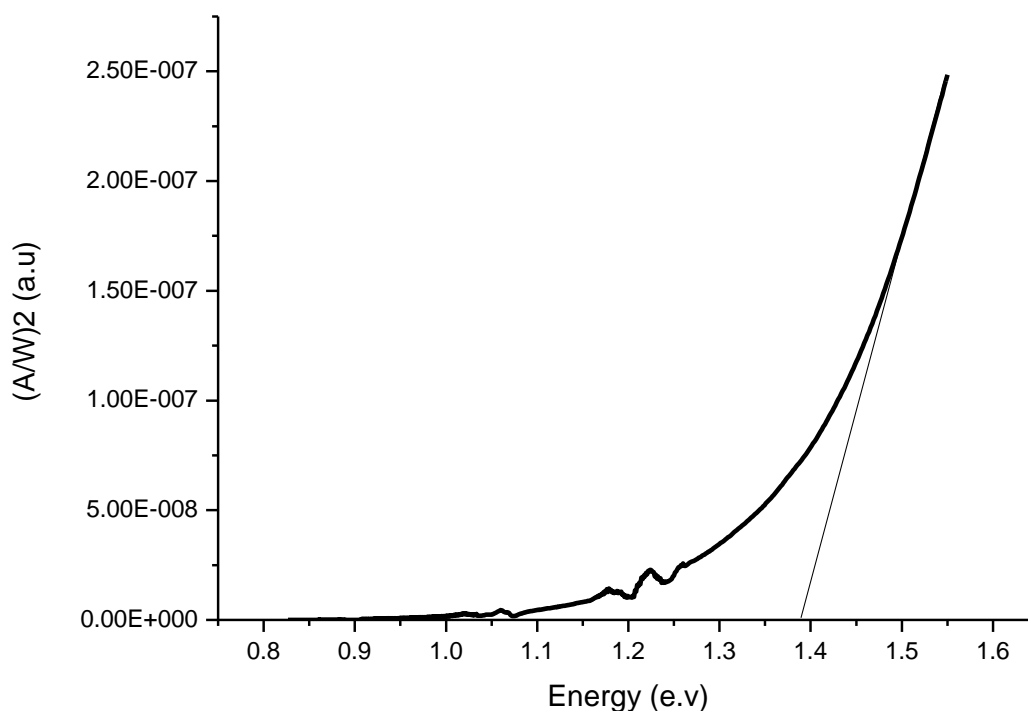


Figure 4.12. Band gap determination using the absorption spectrum fitting procedure for the synthesised nanoparticles from *bis*(imidodiisopropylthioselenophosphinato)lead (II) complex.

A summary of the band gaps obtained for the nanoparticles and their comparison with that of their corresponding bulk materials is shown in Table 4.2.

Table 4.2 Comparison of band gaps obtained for the synthesised nanoparticles with the band gaps of their corresponding bulk material

	Complex	Semiconductor expected	Semiconductor or obtained	Band gap of bulk semiconductor (eV)	Band gap of nanoparticles produced (eV)	Average particle sizes of nanoparticles produced (nm)
1	<i>bis</i> (imidodiisopropyl diselenophosphinato) lead (II)	PbSe	PbSe	0.27	1.17	16.52
2	<i>bis</i> (imidodiisopropyl dithiophosphinato) lead (II)	PbS	PbS	0.41	1.03	16.55
3	<i>bis</i> (imidodiisopropyl thioselenophosphinato) lead (II)	PbS _x Se _{1-x}	PbSe	0.27	1.38	11.71

The band gap of the nanoparticles from the three complexes decreased in the order *bis*(imidodiisopropylthioselenophosphinato) lead (II) > *bis*(imidodiisopropyl diselenophosphinato) lead (II) > *bis*(imidodiisopropyl dithiophosphinato) lead (II). Wider band gaps are attained as size decreases. Bulk PbS has a larger band gap than bulk PbSe (Bakueva *et al.*, 2003). However, PbSe nanoparticles can be tuned over a wider range of band gaps than PbS nanoparticles (Pietryga *et al.*, 2004). PbS QDs that have energy band gap in the range of 0.9–1.1 eV, and PbSe QDs with tuned band gap from 0.7 to 1.7 eV have been reported (Rhee *et al.*, 2013)

4.4.5 Deposition of lead chalcogenide thin films by Aerosol Assisted Chemical Vapour

Deposition (AACVD)

Lead sulphide and lead selenide thin films were deposited on glass substrates by AACVD using *bis*(imidodichalcogenophosphinato) lead (II) Single-source precursors discussed above. The

deposition for all three complexes was done at a constant time of 30 minutes and constant temperature of 450 °C.

4.4.5.1 p-XRD of Lead selenide thin films

Powder X-ray diffraction analysis carried out on the lead selenide thin films deposited from complex (4) showed a pure cubic PbSe and corresponded to ICDD 04-004-4328 standard peak pattern for PbSe (Figure 4.13). The result shows the temperature and time conditions chosen for the experiment were right for a successful production of PbSe thin films. Also, the results show that complex 4 is suitable for producing PbSe thin films.

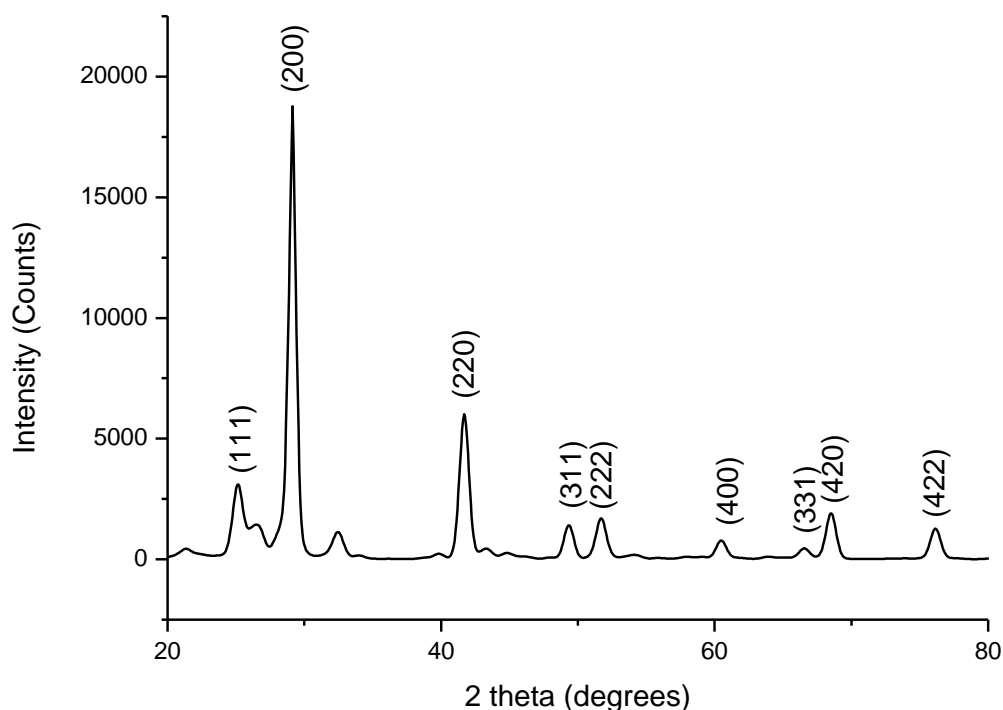


Figure 4.13 p-XRD of PbSe thin films

4.4.5.1.1 SEM images of lead selenide thin films

Scanning electron microscope (SEM) images of thin films deposited from complex 4 by AACVD (Figure 4.14) reveal that at 450 °C, the thin films show isolated particles of disordered cubic lead selenide crystallites.

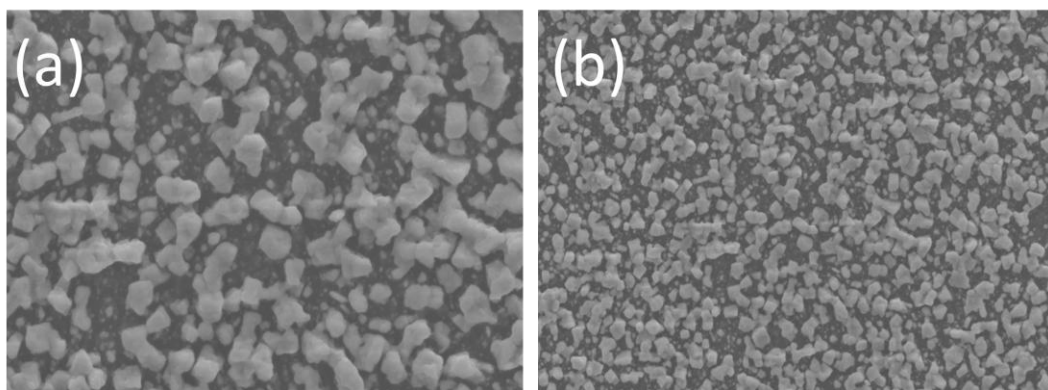


Figure 4.14 SEM images of PbSe thin films at (a) 10000x and (b) 5000x magnification

4.4.5.2 p-XRD of lead sulphide thin films

The powder XRD pattern for PbS thin films produced from complex **5** corresponded mainly to cubic PbS (ICDD 04-004-4329).

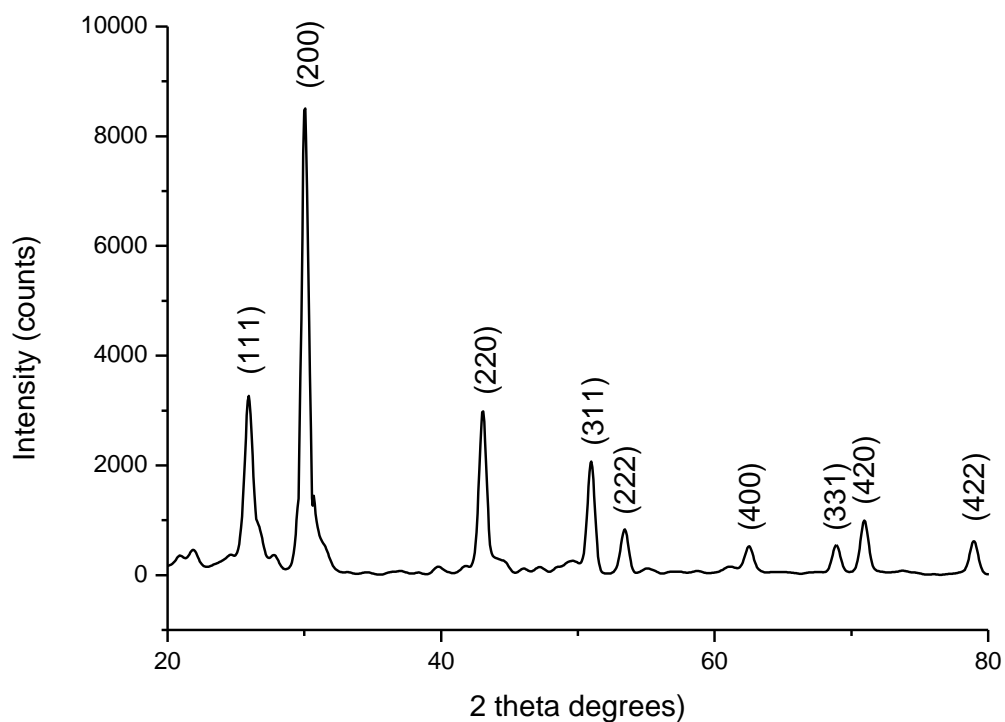


Figure 4.15 p-XRD of PbS thin films

4.4.5.2.1 SEM images of lead sulphide thin films

Scanning electron microscope (SEM) images of thin films deposited from complex **5** by AACVD at 450 °C (Figure 4.16) show clusters of non-uniformly shaped cubic lead sulphide crystallites.

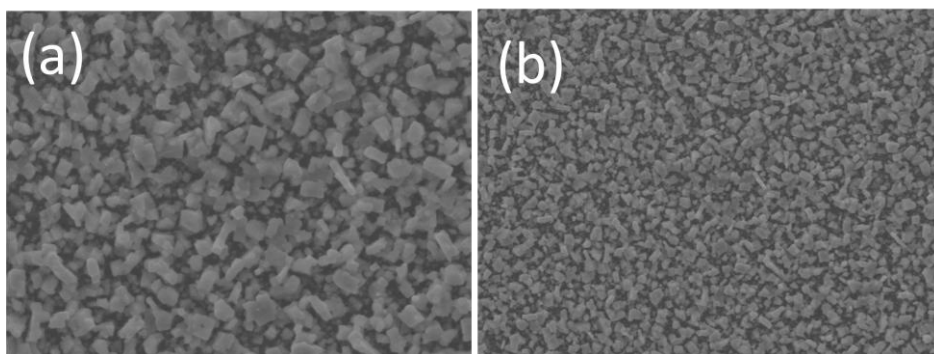


Figure 4.16 SEM images of PbS thin films at (a) 10000x and (b) 5000x magnification

4.4.5.3 p-XRD of lead selenide thin films

The p-XRD pattern for thin films deposited from complex **6** (Figure 4.17) showed peaks that matched mainly with cubic PbSe (ICDD 00-006-0356).

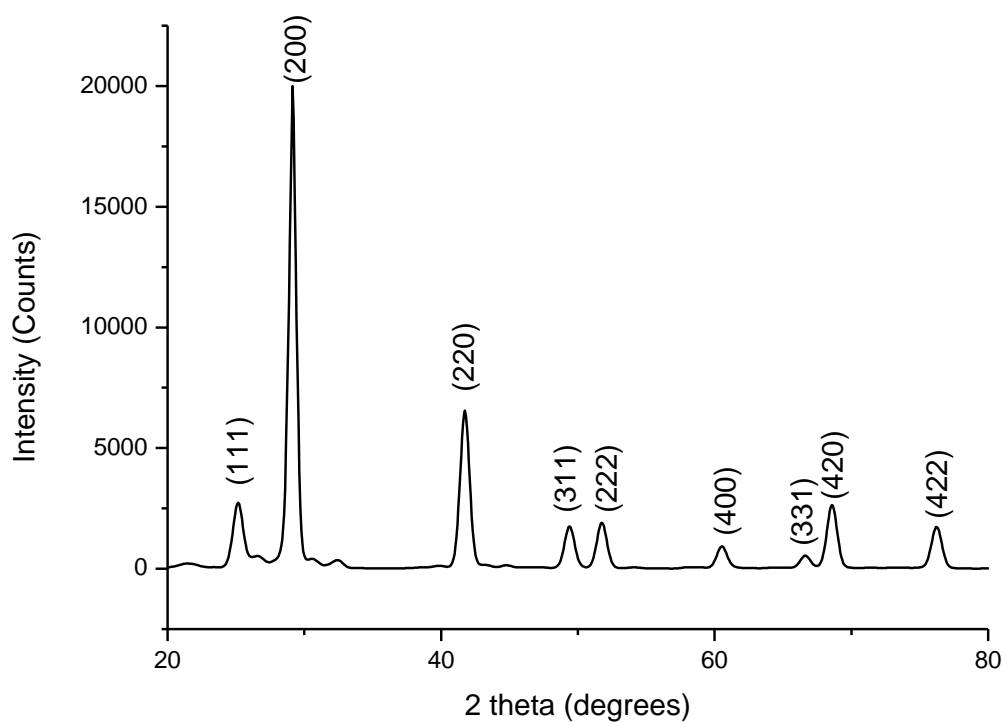


Figure 4.17 p-XRD of PbSe thin films from complex 6

4.4.5.3.1 SEM images of thin films from complex 6

Scanning electron microscope (SEM) images of thin films deposited from complex 6 by AACVD at 450 °C (Figure 4.18) show a mixed phase of isolated sheets and non-uniformly shaped cubic lead chalcogenide crystallites. The energy dispersive X-ray (EDAX) analysis confirms the formation of lead selenide thin films since sulphur was absent.

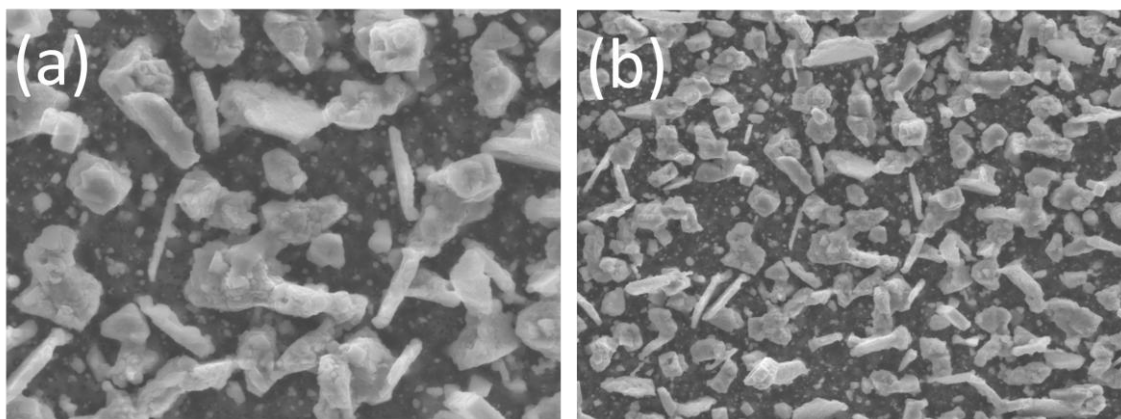


Figure 4.18 SEM images of PbSe thin films deposited from complex **6** at (a) 10000x and (b) 5000x magnification

4.5 Conclusion

In this chapter, single-source routes for the synthesis of lead chalcogenide nanoparticles by thermal decomposition in oleylamine/TOP and deposition of thin films by AACVD have been discussed. The nanoparticles synthesised from $[\text{Pb}((\text{SeP}^i\text{Pr}_2)_2\text{N})_2]$ indicate the growth of a mixture of rod-like and spherical shaped nanoparticles whereas other nanoparticles synthesised from $[\text{Pb}((\text{SP}^i\text{Pr}_2)_2\text{N})_2]$ and $[\text{Pb}(\text{SeS}(\text{P}^i\text{Pr}_2)_2\text{N})_2]$ complexes showed cubic shaped PbE (E= S, Se). The nanoparticles synthesised from $[\text{Pb}(\text{SeS}(\text{P}^i\text{Pr}_2)_2\text{N})_2]$ turned out to be mainly PbSe nanoparticles. The band gap of the nanoparticles from the three complexes decreased in the order $[\text{Pb}(\text{SeS}(\text{P}^i\text{Pr}_2)_2\text{N})_2] > [\text{Pb}((\text{SeP}^i\text{Pr}_2)_2\text{N})_2] > [\text{Pb}((\text{SP}^i\text{Pr}_2)_2\text{N})_2]$. The thin films deposited from $[\text{Pb}((\text{SeP}^i\text{Pr}_2)_2\text{N})_2]$ and $[\text{Pb}(\text{SeS}(\text{P}^i\text{Pr}_2)_2\text{N})_2]$ were PbSe and that from $[\text{Pb}((\text{SP}^i\text{Pr}_2)_2\text{N})_2]$ was PbS.

Chapter 5

Synthesis of novel Single-source precursors for the production of ternary lead chalcogenides

5.1 Summary

Single-source precursors suitable for the synthesis and deposition of ternary lead chalcogenide nanoparticles and thin films respectively have been synthesised and characterised.

5.2 Introduction

The development of flexible light weight solar cells is of high importance for several applications. Thin film solar cells use 30 to 100 times less semiconducting materials and are less expensive to manufacture than conventional silicon cells (Contreras and Egaas, 1999).

The use of multi-source inorganic/organometallic complexes in a CVD is more appealing due to milder process parameters. However, stoichiometric control of deposited films can be difficult to achieve and film contamination has been reported. A novel alternative approach is the use of Single-source precursors, (SSPs), which have the I-III-VI stoichiometry "built in" and are suitable for low temperature deposition (Hollingsworth *et al.*, 2003).

Single-source approaches involve the use of an organometallic or metal-organic molecule as a source for the elements required in the growth of the target compound at the desired stoichiometry (O'Brien and Nomura, 1995). Single-molecule complex approach provides several key advantages over other routes (Arif *et al.*, 1986; Cowley and Jones, 1989). For example, the existence of preformed bonds may lead to material with lower defect concentrations.

Most of Single-source precursors are air-stable, non-toxic and easy to handle, often employ clean, low-temperature decomposition routes and yield crystalline nanomaterials with minimal impurity incorporation (Pickett and O'Brien, 2001).

In this work, Single-source precursors suitable for synthesizing ternary lead chalcogenide nanoparticles and thin films have been synthesised and characterised.

5.3 Experimental

5.3.1 Synthesis of $[\text{Pb}((\text{SeP}^i\text{Pr}_2)(\text{SP}^i\text{Pr}_2)\text{N})_2]$, $[\text{Pb}((\text{SeP}^i\text{Pr}_2)_2\text{N}(\text{S}_2\text{CNET}_2))]$ and $[\text{Pb}((\text{SeP}^i\text{Pr}_2)_2\text{N}(\text{S}_2\text{CNHexMe}))]$ complexes

In a typical synthesis, equal moles (1:1) of the reactant complexes were dissolved in chloroform in a round bottom flask and refluxed for two hours. The solution was cooled to room temperature and precipitated with methanol. The precipitate obtained was filtered out of solution and dried under vacuum.

5.4 Results

5.4.1 Spectroscopic studies of $[\text{Pb}((\text{SeP}^i\text{Pr}_2)(\text{SP}^i\text{Pr}_2)\text{N})_2]$ complex

5.4.1.1 ^1H NMR

A stacked set of ^1H NMR spectra of the starting materials, $[\text{Pb}((\text{SeP}^i\text{Pr}_2)_2\text{N})_2]$ (**A**) and $[\text{Pb}((\text{SP}^i\text{Pr}_2)_2\text{N})_2]$ (**C**) and the product, $[\text{Pb}((\text{SeP}^i\text{Pr}_2)(\text{SP}^i\text{Pr}_2)\text{N})_2]$ (**B**) are shown in Figure 5.1. The product spectrum B is similar to the starting material spectra A and C. The basic elements in all three spectra are the same: a set of four overlapping doublets and two overlapping septets

for the isopropyl groups. The spectrum of **B** however, has slightly different chemical shifts from the individual starting materials.

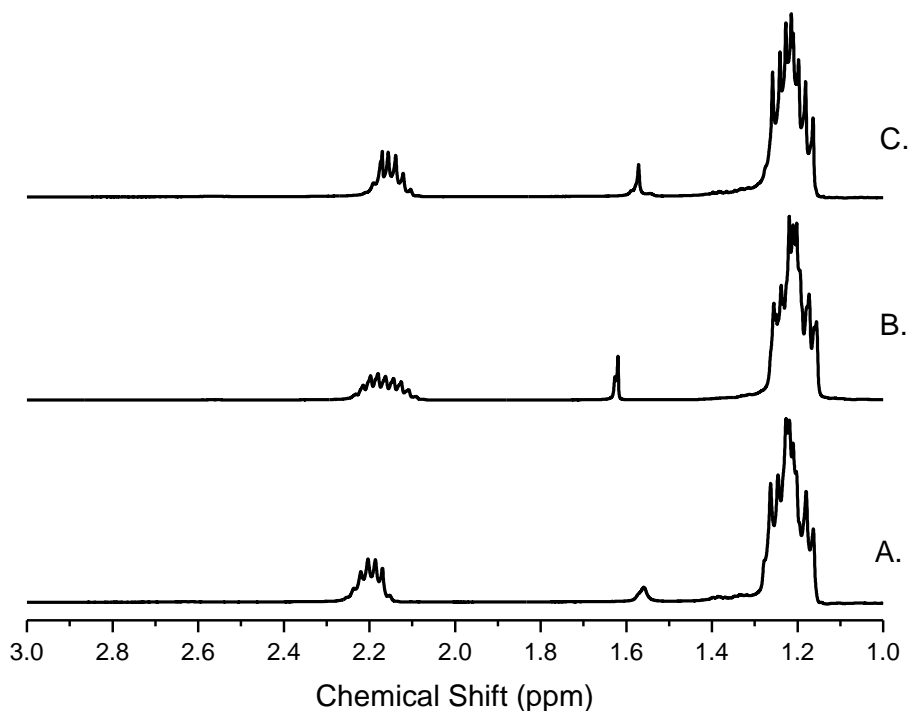


Figure 5.1 A stacked set of three ^1H NMR spectra; the two starting materials, **A**, *bis*(imidodiisopropyldiselenophosphinato) lead(II) **B**, the product and **C**, *bis*(imidodiisopropyldithiophosphinato) lead(II).

5.4.1.2 ^{31}P NMR

There were two phosphorus peaks shown on the spectrum at 60.21 and 55.28 ppm. These peaks do not significantly shift from the individual peaks of the starting materials, 60.07 and 55.59 ppm for $[\text{Pb}((\text{SP}^i\text{Pr}_2)_2\text{N})_2]$ and $[\text{Pb}((\text{SeP}^i\text{Pr}_2)_2\text{N})_2]$ respectively.

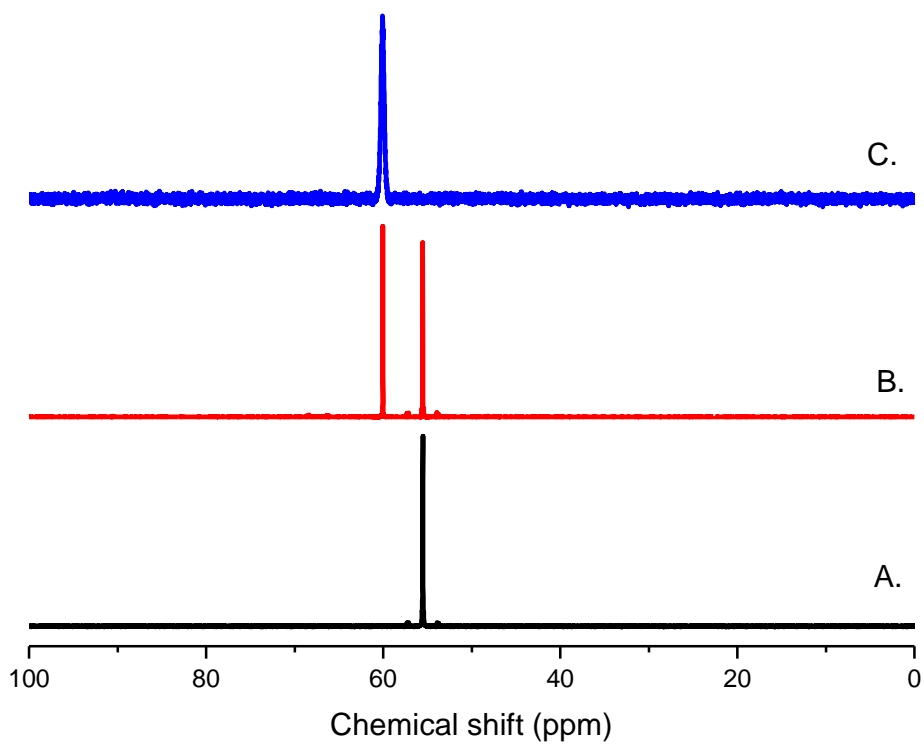


Figure 5.2: A stacked set of three ^{31}P NMR spectra; the two starting materials, **A**, *bis*(imidodiisopropyldiselenophosphinato) lead(II) **B**, the product and **C**, *bis*(imidodiisopropyldithiophosphinato) lead(II).

5.4.1.3 ^{77}Se NMR

The ^{77}Se NMR spectrum showed two peaks at -153.56 and -160.87 ppm. The chemical shifts of the peaks were different from the starting material $[\text{Pb}((\text{SeP}^i\text{Pr}_2)_2\text{N})_2]$ (-161.87, -169.7). However, the differences between the peaks, 7.31 and 7.2 ppm for the product and starting material respectively were similar.

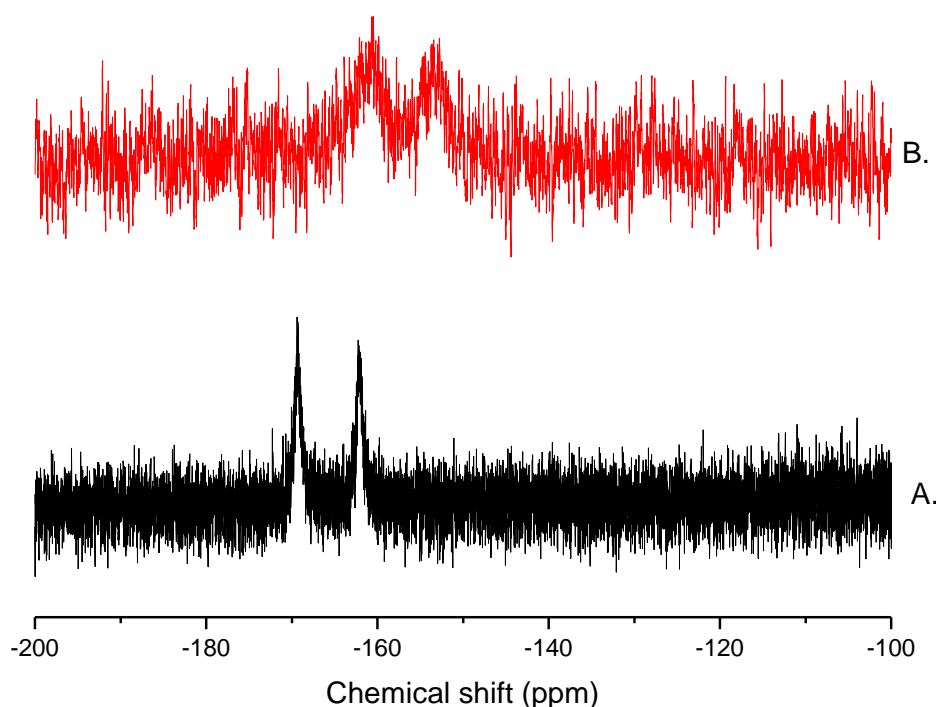


Figure 5.3: A stacked set of two ^{77}Se NMR spectra; the starting material, **A**, *bis*(imidodiisopropyldiselenophosphinato) lead(II) and **B**, the product.

5.4.1.4 Melting point

The melting point for the product $[\text{Pb}((\text{SeP}^i\text{Pr}_2)(\text{SP}^i\text{Pr}_2)\text{N})_2]$ was 111-113 °C and that of the starting materials, 131-133 °C and 98-100 °C for $[\text{Pb}((\text{SeP}^i\text{Pr}_2)_2\text{N})_2]$ and $[\text{Pb}((\text{SP}^i\text{Pr}_2)_2\text{N})_2]$ respectively. This indicates that the product formed is different from the starting materials.

5.4.1.5 FT-IR Analysis of $[\text{Pb}((\text{SeP}^i\text{Pr}_2)(\text{SP}^i\text{Pr}_2)\text{N})_2]$

The FT-IR spectrum of the product **B** was significantly different in the fingerprint region (Figure 5.4) from the starting materials, **A** and **C**. The band frequencies of **B** were not identical to any of frequencies from the individual complexes. The product can therefore be said to be a different compound arising from the reaction of the individual complexes.

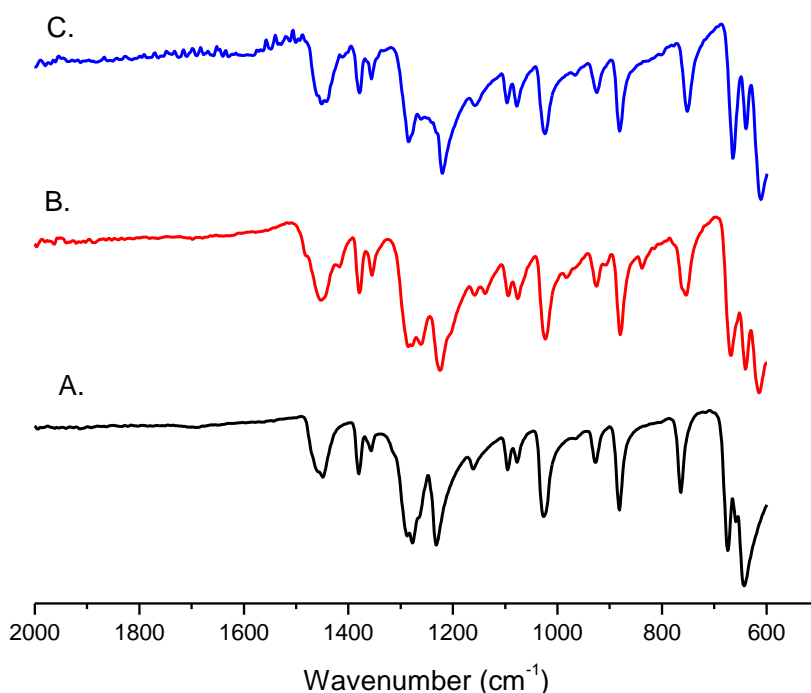


Figure 5.4: A stacked set of three FT-IR spectra; the two starting materials, **A**, *bis*(imidodiisopropyldiselenophosphinato)lead(II) and **C**, *bis*(imidodiisopropyldithiophosphinato) lead(II). **B** is the spectrum of the product.

5.4.1.6 p-XRD Analysis of $[\text{Pb}((\text{SeP}^i\text{Pr}_2)(\text{SP}^i\text{Pr}_2)\text{N})_2]$

The spectrum of **B** (Figure 5.5) shows some peaks that match with the starting materials, **A** and **C**. This indicates the presence of some unreacted starting materials with the product. Prolonged reaction time may reduce the amount of unreacted starting materials. The p-XRD

of the product **B** was done on the product obtained after two hours of refluxing the starting materials **A** and **C** together. Further recrystallization of product **B** gave single crystals suitable for determining the crystal structure.

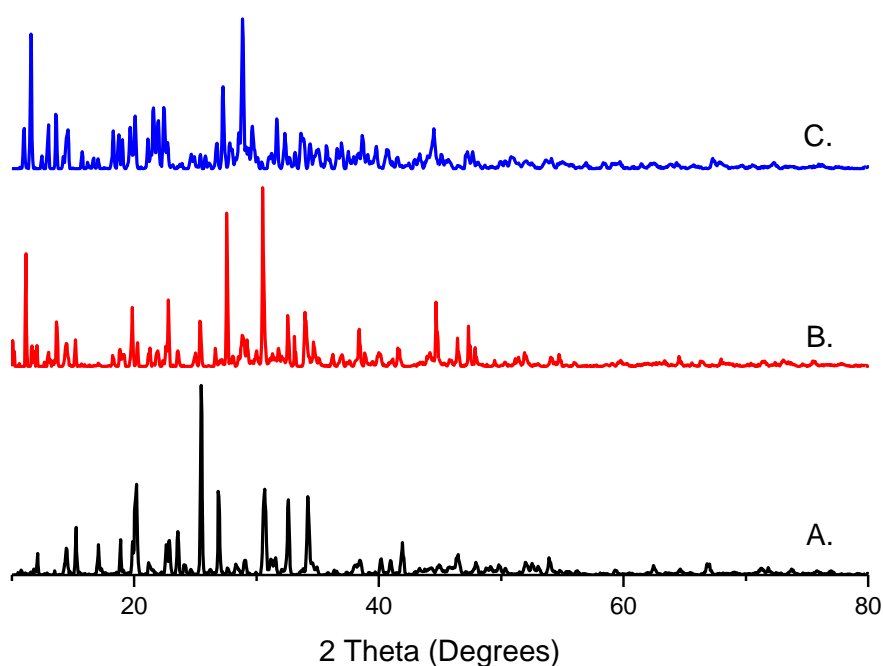


Figure 5.5: A stacked set of three p-XRD spectra showing peaks corresponding to **A**, $[\text{Pb}((\text{SP}^{\text{i}}\text{Pr}_2)_2\text{N})_2]$; **B**, $[\text{Pb}((\text{SeP}^{\text{i}}\text{Pr}_2)(\text{SP}^{\text{i}}\text{Pr}_2)\text{N})_2]$ and **C**, $[\text{Pb}((\text{SeP}^{\text{i}}\text{Pr}_2)_2\text{N})_2]$.

5.4.1.7 X-ray single crystal structures of $[\text{Pb}((\text{SeP}^{\text{i}}\text{Pr}_2)(\text{SP}^{\text{i}}\text{Pr}_2)\text{N})_2]$ (**6**).

Single Crystals of $[\text{Pb}((\text{SeP}^{\text{i}}\text{Pr}_2)(\text{SP}^{\text{i}}\text{Pr}_2)\text{N})_2]$ suitable for crystal structure elucidation were obtained by slow evaporation of chloroform/methanol 1:2 mixture containing dissolved complex. The crystal structure of the compound is shown in Figure 5.6. The geometry at the lead atom in the complex is a distorted trigonal bipyramidal with four chalcogenide (S,Se) atoms, forming the base of the pyramid and the lone pair occupying the axial position. The

occupancy ratio of S/Se at each position is not 1:1 and gives more preference to the Se atom. The crystalline phase of the compounds belongs to the monoclinic crystal system and C2/c space group. The crystallographic refinement data is shown in Table 5.1

Table 5.1 Crystal structure refinement data for [Pb((SePⁱPr₂)(SPⁱPr₂)N)₂]

Chem formula	C ₂₄ H ₅₆ N ₂ P ₄ Pb S _{1.54} Se _{2.46}
Formula wt	947.22
Cryst syst	Monoclinic
Space group	C2/c
a(Å)	31.5574(6) Å
b(Å)	9.3804(2)
c(Å)	27.1301(5)
α(deg)	90
β(deg)	116.5930(10)
γ(deg)	90
V(Å ³)	7181.5(2)
Z	8
D _{calcd} (g cm ⁻³)	1.752
μ(Mo Kα) (mm ⁻¹)	14.629
R1 (I>2σ(I)) ^b	0.0319
wR2 (all data)	0.0742
GOF on F ²	0.988

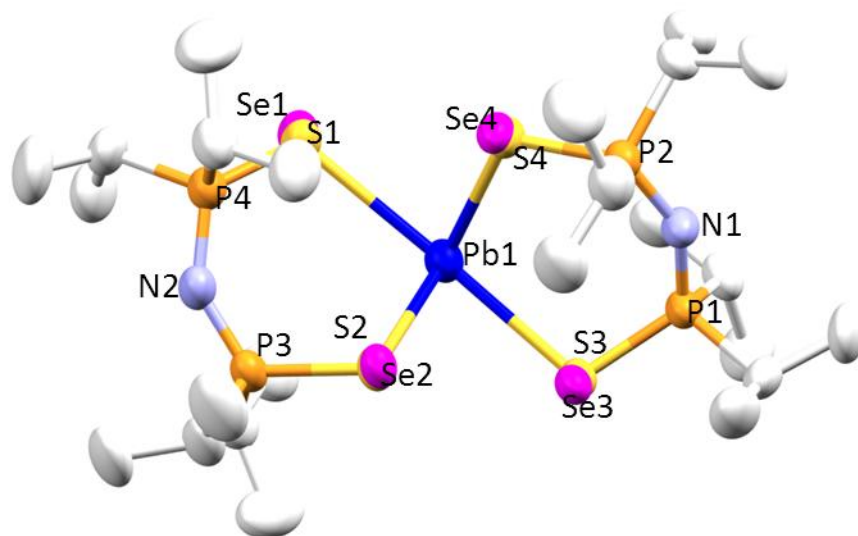


Figure 5.6. Crystal structure for $[\text{Pb}((\text{SeP}^i\text{Pr}_2)(\text{SP}^i\text{Pr}_2)\text{N})_2]$ product

5.4.2 Spectroscopic studies of $[\text{Pb}((\text{SeP}^i\text{Pr}_2)_2\text{N}(\text{S}_2\text{CNEt}_2))]$

5.4.2.1 ^1H NMR

A stacked set of ^1H NMR spectra of the starting materials and the product is shown as Figure 5.7. The basic elements in all three spectra are the same: a coupled quartet and triplet for the ethyl groups, and a set of four overlapping doublets and two overlapping septets for the isopropyl groups.

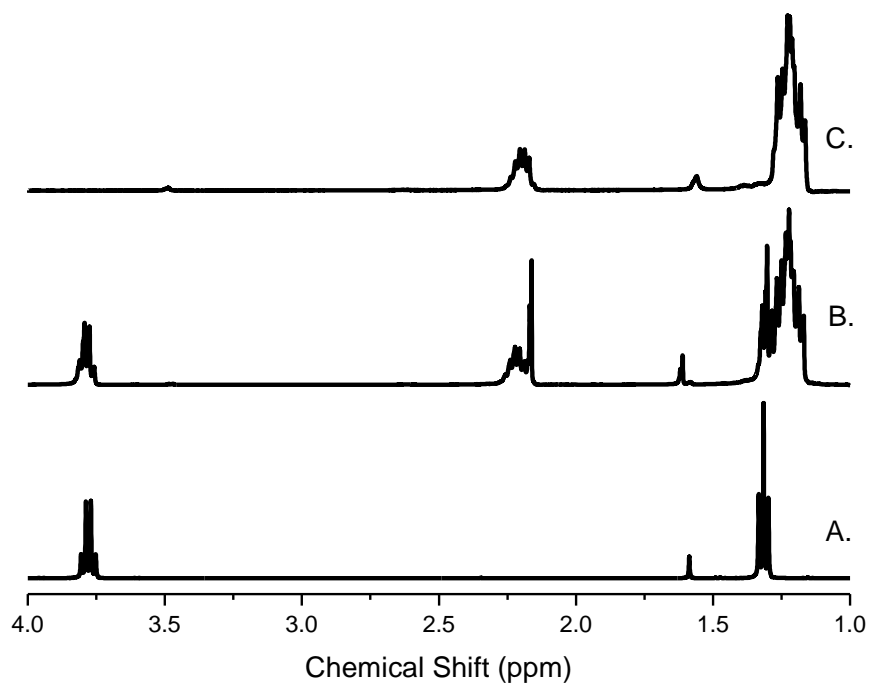


Figure 5.7. A stacked set of three ¹H NMR spectra; the two starting materials, **A**, *bis*(diethyldithiocarbamato) lead (II) and **C**, *bis*(imidodiisopropyldiselenophosphinato) lead(II), and **B**, the product.

5.4.2.2 ³¹P NMR

The phosphorus peak shown on the spectrum of the product had a chemical shift of 55.38 ppm. This does not differ significantly from the chemical shift of [Pb((SePⁱPr₂)₂N)₂] at 55.59 ppm .

5.4.2.3 ^{13}C NMR

The *ipso* carbon for $[\text{Pb}(\text{S}_2\text{CNEt}_2)]$ shows at a chemical shift of 202.04 ppm on the ^{13}C NMR spectrum. Two peaks thought to be for *ipso* carbon appeared on the ^{13}C NMR at 202.03 ppm and 207.03 ppm with a shift difference of 5 ppm. The peak at 202.03 ppm is similar to that of the starting material, however, the one appearing at 207.03 ppm indicates the possible formation of a new product (Figure 5.8).

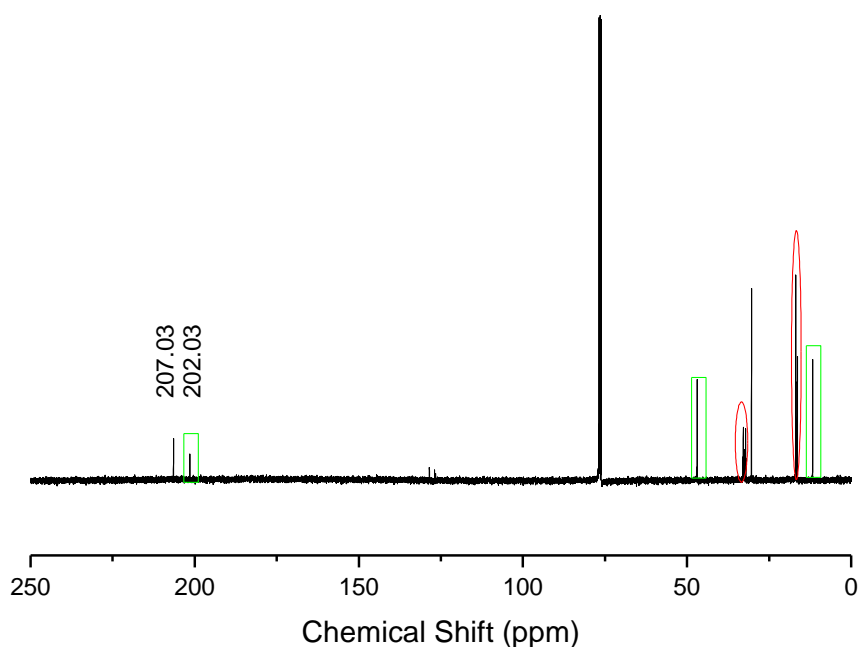


Figure 5.8. ^{13}C NMR spectrum of $[\text{Pb}((\text{SeP}^i\text{Pr}_2)_2\text{N}(\text{S}_2\text{CNEt}_2))]$ showing peaks corresponding to $[\text{Pb}((\text{SeP}^i\text{Pr}_2)_2\text{N})_2]$ in oval and that corresponding to $[\text{Pb}(\text{S}_2\text{CNEt}_2)]$ in rectangles. The other peaks suggest the formation of a new product.

5.4.2.4 ^{77}Se NMR

The ^{77}Se NMR spectrum of $[\text{Pb}((\text{SeP}^i\text{Pr}_2)_2\text{N}(\text{S}_2\text{CNEt}_2))]$ (Figure 5.9) showed two peaks at -175.80 and -182.49 ppm. The chemical shifts of the peaks were significantly different from the starting material $[\text{Pb}((\text{SeP}^i\text{Pr}_2)_2\text{N})_2]$ (-161.87, -169.7). The differences between peaks were 6.69 and 7.2 ppm for the product and starting material respectively which are quite different.

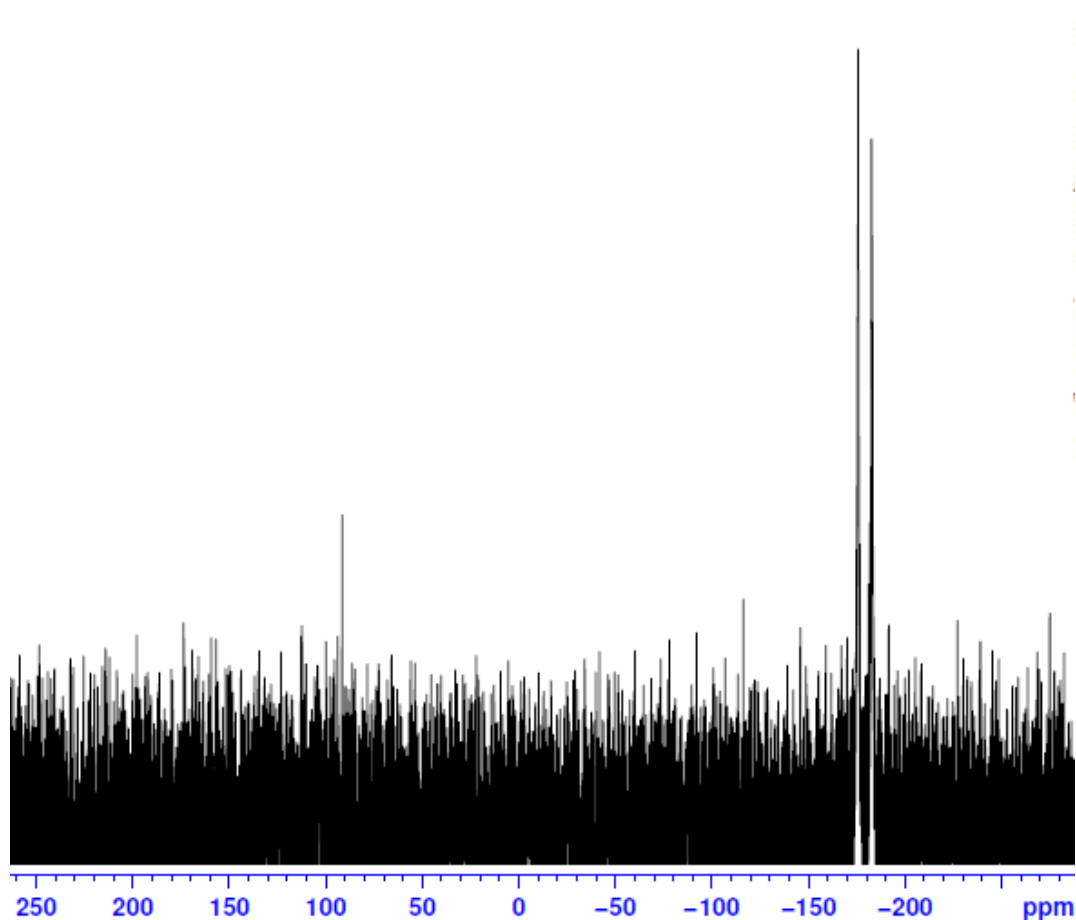


Figure 5.9 ^{77}Se NMR for $[\text{Pb}((\text{SeP}^i\text{Pr}_2)_2\text{N}(\text{S}_2\text{CNEt}_2))]$

5.4.2.5 Melting point for $[\text{Pb}((\text{SeP}^i\text{Pr}_2)_2\text{N}(\text{S}_2\text{CNEt}_2))]$

The melting point for the product was 125-128 °C. The melting points of the two individual mixtures were different from that of the starting materials 131-133 °C and 211-213 °C for $[\text{Pb}((\text{SeP}^i\text{Pr}_2)_2\text{N})_2]$ and $[\text{Pb}(\text{S}_2\text{CNEt}_2)]$ respectively.

5.4.2.6 J-resolved NMR for $[\text{Pb}((\text{SeP}^i\text{Pr}_2)_2\text{N}(\text{S}_2\text{CNEt}_2))]$

Analysis of the J-resolved spectra of the starting materials $[\text{Pb}(\text{S}_2\text{CNEt}_2)_2]$ (**13**) (Figure 5.10) and $[\text{Pb}((\text{SeP}^i\text{Pr}_2)_2\text{N})_2]$ (**4**) (Figure 5.11) clearly showed the scalar couplings of the triplet and quartet from the ethyl groups in (**13**), and in (**4**) the overlapping septets from the isopropyl groups and four doublets in the overlapped region at 1.1 – 1.3 ppm. Analysis of the putative product (Figure 12) showed the same multiplet structure. Of particular interest, the region of overlap was resolved to show a triplet as in (**13**), four doublets and four impurity doublets as in (**4**), plus a new set of impurity peaks, also in the form of four doublets. The product material decomposed in CDCl_3 on a timescale of hours, both sets of impurity signals growing.

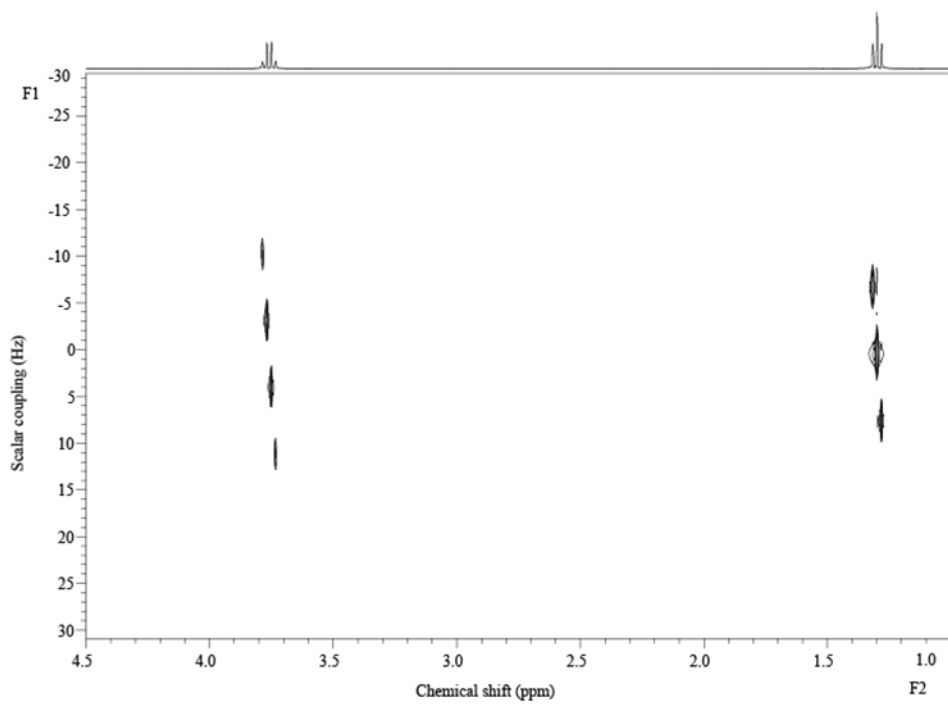


Figure 5.10. A J-resolved spectrum of *bis*(diethyldithiocarbamato) lead II (**13**) showing scalar couplings of the triplet and quartet from the ethyl groups.

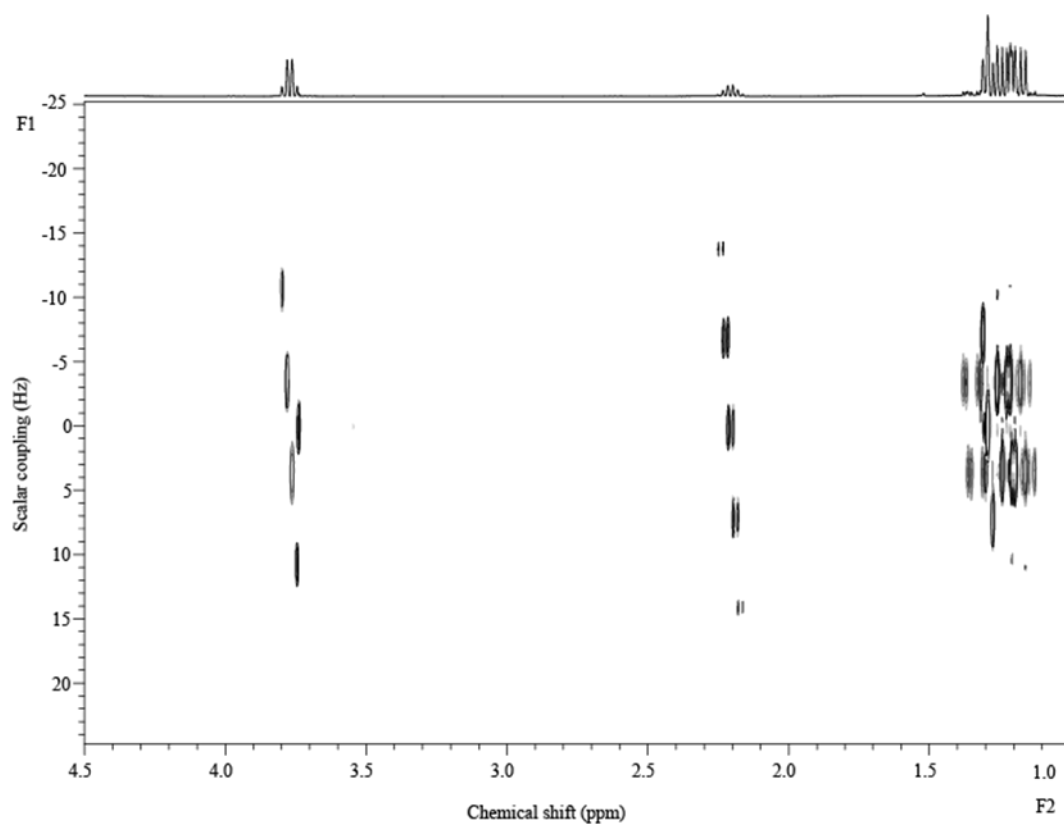


Figure 5.11. A J-resolved spectrum of *bis*(imidodiisopropyldiselenophosphinato) lead(II) (**4**), showing scalar couplings of overlapping septets with the two outer components too weak to be seen and four doublets in the overlap region 1.1 -1.4 ppm.

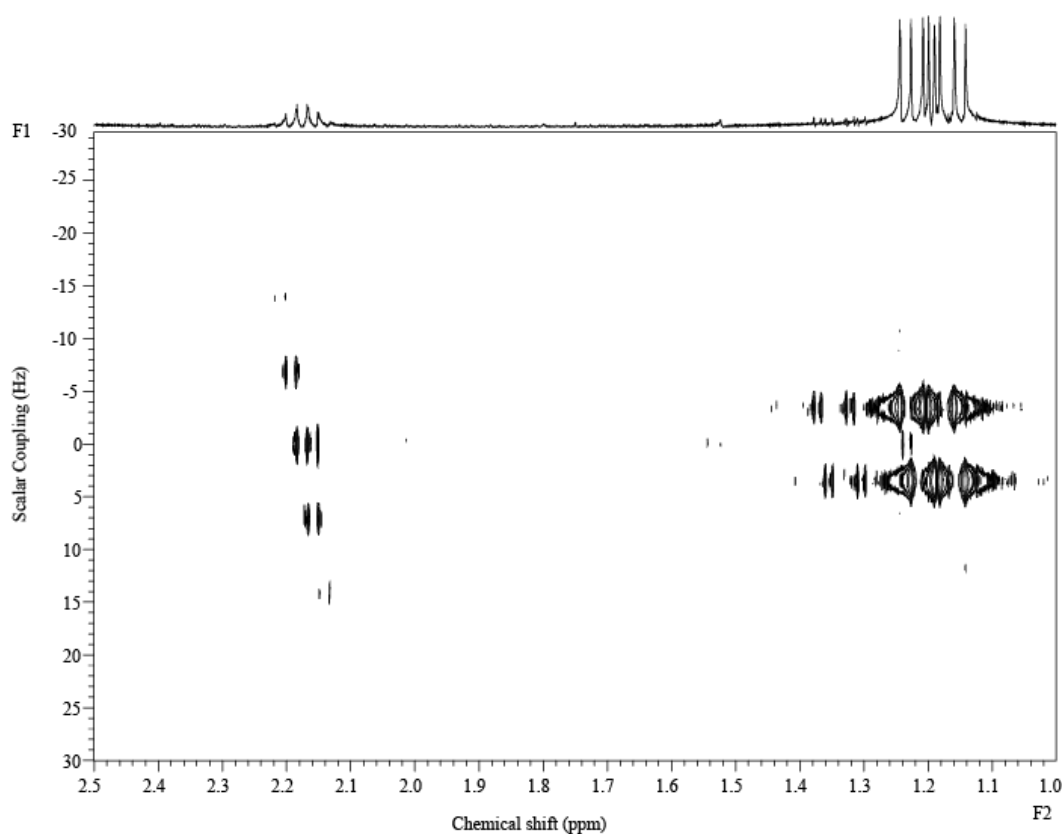


Figure 5.12. A J-resolved spectrum of the product (**18**) showing a quartet superimposed onto a singlet (the latter an impurity), overlapping septets with the two outer components too weak to be seen, and in the region of overlap a triplet, four doublets and two sets of four impurity doublets.

5.4.2.7 Diffusion ordered spectroscopy (DOSY)

Analysis of the starting materials (complexes 13 and 4) showed the presence of species with diffusion coefficients approximately $9 \times 10^{-10} \text{ m}^2 \text{ s}^{-1}$ and $7.6 \times 10^{-10} \text{ m}^2 \text{ s}^{-1}$ respectively. Analysis of a solution of the supposed product (Figure 5.13) showed that the ethyl and isopropyl signals had different diffusion coefficients, inconsistent with a product and consistent with a mixture of the two starting materials. The diffusion coefficients seen for the supposed product, approx. $8 \times 10^{-10} \text{ m}^2 \text{ s}^{-1}$ and $7.2 \times 10^{-10} \text{ m}^2 \text{ s}^{-1}$, were slightly lower than those seen for the isolated starting materials, which could indicate some transient association or could simply reflect different concentrations.

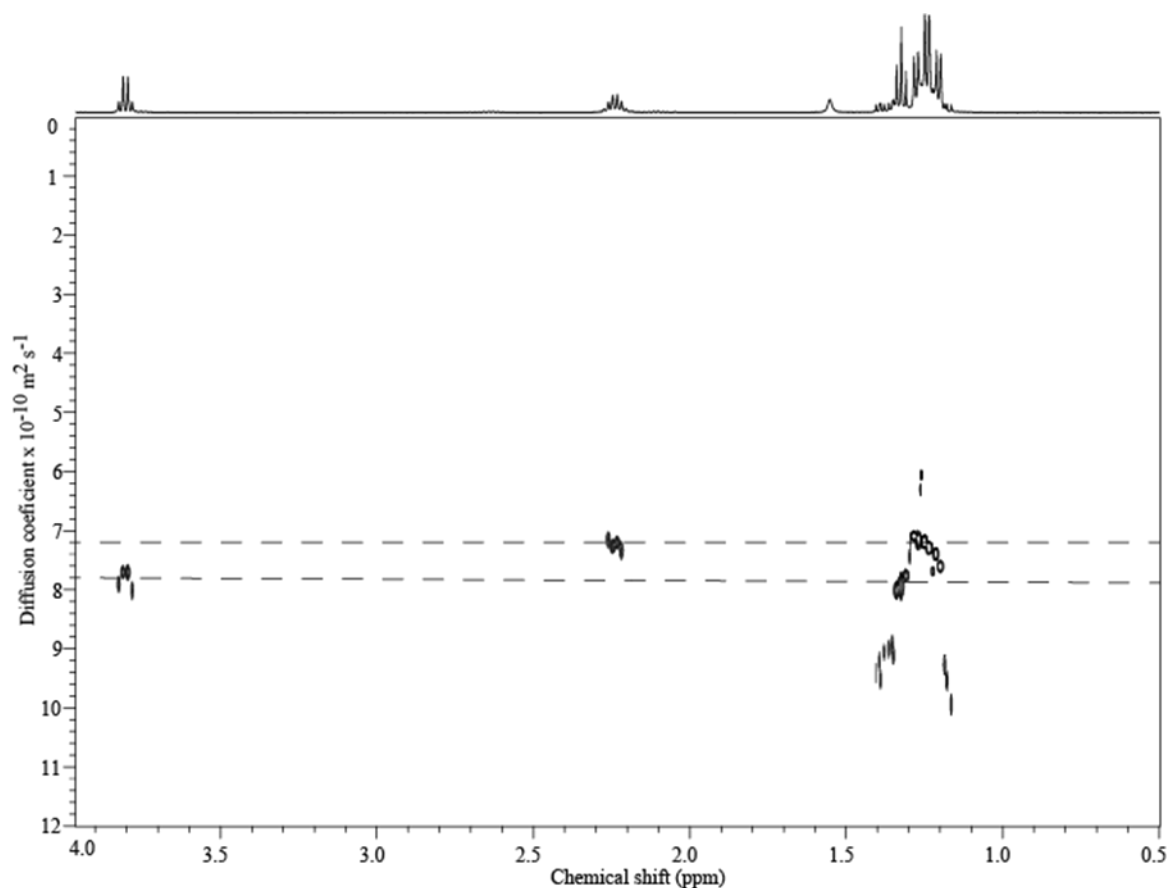


Figure 5.13. A DOSY ^1H NMR spectrum of the synthesised product in the overlap region 1.20 ppm to 1.35 ppm. Good separation is achieved indicating two species of diffusion coefficients approx. $8 \times 10^{-10} \text{ m}^2 \text{ s}^{-1}$ and $7.2 \times 10^{-10} \text{ m}^2 \text{ s}^{-1}$.

5.4.2.8 FT-IR analysis for $[\text{Pb}((\text{SeP}^i\text{Pr}_2)_2\text{N})(\text{S}_2\text{CNEt}_2)]$

The FT-IR spectrum of the mixture was significantly different in the fingerprint region (Figure 5.14) from the individual complexes. The band frequencies of the product (**B**) were not identical to any of frequencies from the individual complexes. For instance, the C-N stretch in the parent compound (**C**) appeared at 1137cm^{-1} whereas that in the product was at 1142cm^{-1} . The shift in band frequency in the product from the starting material indicates a possible formation of a different complex arising from the reaction of the individual complexes.

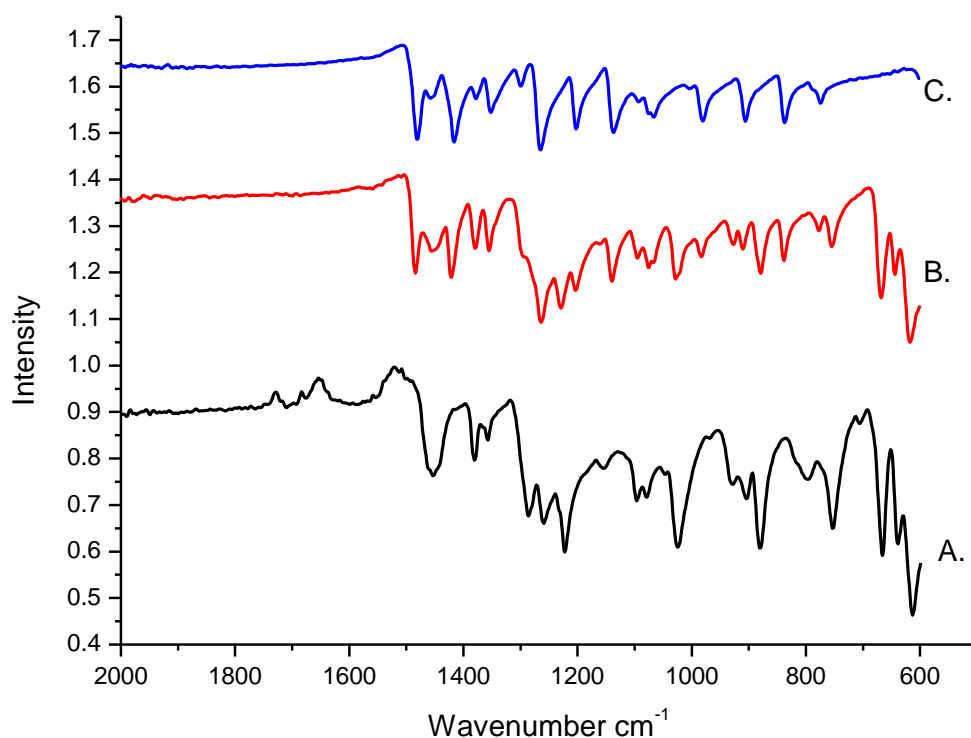


Figure 5.14 FT-IR Spectra for **A.** $[\text{Pb}((\text{SeP}^i\text{Pr}_2)_2\text{N})_2]$ **B.** $[\text{Pb}((\text{SeP}^i\text{Pr}_2)_2\text{N})(\text{S}_2\text{CNEt}_2)]$ and **C.** $[\text{Pb}(\text{S}_2\text{CNEt}_2)_2]$

5.4.2.9 Melting point and micro elemental analysis

The melting points of the individual complexes and $[\text{Pb}((\text{SeP}^i\text{Pr}_2)_2\text{N})(\text{S}_2\text{CNEt}_2)]$ are shown in Table 5.2. The melting point of product ranged from $129\text{ }^\circ\text{C}$ to $132\text{ }^\circ\text{C}$. Though different

from the individual complexes, it was close to the melting point of $[\text{Pb}((\text{SeP}^i\text{Pr}_2)_2\text{N})_2]$ complex and far less than that of $[\text{Pb}(\text{S}_2\text{CNEt}_2)]$ complex. The melting point range of the product is narrow which indicates the purity of the compound.

Micro elemental analysis of $[\text{Pb}((\text{SeP}^i\text{Pr}_2)_2\text{N})(\text{S}_2\text{CNEt}_2)]$ gave the following results: $\text{C}_{17}\text{H}_{28}\text{N}_2\text{P}_2\text{S}_2\text{Se}_2\text{Pb}$. Calculated: C= 26.81, H= 5.03, N= 3.68, S= 8.42, P= 8.13 and Pb= 27.20 %; Observed: C= 26.85, H= 5.11, N= 3.71, S= 8.17, P= 8.16 and Pb= 27.01 %.

The results of the micro elemental analysis add to confirm the formation of the product and its purity.

Table 5.2. Melting point of $[\text{Pb}((\text{SeP}^i\text{Pr}_2)_2\text{N})_2]$, $[\text{Pb}(\text{S}_2\text{CNEt}_2)_2]$ and product $[\text{Pb}((\text{SeP}^i\text{Pr}_2)_2\text{N})(\text{S}_2\text{CNEt}_2)]$ complexes

SN	Complex	Melting Point (°C)
1	$[\text{Pb}((\text{SeP}^i\text{Pr}_2)_2\text{N})_2]$	132 (131-133)
2	$[\text{Pb}(\text{S}_2\text{CNEt}_2)_2]$	212 (211-213)
3	$[\text{Pb}((\text{SeP}^i\text{Pr}_2)_2\text{N})(\text{S}_2\text{CNEt}_2)]$	131 (129-132)

5.4.2.10 p-XRD analysis of $[\text{Pb}((\text{SeP}^i\text{Pr}_2)_2\text{N})(\text{S}_2\text{CNEt}_2)]$ product (18)

The spectrum of the product B (Figure 5.15) shows peaks that are different from its starting materials A and C. This indicates the possibility of a new product formed independent of its starting material.

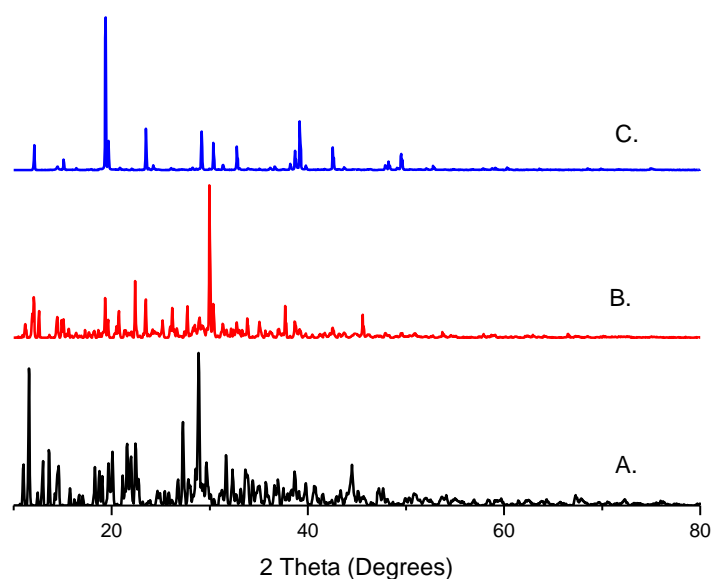


Figure 5.15. A stacked p-XRD spectra showing peaks corresponding to **A**, $[\text{Pb}((\text{SeP}^i\text{Pr}_2)_2\text{N})_2]$, **B**, $[\text{Pb}((\text{SeP}^i\text{Pr}_2)_2\text{N}(\text{S}_2\text{CNEt}_2))]$ and **C**, $[\text{Pb}(\text{S}_2\text{CNEt}_2)_2]$.

5.4.2.11 Single-crystal X-ray diffraction studies

Single crystals of $[\text{Pb}((\text{SeP}^i\text{Pr}_2)_2\text{N})(\text{S}_2\text{CNEt}_2)]$ suitable for X-ray diffraction studies were obtained by slow evaporation of chloroform/methanol 1:2 mixture containing dissolved complex. The crystal structure of the compound is shown in Figure 5.16. The geometry at the lead atom in the complex is a distorted square pyramidal with four chalcogenide, (S, Se) atoms, forming the base of the pyramid and the lone pair on the lead atom occupying the axial position.

In the complex, the lead atoms are coordinated to two sulphur atoms and two selenium atoms, the selenium atoms coming from $[\text{Pb}((\text{SeP}^i\text{Pr}_2)_2\text{N})_2]$ and the sulphur atoms from $[\text{Pb}(\text{S}_2\text{CNEt}_2)_2]$. The crystalline phase of the compound has the monoclinic crystal system and $\text{P}2(1)/n$ space group. The crystal structure refinement data is shown in Table 5.3.

Table 5.3 Crystal structure data for mixed [Pb((SePⁱPr₂)₂N)(S₂CNEt₂)]

Chem. Formula.	C ₁₇ H ₃₈ N ₂ P ₂ PbS ₂ Se ₂
Formula wt.	761.66
Cryst. Syst.	Monoclinic
Space group	P2(1)/n
a(Å)	14.6415(4)
b(Å)	12.9568(3)
c(Å)	15.8270(4)
α(deg)	90
β(deg)	117.5180(10)
γ(deg)	90
V(Å ³)	2662.81(12)
Z	4
D _{calcd} (g cm ⁻³)	1.900
μ(Mo Kα) (mm ⁻¹)	18.086
R1 (I>2σ(I)) ^b	0.0417
wR2 (all data)	0.1228
GOF on F ²	1.089

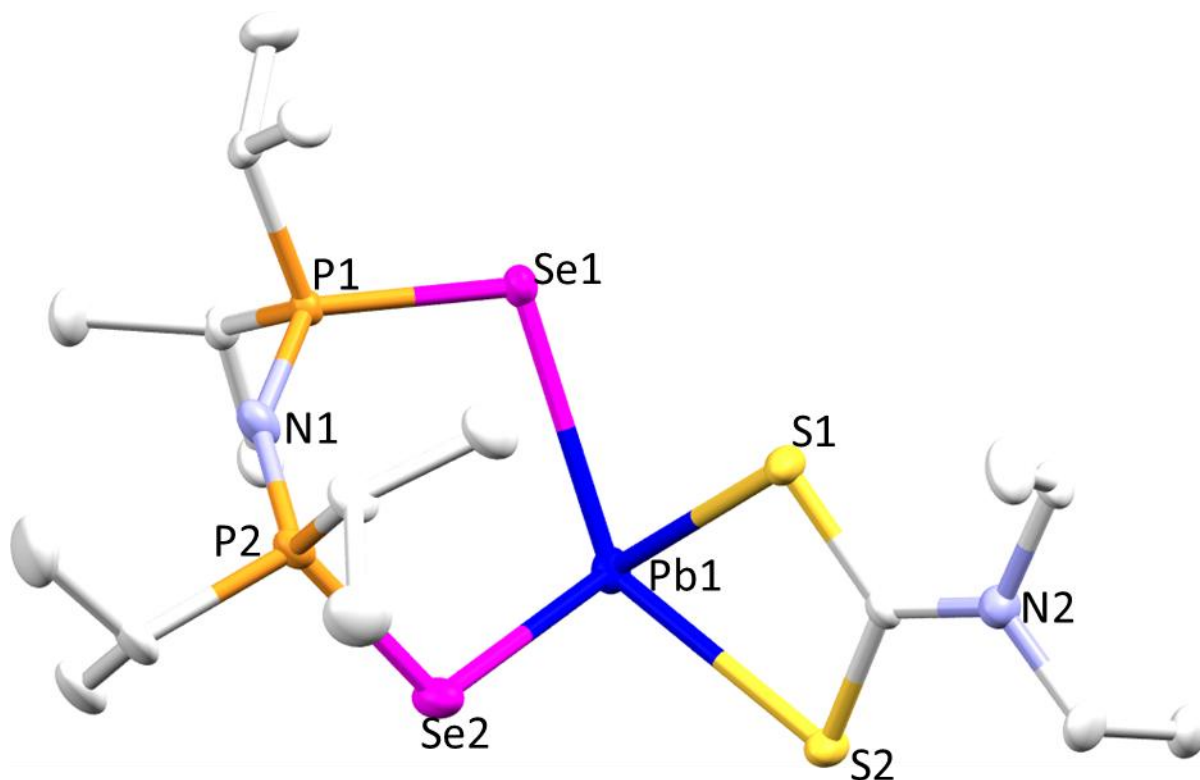


Figure 5.16 Crystal structure of $[\text{Pb}((\text{SeP}^i\text{Pr}_2)_2\text{N})(\text{S}_2\text{CNEt}_2)]$

5.4.3 Spectroscopic studies of $\text{Pb}[\text{((SeP}^i\text{Pr}_2)_2\text{N})(\text{S}_2\text{CNHexMe})]$

5.4.3.1 ^1H NMR

A stacked set of ^1H NMR spectra of the starting materials and the product is shown as Figure 5.17. The spectrum of the product shows peaks that correspond to the individual starting materials. It cannot be concluded at this point that a new product has been formed since the spectrum could show a superimposition of the spectra of the starting materials.

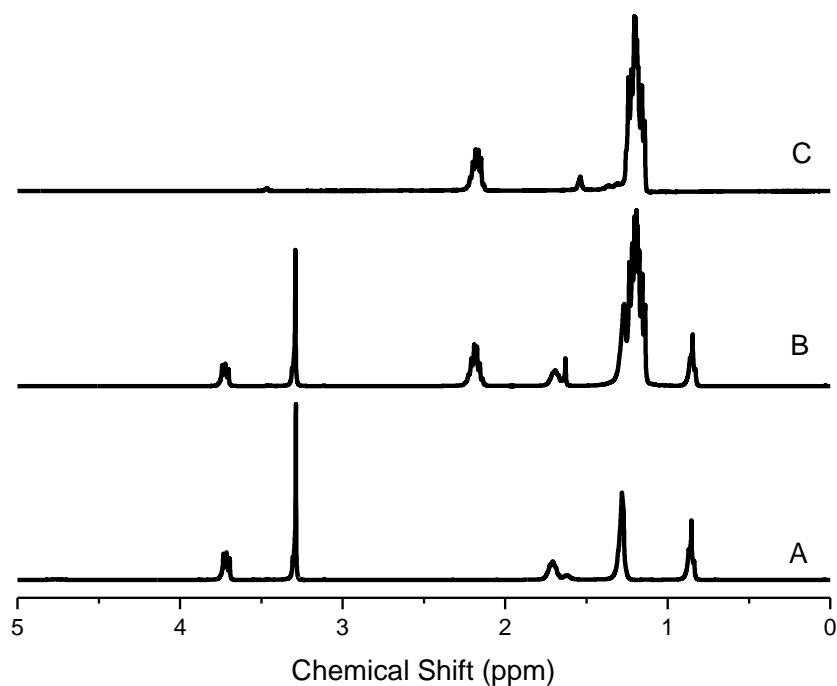


Figure 5.17. Stacked ^1H NMR for **A**, hexylmethyl dithiocarbamate, **B**, product and **C**, imidodiselenophosphate lead(II) complex

5.4.3.2 ^{31}P NMR

The phosphorus peak shown on the spectrum of the product had a chemical shift of 55.41 ppm. This does not differ significantly from the chemical shift of $[\text{Pb}((\text{SeP}^i\text{Pr}_2)_2\text{N})_2]$ at 55.59 ppm. A stacked plot of the ^{31}P -NMR of $[\text{Pb}((\text{SeP}^i\text{Pr}_2)_2\text{N})_2]$ and the product is shown in Figure 5.18.

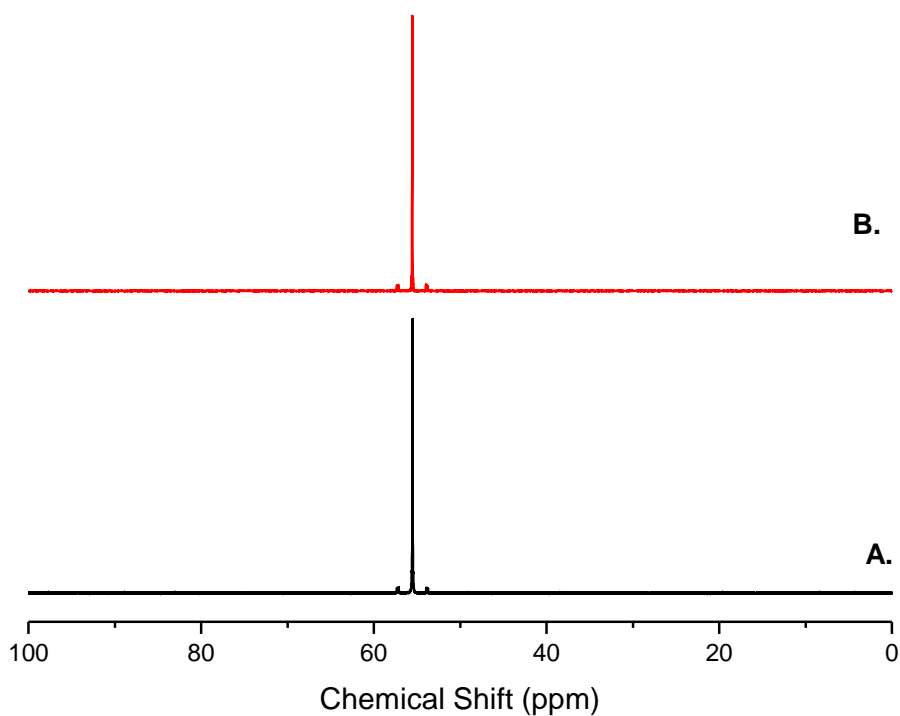


Figure 5.18. Stacked ^{31}P NMR for **A**, imidodiselenophosphinato lead (II) complex and **B**, product.

5.4.3.3 ^{13}C NMR

The *ipso* carbon for $[\text{Pb}(\text{S}_2\text{CNHexMe})_2]$ shows at a chemical shift of 202.64 ppm on the ^{13}C NMR spectrum. The *ipso* carbon appeared on the ^{13}C NMR at 203.00 ppm for the product. The *ipso* carbon peak for the product is similar to that of the starting material and therefore does not conclusively indicate the possible formation of a new product since it can be as a result of superimposition of the spectra of the starting materials (Figure 5.19).

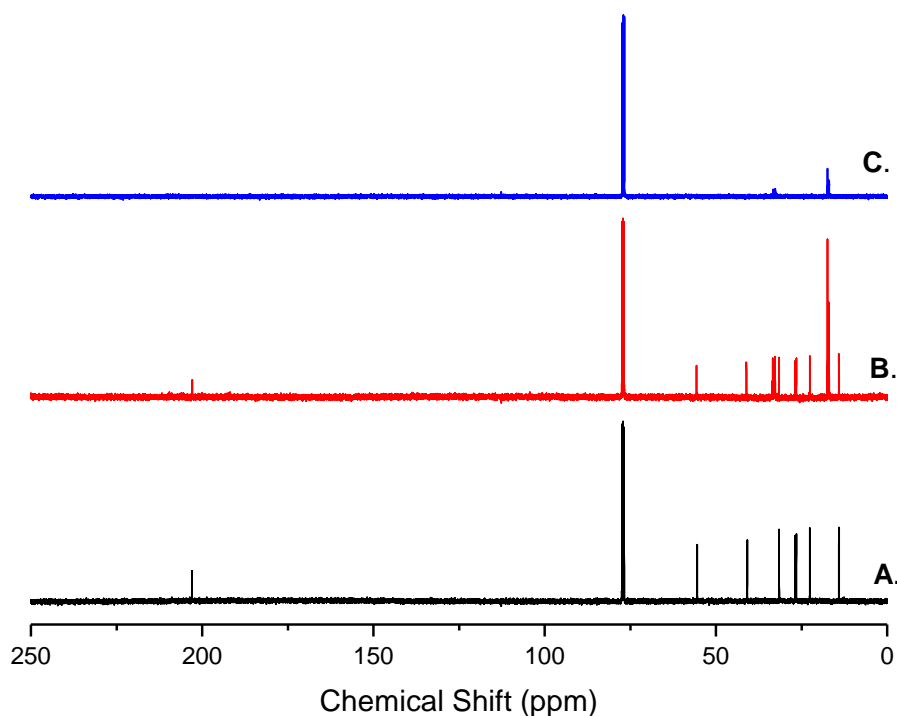


Figure 5.19. Stacked ^{13}C NMR for **A**, hexylmethyl dithiocarbamate, **B** mixed hexylmethyl dithiocarbamate and imidodiselenophosphinato lead(II) complex and **C**, imidodiselenophosphinate lead(II) complex.

5.4.3.4 ^{77}Se NMR

The ^{77}Se NMR spectrum of the product showed two peaks at -175.57 and -183.00 ppm. The chemical shifts of the peaks were significantly different from the starting material $[\text{Pb}((\text{SeP}^i\text{Pr}_2)_2\text{N})_2]$ (-161.87, -169.7). This indicates the possible formation of a new complex. A stacked plot of the ^{77}Se NMR of $[\text{Pb}((\text{SeP}^i\text{Pr}_2)_2\text{N})_2]$ and the product is shown in Figure 5.20.

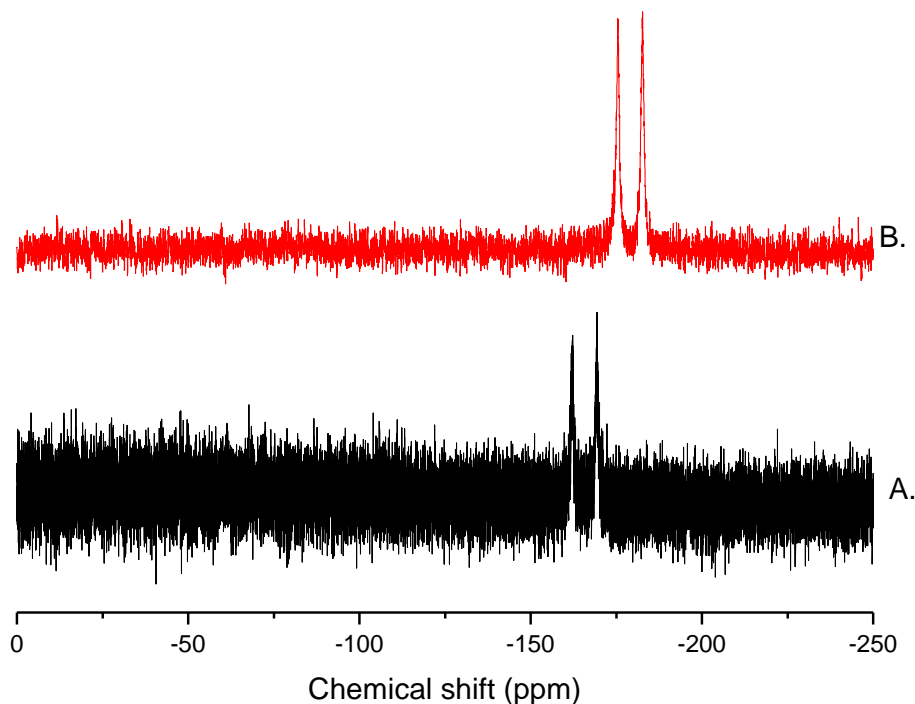


Figure 5.20. Stacked ^{77}Se NMR for **A**, imidodiselenophosphinato lead (II) complex and **B**, product.

5.4.3.5 FT-IR for $\text{Pb}[(\text{SeP}^i\text{Pr}_2)_2\text{N}(\text{S}_2\text{CNHexMe})]$

The FT-IR spectrum of the product was significantly different in the fingerprint region (Figure 5.21) from the individual complex. The band frequencies of the product (**B**) were not identical to any of frequencies from the individual complexes. The C-N stretch in the parent compound (**A**) appeared at 1074 cm^{-1} whereas that in the product was at 1076 cm^{-1} . The shift in band frequency of the product from the starting material indicates a possible formation of a different complex arising from the reaction of the individual complexes.

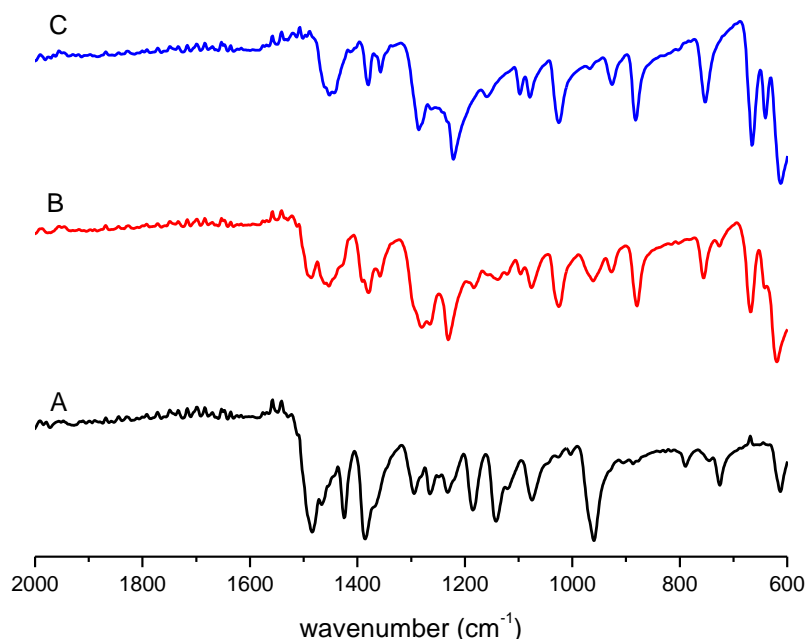


Figure 5.21. Stacked FT-IR spectra of **A**, hexylmethyl dithiocarbamate, **B**, product and **C**, *bis*(imidodiisopropyldiselenophosphinato lead (II)).

5.4.3.6 Melting point and micro elemental analysis

The melting point of the individual complexes and the product are shown in Table 5.4. The melting point of product ranged from 78 °C to 80 °C. Though different from the individual complexes, it was close to the melting point of $[\text{Pb}((\text{SeP}^i\text{Pr}_2)_2\text{N})_2]$ complex and far less than that of $[\text{Pb}(\text{S}_2\text{CNHexMe})_2]$ complex. The melting point range of the product is narrow which indicates the purity of the compound.

Micro elemental analysis of $[\text{Pb}((\text{SeP}^i\text{Pr}_2)_2\text{N})(\text{S}_2\text{CNHexMe})]$ gave the following results: $\text{C}_{20}\text{H}_{44}\text{N}_2\text{P}_2\text{S}_2\text{Se}_2\text{Pb}$. Calculated: C = 29.87, H = 5.52, N = 3.59, S = 7.96, P = 7.71 and Pb = 25.79 %; Observed: C = 29.95, H = 5.81, N = 3.40, S = 7.09, P = 7.97 and Pb = 25.18 %.

The results of the micro elemental analysis add to confirm the formation of $[\text{Pb}((\text{SeP}^i\text{Pr}_2)_2\text{N})(\text{S}_2\text{CNHexMe})]$ product.

Table 5.4. Melting point determination for $[\text{Pb}((\text{SeP}^i\text{Pr}_2)_2\text{N})_2]$, $[\text{Pb}((\text{SP}^i\text{Pr}_2)_2\text{N})_2]$ and product $\text{Pb}[(\text{SeP}^i\text{Pr}_2)_2\text{N}(\text{S}_2\text{CNHexMe})]$ complexes

SN	Complex	Melting Point (°C)
1	$[\text{Pb}((\text{SeP}^i\text{Pr}_2)_2\text{N})_2]$	132 (131-133)
2	$[\text{Pb}(\text{S}_2\text{CNHexMe})_2]$	89 (88-90)
3	$\text{Pb}[(\text{SeP}^i\text{Pr}_2)_2\text{N}(\text{S}_2\text{CNHexMe})]$	79 (78-80)

5.4.3.7 p-XRD for $\text{Pb}[(\text{SeP}^i\text{Pr}_2)_2\text{N}(\text{S}_2\text{CNHexMe})]$

The spectrum of the product **B** (Figure 5.22) shows peaks that are different from its starting materials **A** and **C**. This indicates the possibility of a new product formed independent of its starting material.

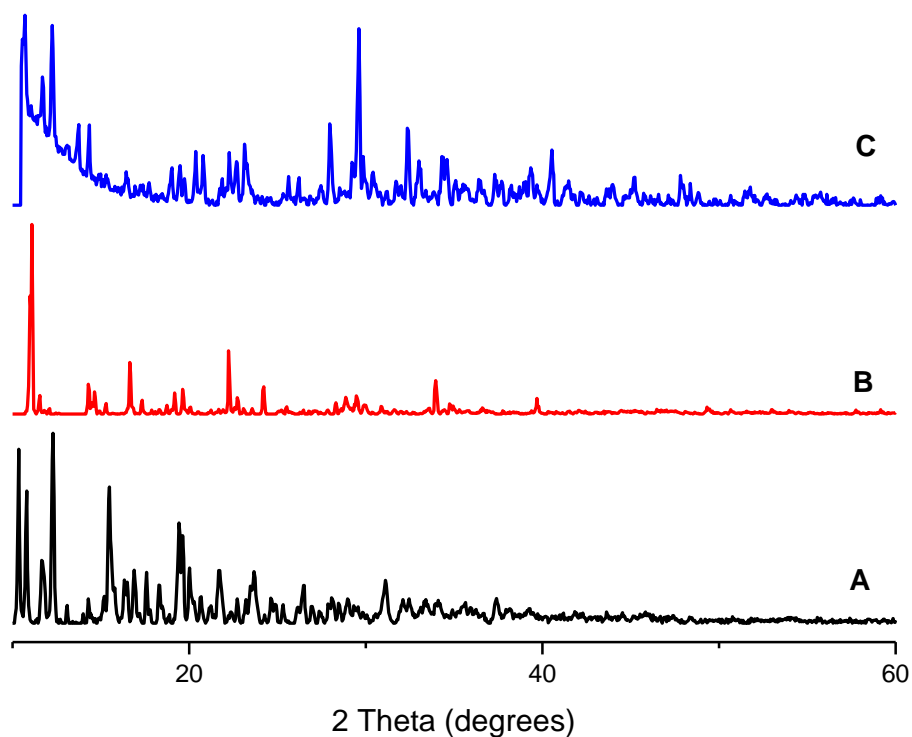


Figure 5.22. A stacked plot of p-XRD for **A**, hexylmethyldithiocarbamate, **B**, $\text{Pb}[(\text{SeP}^i\text{Pr}_2)_2\text{N}(\text{S}_2\text{CNHexMe})]$ and **C**, imidodiselenophosphinato lead (II)

5.4.3.8 Single-crystal X-ray diffraction studies of $\text{Pb}[(\text{SeP}^i\text{Pr}_2)_2\text{N}(\text{S}_2\text{CNHexMe})]$

Single crystals of mixed $[\text{Pb}((\text{SeP}^i\text{Pr}_2)_2\text{N}(\text{S}_2\text{CNHexMe}))]$ suitable for X-ray diffraction studies were obtained by slow evaporation of chloroform/methanol 1:2 mixture containing dissolved complex. The crystal structure of the compound is shown in Figure 5.23. The geometry at the lead atom in the complex is a distorted square pyramidal with four chalcogenide, (S,Se) atoms, forming the base of the pyramid and the lone pair on the lead atom occupying the axial position.

In the complex, the lead atoms are coordinated to two Sulphur atoms and two selenium atoms, the selenium atoms coming from $[\text{Pb}((\text{SeP}^{\text{I}}\text{Pr}_2)_2\text{N})_2]$ and the sulphur atoms from $[\text{Pb}(\text{S}_2\text{CNHexMe})_2]$. The crystalline phase of the compound belongs to the monoclinic crystal system and P2(1)/c space group. Crystallographic details are summarised in Table 5.5.

Table 5.5 Crystal structure data for mixed $\text{Pb}[(\text{SeP}^{\text{I}}\text{Pr}_2)_2\text{N}(\text{S}_2\text{CNHexMe})]$

Chem formula	$\text{C}_{40} \text{H}_{88} \text{N}_4 \text{P}_4 \text{Pb}_2 \text{S}_4 \text{Se}_4$
Formula wt	1607.48
Cryst syst	Monoclinic
Space group	P2(1)/c
a(Å)	10.1790(2)
b(Å)	18.3729(2)
c(Å)	31.7436(4)
α (deg)	90
β (deg)	95.9940(10)
γ (deg)	90
$V(\text{Å}^3)$	5904.16(15)
Z	4
$D_{\text{calcd}} (\text{g cm}^{-3})$	1.808
$\mu(\text{Mo K}\alpha) (\text{mm}^{-1})$	16.351
$R1 (I > 2\sigma(I))^b$	0.0298
wR2 (all data)	0.0721
GOF on F^2	1.101

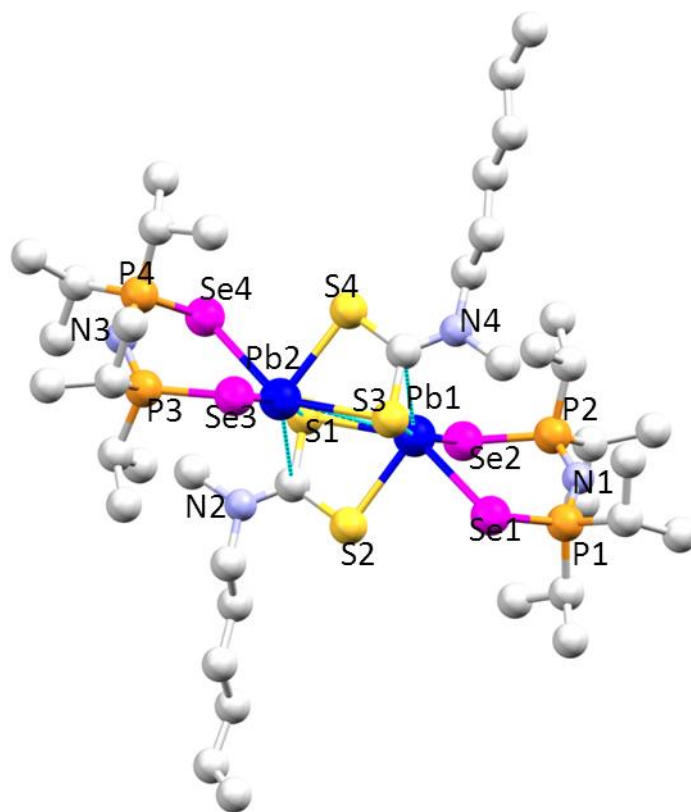


Figure 5.23 Crystal structure of $[\text{Pb}((\text{SeP}^i\text{Pr}_2)_2\text{N})(\text{S}_2\text{CNHexMe})]$

5.5 Conclusion

Three new mixed lead chalcogenide Single-source precursors suitable for making $\text{PbS}_x\text{Se}_{1-x}$ nanoparticles and thin films have been successfully synthesised. They are $[\text{Pb}((\text{SeP}^i\text{Pr}_2)(\text{SP}^i\text{Pr}_2)\text{N})_2]$, $[\text{Pb}((\text{SeP}^i\text{Pr}_2)_2\text{N})(\text{S}_2\text{CNEt}_2)]$ and $[\text{Pb}((\text{SeP}^i\text{Pr}_2)_2\text{N})(\text{S}_2\text{CNHexMe})]$. These complexes have been characterised using ^1H , ^{13}C , ^{31}P , and ^{77}Se NMR spectroscopy. $[\text{Pb}((\text{SeP}^i\text{Pr}_2)_2\text{N})(\text{S}_2\text{CNEt}_2)]$ was further characterised by J-resolved NMR and Diffusion ordered NMR spectroscopic (DOSY) techniques. Other characterisation techniques used were melting point, FT-IR spectroscopy and p-XRD spectroscopy. The crystal structures for all three complexes have been obtained.

Chapter 6

Synthesis of PbS_xSe_{1-x} Thin Films by Pyrolysis and Aerosol Assisted Chemical Vapour Deposition

6.1 Summary

In this chapter, the production of PbS_xSe_{1-x} thin films by pyrolysis and Aerosol Assisted Chemical Vapour Deposition (AACVD) methods is presented.

6.2 Introduction

The Pb chalcogenide family of nanocrystals is actively investigated for nanocrystal solar cell applications because they have large exciton Bohr radii (PbS 18 nm, PbSe 47 nm, and PbTe 46 nm) (Alivisatos *et al.*, 2009). In the limit where the nanocrystals are about a tenth of the bulk exciton diameter, electrons and holes can tunnel through a thin organic surface coating, and therefore strong electronic coupling between particles facilitates transport of charge between nanocrystals (Alivisatos *et al.*, 2009). So far, Schottky solar cells based on binary compositions of PbSe and PbS nanocrystals have been investigated. PbSe nanocrystal solar cells generate larger short circuit photocurrents while PbS nanocrystal devices with similar band gap have shown a larger V_{OC} (Luther *et al.*, 2008). This opens the possibility to better engineer particles, by creating ternary PbS_xSe_{1-x} to simultaneously optimize both carrier transport and voltage. Moreover, the properties of PbS and PbSe lead to an ideal substitutional alloy; the atomic anion radii are within 15 % of each other, the lattice mismatch factor is only 2 % between PbS and PbSe and the anions are isovalent.

Ternary lead sulphide selenide (PbS_xSe_{1-x}) (Brumer *et al.*, 2005) NCs have not been extensively studied in contrast to the parent binary materials PbS and PbSe (Alivisatos *et al.*, 2009). Alloyed semiconductor nanomaterials provide an alternative approach for band gap control in addition to the size-dependent quantum confinement effects; and they give access to families of material with distinct properties. The properties of alloys vary with composition making it possible to tune the band gap while maintaining a similar small size.

The synthesis of ternary PbS_xSe_{1-x} thin films from Single-source precursors have so far not been reported. In this work, three Single-source precursors, $[Pb((SeP^iPr_2)(SP^iPr_2)N)_2]$, $[Pb((SeP^iPr_2)_2N)(S_2CNEt_2)]$ and $[Pb((SeP^iPr_2)_2N)(S_2CNHexMe)]$ have been used to deposit PbS_xSe_{1-x} thin films by Aerosol Assisted Chemical Vapour Deposition (AACVD). $[Pb((SeP^iPr_2)_2N)(S_2CNEt_2)]$ has also been pyrolysed.

6.3 Result

6.3.1 Thermogravimetric analysis

Thermogravimetric analysis of $[Pb((SeP^iPr_2)(SP^iPr_2)N)_2]$ (A), $[Pb((SeP^iPr_2)_2N)(S_2CNEt_2)]$ (B) and $[Pb((SeP^iPr_2)_2N)(S_2CNHexMe)]$ (C) have been presented in Figure 6.1. $[Pb((SeP^iPr_2)(SP^iPr_2)N)_2]$ showed single step decomposition whilst $[Pb((SeP^iPr_2)_2N)(S_2CNEt_2)]$ and $[Pb((SeP^iPr_2)_2N)(S_2CNHexMe)]$ showed a two-step decomposition indicating the formation of an intermediate compound (Figure 5.24). The remaining residue for $[Pb((SeP^iPr_2)(SP^iPr_2)N)_2]$, (25.9 %) was lower than the theoretical value (28.3 %) for PbS_xSe_{1-x} . This may be due to the volatility at elevated temperatures (600°C) thereby leading to a further weight loss. A similar trend was observed in the TGA for $[Pb((SeP^iPr_2)_2N)(S_2CNEt_2)]$ and $[Pb((SeP^iPr_2)_2N)(S_2CNHexMe)]$. The residue remaining for $[Pb((SeP^iPr_2)_2N)(S_2CNEt_2)]$ had a weight percent of 33.2 % of the complex which is lower

than the theoretical value 34.5 % and for $[Pb((SeP^iPr_2)_2N)(S_2CNHexMe)]$, the observed % weight was 32.0 whilst the expected was 32.7 %.

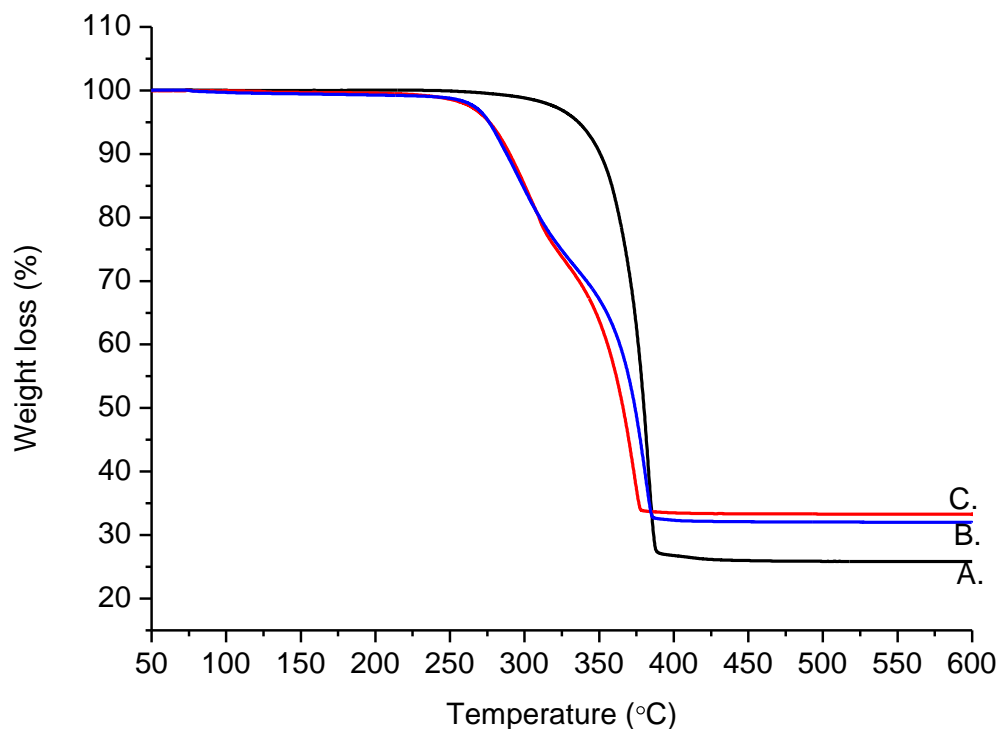


Figure 6.1 TGA Plot for Single-source precursors $[Pb((SeP^iPr_2)(SP^iPr_2)N)_2]$ (A), $[Pb((SeP^iPr_2)_2N)(S_2CNEt_2)]$ (B) and $[Pb((SeP^iPr_2)_2N)(S_2CNHexMe)]$ (C)

6.3.2 Synthesis of PbS_xSe_{1-x} thin films by aerosol assisted chemical vapour deposition (AACVD)

PbS_xSe_{1-x} thin films were deposited on glass substrates by aerosol assisted chemical vapour deposition (AACVD) using $[Pb((SeP^iPr_2)(SP^iPr_2)N)_2]$, $[Pb((SeP^iPr_2)_2N)(S_2CNEt_2)]$ and $[Pb((SeP^iPr_2)_2N)(S_2CNHexMe)]$ Single-source precursors. The deposition for all three complexes was done at a constant time of 30 minutes and temperatures of 300, 350, 400 and 450 °C.

6.3.2.1 p-XRD of thin films

The p-XRD for the thin films deposited from all three complexes at the selected temperatures matched mainly with standard lead selenide peaks. There was, however, some slight shift of the shoulders of the peaks from the standard PbSe peaks (shown as vertical lines) at lower temperatures (300-350 °C) and in some cases, at 400 °C. A stacked set of p-XRD spectra of the thin films deposited from $[Pb((SeP^iPr_2)(SP^iPr_2)N)_2]$, $[Pb((SeP^iPr_2)_2N)(S_2CNEt_2)]$ and $[Pb((SeP^iPr_2)_2N)(S_2CNHexMe)]$ complexes at various temperatures are shown respectively as Figures 6.2, 6.3 and 6.4.

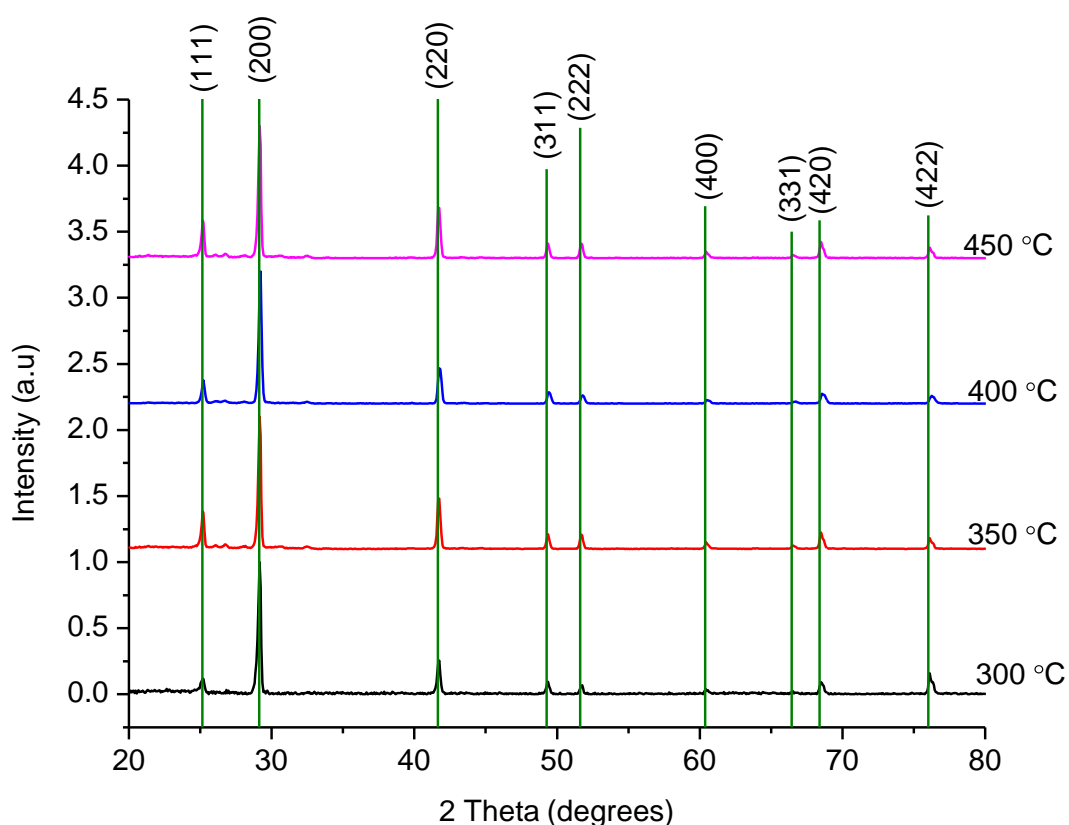


Figure 6.2. A stacked set of four p-XRD spectra showing the diffracting pattern of thin films deposited from $[Pb((SeP^iPr_2)(SP^iPr_2)N)_2]$ complex at 300, 350, 400 and 450 °C.

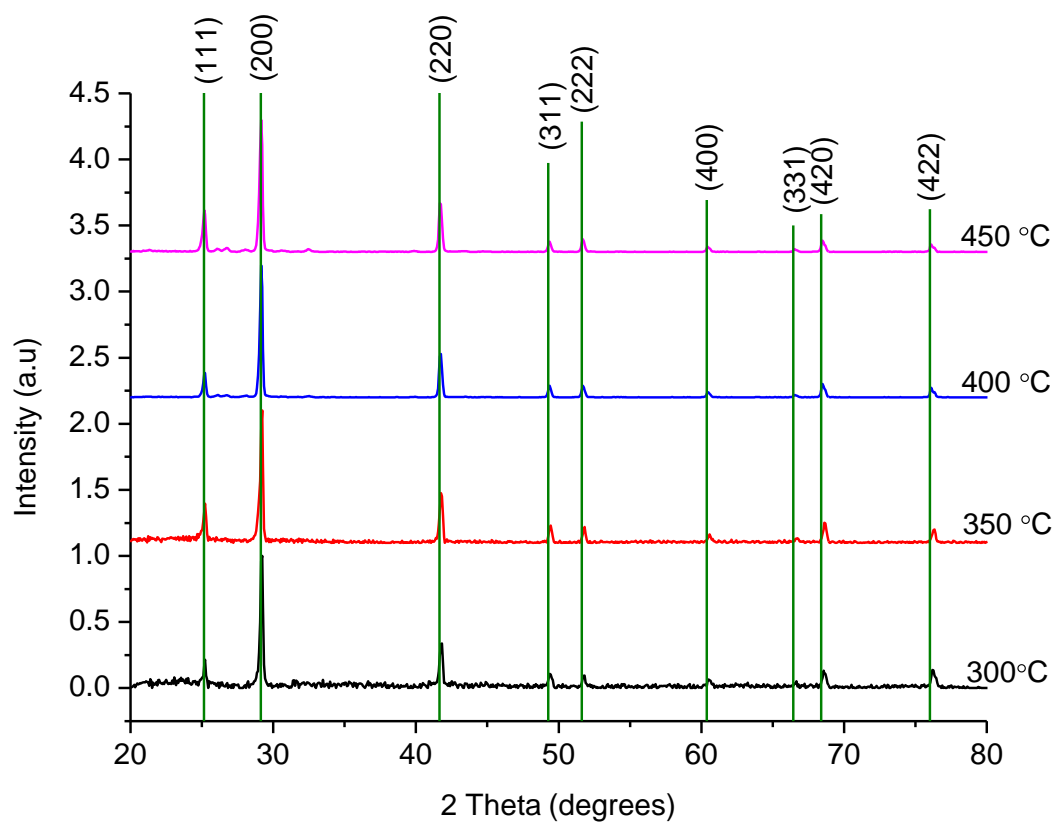


Figure 6.3. A stacked set of four p-XRD spectra showing the diffracting pattern of thin films deposited from $[Pb((SeP^iPr_2)_2N(S_2CNEt_2))]_x$ complex at 300, 350, 400 and 450 °C.

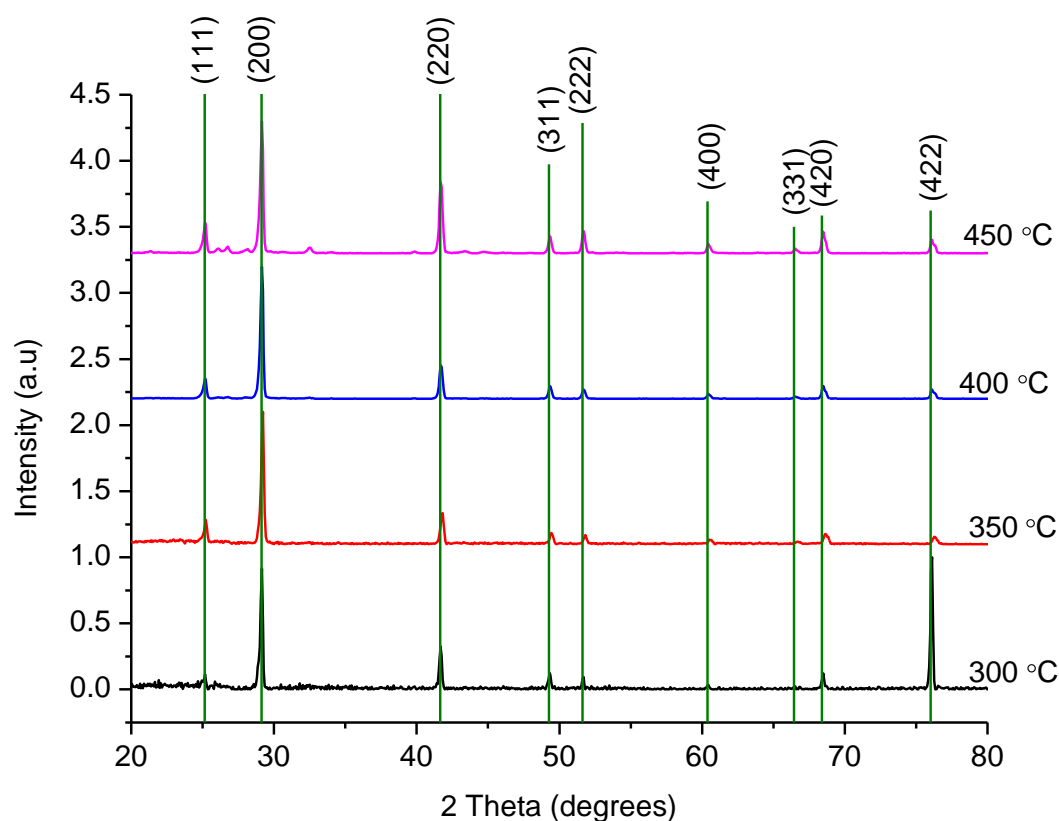


Figure 6.4. A stacked set of four p-XRD spectra showing the diffracting pattern of thin films deposited from $[Pb((SeP^iPr_2)_2N(S_2CNHexMe))]$ complex at 300, 350, 400 and 450 °C.

6.3.2.2 SEM images of thin films

6.3.2.2.1 SEM images of thin films deposited from $[Pb((SeP^iPr_2)(SP^iPr_2)N)_2]$ by AACVD.

Scanning electron microscope (SEM) images of thin films deposited from $[Pb((SeP^iPr_2)(SP^iPr_2)N)_2]$ by AACVD (Figure 6.5) reveal that at 300 °C, the thin films show isolated particles of disordered cubic lead chalcogenide crystallites. As temperature increased, regular shaped particles were obtained until at 450 °C when the particles began to denature. Energy dispersive X-ray spectroscopy (EDAX) (Figure 6.6) quantification on the thin films indicated no sulphur present at 300 °C and 450 °C. However, at 350 °C and 400 °C, sulphur was present. At 350 °C, sulphur was found to be 1.75 % by atom whilst lead and selenium were found to be 78.33 % and 20.01 % respectively. At 400 °C, sulphur was found

to be 3.12 % by atom whilst lead and selenium were found to be 46.47 % and 50.42 % respectively. The absence of sulphur at 300 °C may be attributed to the scattered nature of the particles at that temperature, thereby making it difficult for EDAX to detect and quantify sulphur. Also, the determination of low levels of sulphur in the presence of large amounts of lead is difficult due to the closeness of the sulphur K lines and the lead M lines resulting in poor resolution of these lines by EDAX (SWGGSR, 2011). The absence of sulphur at 450 °C confirms the observation made from the results of the p-XRD.

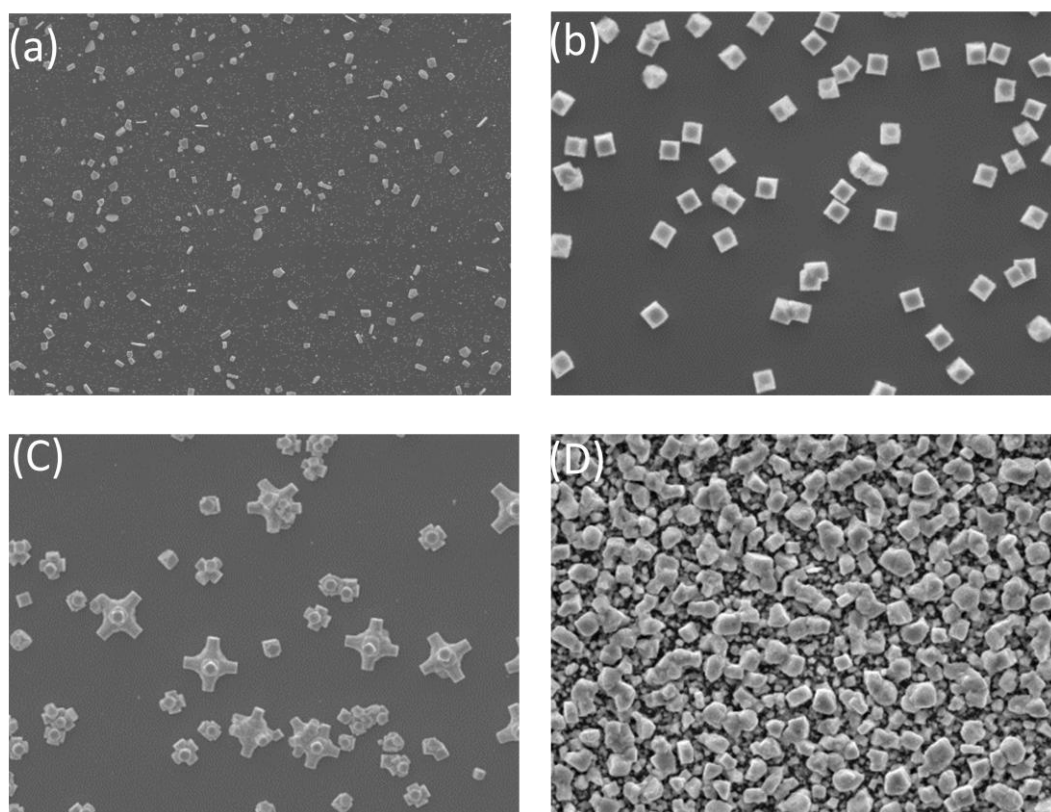


Figure 6.5 SEM images 5000x magnification of thin films deposited from $[Pb((SeP^iPr_2)(SP^iPr_2)N)_2]$ at A. 300 °C, B. 350 °C, C. 400 °C and D. 450 °C

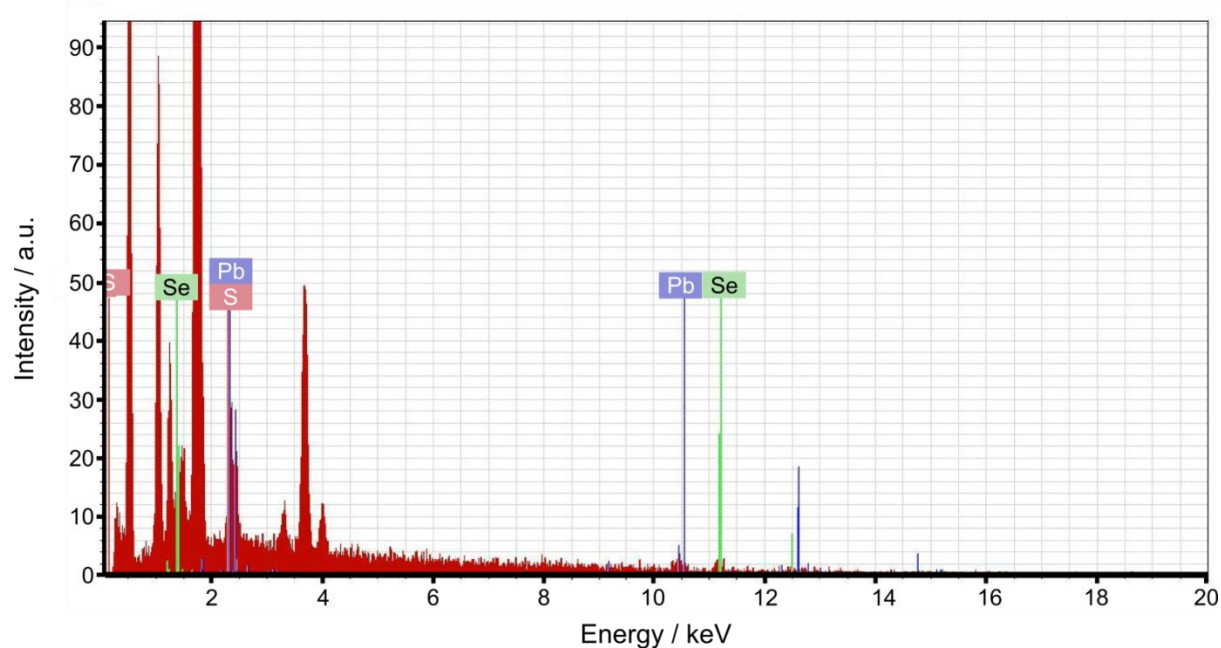


Figure 6.6 EDAX spectrum of thin films deposited from $[Pb((SeP^iPr_2)(SP^iPr_2)N)_2]$

6.3.2.2.2 SEM images of thin films deposited from $[Pb((SeP^iPr_2)_2N(S_2CNEt_2)_2)]$ by AACVD.

Scanning electron microscope (SEM) images of thin films deposited from $[Pb((SeP^iPr_2)_2N(S_2CNEt_2)_2)]$ by AACVD at 300 °C, 350 °C, 400 °C and 450 °C (Figure 6.7) show cubic lead chalcogenide crystals for the deposits at all temperatures. Energy dispersive X-ray spectroscopy (EDAX) quantification on the thin films (Figure 6.8) indicated 0.03 % sulphur present at 300 °C. However, at higher temperatures, there was no sulphur present. The absence of sulphur at 450 °C may be as a result of the high temperature breaking the Pb-S bond and thereby causing the sulphur to volatilize.

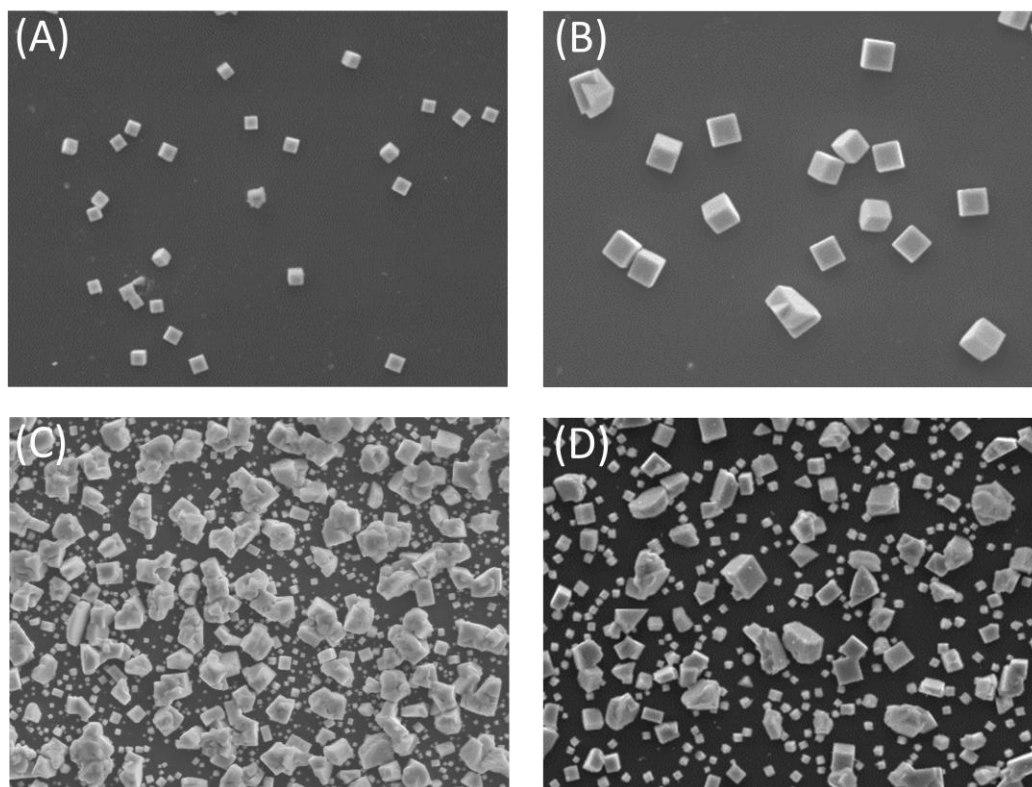


Figure 6.7 SEM images 5000x magnification of thin films deposited from $[Pb((SeP^I Pr_2)_2 N(S_2 C N E t_2))]]$ at A. 300 °C, B. 350 °C, C. 400 °C and D. 450 °C.

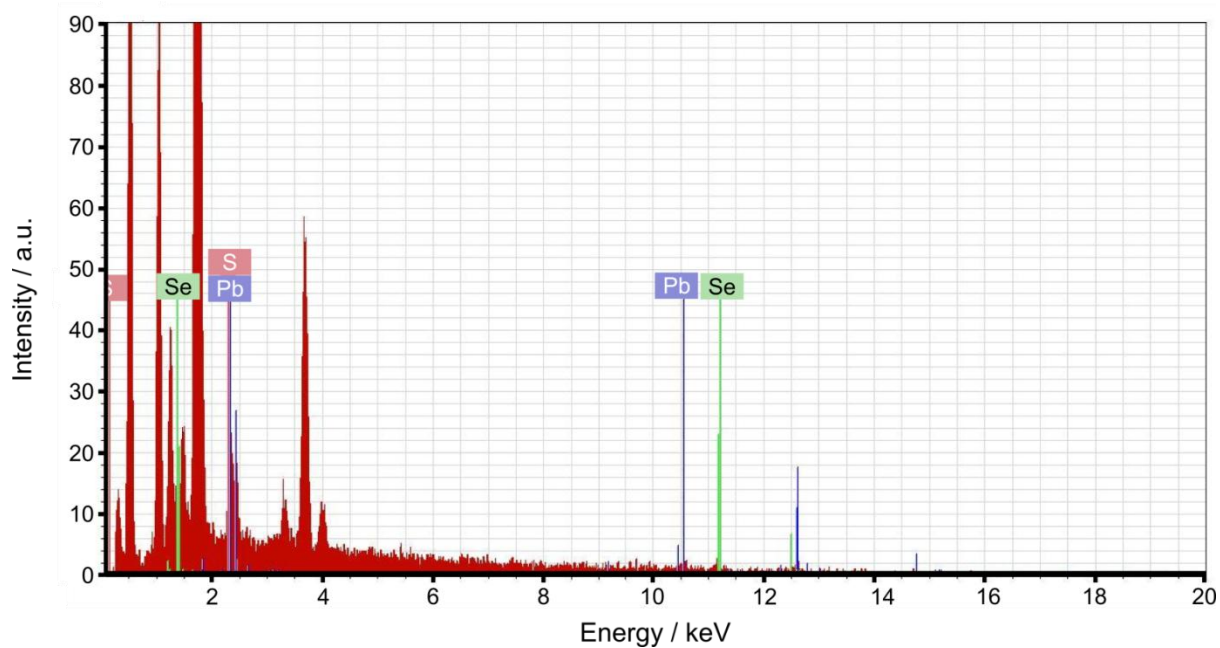


Figure 6.8 EDAX spectrum of thin films deposited from $[Pb((SeP^I Pr_2)_2 N(S_2 C N E t_2))]]$

6.3.2.2.3 SEM images of thin films deposited from $[Pb((SeP^iPr_2)_2N(S_2CNHexMe))]$ by AACVD.

Scanning electron microscope (SEM) images of thin films deposited from $[Pb((SeP^iPr_2)_2N(S_2CNHexMe))]$ by AACVD at 300 °C, 350 °C, 400 °C and 450 °C (Figure 6.9) show cubic lead chalcogenide crystals for the deposits at all temperatures. Energy dispersive X-ray spectroscopy (EDAX) quantification on the thin films (Figure 6.10) showed traces (0.01 %) sulphur present at 300 °C. However, at higher temperatures, there was no sulphur present. The thin films deposited at all temperatures can therefore be said to be predominantly lead selenide.

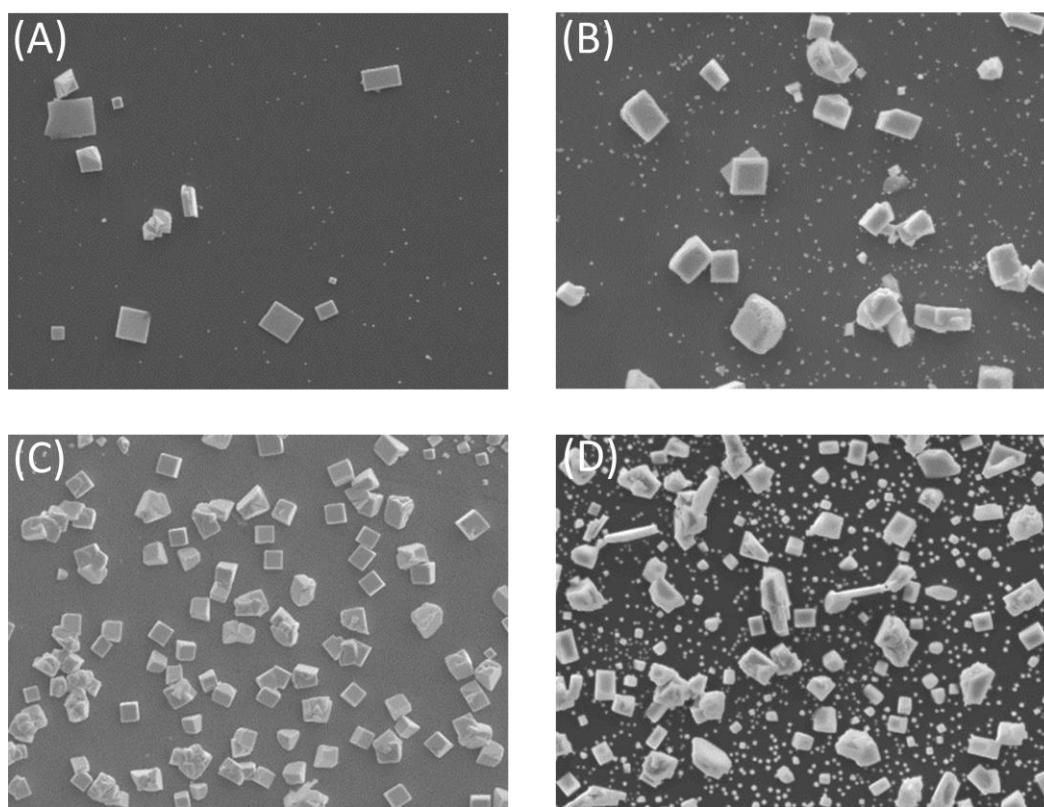


Figure 6.9 SEM images 5000x magnification of thin films deposited from $[Pb((SeP^iPr_2)_2N(S_2CNHexMe))]$ at A. 300 °C, B. 350 °C, C. 400 °C and D. 450 °C.

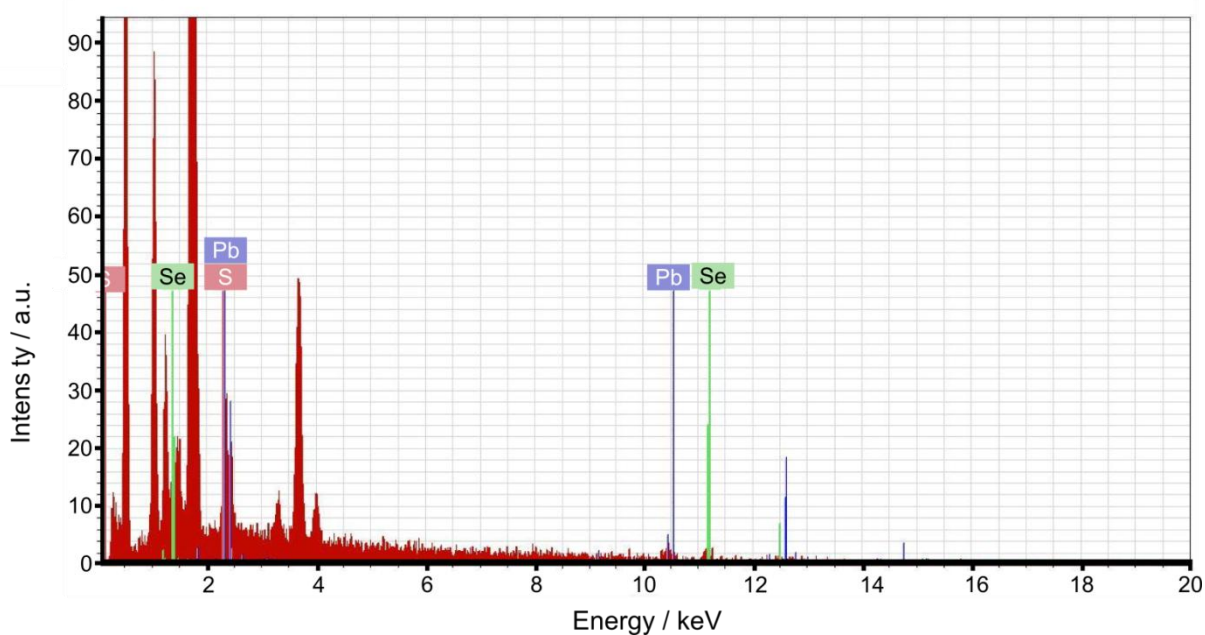


Figure 6.10 EDAX spectrum of thin films deposited from $[Pb((SeP^iPr_2)_2N(S_2CNHexMe))]$

6.3.2.3 Effect of temperature on particle size distribution for PbS_xSe_{1-x} thin films from $[Pb((SeP^iPr_2)(SP^iPr_2)N)_2]$, $[Pb((SeP^iPr_2)N(S_2CNEt_2))]$, $[Pb((SeP^iPr_2)N(S_2CNHexMe))]$

The particle sizes of thin films produced were measured from the SEM images using image j software. A plot of mean particle sizes \pm standard deviation against temperature is shown in Figures 6.11, 6.12 and 6.13 below. The bars indicate the non-uniformity of the sizes of particles at a set temperature. The effect of temperature on the particle size distribution for PbS_xSe_{1-x} thin films from $[Pb((SeP^iPr_2)(SP^iPr_2)N)_2]$ is shown in Figure 6.11. The particle size increased from 300 to 350 °C and reduced at 400 °C. It however increased marginally at 450 °C. The formation of crystalline particles increases with increasing temperature (Cavicchioli et al., 2005; Kim et al., 2009). As the temperature goes beyond the threshold, the particles begin to disintegrate and also agglomerate. The particle size distribution indicates that the threshold temperature for the formation of the crystals was 350 °C. The plot suggests that the

particles disintegrated as the temperature increased to 400 °C and began to agglomerate as the temperature was increased.

A similar trend was observed in Figure 6.12 which shows the effect of temperature on the particle size distribution for PbS_xSe_{1-x} thin films from $[Pb((SeP^iPr_2)N(S_2CNEt_2))]$. The particle size increased from 300 to 350 °C and reduced at 400 °C. It however increased at 450 °C.

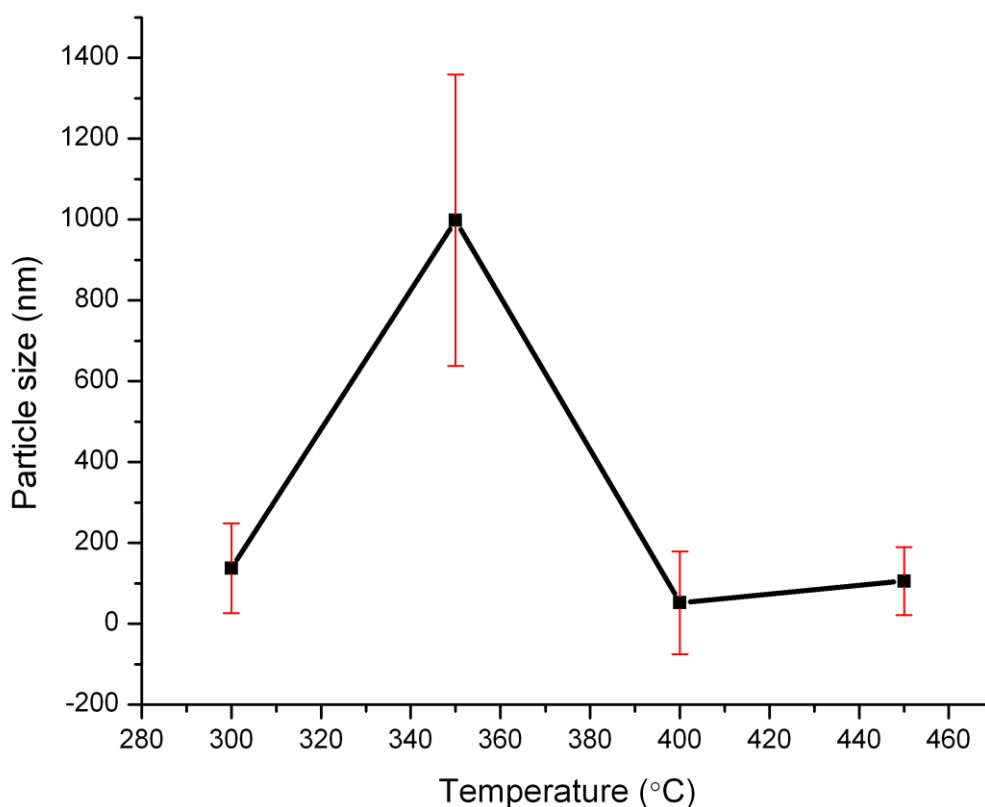


Figure 6.11 A graph of particle size against temperature for PbS_xSe_{1-x} thin films deposited from $[Pb((SeP^iPr_2)(SP^iPr_2)N)_2]$

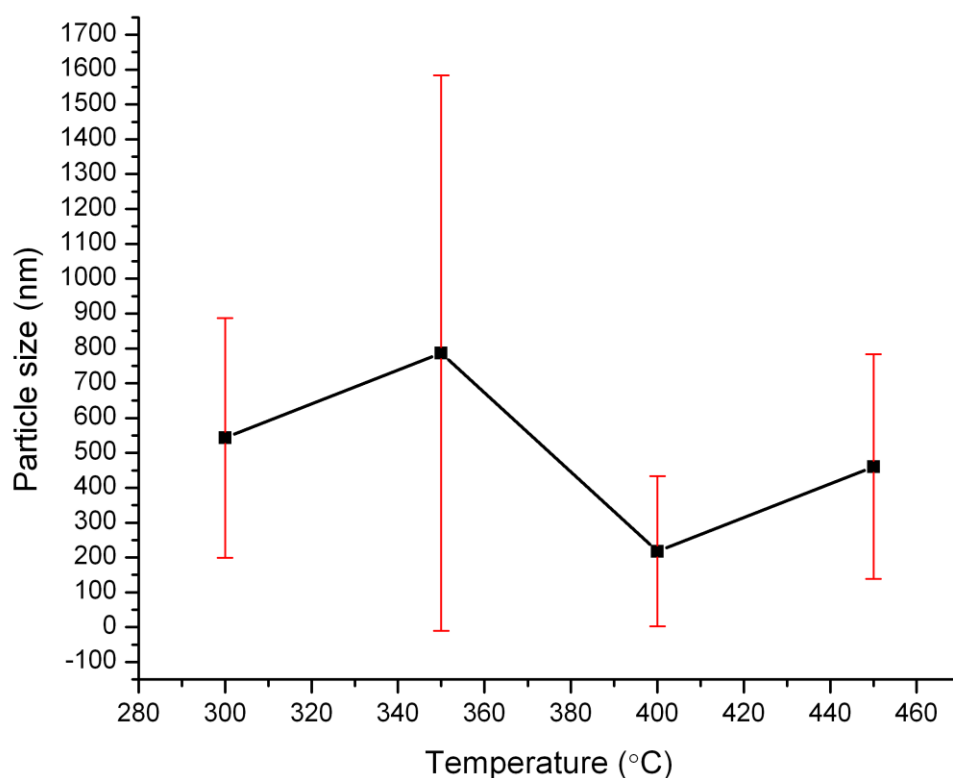


Figure 6.12 A graph of particle size against temperature for PbS_xSe_{1-x} thin films deposited from $[Pb((SeP^iPr_2)N(S_2CNEt_2))]$

The particle sizes of PbS_xSe_{1-x} thin films deposited from $[Pb((SeP^iPr_2)_2N(S_2CNHexMe))]$ (Figure 6.13) decreased from 300 to 350 °C and reduced further at 400 °C. It however increased at 450 °C. From the graph, the mean particle sizes at the various temperatures all fell within a range of 100 to 400 nm. The increase in particle size from 400 °C increased to 450 °C may be due to agglomeration.

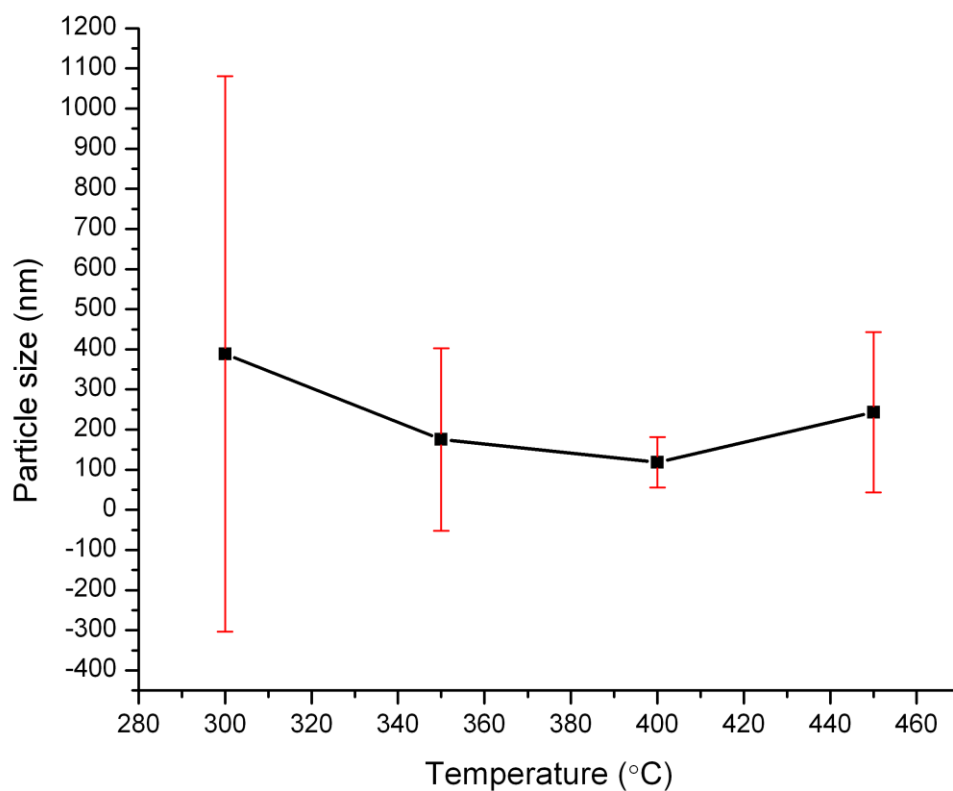


Figure 6.13 A graph of particle size against temperature for PbS_xSe_{1-x} thin films deposited from $[Pb((SeP^iPr_2)N(S_2HexMe))]$

6.3.3 Comparison of PbSe thin films obtained from Single-source precursors suitable for depositing binary and ternary lead chalcogenides.

PbSe thin films deposited by AACVD at 450 °C from different Single-source precursors suitable for the deposition of binary and ternary lead chalcogenides have been compared and shown in table 1.

Table 6.1 Comparison of PbSe thin films obtained at 450 °C from Single-source precursors suitable for depositing binary and ternary lead chalcogenides.

Compound complex	PbSe [Pb((SeP ⁱ Pr ₂) ₂ N) ₂] (1)	PbSe [Pb((SeP ⁱ Pr ₂)(SP ⁱ Pr ₂)N) ₂] (2)	PbSe [Pb((Se ₂ P ⁱ Pr ₂ N)(S ₂ CNEt ₂))] (3)	PbSe [Pb((Se ₂ P ⁱ Pr ₂ N)(S ₂ CNHexMe))] (3)
TGA (%)	20.7 (28.1)	25.9 (28.3)	33.2 (34.5)	32.0 (32.7)
Average particle size (nm)	178.58	105.90	460.82	243.51
EDAX (%)	Pb-70 Se-30	Pb-58 Se-42	Pb-69 Se-31	Pb-48 Se-52

From the table it can be observed that the percentage residue obtained for all the complexes from the thermogravimetric analysis were below the theoretical value. This may be due to the volatility of PbSe at elevated temperatures.

The average particle size for PbSe from [Pb((SePⁱPr₂)₂N)₂] **(1)** was bigger than that obtained from [Pb((SePⁱPr₂)(SPⁱPr₂)N)₂] **(2)**. The presence of the two sulphur atoms in [Pb((SePⁱPr₂)(SPⁱPr₂)N)₂] reduces the selenium content relative to [Pb((SePⁱPr₂)₂N)₂] which has four selenium atoms. The loss of sulphur during deposition at high temperature therefore reduces the particle size.

The particle size for PbSe from [Pb((SePⁱPr₂)₂N(S₂CNEt₂))] **(3)** was larger than that of [Pb((SePⁱPr₂)₂N(S₂CNHexMe)₂)] **(4)**. The smaller particles for PbSe from [Pb((SePⁱPr₂)₂N(S₂CNHexMe)₂)] relative to [Pb((SePⁱPr₂)₂N(S₂CNEt₂))] may be due to the effect of the long alkyl chain (Yamamoto and Nakamoto, 2003).

The energy dispersive X-ray analysis (EDAX) for all the complexes indicated the presence of only lead and selenium. It can be observed from the EDAX that as the percentage of lead increases, the particle size also increases. This is due to the large atomic radius of lead relative to selenium.

6.3.4 Pyrolysis of $[Pb((SeP^iPr_2)_2N(S_2CNEt_2))_2]$

Pyrolysis of mixed $[Pb((SeP^iPr_2)_2N(S_2CNEt_2))_2]$ at 600 °C in inert gas deposited black powdery residue which was dispersed in toluene. The dispersed sample was deposited on glass substrate as a thin film.

6.3.4.1 Powder XRD of pyrolysed mixed $[Pb((SeP^iPr_2)_2N(S_2CNEt_2))_2]$

Powder XRD analysis of the pyrolysed sample (Figure 6.14) indicated the cubic PbSe (ICDD 04-004-4328) phase instead of the expected PbS_xSe_{1-x} . The strong (200) peak suggests a (100) oriented growth. DFT calculations on the decomposition of a mixed ligand single-source lead complex (Akhtar *et al.*, 2011b) concluded that the formation of PbSe may involve more than one mechanism but, the steps that lead to the formation of PbSe are more favourable on thermodynamic grounds, than those that lead to PbS formation. These conclusions agree with our findings.

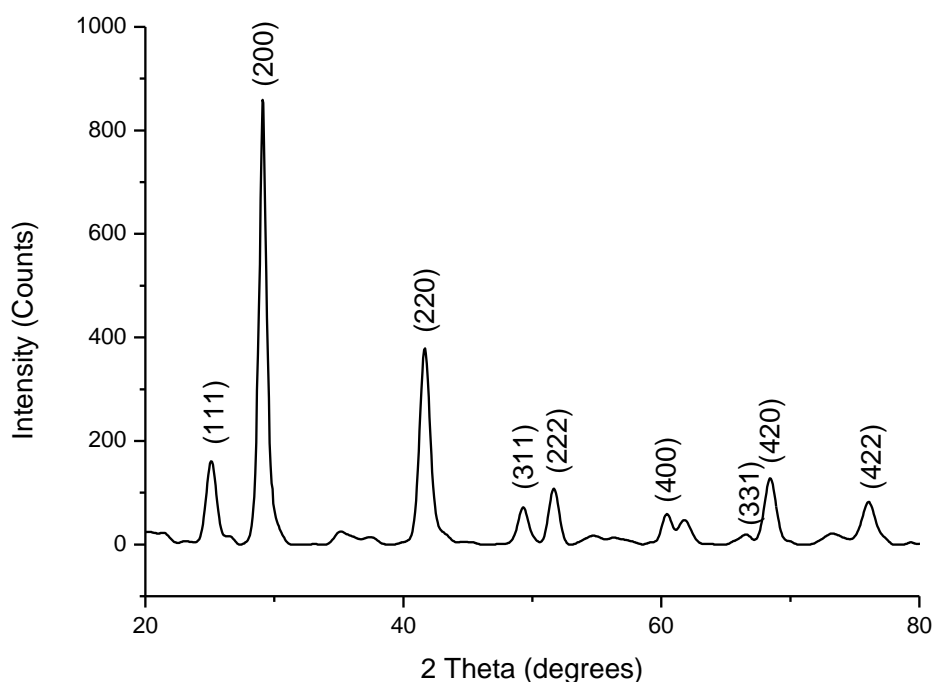


Figure 6.14 p-XRD of thin films synthesised from $[Pb((SeP^iPr_2)_2N)(S_2CNET_2)]$ indicating a PbSe phase.

6.3.4.1.1 SEM analysis of pyrolysed $[Pb((SeP^iPr_2)_2N)(S_2CNET_2)]$

Scanning electron microscope (SEM) images (Figure 6.15) reveal that the deposit shows clusters of disordered cubic PbSe crystallites. The average particle size measured from SEM image was 119.7 nm. The particle size distribution fell within a range of 38.8 – 727.4 nm. Energy dispersive X-ray spectroscopy (EDAX) analysis (Figure 6.16) on the thin film indicated no sulphur present. Lead (Pb) was found to be 72.03 % and selenium, 27.82 %. A trace of phosphorus accumulated (0.14 %) during the decomposition of the complex was found.

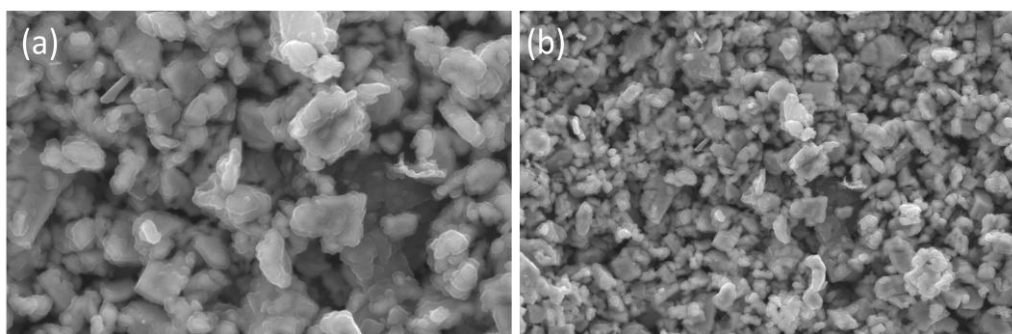


Figure 6.15 SEM images of mixed $[Pb((SeP^iPr_2)_2N(S_2CNEt_2))]$ at (a) 10000x and (b) 5000x magnification

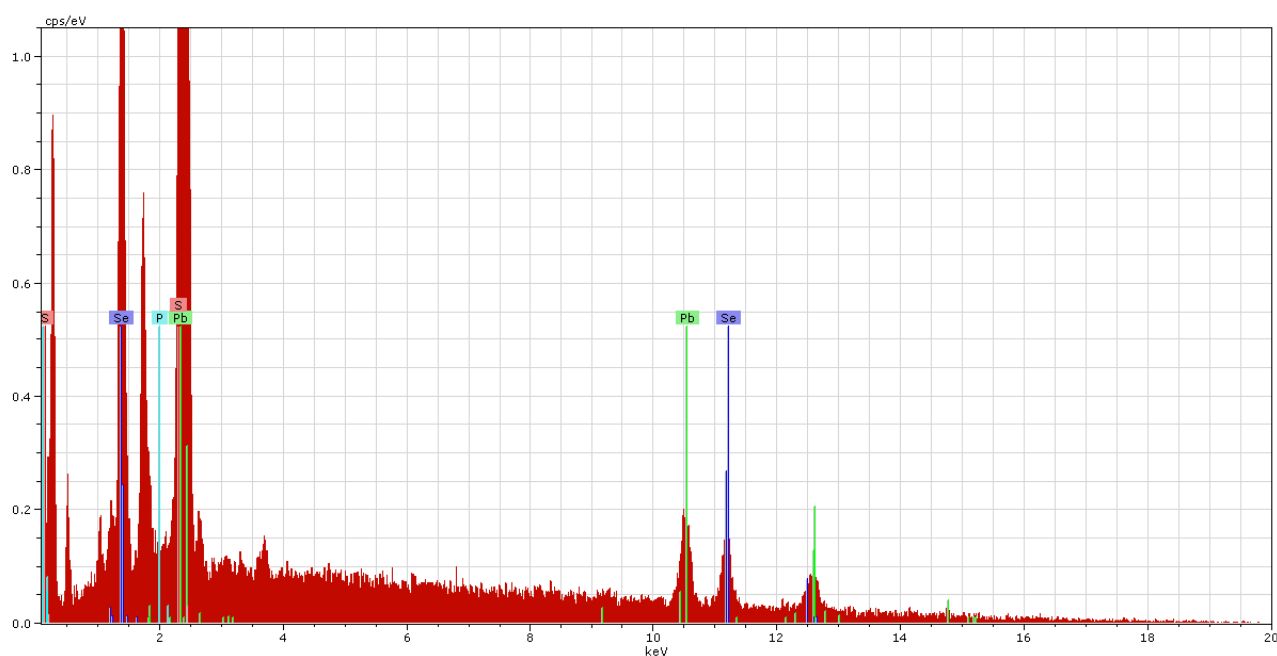


Figure 6.16 EDAX spectrum of mixed $[Pb((SeP^iPr_2)_2N(S_2CNEt_2))]$

6.4 Conclusion

Three complexes, $[Pb((SeP^iPr_2)(SP^iPr_2)N)_2]$, $[Pb((SeP^iPr_2)_2N(S_2CNEt_2))]$ and $[Pb((SeP^iPr_2)_2N(S_2CNHexMe))]$ have been used to deposit lead chalcogenide thin films by AACVD. The thin films were characterised by using p-XRD, SEM and EDAX. The results for the thin films deposited from all three complexes showed the formation of PbS_xSe_{1-x} at

lower temperatures (300 °C to 350 °C) and PbSe at higher temperatures (400 °C to 450 °C). PbSe thin films deposited by AACVD at 450 °C from different Single-source precursors suitable for the deposition of binary and ternary lead chalcogenides have been compared. The particle sizes of the thin films were found to increase as the percentage of elemental lead increased with respect to selenium. $[Pb((SeP^iPr_2)_2N(S_2CNEt_2))]$ complex was also pyrolysed at 600 °C in inert gas (N_2) to produce lead chalcogenide nanoparticles. Powder X-ray diffraction (p-XRD) of the deposited material corresponds to cubic PbSe (ICDD No. 04-004-4328). Energy dispersive X-ray spectroscopy (EDAX) analysis showed no Sulphur peaks. However, a trace of phosphorus accumulated during the decomposition of the complex was found.

Chapter 7

Summary and conclusions

In this thesis, synthesis of lead chalcogenide nanocrystals (NCs) and thin films have been described. Section 7.1 contains a short summary of research work. The conclusion drawn from this research work is described in section 7.2.

7.1 Summary

Lead chalcogenides PbE (E = S, Se, Te) are important semiconductor materials, which have found applications in optoelectronic devices. Lead chalcogenide as thin films and nanocrystals have received considerable interest in low-cost photovoltaic devices. The work described in this thesis deals with the synthesis of Single-source precursors, the controlled colloidal synthesis of binary nanocrystals by hot injection method and the preparation of binary and ternary lead chalcogenide thin films by Aerosol Assisted Chemical Vapour Deposition (AACVD) and pyrolysis using the Single-source precursors synthesised. Chapter one gives a general introduction underlining the interest and the aims of this work. Chapter two reviews literature that defines the main notions used throughout this study and summarises the scientific knowledge related to the subjects mentioned in this thesis. Chapter three gives all the details necessary to understand the experiments performed and eventually how to reproduce them.

Chapter four is the first result chapter, regarding the synthesis of binary lead chalcogenide nanoparticles and thin films. In Chapter four, *bis*(diisopropyl(dithio/diseleno)phosphinato) lead (II) complexes were synthesised and characterised. These complexes were used to

synthesize PbSe or PbS nanocrystals by solution thermolysis and to deposit PbSe and PbS thin films by aerosol assisted chemical vapour deposition (AACVD). Chapter five is the second result chapter in which the syntheses of Single-source precursors suitable for making ternary lead chalcogenide nanoparticles and thin films are investigated. In this chapter, potential Single-source precursors suitable for the synthesis of ternary lead chalcogenide nanocrystals and thin films were prepared. The process involved the reaction between a lead selenide rich Single-source precursor and a lead sulphide rich Single-source precursor, to produce a ternary lead chalcogenide Single-source precursor. Chapter 6 discusses the synthesis of $\text{PbS}_x\text{Se}_{1-x}$ thin films by aerosol assisted chemical vapour deposition. The complexes synthesised in Chapter five were used to deposit lead chalcogenide thin films by AACVD. $[\text{Pb}((\text{SeP}^i\text{Pr}_2)_2\text{N})(\text{S}_2\text{CNEt}_2)]$ complex was also pyrolysed and the residue used to produce lead chalcogenide thin films.

7.2 Conclusion

A number of lead complexes of type, imidodiisopropyldithio-, diseleno- and thioseleno-phosphinato have been synthesised and used as complexes for the deposition of binary PbS and PbSe thin films by AACVD. The nanocrystals of PbS and PbSe were also synthesised by using the hot injection method. The synthesis was done in trioctylphosphine/oleylamine.

Three new mixed lead chalcogenide Single-source precursors suitable for making $\text{PbS}_x\text{Se}_{1-x}$ nanoparticles and thin films have been successfully synthesised. They are $[\text{Pb}((\text{SeP}^i\text{Pr}_2)(\text{SP}^i\text{Pr}_2)\text{N})_2]$, $[\text{Pb}((\text{SeP}^i\text{Pr}_2)_2\text{N})(\text{S}_2\text{CNEt}_2)]$ and $[\text{Pb}((\text{SeP}^i\text{Pr}_2)_2\text{N})(\text{S}_2\text{CNHexMe})]$. The complexes have been characterised and their crystal structures obtained. These complexes have been used to deposit lead chalcogenide thin films by AACVD. The thin films deposited from all three complexes showed the formation of $\text{PbS}_x\text{Se}_{1-x}$ at temperatures

ranging from 300 °C to 400 °C and PbSe at 450 °C. Pyrolysis of [Pb((SePⁱPr₂)₂N)(S₂CNEt₂)] at 600 °C under nitrogen yielded pure PbSe nanoparticles.

7.3 Future work

The complexes suitable for the synthesis of ternary lead chalcogenide thin films (PbS_xSe_{1-x}) described in the thesis could be used to synthesise lead chalcogenide nanoparticles by hot injection method.

Since alloyed semiconductor nanomaterials provide an alternative approach to band gap control, the alloyed materials prepared in this work (PbS/ PbSe/ PbS_xSe_{1-x}) could be investigated for their multiple exciton generation (MEG) properties. These studies would be helpful for fabricating solar cells with enhanced efficiency.

References

- Acharya, S., Gautam, U.K., Sasaki, T., Bando, Y., Golan, Y. and Ariga, K. (2008), “Ultra narrow PbS nanorods with intense fluorescence.”, *Journal of the American Chemical Society*, Vol. 130 No. 14, pp. 4594–4595.
- Afzaal, M., Crouch, D., Malik, M.A., Motevalli, M., O’Brien, P. and Park, J.-H. (2003), “Deposition of CdSe thin films using a novel single-source precursor; [MeCd{(SePⁱPr₂)₂N}]₂”, *Journal of Materials Chemistry*, Vol. 13 No. 4, pp. 639–640.
- Afzaal, M., Ellwood, K., Pickett, N., O’Brien, P., Raftery, J. and Waters, J. (2004), “Growth of lead chalcogenide thin films using single-source precursors”, *Journal of Materials Chemistry*, Vol. 14, pp. 1310–1315.
- Afzaal, M. and O’Brien, P. (2006), “Recent developments in II-VI and III-VI semiconductors and their applications in solar cells”, *Journal of Materials Chemistry*, Vol. 16 No. 17, p. 1597.
- Akhtar, J., Afzaal, M., Banski, M., Podhorodecki, A., Syperek, M., Misiewicz, J., Bangert, U., and O'Brien, P. (2011a), “Controlled synthesis of tuned bandgap nanodimensional alloys of PbS(x)Se(1-x).”, *Journal of the American Chemical Society*, Vol. 133 No. 14, pp. 5602–5609.
- Akhtar, J., Afzaal, M., Vincent, M.A., Burton, N.A., Hillier, I.H. and O’Brien, P. (2011d), “Low temperature CVD growth of PbS films on plastic substrates.”, *Chemical communications (Cambridge, England)*, Vol. 47 No. 7, pp. 1991–1993.

- Akhtar, J., Afzaal, M., Vincent, M.A., Burton, N.A., Raftery, J., Hillier, I.H. and O'Brien, P. (2011b), "Understanding the Decomposition Pathways of Mixed Sulfur/Selenium Lead Phosphinato Complexes Explaining the Formation of Lead Selenide", *The Journal of Physical Chemistry C*, Vol. 115 No. 34, pp. 16904–16909.
- Akhtar, J., Malik, M.A., Stubbs, S.K., O'Brien, P., Helliwell, M. and Binks, D.J. (2011c), "Morphology-Tailored Synthesis of PbSe Nanocrystals and Thin Films from Bis[N,N-diisobutyl-N'-(4-nitrobenzoyl)selenoureato]lead(II)", *European Journal of Inorganic Chemistry*, Vol. 2011 No. 19, pp. 2984–2990.
- Alam, N., Hill, M.S., Kociok-ko, G., Zeller, M., Mazhar, M. and Molloy, K.C. (2008), "Pyridine Adducts of Nickel (II) Xanthates as Single-Source Precursors for the Aerosol-Assisted Chemical Vapor Deposition of Nickel Sulfide", *Chemistry of Materials*, Vol. 20, pp. 6157–6162.
- Albright, T., Burdett, J. and Whangbo, M. (2013), *Orbital interactions in chemistry*, John Wiley and Sons.
- Alivisatos, A.P., Ma, W., Luther, J.M., Zheng, H. and Wu, Y. (2009), "Photovoltaic devices employing ternary $\text{PbS}_x\text{Se}_{1-x}$ nanocrystals.", *Nano Letters*, American Chemical Society, Vol. 9 No. 4, pp. 1699–1703.
- Arif, A.M., Benac, B.L., Cowley, A.H., Geerts, R., Jones, R.A., Kidd, K.B., John, M., et al. (1986), "Mono- and Di-nuclear Phosphido and Arsenido Complexes of Gallium; $\text{Ga}(\text{EBu}_2)_3$, $\text{Ga}[\text{PH}(2,4,6\text{-But}_3\text{C}_6\text{H}_2)]_3$ and $[\text{Ga}(\mu\text{-EBu}_2)\text{R}_2]_2$, (E = P, As; R = Me, Bu)", *J. Chem. Soc., Chem. Commun.*, Vol. 1543, pp. 1543–1545.

- Asano, T., Song, B.-S. and Noda, S. (2006), “Analysis of the experimental Q factors (~ 1 million) of photonic crystal nanocavities.”, *Optics express*, Vol. 14 No. 5, pp. 1996–2002.
- Bakueva, L., Musikhin, S., Hines, M.A., Chang, T.-W.F., Tzolov, M., Scholes, G.D. and Sargent, E.H. (2003), “Size-tunable infrared (1000–1600 nm) electroluminescence from PbS quantum-dot nanocrystals in a semiconducting polymer”, *Applied Physics Letters*, Vol. 82 No. 17, p. 2895.
- Barkhouse, D.A.R., Pattantyus-Abraham, A.G., Levina, L. and Sargent, E.H. (2008), “Thiols passivate recombination centers in colloidal quantum dots leading to enhanced photovoltaic device efficiency.”, *ACS nano*, Vol. 2 No. 11, pp. 2356–2362.
- Beck-Broichsitter, M., Nicolas, J. and Couvreur, P. (2015), “Design attributes of long-circulating polymeric drug delivery vehicles.”, *European journal of pharmaceuticals and biopharmaceutics*, doi:10.1016/j.ejpb.2015.03.033.
- Bencherif, Y., Boukra, a., Zaoui, a. and Ferhat, M. (2011), “Lattice dynamics study of lead chalcogenides”, *Infrared Physics & Technology*, Elsevier B.V., Vol. 54 No. 1, pp. 39–43.
- Boadi, N.O., Malik, M.A., O’Brien, P. and Awudza, J.A.M. (2012), “Single source molecular precursor routes to lead chalcogenides.”, *Dalton transactions*, Vol. 41, pp. 10497–10506.
- Bode, D., Johnson, T.H. and McLean, B.. (1965), “Lead Selenide Detectors for Intermediate Temperature Operation”, *Applied optics*, Vol. 4 No. 3, pp. 327–331.

- Bolundut, L., Haiduc, I., Kociok-köhn, G. and Molloy, K.C. (2010), “Supramolecular Self-Assembly in The Lead(II) Bis(di-iso-butyldithiophosphate). 1,10-Phenanthroline Adduct, $\text{Pb}[\text{S}_2\text{P}(\text{OBui})_2]_2\cdot\text{Phen}$ ”, *Revue Roumaine De Chimie*, Vol. 55 No. 11-12, pp. 741–746.
- Boudjouk, P., Jarabek, B.R., Simonson, D. D.L., Seidler, D.J., Grier, D.G., Mccarthy, G.J. and Keller, L.P. (1998), “Metal bis (benzylthiolates): Efficient single source precursors to solid solutions and nanoparticles of metal sulfides”, *Chemistry of materials*, Vol. 10 No. 18, pp. 2358–2364.
- Bourdakos, K.N., Dissanayake, D.M.N.M., Lutz, T., Silva, S.R.P. and Curry, R.J. (2008), “Highly efficient near-infrared hybrid organic-inorganic nanocrystal electroluminescence device”, *Applied Physics Letters*, Vol. 92 No. 15, p. 153311.
- Briand, G., Chivers, T. and Parvez, M. (2002), “A new approach to metalated imido and amido tellurophosphoranes”, *Angewandte Chemie (International ed. in English)*, Vol. 41 No. 18, pp. 3468–3470.
- Bruchez Jr., M., Morome, M., Gin, P., Weiss, S. and Alivisatos, P.A. (1998), “Semiconductor Nanocrystals as Fluorescent Biological Labels”, *Science*, Vol. 281 No. 5385, pp. 2013–2016.
- Brumer, M., Kigel, A., Amirav, L., Sashchiuk, A., Solomesch, O., Tessler, N. and Lifshitz, E. (2005), “PbSe/PbS and PbSe/PbSe_xS_{1-x} Core/Shell Nanocrystals”, *Advanced Functional Materials*, Wiley-VCH, Vol. 15 No. 7, pp. 1111–1116.

- Brus, L.E. (1984), "Electron–electron and electron-hole interactions in small semiconductor crystallites: The size dependence of the lowest excited electronic state", *The Journal of Chemical Physics*, Vol. 80 No. 9, p. 4403.
- Cademartiri, L., Bertolotti, J., Sapienza, R., Wiersma, D.S., von Freymann, G. and Ozin, G.A. (2006), "Multigram scale, solventless, and diffusion-controlled route to highly monodisperse PbS nanocrystals.", *The journal of physical chemistry. B*, Vol. 110 No. 2, pp. 671–673.
- Calvert, P. (1999), "Nanotube composites: a recipe for strength", *Nature*, Vol. 399 No. May, pp. 210–211.
- Castro, J.R., Molloy, K.C., Liu, Y., Lai, C.S., Dong, Z., White, T.J. and Tiekink, E.R.T. (2008), "Formation of antimony sulfide powders and thin films from single-source antimony precursors", *Journal of Materials Chemistry*, Vol. 18 No. 44, p. 5399.
- Cauletti, C. and Cervone, E. (1973), "Some transition metal complexes with ethyldiselenoxanthogenate", *Journal of Inorganic and Nuclear Chemistry*, Vol. 35 No. 2, pp. 593–601.
- Cavicchioli, M., Varanda, L.C., Massabni, A.C. and Melnikov, P. (2005), "Silver nanoparticles synthesized by thermal reduction of a silver(I)–aspartame complex in inert atmosphere", *Materials Letters*, Vol. 59 No. 28, pp. 3585–3589.

- Chatterjee, A., Faktor, M., Moss, R. and White, E.A. (1982), "A Simplified Technique for MOCVD of III-IV Compounds", *J. Phys. Colloques*, Vol. 43, pp. 5491–5503.
- Chen, J., Chen, L. and Wu, L. (2007), "The solventless syntheses of unique PbS nanowires of x-shaped cross sections and the cooperative effects of ethylenediamine and a second salt", *Inorganic chemistry*, Vol. 46, pp. 8038–8043.
- Chen, J., Yang, B., Semendy, F., Clark III, W., Boyd, P. and Bambha, N. (1994), "MOCVD Growth and Characterisation of High-Quality Zne on GaAs", *Materials Research Society Symposium Proceedings*, Vol. 340, p. 2299.
- Chen, X., Lou, Y. and Burda, C. (2004), "Spectroscopic investigation of II–VI core-shell nanoparticles: CdSe/CdS", *International journal of nanotechnology*, Vol. 1 No. 1-2, pp. 105–118.
- Cheng, Y., Emge, T. and Brennan, J. (1996), "Pyridineselenolate Complexes of Tin and Lead: $\text{Sn}(2\text{-SeNC}_5\text{H}_4)_2$, $\text{Sn}(2\text{-SeNC}_5\text{H}_4)_4$, $\text{Pb}(2\text{-SeNC}_5\text{H}_4)_2$, and $\text{Pb}(3\text{-Me}_3\text{Si-2-SeNC}_5\text{H}_3)_2$. Volatile CVD Precursors to Group IV–Group VI Semiconductors", *Inorganic chemistry*, Vol. 35 No. 2, pp. 342–346.
- Chivers, T., Eisler, D.J. and Ritch, J.S. (2005), "Synthesis and structures of $\text{M}[\text{N}(\text{TePPr}^i_2)_2\text{-Te,Te}']_n$ ($n=2$, $\text{M}=\text{Zn}$, Cd , Hg ; $n=3$, $\text{M}=\text{Sb}$, Bi): the first ditelluroimidophosphinato p- and d-block metal complexes", *Dalton transactions*, pp. 2675–2677.
- Chivers, T., Eisler, D.J., Ritch, J.S. and Tuononen, H.M. (2005), "An unusual ditelluride: synthesis and molecular and electronic structures of the dimer of the tellurium-centered radical $[\text{TeP}^i\text{Pr}_2\text{N}^i\text{Pr}_2\text{P}^i\text{Te}]$.", *Angewandte Chemie (International ed. in English)*, Vol. 44 No. 31, pp. 4953–4956.

- Chivers, T., Ritch, J.S., Robertson, S.D., Konu, J. and Tuononen, H.M. (2010), “New insights into the chemistry of imidodiphosphinates from investigations of tellurium-centered systems.”, *Accounts of chemical research*, Vol. 43 No. 8, pp. 1053–1062.
- Cho, K. and Talapin, D. (2005), “Designing PbSe nanowires and nanorings through oriented attachment of nanoparticles”, *Journal of the American Chemical ...*, Vol. 127 No. 19, pp. 7140–7147.
- Choi, J.J., Lim, Y.-F., Santiago-Berrios, M.B., Oh, M., Hyun, B.-R., Sun, L., Bartnik, A.C., et al. (2009), “PbSe nanocrystal excitonic solar cells.”, *Nano letters*, American Chemical Society, Vol. 9 No. 11, pp. 3749–3755.
- Chopra, K.L., Paulson, P.D. and Dutta, V. (2004), “Thin-film solar cells: an overview”, *Progress in Photovoltaics: Research and Applications*, Vol. 12 No. 23, pp. 69–92.
- Clark, J.M., Kociok-Köhn, G., Harnett, N.J., Hill, M.S., Hill, R., Molloy, K.C., Saponia, H., et al. (2011), “Formation of PbS materials from lead xanthate precursors.”, *Dalton transactions (Cambridge, England : 2003)*, Vol. 40 No. 26, pp. 6893–6900.
- Claudio, E.S., Goldwin, H.A. and Magyar, J.S. (2003), “Fundamental coordination chemistry, environmental chemistry, and biochemistry of lead (II)”, *Progress in inorganic chemistry*, Vol. 51, p. 1.
- Cockayne, B. and Wright, P.J. (1984), “Metal Organic Chemical Vapour Deposition of Wide Band Gap II-VI Compounds.”, *Journal of Crystal Growth*, Vol. 68, pp. 223–230.
- Colvin, V., Schlamp, M. and Alivisatos, A. (1994), “Light-emitting diodes made from cadmium selenide nanocrystals and a semiconducting polymer”, *Nature*, Vol. 370, pp. 354–357.

- Contreras, M. and Egaas, B. (1999), “Progress toward 20% efficiency in Cu (In, Ga) Se₂ polycrystalline thin-film solar cells”, *Progress in Photovoltaics: Research and Applications*, Vol. 7, pp. 311–316.
- Cowley, A.H. and Jones, R.A. (1989), “Single-Source III/V Precursors: A New Approach to Gallium Arsenide and Related Semiconductors”, *Angewandte Chemie International Edition in English*, Vol. 28 No. 9, pp. 1208–1215.
- Crouch, D., O’Brien, P., Malik, M., Skabara, P.J. and Wright, S. (2003), “A one-step synthesis of cadmium selenide quantum dots from a novel single source precursor”, *Chemical communications (Cambridge, England)*, Vol. 1, pp. 1454–1455.
- Cui, D., Xu, J., Zhu, T., Paradee, G., Ashok, S. and Gerhold, M. (2006), “Harvest of near infrared light in PbSe nanocrystal-polymer hybrid photovoltaic cells”, *Applied Physics Letters*, Vol. 88 No. 18, p. 183111.
- Cupertino, D., Birdsall, D.J., Slawin, A.M.Z. and Woollins, J.D. (1999), “The preparation and coordination chemistry of Pr₂P(E)NHP(E')ⁱPr₂ (E, E' = Se; E = Se, E' = S; E = S, E' = O; E, E' = O)”, *Inorganica Chimica Acta*, Vol. 290, pp. 1–7.
- Cupertino, D., Keyte, R., Slawin, A.M.Z., Williams, D.J. and Woollins, J.D. (1996), “Preparation and Single-Crystal Characterisation of ⁱPr₂PSNHPSⁱPr₂ and Homoleptic [ⁱPr₂PSNPSⁱPr]⁻ Complexes of Zinc, Cadmium, and Nickel.”, *Inorganic chemistry*, Vol. 35 No. 9, pp. 2695–2697.
- Davidovich, R.L., Stavila, V. and Whitmire, K.H. (2010), “Stereochemistry of lead(II) complexes containing sulfur and selenium donor atom ligands”, *Coordination Chemistry Reviews*, Vol. 254 No. 17-18, pp. 2193–2226.

- Davies, R.P., Francis, C. V, Jurd, A.P.S., Martinelli, M.G., White, A.J.P. and Williams, D.J. (2004), "Coordination chemistry of diselenophosphinate complexes: the X-ray single-crystal structures of $[\text{K}(\text{Se}_2\text{PPh}_2)(\text{THF})_2]_2$ and $[\text{In}(\text{Se}_2\text{PPh}_2)_3]\cdot\text{L}$ (L = THF, PhMe).", *Inorganic chemistry*, Vol. 43 No. 16, pp. 4802–4804.
- Ding, B., Shi, M., Chen, F., Zhou, R., Deng, M., Wang, M. and Chen, H. (2009), "Shape-controlled syntheses of PbS submicro-/nano-crystals via hydrothermal method", *Journal of Crystal Growth*, Vol. 311 No. 6, pp. 1533–1538.
- Dorfner, D.F., Hürlimann, T., Abstreiter, G. and Finley, J.J. (2007), "Optical characterisation of silicon on insulator photonic crystal nanocavities infiltrated with colloidal PbS quantum dots", *Applied Physics Letters*, Vol. 91 No. 23, p. 233111.
- Douglass, I. (1937), "Acylselenoureas", *Journal of the American Chemical Society*, Vol. 59 No. 4, pp. 740–742.
- Dresselhaus, M.S. and Thomas, I.L. (2001), "Alternative energy technologies.", *Nature*, Vol. 414 No. 6861, pp. 332–337.
- Duchemin, J.P. (1981), "Low pressure CVD of III–V compounds", *Journal of Vacuum Science and Technology*, Vol. 18 No. 3, p. 753.
- Duchemin, J.P., Hersee, S., Razeghi, M. and Poisson, M.. (1985), "Metal Organic Chemical Vapor Deposition", *NATO ASI Series*, Vol. 87, pp. 677–719.
- Dusastre, V., Omar, B., Parkin, I. and Shaw, G. (1997), "Convenient, room-temperature, amine-assisted routes to metal sulfides, selenides and tellurides", *Journal of the Chemical Society, Dalton Transactions*, pp. 3505–3508.

- Ehrler, B., Walker, B.J., Böhm, M.L., Wilson, M.W.B., Vaynzof, Y., Friend, R.H. and Greenham, N.C. (2012), “In situ measurement of exciton energy in hybrid singlet-fission solar cells”, *Nature communications*, Vol. 3, p. 1019.
- Ellingson, R.R.J., Beard, M.C.M., Johnson, J.J.C., Yu, P., Micic, O.I., Nozik, A.J. and Shabaev, A.(2005), “Highly efficient multiple exciton generation in colloidal PbSe and PbS quantum dots.”, *Nano letters*, Vol. 5 No. 5, pp. 865–871.
- Englund, D., Fattal, D., Waks, E., Solomon, G., Zhang, B., Nakaoka, T., Arakawa, Y., et al. (2005), “Controlling the Spontaneous Emission Rate of Single Quantum Dots in a Two-Dimensional Photonic Crystal”, *Physical Review Letters*, Vol. 95 No. 1, p. 013904.
- Erk, C., Berger, A., Wendorff, J.H. and Schlecht, S. (2010), “Polymer-assisted preparation of nanoscale films of thermoelectric PbSe and PbTe and of lead chalcogenide-polymer composite films”, *Dalton Transactions*, Vol. 39, pp. 11248–11254.
- Fan, D., Afzaal, M., Mallik, M.A., Nguyen, C.Q., O’Brien, P. and Thomas, P.J. (2007), “Using coordination chemistry to develop new routes to semiconductor and other materials”, *Coordination Chemistry Reviews*, Vol. 251 No. 13-14, pp. 1878–1888.
- Fritz, K.P., Guenes, S., Luther, J., Kumar, S., Sariciftci, N.S. and Scholes, G.D. (2008), “IV–VI Nanocrystal–polymer solar cells”, *Journal of Photochemistry and Photobiology A: Chemistry*, Vol. 195 No. 1, pp. 39–46.
- “Front Cover Picture: Laser & Photon. Rev. 7(1)/2013.” (2013), *Laser & Photonics Reviews*, Vol. 7 No. 1, p. NA–NA.

- Fu, H. and Tsang, S.-W.S. (2012), “Infrared colloidal lead chalcogenide nanocrystals: synthesis, properties, and photovoltaic applications.”, *Nanoscale*, Vol. 4 No. 7, pp. 2187–201.
- Fushman, I., Englund, D. and Vučković, J. (2005), “Coupling of PbS quantum dots to photonic crystal cavities at room temperature”, *Applied Physics Letters*, Vol. 87 No. 24, p. 241102.
- Ghobadi, N. (2013), “Band gap determination using absorption spectrum fitting procedure”, *International Nano Letters*, Vol. 3 No. 1, p. 2.
- Gillespie, R.. and Nyholm, R.. (1957), “Inorganic stereochemistry”, *Quarterly Reviews, Chemical Society*, Vol. 11 No. 4, pp. 339–380.
- Grätzel, M. (2001), “Photoelectrochemical cells.”, *Nature*, Vol. 414 No. 6861, pp. 338–344.
- Gur, I., Fromer, N.A., Chen, C.-P., Kanaras, A.G. and Alivisatos, A.P. (2007), “Hybrid solar cells with prescribed nanoscale morphologies based on hyperbranched semiconductor nanocrystals.”, *Nano letters*, Vol. 7 No. 2, pp. 409–414.
- Hagihara, H., Watanabe, Y. and Yamashita, S. (1968), “The crystal structure of lead n-butylxanthate. I. Disordered structure”, *Acta Crystallographica Section B Structural Crystallography and Crystal Chemistry*, International Union of Crystallography, Vol. 24 No. 7, pp. 960–966.
- Haiduc, I. (2001), “Thiophosphorus and related ligands in coordination, organometallic and supramolecular chemistry. A personal account”, *Journal of Organometallic Chemistry*, Vol. 623 No. 1-2, pp. 29–42.

- Haiduc, I. and Sowerby, D. (1996), “Stereochemical Aspects of Phosphor-1,1-dithiolato metal complexes: coordination patterns, molecular structures and supramolecular associations in dithiophosphinates and related compounds”, *Polyhedron*, Vol. 15 No. 15, pp. 2469–2521.
- Haiduc, I., Sowerby, D. and Lu, S. (1995), “Stereochemical aspects of phosphor-1, 1-dithiolato metal complexes (dithiophosphates, dithiophosphinates): Coordination patterns, molecular structures”, *Polyhedron*, Vol. 14 No. 23-24, pp. 3389–3472.
- Hansen, J.A., Wang, J., Kawde, A.-N., Xiang, Y., Gothelf, K. V and Collins, G. (2006), “Quantum-dot/aptamer-based ultrasensitive multi-analyte electrochemical biosensor.”, *Journal of the American Chemical Society*, Vol. 128 No. 7, pp. 2228–2229.
- Harman, T.C., Taylor, P.J., Walsh, M.P. and Laforge, B.E. (2002), “Quantum Dot Superlattice Thermoelectric Materials and Devices”, *Science*, Vol. 297 No. 5590, pp. 2229–2232.
- He, Y. and Wang, R.K. (2004), “Dynamic optical clearing effect of tissue impregnated with hyperosmotic agents and studied with optical coherence tomography.”, *Journal of biomedical optics*, Vol. 9 No. 1, pp. 200–206.
- Heard, P. (2005), “Main group dithiocarbamate complexes”, *Progress in inorganic chemistry*, Vol. 53, pp. 1–70.
- Heath, J.R. and Shiang, J.J. (1998), “Covalency in semiconductor quantum dots”, *Chemical Society reviews*, Vol. 27, pp. 65–71.

- Hines, M.A. and Scholes, G.D. (2003), “Colloidal PbS Nanocrystals with Size-Tunable Near-Infrared Emission: Observation of Post-Synthesis Self-Narrowing of the Particle Size Distribution”, *Advanced Materials*, Vol. 15 No. 21, pp. 1844–1849.
- Hollingsworth, J.A., Banger, K.K., Jin, M.H.-C., Harris, J.D., Cowen, J.E., Bohannon, E.W., and Switzer, J.A. (2003), “Single source precursors for fabrication of I–III–VI₂ thin-film solar cells via spray CVD”, *Thin Solid Films*, Vol. 431-432, pp. 63–67.
- Holloway, C. and Melnik, M. (1997), “Lead coordination and organometallic compounds: classification and analysis of crystallographic and structural data”, *Main Group Metal Chemistry*, Vol. 20, pp. 399–495.
- House, J.E. (2008), *Inorganic Chemistry*, Elsevier.
- Hsu, K.F., Loo, S., Guo, F., Chen, W., Dyck, J.S., Uher, C., and Hogan, T. (2004), “Cubic AgPb(m)SbTe(2+m): bulk thermoelectric materials with high figure of merit.”, *Science (New York, N.Y.)*, Vol. 303 No. 5659, pp. 818–821.
- Huynh, W.U., Dittmer, J.J. and Alivisatos, A.P. (2002), “Hybrid nanorod-polymer solar cells.”, *Science (New York, N.Y.)*, Vol. 295 No. 5564, pp. 2425–2427.
- Hyun, B.-R., Chen, H., Rey, D.A., Wise, F.W. and Batt, C.A. (2007), “Near-infrared fluorescence imaging with water-soluble lead salt quantum dots.”, *The journal of physical chemistry. B*, Vol. 111 No. 20, pp. 5726–5730.
- Jiang, X., Schaller, R.D. and Lee, S. (2007), “PbSe nanocrystal/conducting polymer solar cells with an infrared response to 2 micron”, *Journal of Materials Research*, Vol. 22 No. 8, pp. 2204–2210.

- Johnston, K.W., Pattantyus-Abraham, A.G., Clifford, J.P., Myrskog, S.H., MacNeil, D.D., Levina, L. and Sargent, E.H. (2008), “Schottky-quantum dot photovoltaics for efficient infrared power conversion”, *Applied Physics Letters*, Vol. 92 No. 15, p. 151115.
- Jones, A. and O’Brien, P. (1997), *CVD of Compound Semiconductors: Precursors Synthesis, Development and Applications*, John Wiley and Sons.
- Joo, J., Na, H. B., Yu, T., Yu, J.H., Kim, Y.W., Wu, F., and Zhang, J.Z. (2003), “Generalized and facile synthesis of semiconducting metal sulfide nanocrystals.”, *Journal of the American Chemical Society*, Vol. 125 No. 36, pp. 11100–11105.
- Jung, Y.K., Kim, J. II and Lee, J. (2010), “Thermal Decomposition Mechanism of Single-Molecule Precursors Forming Metal Sulfide Nanoparticles”, *Journal of the American Chemical Society*, Vol. 132 No. 21, pp. 178–184.
- Jungwirth, T., Sinova, J. and Mašek, J. (2006), “Theory of ferromagnetic (III, Mn) V semiconductors”, *Reviews of Modern Physics*, Vol. 78 No. 3, p. 809.
- Kaish, N., Fraser, J. and Durst, D. (1999), “System and method for authentication of goods”, *US Patent 5,974,150*, available at: <https://www.google.com/patents/US5974150> (accessed 1 May 2015).
- Kamat, P. V. (2008), “Quantum Dot Solar Cells. Semiconductor Nanocrystals as Light Harvesters”, *Journal of Physical Chemistry C*, American Chemical Society, Vol. 112 No. 48, pp. 18737–18753.
- Kamata, A. and Yoshida, H. (1996), “Highly Conductive P-Type ZnTeAs Grown by Atmospheric Metalorganic Chemical Vapor Deposition Using Trimethylarsine”, *Japanese Journal of Applied Physics*, Vol. 35 No. Part2, No. 1B, pp. 87–89.

- Kigel, A., Brumer, M., Sashchiuk, A., Amirav, L. and Lifshitz, E. (2005), “PbSe/PbSeS core-alloyed shell nanocrystals”, *Materials Science and Engineering C*, Vol. 25 No. 5-8, pp. 604–608.
- Kim, K. Do and Kim, H.T. (2003), “Comparison of the effect of reaction parameters on particle size in the formation of SiO₂, TiO₂, and ZrO₂ nanoparticles”, *Materials Letters*, Vol. 57 No. 21, pp. 3211–3216.
- Kim, S.-G., Terashi, Y., Purwanto, A. and Okuyama, K. (2009), “Synthesis and film deposition of Ni nanoparticles for base metal electrode applications”, *Colloids and Surfaces A: Physicochemical and Engineering Aspects*, Vol. 337 No. 1-3, pp. 96–101.
- Kirkman, S. (2002), “Labels for detecting counterfeit products”, *US Patent 6,361,079*, available at: <https://www.google.com/patents/US6361079> (accessed 1 May 2015).
- Klem, E.J.D., MacNeil, D.D., Cyr, P.W., Levina, L. and Sargent, E.H. (2007), “Efficient solution-processed infrared photovoltaic cells: Planarized all-inorganic bulk heterojunction devices via inter-quantum-dot bridging during growth from solution”, *Applied Physics Letters*, Vol. 90 No. 18, p. 183113.
- Klokkenburg, M., Houtepen, A.J., Koole, R., de Folter, J.W.J., Ern , B.H., van Faassen, E. and Vanmaekelbergh, D. (2007), “Dipolar structures in colloidal dispersions of PbSe and CdSe quantum dots.”, *Nano letters*, Vol. 7 No. 9, pp. 2931–2936.
- Kohn, S.E., Yu, P.Y., Petroff, Y., Shen, Y.R. and Cohen, M.L. (1973), “Electronic band structure and optical properties of PbTe, PbSe, and PbS”, *Physical Review B*, Vol. 8 No. 4, pp. 1477–1488.

- Koleilat, G., Levina, L., Shukla, H. and Myrskog, S. (2008), “Efficient, stable infrared photovoltaics based on solution-cast colloidal quantum dots”, *Acs Nano*, Vol. 2 No. 5, pp. 833–840.
- Kothiyal, G. and Ghosh, B. (1990), “On conductivity in lead chalcogenides”, *Progress in Crystal Growth and Characterisation*, Vol. 20, pp. 313–332.
- Kraeuter, G., Favreau, P. and Rees, W. (1994), “Use of lead bis (butylthiolate) compounds in a new low-temperature route to highly crystalline lead sulfide: identity and source of reaction byproducts”, *Chemistry of materials*, Vol. 6 No. 4, pp. 543–549.
- Krishnan, V. and Zingaro, R. (1969), “O, O’-Diethyl diselenophosphate as a ligand. Compounds of nontransition elements”, *Inorganic Chemistry*, Vol. 8 No. November, pp. 2337–2340.
- Kudera, S., Carbone, L., Casula, M.F., Cingolani, R., Falqui, A., Snoeck, E., Parak, W.J., et al. (2005), “Selective growth of PbSe on one or both tips of colloidal semiconductor nanorods.”, *Nano letters*, Vol. 5 No. 3, pp. 445–449.
- Kudman, I. and Seidel, T. (1962), “Absorption Edge in Degenerate p-Type GaAs”, *Journal of Applied Physics*, Vol. 33 No. 3, p. 771.
- Labgold, M. and Kolo, L. (2006), “Method and means for detection of counterfeit items and prevention of counterfeiting activities”, *US Patent App. 11/526,211*, available at: <https://www.google.com/patents/US20070199988> (accessed 1 May 2015).
- LaMer, V. and Dinegar, R. (1950), “Theory, production and mechanism of formation of monodispersed hydrosols”, *Journal of the American Chemical Society*, Vol. 72 No. 11, pp. 4847–4854.

- Lee, R., Feinbaum, R. and Ambros, V. (2004), "A Short History", *Cell*, Vol. 116 No. October, p. 2004.
- Lee, S.M., Cho, S.N. and Cheon, J. (2003), "Anisotropic Shape Control of Colloidal Inorganic Nanocrystals", *Advanced Materials*, Vol. 15 No. 5, pp. 441–444.
- Lee, S.-M., Jun, Y., Cho, S.-N. and Cheon, J. (2002), "Single-crystalline star-shaped nanocrystals and their evolution: programming the geometry of nano-building blocks.", *Journal of the American Chemical Society*, American Chemical Society, Vol. 124 No. 38, pp. 11244–11245.
- Li, Q., Ding, Y., Shao, M., Wu, J., Yu, G. and Qian, Y. (2003), "Sonochemical synthesis of nanocrystalline lead chalcogenides: PbE (E = S, Se, Te)", *Materials Research Bulletin*, Vol. 38 No. 3, pp. 539–543.
- Lifshitz, E., Bashouti, M., Kloper, V., Kigel, a., Eisen, M.S. and Berger, S. (2003), "Synthesis and Characterisation of PbSe Quantum Wires, Multipods, Quantum Rods, and Cubes", *Nano Letters*, Vol. 3 No. 6, pp. 857–862.
- Lifshitz, E., Brumer, M., Kigel, a, Sashchiuk, A., Bashouti, M., Sirota, M., and Galun, E. (2006), "Air-stable PbSe/PbS and PbSe/PbSexS1-x core-shell nanocrystal quantum dots and their applications.", *The journal of physical chemistry. B*, Vol. 110 No. 50, pp. 25356–25365.
- Lim, Y.T., Kim, S., Nakayama, A., Stott, N.E., Bawendi, M.G. and Frangioni, J. V. (2003), "Selection of quantum dot wavelengths for biomedical assays and imaging.", *Molecular imaging*, Vol. 2 No. 1, pp. 50–64.

- Liu, G. and Lin, Y. (2007), "Nanomaterial labels in electrochemical immunosensors and immunoassays.", *Talanta*, Vol. 74 No. 3, pp. 308–317.
- Liu, G., Wang, J., Kim, J., Jan, M.R. and Collins, G.E. (2004), "Electrochemical coding for multiplexed immunoassays of proteins.", *Analytical chemistry*, Vol. 76 No. 23, pp. 7126–7130.
- Liu, J., Yu, H., Wu, Z., Wang, W., Peng, J. and Cao, Y. (2008), "Size-tunable near-infrared PbS nanoparticles synthesized from lead carboxylate and sulfur with oleylamine as stabilizer.", *Nanotechnology*, Vol. 19 No. 34, p. 345602.
- Lobana, T., Wang, J. and Liu, C. (2007), "Recent advances in the coordination chemistry of diselenophosphates and allied ligands", *Coordination Chemistry Reviews*, Vol. 251 No. 1-2, pp. 91–110.
- Lu, J., Xie, Y., Xu, F. and Zhu, L. (2002), "Study of the dissolution behavior of selenium and tellurium in different solvents??a novel route to Se, Te tubular bulk single crystals", *Journal of Materials Chemistry*, Vol. 12 No. 9, pp. 2755–2761.
- Luther, J., Law, M., Beard, M. and Song, Q. (2008), "Schottky solar cells based on colloidal nanocrystal films", *Nano Letters*, Vol. 49 No. 10, pp. 3488–3492.
- Ma, J., Wong, H., Kong, L.B. and Peng, K.W. (2003), "Biomimetic processing of nanocrystallite bioactive apatite coating on titanium", *Nanotechnology*, Vol. 14 No. 6, pp. 619–623.
- Ma, W., Luther, J., Zheng, H., Wu, Y. and Alivisatos, A. (2009), "Photovoltaic Devices Employing Ternary PbS x Se_{1-x} Nanocrystals", *Nano letters*, Vol. 9 No. 4, pp. 1699–1703.

- Ma, W., Swisher, S., Ewers, T. and Engel, J. (2011), “Photovoltaic performance of ultrasmall PbSe quantum dots”, *ACS nano*, Vol. 5 No. 10, pp. 8140–8147.
- Manasevit, H. (1968), “Single Crystal Gallium Arsenide on Insulating Substrates”, *Applied Physics Letters*, Vol. 12 No. 4, pp. 156–159.
- Manasevit, H.M., Erdmann, F.M. and Simpson, W.I. (1971), “The Use of Metalorganics in the Preparation of Semiconductor Materials”, *Journal of The Electrochemical Society*, The Electrochemical Society, Vol. 118 No. 11, p. 1864.
- Mandal, T., Piburn, G., Stavila, V., Rusakova, I., Ould-ely, T., Colson, A.C. and Whitmire, K.H. (2011), “New Mixed Ligand Single-Source Precursors for PbS Nanoparticles and Their Solvothermal Decomposition to Anisotropic Nano- And Microstructures”, *Chemistry of Materials*, Vol. 23, pp. 4158–4169.
- Maria, A., Cyr, P.W., Klem, E.J.D., Levina, L. and Sargent, E.H. (2005), “Solution-processed infrared photovoltaic devices with >10% monochromatic internal quantum efficiency”, *Applied Physics Letters*, Vol. 87 No. 21, p. 213112.
- McDonald, S.A., Cyr, P.W., Levina, L. and Sargent, E.H. (2004), “Photoconductivity from PbS-nanocrystal/semiconducting polymer composites for solution-processible, quantum-size tunable infrared photodetectors”, *Applied Physics Letters*, Vol. 85 No. 11, p. 2089.
- Mokari, T., Zhang, M. and Yang, P. (2007), “Shape, size, and assembly control of PbTe nanocrystals.”, *Journal of the American Chemical Society*, Vol. 129 No. 32, pp. 9864–9865.

- Mora-Seró, I. and Bisquert, J. (2010), “Breakthroughs in the Development of Semiconductor-Sensitized Solar Cells”, *The Journal of Physical Chemistry Letters*, Vol. 1 No. 20, pp. 3046–3052.
- Murray, C., Sun, S. and Gaschler, W. (2001), “Colloidal synthesis of nanocrystals and nanocrystal superlattices”, *IBM Journal of Research and Development*, Vol. 45 No. 1, pp. 47–56.
- Murray, C.B., Norris, D.J. and Bawendi, M.G. (1993), “Synthesis and Characterisation of Nearly Monodisperse CdE (E=S, Se, Te) Semiconductor Nanocrystallites”, *Journal of American Chemical Society*, Vol. 115 No. 19, pp. 8706–8715.
- Nanda, K., Kruis, F., Fissan, H. and Acet, M. (2002), “Band-gap tuning of PbS nanoparticles by in-flight sintering of size classified aerosols”, *Journal of applied physics*, Vol. 91 No. 3, pp. 2315–2321.
- Nguyen, C.Q., Adeogun, A., Afzaal, M., Malik, M. a and O’Brien, P. (2006), “Metal complexes of selenophosphinates from reactions with $(R_2PSe)_2Se$: $[M(R_2PSe)_n]$ (M = Zn(II), Cd(II), Pb(II), In(III), Ga(III), Cu(I), Bi(III), Ni(II); R = (i)Pr, Ph) and $[Mo(V)_2O_2Se_2(Se_2P(i)Pr)_2]$.”, *Chemical communications (Cambridge, England)*, Vol. 454 No. 20, pp. 2182–2184.
- O’Brien, P. and Nomura, R. (1995), “Single-molecule Precursor Chemistry for the Deposition of Chalcogenide(S or Se)-containing Compound Semiconductors by MOCVD and Related Methods”, *Journal of Materials Chemistry*, Vol. 5 No. 11, pp. 1761–1773.

- Onicha, A.C., Petchsang, N., Kosel, T.H. and Kuno, M. (2012), “Controlled Synthesis of Compositionally Tunable Ternary PbSe_xS_{1-x} as Well as Binary PbSe and PbS Nanowires”, *ACS nano*, Vol. 6 No. 3, pp. 2833–2843.
- Orgel, L. (1959), “The stereochemistry of B subgroup metals. Part II. The inert pair”, *Journal of the Chemical Society (Resumed)*, pp. 3815–3819.
- Pantarotto, D., Partidos, C.D., Hoebeke, J., Brown, F., Kramer, E., Briand, J., Muller, S., et al. (2003), “Immunization with Peptide-Functionalized Carbon Nanotubes Enhances Virus-Specific Neutralizing Antibody Responses”, *chemistry and Biology*, Vol. 10 No. Figure 1, pp. 961–966.
- Paquet, C., Yoshino, F., Levina, L., Gourevich, I., Sargent, E.H. and Kumacheva, E. (2006), “High-Quality Photonic Crystals Infiltrated with Quantum Dots”, *Advanced Functional Materials*, Vol. 16 No. 14, pp. 1892–1896.
- Parr, J. (1997), “Some recent coordination chemistry of lead (II)”, *Polyhedron*, Vol. 16 No. 4, pp. 551–566.
- Parr, J. (2004), “Germanium, tin, and lead”, in McCleverty, J.A. and Meyer, T.J. (Eds.), *Comprehensive Coordination Chemistry II*, Elsevier, pp. 545–608.
- Pearson, R. (1963), “Hard and soft acids and bases”, *Journal of the American Chemical Society*, Vol. 85 No. 22, pp. 3533–3539.
- Pickett, N.L. and O’Brien, P. (2001), “Syntheses of semiconductor nanoparticles using single-molecular precursors.”, *Chemical record (New York, N.Y.)*, Vol. 1 No. 6, pp. 467–479.

- Pietryga, J.M., Schaller, R.D., Werder, D., Stewart, M.H., Klimov, V.I. and Hollingsworth, J. a. (2004), “Pushing the band gap envelope: mid-infrared emitting colloidal PbSe quantum dots.”, *Journal of the American Chemical Society*, Vol. 126 No. 38, pp. 11752–11753.
- Pilkington, M., Slawin, A., Williams, D. and Woollins, J. (1991), “The X-ray crystal structure of Na[Ph₂PSe₂]₂.THF.5H₂O: a polymer containing six-membered sodium-water rings and sodium coordinated by selenium”, *Polyhedron*, Vol. 10 No. 22, pp. 2641–2645.
- Pradhan, N., Katz, B. and Efrima, S. (2003), “Synthesis of High-Quality Metal Sulfide Nanoparticles from Alkyl Xanthate Single Precursors in Alkylamine Solvents”, *The Journal of Physical Chemistry B*, Vol. 107 No. 50, pp. 13843–13854.
- Pyykko, P. and Desclaux, J. (1979), “Relativity and the periodic system of elements”, *Accounts of Chemical Research*, pp. 276–281.
- Qi, D., Fischbein, M., Drndić, M. and Selmić, S. (2005), “Efficient polymer-nanocrystal quantum-dot photodetectors”, *Applied Physics Letters*, Vol. 86 No. 9, p. 093103.
- Qi, X. and Zhang, S. (2011), “Topological insulators and superconductors”, *Reviews of Modern Physics*, available at: http://rmp.aps.org/abstract/RMP/v83/i4/p1057_1 (accessed 17 March 2014).
- Rakhshani, A.E. (1997), “Electrodeposited CdTe—optical properties”, *Journal of Applied Physics*, Vol. 81 No. 12, p. 7988.
- Ramasamy, K., Malik, M.A. and O’Brien, P. (2011), “The chemical vapor deposition of Cu₂ZnSnS₄ thin films”, *Chemical Science*, The Royal Society of Chemistry, Vol. 2 No. 6, p. 1170.

- Ramesh, K.T. (2009), *Nanomaterials*, Springer US, Boston, MA, pp. 1–20.
- Rao, C., Müller, A. and Cheetham, A. (2006), “The chemistry of nanomaterials: Synthesis, Properties and Applications”, Wiley-VCH Verlag GmbH and Co. KGaA, Vol. 1.
- Rees, W. and Kräuter, G. (1993), “Processable, Chemical Routes to Binary Metal Sulfides”, *MRS Proceedings*, Vol. 327, p. 3.
- Rees, W. and Kräuter, G. (1996), “Preparation and characterisation of several group 12 element (Zn, Cd)-bis (thiolate) complexes and evaluation of their potential as precursors for 12–16”, *Journal of materials research*, Vol. 11 No. 12, pp. 3005–3016.
- Rees, W.S. and Kräuter, G. (1994a), “New Molecular-Based Routes to Binary Main Group Metal Sulfides”, *Phosphorus, Sulfur, and Silicon and the Related Elements*, Vol. 87 No. 1-4, pp. 219–228.
- Rees, W.S. and Kräuter, G. (1994b), “Intra-Ring Differentiation Between MS and MX in the Preparation of Electronic Materials from Metal Thiolate Precursors”, *Phosphorus, Sulfur, and Silicon and the Related Elements*, Vol. 93 No. 1-4, pp. 339–344.
- Rhee, J.H., Chung, C.-C. and Diau, E.W.-G. (2013), “A perspective of mesoscopic solar cells based on metal chalcogenide quantum dots and organometal-halide perovskites”, *NPG Asia Materials*, Nature Publishing Group, Vol. 5 No. 10, p. e68.
- Ritch, J.S., Chivers, T., Ahmad, K., Afzaal, M. and O’Brien, P. (2010), “Synthesis, structures, and multinuclear NMR spectra of tin(II) and lead(II) complexes of tellurium-containing imidodiphosphate ligands: preparation of two morphologies of phase-pure PbTe from a single-source precursor.”, *Inorganic chemistry*, Vol. 49 No. 3, pp. 1198–1205.

- Ritch, J.S., Chivers, T., Eisler, D.J. and Tuononen, H.M. (2007), “Experimental and theoretical investigations of structural isomers of dichalcogenoimidodiphosphate dimers: dichalcogenides or spirocyclic contact ion pairs?”, *Chemistry (Weinheim an der Bergstrasse, Germany)*, Vol. 13 No. 16, pp. 4643–4653.
- Robertson, S.D. and Chivers, T. (2008), “Synthesis, NMR characterisation and X-ray structures of mixed chalcogenido PNP ligands containing tellurium: crystal structures of $\text{SeiPr}_2\text{PNP(H)iPr}_2$ and $[\text{NaN(EPiPr}_2)_2]_{\text{infinity}}$ (E = Se, Te).”, *Dalton transactions (Cambridge, England : 2003)*, Vol. 2 No. 13, pp. 1765–1772.
- Roduner, E. (2006), *Nanoscopic materials: size-dependent phenomena*, Royal Society of Chemistry.
- Rogach, A.L., Eychmüller, A., Hickey, S.G. and Kershaw, S. V. (2007), “Infrared-emitting colloidal nanocrystals: synthesis, assembly, spectroscopy, and applications.”, *Small (Weinheim an der Bergstrasse, Germany)*, Vol. 3 No. 4, pp. 536–557.
- Rowell, M.W., Topinka, M. a., McGehee, M.D., Prall, H.-J., Dennler, G., Sariciftci, N.S., Hu, L., et al. (2006), “Organic solar cells with carbon nanotube network electrodes”, *Applied Physics Letters*, Vol. 88 No. 23, p. 233506.
- Saeed, S., Rashid, N., Azad Malik, M., O’Brien, P. and Wong, W.-T. (2013), “Nickel(II) complexes of N -(dialkylcarbamothioyl)-4-nitrobenzamide as single-source precursors for the deposition of nanostructured nickel sulfide thin films by chemical vapor deposition”, *Journal of Coordination Chemistry*, Taylor & Francis, Vol. 66 No. 16, pp. 2788–2801.

- Saga, T. (2010), “Advances in crystalline silicon solar cell technology for industrial mass production”, *NPG Asia Materials*, Vol. 2 No. July, pp. 96–102.
- Salavati-Niasari, M., Sobhani, A. and Davar, F. (2010), “Synthesis of star-shaped PbS nanocrystals using single-source precursor”, *Journal of Alloys and Compounds*, Elsevier B.V., Vol. 507 No. 1, pp. 77–83.
- Sankaran, V., Cummins, C., Schrock, R., Cohen, R. and Silbey, R. (1990), “Small lead sulfide (PbS) clusters prepared via ROMP block copolymer technology”, *Journal of the American Chemical Society*, Vol. 112 No. 19, pp. 6858–6859.
- Schaller, R.D., Petruska, M. a. and Klimov, V.I. (2003), “Tunable Near-Infrared Optical Gain and Amplified Spontaneous Emission Using PbSe Nanocrystals”, *The Journal of Physical Chemistry B*, Vol. 107 No. 50, pp. 13765–13768.
- Schmidpeter, A., Böhm, R. and Groeger, H. (1964), “Imidodiphosphinatometal Chelates, Neutral Complexes with Carbon-Free Chelate Rings”, *Angewandte Chemie (International ed. in English)*, Vol. 3 No. 10, p. 704.
- Schneider, J., Hagen, J. and Heinemann, O. (1997), “Synthesis and characterisation of organometallic precursors for the preparation of Sn/chalcogenide heterostructures”, *Thin Solid Films*, Vol. 304, pp. 144–148.
- Schneider, T., Haase, M., Kornowski, A., Naused, S., Weller, H., Förster, S. and Antonietti, M. (1997), “Synthesis and characterisation of PbS nanoparticles in block copolymer micelles”, *Berichte der Bunsengesellschaft für physikalische Chemie*, Vol. 101, pp. 1654–1656.

- Schultz, O., Glunz, S. and Willeke, G. (2004), "Short communication: Accelerated publication: Multicrystalline silicon solar cells exceeding 20% efficiency", *Progress in Photovoltaics: Research and Applications*, Vol. 12 No. 7, pp. 553–558.
- Seligson, A.L. and Arnold, J. (1993), "Synthesis, Structure, and Reactivity of Homoleptic Tin (II) and Lead (II) Chalcogenolates and Their Conversion to Metal Chalcogenides. X-ray Crystal Structures of $\{\text{Sn}[\text{TeSi}(\text{SiMe}_3)_3]_2\}_2$ and $(\text{PMe}_3)\text{Sn}[\text{TeSi}(\text{SiMe}_3)_3]_2$ ", *Journal of American Chemical Society*, Vol. 115 No. 18, pp. 8214–8220.
- Shchennikov, V. V and Ovsyannikov, S. V. (2003), "Thermoelectric power, magnetoresistance of lead chalcogenides in the region of phase transitions under pressure", *Solid State Communications*, Vol. 126 No. 7, pp. 373–378.
- Sheldrick, G.. (1997), *SHELXL97, Program for refinement of crystal structures*, University of Göttingen, Germany, Vol. 39, doi:10.1177/004057368303900411.
- Sheldrick, G.M. (2008), "A short history of SHELX.", *Acta crystallographica. Section A, Foundations of crystallography*, International Union of Crystallography, Vol. 64 No. Pt 1, pp. 112–122.
- Shih, H.D. and Jona, F. (1976), "Atomic Underlayer Formation During The Reaction of Ti $\{0001\}$ with Nitrogen", *Surface Science*, Vol. 60, pp. 445–465.
- Shimoni-Livny, L., Glusker, J. and Bock, C. (1998), "Lone pair functionality in divalent lead compounds", *Inorganic Chemistry*, Vol. 37, pp. 1853–1867.
- Sidgwick, N.. and Powell, H.. (1940), "Stereochemical types and valency groups", *Proceedings of the Royal Society of London A*, Vol. 176, pp. 153–180.

- Singh, J. (2006), “Optical properties of condensed matter and applications”, John Wiley and Sons, Vol. 6.
- Solomeshch, O., Kigel, A., Saschiuk, A., Medvedev, V., Aharoni, A., Razin, A., Eichen, Y., et al. (2005), “Optoelectronic properties of polymer-nanocrystal composites active at near-infrared wavelengths”, *Journal of Applied Physics*, Vol. 98 No. 7, pp. 074310–074316.
- Sun, J., Zhu, M.-Q., Fu, K., Lewinski, N. and Drezek, R. A. (2007), “Lead sulfide near-infrared quantum dot bioconjugates for targeted molecular imaging.”, *International journal of nanomedicine*, Vol. 2 No. 2, pp. 235–240.
- Sun, S., Han, Q., Wu, X., Zhu, J. and Wang, X. (2011), “The facile synthesis of PbS cubes and Bi₂S₃ nanoflowers from molecular precursors at room temperature”, *Materials Letters*, Elsevier B.V., Vol. 65 No. 21-22, pp. 3344–3347.
- Suresh, R., Ponnuswamy, V., Chandrasekaran, J., Manoharan, D. and Mariappan, R. (2013), “The effect of annealing temperature and the characteristics of p–n junction diodes based on sprayed polyaniline/ZnO thin films”, *Journal of Semiconductors*, Vol. 34 No. 8, p. 083001.
- SWGSR. (2011), *Guide for Primer Gunshot Residue Analysis by Scanning Electron Microscopy / Energy Dispersive X-Ray Spectrometry 11-29-11*, pp. 1–100.
- Tai, G., Guo, W. and Zhang, Z. (2008), “Hydrothermal synthesis and thermoelectric transport properties of uniform single-crystalline pearl-necklace-shaped PbTe nanowires”, *Crystal Growth and Design*, Vol. 8 No. 8, pp. 2906–2911.

- Takagahara, T. (1993), "Electron-Phonon Interactions and Excitonic Dephasing in Semiconductor Nanocrystals", *Physical Review Letters*, Vol. 71 No. 21, pp. 3577–3580.
- Tamari, N. and Shtrikman, H. (1979), "Growth study of large non-seeded $Pb_{1-x}Sn_xTe$ single crystals", *Journal of Electronic Materials*, Vol. 8 No. 3, pp. 269–288.
- Tang, J., Kemp, K.W., Hoogland, S., Jeong, K.S., Liu, H., Levina, L., Furukawa, M., et al. (2011), "Colloidal-quantum-dot photovoltaics using atomic-ligand passivation", *Nature materials*, Nature Publishing Group, Vol. 10 No. 10, pp. 765–771.
- Tiekink, E. and Haiduc, I. (2005), "Stereochemical aspects of metal xanthate complexes. Molecular structures and supramolecular self-assembly", *Prog. Inorg. Chem*, Vol. 54, p. 127.
- Tong, H., Zhu, Y.-J., Yang, L.-X., Li, L. and Zhang, L. (2006), "Lead chalcogenide nanotubes synthesized by biomolecule-assisted self-assembly of nanocrystals at room temperature.", *Angewandte Chemie (International ed. in English)*, Vol. 45 No. 46, pp. 7739–7742.
- Trindade, T., Monteiro, O.C., O'Brien, P. and Motevalli, M. (1999), "Synthesis of PbSe nanocrystallites using a single-source method. The X-ray crystal structure of lead (II) diethyldiselenocarbamate", *Polyhedron*, Vol. 18 No. 8-9, pp. 1171–1175.
- Trindade, T., O'Brien, P., Zhang, X. and Motevalli, M. (1997), "Synthesis of PbS nanocrystallites using a novel single molecule precursors approach : X-ray single-crystal structure of $Pb(SCN)_2$ ", *Journal of Materials Chemistry*, Vol. 7 No. 6, pp. 1011–1016.

- Urban, J.J., Talapin, D. V, Shevchenko, E. V and Murray, C.B. (2006), “Self-assembly of PbTe quantum dots into nanocrystal superlattices and glassy films.”, *Journal of the American Chemical Society*, Vol. 128 No. 10, pp. 3248–3255.
- Varadarajan, J., Resan, M., Wu, F., Pfenninger, W.M., Vockic, N. and Kenney, J. (2010), “doped cesium tin halides and electron acceptors and electron donors; use in anti-counterfeiting, inventory, photovoltaic devices; photoluminescence”, *US Patent 7,641,815*, Google Patents, available at: <https://www.google.com/patents/US7641815> (accessed 1 May 2015).
- Walker, B.K. (2013), “Anti-Counterfeiting Technology in Materials Science”, pp. 1–3. <http://www.azom.com/article.aspx?ArticleID=10252> P. (accessed 3 May 2015)
- Walsh, A. and Watson, G.W. (2005), “The origin of the stereochemically active Pb(II) lone pair: DFT calculations on PbO and PbS”, *Journal of Solid State Chemistry*, Vol. 178 No. 5, pp. 1422–1428.
- Wang, F., Najdzionek, J., Leneker, K.L., Wasserman, H. and Braitsch, D.M. (1978), “A Facile Synthesis of Imidotetraphenyldiphosphinic Acids”, *Synthesis and Reactivity in Inorganic and Metal-Organic Chemistry*, Vol. 8 No. 2, pp. 119–125.
- Wang, J. (2005), “Nanomaterial-based amplified transduction of biomolecular interactions.”, *Small (Weinheim an der Bergstrasse, Germany)*, Vol. 1 No. 11, pp. 1036–1043.
- Wang, J. (2007), “Nanoparticle-Based Electrochemical Bioassays of Proteins”, *Electroanalysis*, Vol. 19 No. 7-8, pp. 769–776.

- Wang, J., Liu, G. and Merkoçi, A. (2003), “Electrochemical coding technology for simultaneous detection of multiple DNA targets.”, *Journal of the American Chemical Society*, Vol. 125 No. 11, pp. 3214–3215.
- Warner, J.H., Thomsen, E., Watt, A.R., Heckenberg, N.R. and Rubinsztein-Dunlop, H. (2005), “Time-resolved photoluminescence spectroscopy of ligand-capped PbS nanocrystals.”, *Nanotechnology*, Vol. 16 No. 2, pp. 175–179.
- Waters, J., Crouch, D., Raftery, J. and O’Brien, P. (2004), “Deposition of bismuth chalcogenide thin films using novel single-source precursors by metal-organic chemical vapor deposition”, *Chemistry of materials*, Vol. 16, pp. 3289–3298.
- West, A.R. (1999), *Basic Solid State Chemistry*, Wiley, p. 496.
- Wijayantha, K.G.U., Peter, L.M. and Otley, L.C. (2004), “Fabrication of CdS quantum dot sensitized solar cells via a pressing route”, *Solar Energy Materials and Solar Cells*, Vol. 83 No. 4, pp. 363–369.
- Wilhelmy, D. and Matijević, E. (1984), “Preparation and properties of monodispersed spherical-colloidal particles of zinc sulphide”, *J. Chem. Soc., Faraday Trans. 1*, Vol. 80, pp. 563–570.
- Wu, Z., Mi, Z., Bhattacharya, P., Zhu, T. and Xu, J. (2007), “Enhanced spontaneous emission at 1.55 μm from colloidal PbSe quantum dots in a Si photonic crystal microcavity”, *Applied Physics Letters*, Vol. 90 No. 17, p. 171105.
- Xu, J., Ge, J.-P. and Li, Y.-D. (2006), “Solvothermal synthesis of monodisperse PbSe nanocrystals.”, *The journal of physical chemistry. B*, Vol. 110 No. 6, pp. 2497–2501.

- Yamamoto, M. and Nakamoto, M. (2003), "Novel preparation of monodispersed silver nanoparticles via amine adducts derived from insoluble silver myristate in tertiary alkylamine", *Journal of Materials Chemistry*, Vol. 13 No. 9, p. 2064.
- Yellin, N. and Ben-Dor, L. (1983), "Low temperature synthesis of binary chalcogenides", *Materials Research Bulletin*, Vol. 18 No. 7, pp. 823–827.
- Yong, K. and Sahoo, Y. (2006), "Control of the morphology and size of PbS nanowires using gold nanoparticles", *Chemistry of Materials*, Vol. 18, pp. 5965–5972.
- Yoshikawa, A., Sirai, A., Yamaga, S. and Kasai, H. (1986), "Growth Mechanism of ZnS and ZnSe Films in Low-Pressure MOCVD", *Japanese Journal of Applied Physics*, Vol. 25, pp. 673–678.
- Zhang, L., Yu, J.C., Mo, M., Wu, L., Kwong, K.W. and Li, Q. (2005), "A general in situ hydrothermal rolling-up formation of one-dimensional, single-crystalline lead telluride nanostructures.", *Small (Weinheim an der Bergstrasse, Germany)*, Vol. 1 No. 3, pp. 349–354.
- Zhang, S., Cyr, P.W., McDonald, S.A., Konstantatos, G. and Sargent, E.H. (2005), "Enhanced infrared photovoltaic efficiency in PbS nanocrystal/semiconducting polymer composites: 600-fold increase in maximum power output via control of the ligand barrier", *Applied Physics Letters*, Vol. 87 No. 23, p. 233101.
- Zhang, W., Zhang, L., Cheng, Y. and Hui, Z. (2000), "Synthesis of nanocrystalline lead chalcogenides PbE (E= S, Se, or Te) from alkaline aqueous solutions", *Materials Research Bulletin*, Vol. 35 No. 12, pp. 2009–2015.

- Zhang, Y.C., Qiao, T., Hu, X.Y., Wang, G.Y. and Wu, X. (2005), "Shape-controlled synthesis of PbS microcrystallites by mild solvothermal decomposition of a single-source molecular precursor", *Journal of Crystal Growth*, Vol. 277 No. 1-4, pp. 518–523.
- Zhang, Z., Lee, S., Vittal, J. and Chin, W. (2006), "A simple way to prepare PbS nanocrystals with morphology tuning at room temperature", *The Journal of Physical Chemistry B*, Vol. 110, pp. 6649–6654.
- Zhou, G., Lü, M., Xiu, Z., Wang, S., Zhang, H., Zhou, Y. and Wang, S. (2006), "Controlled synthesis of high-quality PbS star-shaped dendrites, multipods, truncated nanocubes, and nanocubes and their shape evolution process.", *The journal of physical chemistry. B*, Vol. 110 No. 13, pp. 6543–6548.
- Zhu, J., Aruna, S.T., Koltypin, Y. and Gedanken, A. (2000), "A novel method for the preparation of lead selenide: pulse sonoelectrochemical synthesis of lead selenide nanoparticles", *Chemistry of Materials*, Vol. 12 No. 1, pp. 143–147.
- Zhu, J., Wang, H., Xu, S. and Chen, H. (2002), "Sonochemical method for the preparation of monodisperse spherical and rectangular lead selenide nanoparticles", *Langmuir*, Vol. 18, pp. 3306–3310.
- Zhu, W., Wang, W. and Shi, J. (2006), "A reverse cation-exchange route to hollow PbSe nanospheres evolving from Se/Ag₂Se core/shell colloids.", *The journal of physical chemistry. B*, Vol. 110 No. 20, pp. 9785–9790.

APPENDICES

Appendix 1

List of Publications

Boadi, N.O., Malik, M.A., O'Brien, P. and Awudza, J.A.M. (2012), "Single-source molecular complex routes to lead chalcogenides.", *Dalton Transactions*, Vol. 41, pp. 10497–10506.

Boadi, N.O., McNaughter, P., Awudza, J.A.M., Malik, M.A., Helliwell, M. and O'Brien, P. (2014). *Bis*(diisopropylphosphinechalcogeno)amine lead(II) complexes for the deposition of PbS and PbSe thin films by AACVD. (*In preparation*)

Boadi, N.O., McNaughter, P., Awudza, J.A.M., Malik, M.A., Raftery, J. and O'Brien, P. (2014). Potential Single Source Complexes for the synthesis of $\text{PbS}_x\text{Se}_{1-x}$ nanoparticles and thin films. (*In preparation*)